UNIVERSITY OF CALIFORNIA SAN DIEGO

Decoding Environmentally Driven Gene Regulatory Networks in Hepatic Macrophages

A dissertation submitted in partial satisfaction of the requirements for the degree Doctor of Philosophy

in

Biomedical Sciences

by

Jason Samuel Seidman

Committee in charge:

Professor Christopher K. Glass, Chair
Professor Michael Karin
Professor Anjana Rao
Professor Michael G. Rosenfeld
Professor Joseph L. Witztum

2019

The Dissertation of Jason Samuel Seidman is approved, and it is acceptable in quality and form for publication on microfilm and electronically:

_____

_____

_____

_____

_____

_____

Chair

University of California San Diego

2019

TABLE OF CONTENTS

LIST OF ABBREVIATIONS

ATAC-seq	Assay for Transposase-Accessible Chromatin using sequencing
BMDM	Bone Marrow Derived Macrophage
BP	Base Pair
bZIP	Basic Leucine Zipper Domain
ChIP-seq	Chromatin Immunoprecipitation
CNS	Central Nervous System
DKO	Double Knockout
DNA	Deoxyribonucleic acid
DT	Diphtheria Toxin
DTR	Diphtheria Toxin Receptor
FACS	Fluorescence Activated Cell Sorting
FDR	False Discovery Rate
HSC	Hematopoietic Stem Cell
IDR	Irreproducible Discovery Rate
IRES	Internal Ribosome Entry Site
KC	Kupffer cell
KO	Knockout
Log2FC	Log(2) Fold Change
LPS	Lipopolysaccharide
LSL	Lox-stop-lox
M-CSF	Macrophage Colony Stimulating Factor

MHC	Major Histocompatibility Complex
NALFD	Nonalcoholic Fatty Liver Disease
NASH	Nonalcoholic Steatohepatitis
NF-KB	Nuclear Localization Signal
p-adj	Adjusted p value
PCR	Polymerase Chain Reaction
PFA	Paraformaldehyde
qPCR	quantitative Polymerase Chain Reaction
RBC	Red Blood Cell
RLM	Recruited Liver M
RNA-seq	RNA-sequencing
ROS	Reactive Oxygen Species
SD	Standard Deviation
TF	Transcription Factor
TPM	Transcripts per million
TSNE	t-distributed stochastic neighbor embedding
TSS	Transcription Start Site
TUNEL	terminal deoxynucleotidyl transferase dUTP nick end labeling

LIST OF FIGURES

LIST OF TABLES

ACKNOWLEDGEMENTS

I would like to acknowledge Professor Christopher K. Glass for his guidance and support over the past five years. Glass lab members Ty Troutman and Mashito Sakai were outstanding scientific mentors and colleagues. I would also like to thank my other committee members for their valuable feedback on these projects. My graduate study was supported in part by funds provided through the Rosenfeld T32 Training Grant, the UCSD Medical Scientist Training Program, the UCSD Biomedical Sciences Program, and an American Heart Association Pre-doctoral Fellowship.

Chapter 2, in full, is adapted from a manuscript currently in review at *Immunity*. The dissertation author was the co-primary author of this paper along with Ty D. Troutman and Mashito Sakai. Other authors include Zhengyu Ouyang, Nathanael J. Spann, Yohei Abe, Kaori M. Ego, Cassi M. Bruni, Johannes C. M Schlachetzki, Alexi, Nott, Hunter Bennett, Jonathan Chang, BaoChau T. Vu, Martina P. Pasillas, Verena M. Link, Bonne M. Thompson, Jeffrey G. McDonald, and Christopher K. Glass.

These studies were supported by NIH grants DK091183, HL088083 and GM085764. MS was supported by the Manpei Suzuki Diabetes Foundation of Tokyo, Japan, and the Osamu Hayaishi Memorial Scholarship for Study Abroad, Japan. TDT was supported by P30 DK063491, T32DK007044, and NRSA T32CA009523. JSS was supported by American Heart Association Fellowship 16PRE30980030 and NIH Predoctoral Training Grant 5T32DK007541. YA was supported by Japan Society for the Promotion of Science Overseas Research Fellowship.

Chapter 3, in full, is adapted from a manuscript currently in review at *Cell*. The dissertation author was the co-primary author of this paper along with Ty D. Troutman and Mashito Sakai. Other authors include Anita Gola, Zhengyu Ouyang, Nathanael J. Spann, Cassi M. Bruni, Hunter Bennett, Xiaoli Sun, BaoChau T. Vu, Martina P. Pasillas, Kaori M. Ego , David Gosselin, Verena M. Link, Bonne M. Thompson, Jeffery G. McDonald, Joseph L. Witztum, Ronald N. Germain, and Christopher K. Glass.

These studies were supported by NIH grants DK091183, HL088083 and GM085764. JSS was supported by American Heart Association Fellowship 16PRE30980030 and NIH Predoctoral Training Grant 5T32DK007541. TDT was supported by P30 DK063491, T32DK007044, and NRSA T32CA009523. M.S. was supported by the Manpei Suzuki Diabetes Foundation of Tokyo, Japan, and the Osamu Hayaishi Memorial Scholarship for Study Abroad, Japan. X.S was supported by The American Heart Association Grant 18POST34060088. This work as also supported in part by the Intramural Research program of NIAID, NIH.

VITA

2004-2008 Bachelor of Science, University of California, Santa Barbara, Santa Barbara, California

2008-2010 Master of Arts, University of California, Santa Barbara, Santa Barbara, California

2012-2014 University of California, San Diego, School of Medicine

2019 Doctor of Philosophy, University of California, San Diego

PUBLICATIONS

Zisser H, Gong P, Kelley CM, **Seidman JS**, Riddell MC. Exercise and diabetes. International journal of clinical practice. Supplement. 2011; (170):71-5. PubMed [journal] PMID: 21323815

Seidman JS, Janssen BD, Hayes CS. Alternative fates of paused ribosomes during translation termination. The Journal of biological chemistry. 2011; 286(36):31105-12. PubMed [journal] PMID: 21757758, PMCID: PMC3173060

Fonseca GJ, **Seidman JS**, Glass CK. Genome-Wide Approaches to Defining Macrophage Identity and Function. Microbiology spectrum. 2016; 4(5). NIHMSID: NIHMS811570 PubMed [journal] PMID: 28087927, PMCID: PMC5240536

Pirzgalska RM, Seixas E**, Seidman JS**, Link VM, Sánchez NM, Mahú I, Mendes R, Gres V, Kubasova N, Morris I, Arús BA, Larabee CM, Vasques M, Tortosa F, Sousa AL, Anandan S, Tranfield E, Hahn MK, Iannacone M, Spann NJ, Glass CK, Domingos AI. Sympathetic neuron-associated macrophages contribute to obesity by importing and metabolizing norepinephrine. Nature medicine. 2017; 23(11):1309-1318. PubMed [journal] PMID: 29035364

Muse ED, Yu S, Edillor CR, Tao J, Spann NJ, Troutman TD, **Seidman JS**, Henke A, Roland JT, Ozeki KA, Thompson BM, McDonald JG, Bahadorani J, Tsimikas S, Grossman TR, Tremblay MS, Glass CK. Cell-specific discrimination of desmosterol and desmosterol mimetics confers selective regulation of LXR and SREBP in macrophages. Proceedings of the National Academy of Sciences of the United States of America. 2018; 115(20):E4680-E4689. PubMed [journal] PMID: 29632203, PMCID: PMC5960280

Ying W, Lee YS, Dong Y, **Seidman JS**, Yang M, Isaac R, Seo JB, Yang BH, Wollam J, Riopel M, McNelis J, Glass CK, Olefsky JM, Fu W. Expansion of Islet-Resident Macrophages Leads to Inflammation Affecting β Cell Proliferation and Function in Obesity. Cell metabolism. 2018; PubMed [journal] PMID: 30595478

Moore SM, **Seidman JS**, Ellegood J, Gao R, Savchenko A, Troutman TD, Abe Y, Stender J, Lee D, Wang S, Voytek B, Lerch JP, Suh H, Glass CK, Muotri AR. Setd5 haploinsufficiency alters neuronal network connectivity and leads to autistic-like behaviors in mice. Translational psychiatry. 2019; 9(1):24. PubMed [journal] PMID: 30655503

ABSTRACT OF THE DISSERTATION

Decoding Environmentally Driven Gene Regulatory Networks in Hepatic Macrophages

by

Jason Samuel Seidman

Doctor of Philosophy in Biomedical Sciences

University of California, San Diego, 2019

Professor Christopher K. Glass, Chair

The following work uses multi-level genomics approaches coupled with mouse models to study the gene regulatory networks in hepatic macrophages during both healthy conditions and liver disease. Chapter 1 will serve as an introduction, reviewing what is currently known about regulation of gene expression by sequence specific transcription factors and enhancers, how niche specific environmental signals are relayed through this regulatory machinery to produce the unique phenotypes of different populations of tissue resident macrophages, and how Kupffer cells and recruited macrophages function in the liver during nonalcoholic steatohepatitis. Chapter 2 utilizes a model system of experimental Kupffer cell ablation and repopulation to dissect the pathways that allow bone marrow derived monocytes to differentiate into Kupffer cell-like macrophages. Using this system, we found that TGF/SMAD, Notch/RBPJ, and LXR are critical pathways underlying Kupffer cell identity. Chapter 3 investigates the changes that occur to macrophages during experimentally induced fatty liver disease in mice. Bone marrow derived monocytes were recruited to both liver sinusoids (the Kupffer cell niche) and large diameter vessels and displayed divergent patterns of open chromatin and gene expression based on their destination. Further, embryonically derived Kupffer cells lost enhancer activity disproportionately at regulatory regions important for Kupffer cell identity. This loss of enhancer activity correlated with a selective loss of LXR binding at these regions. Liver disease also selectively resulted in apoptosis of embryonically derived Kupffer cells and their replacement with bone marrow derived precursors. Chapter 4 will discuss the broader implications of these studies.

Chapter 1. Introduction to Transcriptional Regulation, Tissue Resident Macrophages, and Nonalcoholic Fatty Liver Disease

A. Basic Mechanisms for Regulation of Gene Expression

A central question in biology is how gene expression is regulated to allow for cell type specific phenotypes, cellular differentiation, and signal dependent responses. While all cells within the body of a multicellular organism essentially share the same DNA sequences, epigenetic modifications provide instructions for how, when and to what degree specific genes should be expressed. These modifications function primarily to control the ability of the transcriptional machinery to access target DNA sequences.

DNA exists in the nucleus in complexes with histone proteins, forming chromatin. Chromatin formation is essential to organize and compact the two meters of DNA that exists in every human cell so that can be stored inside the nucleus (1). Importantly, formation of chromatin also provides the basis for epigenetic regulation of the genome. At the most basic structural level, an octamer of histone proteins forms a bead shaped core nucleosome, around which 145-147 of DNA base pairs is wrapped twice. Nucleosome bound DNA provides steric hinderance to RNA-polymerase and associated factors that can promote transcription, and thus limits expression of nucleosome bound genes. Nucleosomes can be tightly packed together with little free chromatin between them, or spread out to allow RNA-polymerase and transcriptional activators to interact with the DNA. Further, nucleosomes can be arranged in much larger and more complex

3D structures to further compact chromatin. Highly condensed chromatin is referred to as heterochromatin, and is transcriptionally silent, while relaxed chromatin is called euchromatin, and can be transcriptionally active or in a poised state to be quickly accessible for transcription during an appropriate context. The organization of specific regions of the genome into heterochromatin and euchromatin is cell type specific and tightly regulated to ensure that each cell has the potential to express its appropriate set of genes.

Chromatin reorganization can occur through covalent modifications to histone proteins and through energy dependent remodeling of nucleosomes. ATP driven chromatin remodeling complexes such as the SWI/SNF complex hydrolyze ATP to power physically adding, removing or repositioning nucleosomes (2). These complexes are also critical for other cellular processes that require regulation of DNA-histone interactions, such as replication and DNA repair. To enhance the potential for transcriptional activity, these complexes can move or eject nucleosomes to expose the underlying DNA to transcription factors and RNA polymerase. Chromatin remodeling complexes can be recruited to specific genomic loci in response to specific posttranslational modifications to histones. For example, the nucleosome remodeling factor (NURF) complex binds trimethylated histone H3 lysine 4 (H3K4me3), which is a chromatin mark associated with gene activation, and NURF remodels chromatin by sliding histones to create open chromatin regions for the binding of transcriptional activators (2). In addition to histone methylation, many other types of posttranslational modifications have been described, including acetylation, ubiquitination, sumoylation

and phosphorylation, which have varying effects on transcriptional activity (3). These modifications are performed by histone modifying enzymes, such as histone acetylates and deacetylases (HATs and HDACs, respectively) and histone methyltransferases (HMTs)(3). The best characterized of these modifications occur on histone tails, which extend like a string away from the core nucleosome, although more recently a growing body of research has elucidated roles of modifications to the histone bodies (4). In addition to recruiting chromatin remodeling complexes, certain modifications such as acetylation of histone H3 lysine 27 (H3K27ac), can affect the affinity of histone proteins for DNA. The addition of an acetyl moiety to a lysine residue converts a positively charged group to a negatively charged group, thus weakening the interaction with the negatively charged phosphodiester backbone of DNA and increasing DNA accessibility.

Unlike histone acetylation, which is almost always associated with activation, other histone marks can be repressive or activating. For example, while H3K4me3 is associate with gene activation (through NURF recruitment, as previously described), trimethylation of H3K27 is associated with transcriptional repression. The Polycomb complex group complex 2 (PRC2) contains the methyltransferase EZH2, which modifies H3K27 (5). Another Polycomb group complex, PRC1, recognizes the H3K27me3 mark, adds an additional repressive mark (H2A mono-ubiquitination) and promotes heterochromatin formation. The examples of H3K4me3 (activating), H3K27me3 (repressive), and H3K27ac (activating), illustrate that the role of histone posttranslational modifications can depend on both the types of moiety added as well as the specific amino acid residue that is modified.

Transcription of a target gene is regulated near the transcriptional start site at the region known as the promoter (6). This region typically bears a DNA sequence called a promoter motif where RNA polymerase can bind. The binding of RNA polymerase at the promoter region is further enhanced and stabilized through the assembly of a large protein complex of transcriptional activator proteins, including sequence specific transcription factors. Transcription factors typically feature a DNA binding domain that recognizes specific DNA sequences or “motifs”, as well as additional protein-protein interaction domains that can bind to RNA polymerase itself, histone modifying enzymes or other transcription factors. Transcription factors are often expressed in a cell type dependent manner, thus promoting cell type specific patterns of gene expression, or may change their association with DNA in response to cell signaling events to promote dynamic responses. Genomic regulatory elements located outside the promoter region called enhancers can also exert a profound impact on gene expression. These elements can be located up to hundreds of kilobases away from the transcriptional start site of their target gene, and are thought to enhance activity at the promoter through enhancer-promoter looping (7). While different cell types generally use the same promoter to drive expression of a gene, they may use completely different sets of enhancers, contributing to cell type specific patterns of gene expression (8).

B. Macrophages as tools to understand regulation of gene expression.

Macrophages are innate immune cells found in all almost all metazoan organisms that play important roles in both tissue homeostasis and disease. Present in

nearly every tissue of the body, macrophages display unique cellular functions, such as bone resorption by osteoclasts, detoxification of gut-derived microbial products by Kupffer cells, and phagocytosis of senescent red blood cells in splenic macrophages (9). Context specific gene expression forms the basis for the diversity of phenotypes of tissue macrophages and their ability to respond to external stimuli. Macrophages participate in a variety of stress responses including wound repair and defense against pathogens (10), requiring them to be highly flexible in their ability to produce specific responses to a wide range of external signals. Macrophages are also involved in the pathogenesis of numerous chronic inflammatory diseases (11-13), where they can contribute to disease progression by perpetuating inflammation and deleterious tissue remodeling. Thus, macrophages are an attractive model system for studying mechanisms of regulation of gene expression.

Transcription in macrophages is regulated by a multitude of different transcription factor families, including C/EBP, IRFs, NF-κB, AP-1, LXRs, the PPAR family and associated coactivators and corepressors (14). The transcription factor PU.1 is required for the development of most myeloid cells and mature B cells (15), and is thus considered a lineage determining transcription factor (LDTF) in both macrophages and B cells. Using chromatin immunoprecipitation sequencing (ChIP-seq) to identify the genome-wide binding patterns of PU.1 in macrophages and B cells, Heinz et al. found that while PU.1 binds to a similar number of total locations in both cell types, thousands of binding sites displayed cell type specific binding patterns (16). Most of the differentially bound sites were located in enhancers, while greater than 80% of PU.1

binding sites at promoter regions had equivalent binding. The differentially bound enhancers had the same PU.1 binding motif as equivalently bound enhancers. However, B cell specific PU.1 binding sites were found to be enriched for B cell specific motifs such as E2A and EBF within 100 bp of the PU.1 motif, while macrophage specific PU.1 binding sites were enriched for C/EBP and AP-1 motifs. At many of these binding sites, PU.1 binding was dependent upon another cell type specific LDTF bound to these motifs at the same enhancer, suggesting that collaboration between lineage determining factors is necessary for selecting cell type specific enhancers. A different type of interaction was seen between LDTFs and various signal dependent factors transcription factors (SDTFs) such as NF-κB and LXRs. These factors depended upon PU.1 and other LDTFs, but the LDTFs were not dependent on these “second tier” factors, indicating a “hierarchical” component to transcription factor binding. These findings establish what is now referred to as the hierarchical collaborative model of transcription factors (17): collaborative interactions between combinations of LDTFs create cell type specific enhancer landscapes, and second tier (often signal responsive) factors can then bind to these previously established enhancer regions to further enable cell type specific and signal dependent gene regulation.

While PU.1, C/EBP and AP-1 are general macrophage LDTFs, there are several examples of transcription factors that are required for normal development and function of specific tissue macrophage subsets. Joncke et al. recently reviewed several well studied cases (18). For example, c-Fos is required for specification of osteoclasts, and mice lacking this factor exhibit an osteopetrotic bone phenotype (19-22), alveolar

macrophages depend on expression of PPARγ (23), and LXRα is required for splenic marginal zone and metallophilic macrophages (24). In some cases, the signaling cascade between niche specific signals and the lineage determining transcription factor have been studied in detail. For example, SPI-C is required for development of red pulp macrophages (25) and is induced by heme, which is constantly produced as these macrophages engulf and degrade damaged and senescent erythrocytes. Further, in monocytes and bone marrow derived macrophages, heme induces proteasomal degradation of BACH1, which normally suppresses *Spic* expression, and induces and iron-recycling macrophage phenotype (26). This pathway highlights an interesting example of metabolite driven transcriptional regulation. In addition to c-Fos, osteoclast development also relies on NFATc1, which acts downstream of RANKL stimulation produced by osteoblasts (27). Expression of the *Nfatc1* itself is also promoted by RANKL through demethylation of H3K27me3, adding an additional level of regulation (28). Activated NFATc1 collaborates with c-Fos/c-Jun, PU.1, pCREB and MITF to promote the expression of genes involved in acidification and matrix degradation (29, 30). In the peritoneal cavity, retinoic acid binds the retinoic acid receptor and activates transcription of *Gata6*. GATA6 is required for the expression of large peritoneal macrophage specific genes such as TGFβ2, which causes peritoneal B-1 cells to undergo IgA class switching (31). Thus, niche signals instructing macrophage behavior come in many forms, and many new mechanisms will likely be discovered as this topic receives more investigation.

Genomics based experiments have been utilized to decipher tissue macrophage specific gene regulatory mechanisms. Many populations of tissue macrophages, including microglia, Kupffer cells and Langerhans cells, are derived from yolk sac derived erythromyeloid progenitors during embryogenesis and play important roles in the development of their tissue during organogenesis (32-36). By analyzing the global transcriptomic changes that occur as these pre-macrophages populate their target organs, Mass et al. were able to identify specific sets of transcription factors whose expression correlates with arrival in their target organ (37). For example, *Nr1h3* (encoding LXRα), *Id3*, *Spic* and *Irf7* were enriched in early Kupffer cells compared to other macrophage populations, and the authors demonstrated that *Id3* knockout mice were deficient for Kupffer cells. Lavin et al. studied tissue resident macrophages in adult mice through another approach that utilized a combination of transcriptomic and enhancer profiling (38). By comparing multiple populations of tissue resident macrophages, they compared the population specific enrichment of transcription factor binding motifs in putative enhancer regions with corresponding expression of transcription factors that could bind identified sequences. Interestingly, this analysis also predicted the importance of LXRα for splenic macrophages and Kupffer cells, as well as GATA6 in peritoneal cavity macrophages and PPARγ in alveolar macrophages. A later study by Scott et al. used a Kupffer cell specific deletion of LXRα which validated its predicted requirement for expression of Kupffer cell signature genes as well as Kupffer cell survival (39).

The environment's effect on gene regulatory networks can also be studied by adoptively transferring a cell from its native environment to a novel environment. Lavin et al. found that when peritoneal macrophages were transferred to lung via intratracheal injection, they partially adopted the alveolar macrophage transcriptomic profile (38). Notably, the transferred cells lost expression of peritoneal cavity macrophage specific genes such as *Gata6* and *Alox15*, and gained expression of alveolar macrophage specific genes such as *Pparg*, *Chil3l3*, and *Car4*. Gosselin et al. showed that placing peritoneal macrophages or microglia *in vitro* in standard cell culture conditions exerted profound effects on the transcriptomic and chromatin features of these cells (40). Importantly, the genes and enhancers most significantly downregulated by removing a cell from its native environment were those most closely associated with that cell type's core identity program. Further, placing two different types of tissue resident macrophages in the same environment resulted in convergence of their transcriptomes and enhancer landscapes. Part of the original tissue macrophage specific program could be induced in vitro by addition of the niche specific signals all-*trans* retinoic acid for peritoneal cavity macrophages or TGFβ for brain microglia. These experiments suggest that tissue macrophages retain a high degree of plasticity when fully developed, and that the local tissue environment maintains tissue macrophage identity trough continuous input of niche specific signals. Further, these studies indicate that an important effect of removing a macrophage from its environment is to selectively deprogram its tissue specific functions, highlighting the importance of in vivo experiments when studying macrophage function.

Another way to infer the environment's influence on macrophage gene expression involves tracking the differentiation of HSC derived monocytes as they are recruited to a particular niche. Radiation induced liver injury in mice was demonstrated to cause resident macrophages to be replaced by bone marrow monocytes that were highly similar to embryonically derived Kupffer cells, but lacked expression of certain genes such as *Cd163*, *Snrpn*, *Marco*, *Timd4*, *Colec12*, and *Xlr* (41). In another study by Scott et al., experimental Kupffer cell ablation was achieved using a Kupffer cell-specific diphtheria toxin receptor mouse model. In this system, monocytes rapidly refill the empty Kupffer cell niche and differentiate into Kupffer cell-like macrophages (42). The transcriptomes of these recruited macrophages at day 15 and day 30 after diphtheria toxin administration were remarkably similar to embryonically derived Kupffer cells from healthy animals. This is the first experimental model system where a specific tissue resident macrophage population can be selectively destroyed without affecting other mononuclear cells, and presumably creates minimal damage to other liver cell types compared to the radiation induced liver injury model. In this model, the only a small subset of genes was not induced in monocyte derived liver macrophages, including *Xlr*, *Timd4*, *Sdc2*, *Raver2*, *Colec12*, *Cd163*, *C2*, and *Bmpr1a*. Interestingly, some of these genes, including *Timd4*, *Xlr*, *Cd209f*, and *C2* were also found to be enriched in the long lived subset of tissue resident intestinal macrophages compared to the other intestinal macrophage subsets which are more rapidly replaced by monocytes (43), indicating that a subset of tissue macrophage specific genes cannot be readily induced in monocytes. An important implication of this finding is that in certain contexts, monocyte derived

macrophages may not be able to fulfill all of the functions of embryonically derived tissue resident macrophages.

In **Chapter 2**, we utilized a variation of the Kupffer cell ablation model system to perform in depth transcriptomic and enhancer profiling of repopulating liver macrophages over a time course spanning 12 hours to 14 days, enabling us to understand the dynamic changes that occur in gene regulatory networks during monocyte to Kupffer cell-like recruited macrophage differentiation. We find that transcripts for key Kupffer cell LDTFs, such as *Nr1h3*, *Tfec*, *Id3*, *Mafb* and *Spic* are all induced within 12 hours in recruited liver macrophages after diphtheria toxin mediated Kupffer cell ablation. We demonstrate the requirement of LXRα to maintain open chromatin at Kupffer cell specific enhancers, and show that Notch/RBPJ and TGF/SMAD signaling pathways induce expression *Nr1h3* and help to establish the Kupffer cell regulatory program. Sinusoidal endothelial cells were found to express high levels of *Bmp2* and *Dll4*, which can activate SMAD and Notch/RBPJ signaling, respectively. Furthermore, mouse liver was found to contain desmosterol, an endogenous LXR ligand, at approximately the receptor's EC50 and roughly 10 times greater than in plasma. These studies substantially advance our understanding of how the liver niche instructs normal Kupffer cell phenotype.

C. Nonalcoholic steatohepatitis as a model system for understanding environmentally driven programming of resident and recruited macrophages.

The liver presents a unique opportunity to study transcriptional regulation in macrophages. Being the largest population of tissue resident macrophages in the body, the Kupffer cells of the liver can be purified in quantities that are suitable for genomics assays such as RNA-seq, ATAC-seq, and ChIP-seq, as demonstrated in **Chapter 2** and **Chapter 3**. Tissue inflammation can both alter the activity of resident macrophages and recruit additional monocyte derived macrophages (44, 45). During acute liver injury or chronic inflammatory conditions such as nonalcoholic steatohepatitis (NASH), Kupffer cells, as well as other liver cells, secrete proinflammatory mediators that recruit monocyte derived macrophages, which add to the diversity of hepatic macrophages and play important roles in disease progression and resolution (46-48). While Kupffer cells are known to reside in liver sinusoids, recruited macrophages may reside in other niches within the diseased liver to participate in phagocytosis and wound healing. Thus, the liver is an intriguing model system for understanding how diverse macrophages regulate their gene expression during chronic tissue inflammation within the same organ.

Non-alcoholic fatty liver disease (NAFLD) is a spectrum of liver conditions strongly coupled with obesity, insulin resistance, cardiovascular disease, and type-2 diabetes mellitus in the absence of excess alcohol consumption. A predominant feature of NAFLD is steatosis, or the accumulation of hepatic fat in excess of 5-10% of the liver

mass (49, 50). While steatosis alone is benign, in some patients it can progress to co-occurring hepatic lobular ballooning and inflammation, and is then classified as non-alcoholic steatohepatitis (NASH). The transition of NAFLD to NASH is thought to involve additional “hits” in the form of ER stress, insulin resistance, or increased gut permeability, which perpetuate a metainflammatory state involving tissue damage, inflammatory cytokine production, immune cell infiltration, and reactive oxygen species generation (51, 52). Individuals with NASH have increased liver complications (fibrosis, cirrhosis, hepatocellular carcinoma, or liver failure necessitating transplant), cardiovascular disease, and mortality rate.

Kupffer cells are derived from yolk sac precursors undergoing local repopulation independent of the circulating mononuclear phagocyte system (53). Residing in the lumen of the sinusoidal endothelium, they play important roles as sentries of circulation and the draining portal system, sensing and detoxify intestinally derived microbial products (49). Depletion of the intestinal flora or disruption of Toll-like receptor signaling was found to protect mice from development of fibrosis and NASH (54-58). Further, human functional variants in the gene encoding Toll-like receptor 4, causing attenuated signaling, were found to be linked to delayed progression of fibrosis (59-61). In NASH, Kupffer cells react to chronic liver injury by perpetuating a wound healing response that over time results in excessive accumulation of scar tissue. In this regard, Kupffer cells secrete CCL2 to promote the recruitment of inflammatory monocytes, which contribute to the pool of hepatic macrophages and help promote hepatic fibrogenesis (48, 62). Secretion of pro-fibrotic mediators such as TGFβ and PDGF induce hepatic stellate

cells to transdifferentiate into myofibroblasts and produce excessive extracellular matrix (63, 64). Furthermore, inflammatory cytokines such as TNF and IL-1β produced by hepatic macrophages promote myofibroblast survival (65). The key role of hepatic macrophages in promoting fibrosis through stellate cell activation has been illustrated by studies showing that depletion of macrophages reduces myofibroblast formation and collagen accumulation in various animal models of liver fibrosis (65-68). However, macrophages are also important contributors to the resolution phase of inflammation and repair of damaged tissue. Liver macrophages contribute to fibrosis resolution through phagocytosis of apoptotic cells and debris (69, 70), secretion of matrix metalloproteinases (MMPs) that dissolve the fibrotic scar (71, 72), and by secreting mediators such as MMP9 and TRAIL that trigger apoptosis of pro-fibrotic stellate cells and myofibroblasts (48). These pro-resolution macrophages are thought to derive from a phenotypic switch from pro-fibrotic macrophages, and express lower levels of pro-inflammatory cytokines and chemokines and higher levels of CX3CR1 and arginase 1, which are associated with anti-fibrotic actions (64, 73, 74). The necessity for these pro-resolution macrophages was demonstrated using a CD11b-DTR model, which showed that macrophage ablation during the first week of recovery from CCl_4 induced fibrosis dramatically impaired scar tissue degradation (68). Thus, hepatic macrophages can function to both promote fibrogenesis as well as fibrosis resolution, depending on instructional cues.

While recruitment of myeloid cells is clearly important for the pathogenesis of NASH, adequately distinguishing resident versus recruited cells with surface markers by

flow cytometry has proven to be challenging, which has limited their study. For example, it was recently demonstrated that in a dietary model of NASH there is heterogeneity with of expression of Tim4 and Clec4f within $CD11b^{Lo}F4/80^{Hi}$ liver macrophages, which most prior studies have uniformly considered to be tissue resident Kupffer cells (75). Further, recent studies have shown that negativity for Tim4 is consistent with monocyte rather than embryonic origin among liver $F4/80^{Hi}$ cells (41, 42, 76). These findings suggest that monocyte derived macrophages within the liver may contribute to the pool of what have previously been considered "resident" cells during NASH. These distinctions are critically important when interpreting the findings of genomics assays. If the lineage of a cell population is uncertain, it becomes impossible to determine if observed effects represent cell-intrinsic changes or are due to the recruitment of a separate group of disease responsive cells. Further, while Kupffer cells are known to reside in hepatic sinusoids, the microanatomical niche for various subsets of recruited macrophages is less clear. Again, this information is a prerequisite for deciphering mechanisms to explain how tissue environment affects macrophage gene expression.

Single cell RNA-seq can define the cell types within a tissue based on gene expression with minimal a priori knowledge, and can lead to development of new cell sorting strategies based on differential expression of mRNAs encoding cell type specific surface markers (77, 78). In **Chapter 3**, we used single cell RNA-seq to identify the major populations of macrophages present during a mouse model of NASH and confirmed the presence of these populations using flow cytometry schemes informed by this analysis. While Kupffer cells represented the only major myeloid population in

healthy livers, mice with NASH contained 3 additional populations of recruited macrophages, one of which was transcriptionally similar to Kupffer cells but lacked expression of Tim4. After confirming that the three recruited macrophage populations were monocyte derived using formal lineage tracing experiments, we studied their microanatomical localization using immunofluorescence. Recruited macrophages colonizing the Kupffer cell niche (e.g. liver sinusoids) adopted a Kupffer cell-like pattern of gene expression and open chromatin, while recruited macrophages localized closer to large diameter vessels did not upregulate Kupffer cell specific genes or adopt similar open chromatin landscapes. Interrogating the open chromatin regions gained as monocytes acquired their specific niche allowed us to identify putative transcription factors that control key identity programs of macrophages in the Kupffer cell and large vessel recruited macrophage niches. While the monocyte to recruited macrophage transition involved dramatic reorganization of open chromatin, chromatin accessibility was only slightly altered in embryonically derived Kupffer cells responding to the NASH diet. Rather, changes in gene expression in embryonically derived Kupffer cells correlated with changes in H3K27ac signal in their pre-existing enhancer landscape. Surprisingly, the NASH model deprogrammed much of the Kupffer cell core identity program, which was due to a specific loss of LXR binding at Kupffer cell signature enhancers. Embryonically derived Kupffer cells underwent apoptosis during the NASH model, allowing recruited macrophages to colonize the Kupffer cell niche. These data demonstrate that NASH may lead to diversification hepatic macrophages by recruiting monocytes to inflamed regions of the liver outside the Kupffer cell niche, as well as to

the Kupffer cell niche itself by interfering with LXR mediated control of Kupffer cell identity and anti-apoptotic genetic programs.

These studies provide the most comprehensive examination to date of how gene expression is regulated in hepatic macrophages in healthy animals and during non-alcoholic steatohepatitis. Similar approaches to those in **Chapter 2** using tissue macrophage subset specific ablation and repopulation models could be used to decipher the environmental signals important for establishing the unique identity programs of other tissue macrophages. The combinatorial approach we used in **Chapter 3** involving single cell RNA-seq, lineage tracing and transcriptomic and enhancer profiling could also be utilized in other tissues and disease models to study the mechanisms driving macrophage diversification and response to disease. Understanding the how the tissue environment influences macrophage function in normal and diseased conditions may open new opportunities to develop therapeutic strategies based on modulating macrophage function.

Chapter 2. Liver-derived signals activate RBPJ, SMADS, and LXRα to initiate and maintain Kupffer cell identity

A. Abstract

Tissue environment plays a powerful role in establishing and maintaining the distinct phenotypes of resident macrophages, but the underlying molecular mechanisms remain poorly understood. Here, we characterize transcriptomic and epigenetic changes in repopulating liver macrophages following acute Kupffer cell depletion as a means to infer signaling pathways and transcription factors that promote Kupffer cell differentiation. We obtain evidence that combinatorial interactions of DLL4 and TGF-β/BMP produced by sinusoidal endothelial cells and endogenous LXR ligands are required for the induction and maintenance of Kupffer cell identity. DLL4 regulation of RBPJ through Notch signaling activates poised enhancers to rapidly induce LXRα and other Kupffer cell lineage-determining factors. These factors in turn reprogram the repopulating liver macrophage enhancer landscape to converge on that of the original resident Kupffer cells. Collectively, these findings provide a framework for understanding how macrophage progenitor cells acquire tissue-specific phenotypes.

B. Introduction

Macrophages reside in nearly all tissues, where they play essential roles in responses to infection and injury (45, 79). These broad functions are conferred by

commonly expressed genes that encode proteins required for pattern recognition, phagocytosis, the production of cytokines and chemokines, and other mediators of immunity and tissue repair. In addition, each tissue-resident macrophage population exhibits a distinct phenotype that is linked to the corresponding functions of that tissue. Well-studied examples include roles of microglia in monitoring synapses (80), alveolar macrophages in the clearance of lung surfactant (81), and Kupffer cells (liver resident macrophages) in iron metabolism and clearance of gut-derived microbial products (82). These tissue-specific functions are associated with corresponding differences in gene expression that can vary strikingly between distinct macrophage subsets (83). For example, ~ 1600 genes are expressed more than 16-fold differently in a comparison of microglia to large peritoneal macrophages, with the ~800 genes preferentially expressed in microglia being strongly enriched for functions linked to trans-synaptic signaling, CNS development, regulation of neurotransmitter levels and gliogenesis (40).

Most tissues initially acquire resident macrophages during fetal development (53, 84). Studies in mice indicate that a wave of primitive macrophages derived from yolk sac progenitor cells can be detected in developing organs by embryonic day 8.5. Microglia are entirely derived from this source of progenitors and persist in the brain as a self-renewing population (35, 85). A second wave of fetal liver derived macrophages begins to enter tissues on embryonic day 10 and contributes to and in some cases replaces the initial population of yolk sac-derived macrophages (53, 84). This pattern is observed for many tissue macrophage subsets, including alveolar macrophages and

Kupffer cells. These populations also persist throughout life in the lung and liver as self-renewing cells. The transition from fetal hematopoiesis to definitive hematopoiesis is associated with the generation of hematopoietic stem cell (HSC)-derived monocytes, which can also contribute to and/or replace fetal-derived macrophages following birth in some tissues, such as the heart and gut.

Under normal conditions, the brain and the liver are closed to colonization by HSC-derived monocytes. However, if the resident population of macrophages is eliminated from these locations, HSC-derived cells are able to occupy the empty niche and take on properties of the original resident cells. Following depletion of microglia, HSC-derived cells enter the brain and acquire many properties of microglia. However, the differentiation process is incomplete and these cells remain significantly different from the embryonically derived microglia at the levels of gene expression and function even months after engraftment (86-88). These observations indicate important roles of the brain environment in reprogramming monocyte gene expression but also demonstrate that the potential to acquire a complete microglia signature is conferred by embryonic origin. In contrast, following depletion of Kupffer cells from the liver, recruited monocytes gradually acquire a gene expression program that is nearly identical to that of the embryonically derived Kupffer cells (42).

Investigation of molecular mechanisms underlying tissue-specific macrophage phenotypes indicated that different macrophage populations express distinct sets of

transcription factors and exhibit distinct patterns of transcriptional enhancers (38, 40). Following entry into the fetal liver, embryonic macrophages rapidly upregulate *Nr1h3* (encoding LXRα), *Spic*, *Id1, Id3* and *Irf7*, suggesting roles in establishing Kupffer cell-specific gene expression (37). The LXR recognition motif is enriched in Kupffer cell enhancers (38) and recent studies of loss of function of *Nr1h3* in Kupffer cells are consistent with it playing a key role in establishing Kupffer cell identity (39). Evidence linking tissue environment to the selection and maintenance of enhancers that specify tissue resident macrophage phenotypes was provided by changes in enhancer activity states and gene expression following transfer of microglia or peritoneal macrophages to a tissue culture environment. This transition was associated with rapid loss of features associated with enhancer activity at microglia or peritoneal macrophage-specific enhancers, respectively, and down-regulation of nearby genes (40, 89). These findings support the concept that tissue derived signals are constantly sensed and integrated at the level of enhancers, which in turn are required to maintain tissue-specific programs of macrophage gene expression.

While instructive roles of tissue environments are established, the key signaling molecules that are necessary to drive the differentiation and specialized functions of most tissue resident macrophages are largely unknown. Furthermore, the mechanisms by which these factors act in newly recruited cells to simultaneously down-regulate progenitor cell gene expression and up-regulate the appropriate tissue specific program of genes has to our knowledge not been investigated for any resident macrophage

population. To address these questions, we leveraged the anatomical relationship of Kupffer cells with liver sinusoidal endothelial cells and the power of Kupffer cell depletion/repopulation in the mouse as a model system (42). Treatment of mice expressing the diphtheria toxin receptor (DTR) specifically in Kupffer cells with diphtheria toxin (DT) results in nearly complete ablation of the Kupffer cell population within 12 hours. This results in rapid colonization of the empty niche by circulating monocytes and their subsequent differentiation to Kupffer-like cells. Sufficient cells can be obtained throughout this time course for detailed transcriptomic, cistromic and epigenetic analyses, enabling inference of transcription factors and upstream signaling pathways that drive the differentiation process.

Using this model system, we find that liver-derived signals rapidly induce expression of Kupffer cell lineage-determining transcription factors within 24 hours of monocyte entry by acting upon a pre-existing but poised enhancer landscape. The induction of these factors in turn drives the selection and function of thousands of new enhancers that establish Kupffer cell identity. We provide evidence that TGF-β/BMP family members and DLL4 expressed by sinusoidal endothelial cells function in a combinatorial manner with liver-derived LXR ligands to drive the Kupffer cell differentiation program and maintain the Kupffer cell phenotype at steady state.

C. Results

Rapid differentiation of recruited monocytes following Kupffer cell ablation

To establish a Kupffer cell depletion/repopulation system, we first generated mice in which Cre-recombinase was inserted into the 3' UTR of the Kupffer cell-specific *Clec4f* gene under translational control of an internal ribosome entry site (**Figure 2.S1A, B**). The Cre open reading frame was in turn fused in frame with a T2A recognition site and the coding sequence for nuclear localization signal-tagged tdTomato (tdTomato-NLS), providing a bright nuclear marker of Kupffer cells that can be readily detected by flow cytometry. To establish specificity and function of the integrated Cre-tdTomato transgene, mice were crossed to Rosa26 Lox-Stop-Lox ZsGreen mice. ZsGreen and tdTomato were both expressed in Kupffer cells, but not in hepatic $CD11b^{Hi}F4/80^{Lo}$ cells, while LysM-Cre activity was observed in both cell populations (**Figure 2.S1C**). We then crossed these mice to mice in which the Diphtheria Toxin Receptor (DTR) was knocked into the Rosa26 locus behind a Lox-Stop-Lox cassette (**Figure 2.1A**) (90), resulting in Kupffer cell-specific expression of the DTR. Treatment of these animals with diphtheria toxin (DT) led to a near complete elimination of Kupffer cells ($CD11b^{Int}F4/80^{Hi}$Clec4f-$tdTomato^{Pos}$) from the liver by 12 h following injection (**Figure 2.1B**). At 12h following DT treatment, adherent monocyte-derived cells ($CD11b^{Hi}Ly6C^{Hi}F4/80^{Neg}$Clec4f-$tdTomato^{Neg}$) were already present in the liver, in contrast to control animals (**Figure 2.1B**). RNA-seq analysis was performed on circulating $Ly6C^{Hi}$ monocytes, the recruited cells at 12h, 1d, 2d, 3d, 7d and 14d, and resident Kupffer cells. Replicate samples exhibited a high degree of consistency and clustered according to condition (**Figure 2.S1D**). We refer to cells recovered within the first 12 hours of DT depletion as recruited

liver monocytes and cells recovered from 24h to 14 days after DT depletion as repopulating liver macrophages (RLMs).

RNA-seq analysis indicated that more than 1500 mRNAs were up-regulated and more than 1500 mRNAs were down-regulated (fold change > 2, adjusted p value <0.05) in recruited liver macrophages at 24h after DT (**Figure 2.1C**). Even at this early time point, recruited monocytes gained expression of 170 of a previously defined list of 303 Kupffer cell identity genes (**Figure 2.S1E**). Recruited liver macrophages progressively acquired a pattern of gene expression that converged with the Kupffer cell gene expression signature over a 14 day time frame (**Figure 2.1D, E**). Cell cycle control genes and *Mki67* (encoding Ki67) were transiently upregulated at 2 and 3 days post DT depletion, suggesting proliferation of recruited cells during this time frame (**Figure 2.S1F, G**). Collectively, these findings are in agreement with recent studies using *Clec4f* regulatory elements to directly drive expression of the DTR in Kupffer cells (42). Notably, genes encoding transcription factors proposed to be important for Kupffer cell identity, including *Nr1h3* (encoding LXRα), *Spic* and *Id3*, are strongly activated within the first 12h following DT treatment, while the monocyte-specific gene *Ccr2* is strongly down-regulated (**Figure 2.1F**). Most Kupffer cell identity genes exhibit a more delayed pattern of activation. For example, *Clec4f* shows the strongest upregulation between 72h and 7d. *Timd4*, encoding a surrogate marker of many tissue macrophages of embryonic origin and/or prolonged tissue residence (42, 91), was also upregulated during this time period, but did not approach levels of expression observed in resident

Kupffer cells (**Figure 2.1F**), as previously reported (42). In this study, by 14d less than 100 genes were more than 4-fold differentially expressed compared to Kupffer cells, supporting the use of the Kupffer cell depletion/repopulation system as a model for investigation of Kupffer cell differentiation.

Liver environment reprograms the recruited monocyte enhancer landscape

To investigate transcriptional mechanisms by which the liver environment induces a Kupffer cell-like program of gene expression, we performed ATAC-seq to identify regions of open chromatin in circulating monocytes, repopulating liver macrophages at 1d and 2d post DT injection, and in resident Kupffer cells. Replicate samples were highly correlated and clustered according to condition (**Figure 2.S2A**). Recruited cells exhibited marked changes in open chromatin that progressed towards the pattern observed in Kupffer cells (**Figure 2.2A**). De novo motif analysis of the induced ATAC-seq peaks present at 48h in RLMs indicated significant enrichment for motifs recognized by CREB/AP-1 family members, MAF/MAFB, NFκB, TFEB/TFEC, LXRs, RBPJ and SMADs (**Figure 2.2B**). In parallel, we identified putative KC-specific enhancers using a combination of open chromatin and histone H3 lysine 27 acetylation (H3K27ac), which is a dynamic histone modification that is highly correlated with transcriptional activity (92). KC-specific enhancers were defined as distal accessible chromatin regions with preferential enrichment of H3K27ac in Kupffer cells in at least 3/4 comparisons with resident peritoneal macrophages, microglia, monocytes, and bone marrow-derived macrophages (**Figure 2.S2B**). Enrichment analysis for de novo motifs

returned a slightly larger but fully overlapping set of enriched motifs (**Figure 2.S2C** and **Figure 2.2B**). The most significantly enriched additional motif corresponding to an IRF binding site, which is highly induced when EMP-derived cells enter the fetal liver (37). Genes encoding transcription factors recognizing SMAD, RBPJ and NFκB motifs are of particular interest because the activities of these factors are regulated in a signal-dependent manner, and could therefore play roles in transmitting liver environmental signals (93-95). The LXR response element and the motifs for MAF and TFE factors are consistent with the very rapid (12h-1d) upregulation of *Nr1h3*, *Maf, Mafb*, and *Tfec* mRNAs following monocyte retention in the liver (**Figure 2.1F and 2.2C**). *Irf7*, the most highly expressed member of the IRF family in Kupffer cells, is expressed in circulating monocytes and increases more slowly following recruitment to the liver (**Figure 2.S2D**). Interpretation of enrichment for CREB/ATF/AP-1 motif is complex because there are high magnitude changes in the expression of several CREB/ATF/AP-1 family members in recruited monocytes that go in opposite directions. For example, *Junb* and *Fosl2* are strongly downregulated, *Jdp2* is strongly upregulated, and *Jund* is consistently expressed at high levels (**Figure 2.S2E**). In addition, the activities of these factors are differentially influenced by signal-dependent post-translational modifications (96, 97)

Although the marked changes in open chromatin as assessed by ATAC-seq indicate rapid and widespread remodeling of the chromatin landscape, changes in gene expression can also be mediated through alterations in the activities of pre-existing regulatory elements. To investigate this possibility, we performed ChIP-seq for

H3K27ac, in circulating monocytes, repopulating liver macrophages at 24h post DT injection, and in resident Kupffer cells. These experiments identified nearly 2000 upregulated H3K27ac peaks in recruited monocytes, ~2/3 of which were associated with pre-existing ATAC-seq peaks (**Figure 2.2D**). Sites gaining H3K27ac were enriched for LXR, MAF, MITF and RBPJ motifs (**Figure 2.S2F**), consistent with rapid increases in the activities of these factors. Conversely, more than 2000 H3K27ac peaks were lost from circulating monocytes within the first 24 hours following DT treatment, ~1/4 of which were associated with a loss of a corresponding ATAC-seq peak. Sites of reduced H3K27ac were enriched for motifs associated with KLF, C/EBP, RUNX, SP2 and bZIP motifs (**Figure 2.S2F**), consistent with rapid down regulation of their expression levels and/or activities.

Composite ATAC-seq and H3K27ac ChIP-seq tracks are illustrated for *Nr1h3*, *Mafb*, *Clec4f* and *Cd5l* in **Figure 2.2E**. Pre-existing ATAC-seq peaks are observed at the promoters and putative distal regulatory elements of *Nr1h3* and *Mafb* that exhibit increased H3K27ac in RLMs 24h after DT injection in comparison to circulating monocytes (yellow shading, **Figure 2.2E**). These locations exhibit further H3K27ac in resident Kupffer cells. Pre-existing ATAC-seq peaks that gain H3K27ac are also observed for *Id1*, *Id3*, *Maf*, and *Tfec* (data not shown). In contrast, *Clec4f* and *Cd5l* provide examples in which ATAC-seq peaks associated with putative regulatory elements in resident Kupffer cells are not present in circulating monocytes and do not become apparent until at least 48h after DT depletion (light blue shading, **Figure 2.2E**).

Collectively, these results support a model in which liver environmental signals act on pre-existing but poised regulatory elements to rapidly induce the expression of a set of transcription factors necessary for selection of new enhancers that specify Kupffer cell differentiation.

LXRα is a Kupffer cell lineage-determining factor

LXRα and LXRβ are best understood as nuclear receptors that regulate cellular cholesterol homeostasis and fatty acid homeostasis in many cell types in response to endogenous sterol and oxysterol ligands (98, 99). However, *Nr1h3* is one of the most rapidly and highly induced genes in repopulating liver macrophages following Kupffer cell depletion (**Figure 2.1F**), suggesting that its induction also plays a key role in driving the Kupffer cell differentiation program. To address this question, we bred Clec4f-Cre-tdTomato mice to LXRα$^{fl/fl}$ mice to generate a Kupffer cell specific knockout. Flow cytometry indicated that expression of Clec4f-Cre-tdTomato was associated with a population of Kupffer cells that expressed Tim4 at levels similar to control Kupffer cells and a new population of Tim4-negative cells (**Figure 2.S3A**). The origin of Tim4-negative cells remains to be established. Reduced Tim4 expression could be due to it being a direct LXRα target gene, resulting in reduced expression in embryonically derived Kupffer cells. Alternatively, but not mutually exclusively, lack of LXRα could result in reduced embryonic Kupffer cell survival and replacement by monocyte derived cells which express lower levels of Tim4. Because of this ambiguity we sorted both Clec4f-tdTomato^{Pos}Tim4^{Pos} and Clec4f-tdTomato^{Pos}Tim4^{Neg} cells from KC-LXRα-KO

mice for RNA-Seq and epigenetic analysis. LXRα knockout in both populations was confirmed by loss of specific exons of *Nr1h3* gene (**Figure 2.S3B**).

Comparison of the transcriptomes of Tim4^{Neg} LXRα KO Kupffer cells to control Kupffer cells revealed more than 250 differentially expressed genes (>2-fold difference, adjusted p value <0.05, **Figure 2.3A**). Taking the signature gene set defined by Lavin et al. (38), 22 Kupffer cell-specific genes were among the 164 transcripts down-regulated in the KC-specific LXRα KO. In addition to *Timd4*, these included *Clec4f*, *Cd5l*, *Kcna2*, *Arg2* and *Il18bp* (**Figure 2.3B**). In contrast, only 3 KC-specific genes were among the 102 transcripts upregulated in the KC-specific LXRα KO. A similar pattern was observed in the Tim4^{Pos} population of LXRα KO Kupffer cells, although the total number of differentially regulated genes was less than observed for Tim4^{Neg} cells (**Figure 2.S3C**, **Figure 2.S3D**). In contrast, deletion of LXRα from BMDMs had almost no effect on basal gene expression, (**Figure 2.S3E**).

To investigate the role of LXRα in establishing the Kupffer cell regulatory landscape, we performed ATAC-seq analysis of control and both Tim4^{Pos} and Tim4^{Neg} LXRα KO Kupffer cells. Comparison of Tim4^{Neg} LXRα KO KCs to control KCs indicated more than 3700 differential ATAC-seq peaks, with loss of >2900 peaks in Tim4^{Neg} LXRα KO KCs (**Figure 2.3C**). More than half of the lost peaks correspond to Kupffer cell-specific enhancers (from **Figure 2.S2B**). Comparison of Tim4^{Pos} LXRα KO KCs to control KCs indicated ~800 differential ATAC-seq peaks, with loss of 725 peaks in

Tim4^{Pos} LXRα KO KCs (**Figure 2.S3F**). Again, more than half of the lost peaks correspond to Kupffer cell specific enhancers.

The marked alterations in ATAC-seq peaks in LXRα KO KCs compared to control KCs suggested a direct role of LXRα in selection and maintenance of the Kupffer cell-specific enhancer landscape. To generate a genome-wide profile of LXR binding in Kupffer cells, we took advantage of Clec4f-Cre-tdTomato mice in which nuclei of Kupffer cells are specifically marked by tdTomato. This enabled fluorescence-activated sorting of crosslinked tdTomato-positive nuclei from total liver nuclei that were rapidly isolated from intact liver tissue (**Figure 2.S3G**). This procedure eliminated the need for tissue digestion and resulted in substantial improvements in ChIP efficiency as compared to experiments using sorted cells. Using this approach, we identified more than 22,000 reproducible LXR binding in Kupffer cells (**Figure 2.3D**). As current ChIP-protocols do not yet allow discrimination of LXRα from LXRβ, this cistrome corresponds to an aggregate of LXRα and LXRβ binding sites. Comparison of these sites to LXR binding sites determined in BMDMs treated with the synthetic LXR agonist GW3965 (an LXR ligand) indicated that a large fraction was specific to Kupffer cells (**Figure 2.3D**). Motif analysis of KC-specific LXR peaks against genomic background indicated significant enrichment for the LXR binding site itself and co-enrichment for motifs for general macrophage lineage-determining factors PU.1 and C/EBP. In addition, motifs for IRFs, TFEB/C and MAF factors were all highly enriched (**Figure 2.3E**), suggesting a role for collaborative interactions between LXRs and these factors for establishing KC-

specific enhancers. Consistent with this possibility, intersecting LXR binding sites with KC ATAC-seq peaks indicated that LXR binding sites were associated with approximately half of ATAC-seq peaks that are lost in Tim4-negative LXRα knockout cells, including ATAC-seq peaks that are KC-specific (**Figure 2.3F**). A similar pattern was observed in comparison to Tim4^{Pos} LXRα KO Kupffer cell ATAC-seq peaks (**Figure 2.S3H**). Examples are provided for KC-specific LXR binding sites in the vicinities of the *Cd5l*, *Kcna2* and *Arg2* genes at which corresponding ATAC-seq peaks are lost in Tim4^{Pos} or Tim4^{Neg} LXRα KO Kupffer cells (Blue shading in **Figure 2.3G**). In contrast, ATAC-seq peaks associated with LXR binding sites in the vicinity of the *Abca1* locus were not lost in LXRα KO Kupffer cells (yellow shading in **Figure 2.3G**). Of interest, RBPJ and SMAD binding motifs were significantly enriched in the intersection of lost ATAC-seq peaks in the Tim4^{Pos} LXRα KO and Kupffer cell-specific LXR binding sites (**Figure 2.S3I**), suggesting co-occupancy of LXRs and these transcription factors at these locations. Collectively, these results provide evidence that LXRα functions as a Kupffer cell lineage-determining factor by driving the selection and function of enhancers that regulate Kupffer cell-specific gene expression.

SMAD4 regulates LXRα expression and Kupffer cell identity

Having established rapid activation of pre-existing enhancer landscapes associated with LXRα and other putative Kupffer cell lineage-determining factors in repopulating liver macrophages, we next sought to identify liver-derived signals responsible for these effects. The enrichment of motifs for SMAD and RBPJ

transcription factors in Kupffer cell-specific enhancers (**Figure 2.2B** and **Figure 2.S2C**) suggested potential roles of liver-derived TGF-β/BMP family members and activators of Notch signaling as candidate molecules. In the liver, Kupffer cells exclusively reside in contact with sinusoidal endothelial cells within the hepatic sinusoids (100). We therefore isolated these cells ($CD146^{Pos}CD31^{Pos}F4/80^{Neg}$), and stratified them based on expression of STAB2 (101) (**Figure 2.S4A**), and performed RNA-Seq analysis. These studies demonstrated high levels of expression of *Tgfb1* and *Bmp2* (**Figure 2.4A**). Parallel evaluation of receptors for these ligands in Kupffer cells indicated high levels of *Tgfbr1, Acvr1b*, *Bmpr1a, Tgfbr2*, and *Bmpr2* (**Figure 2.4B**).

To investigate the potential for sinusoidal endothelial cells to communicate with Kupffer cells via TGF-β/BMP signaling, we crossed Clec4f-Cre-tdTomato mice with floxed Smad4 mice to generate a Kupffer cell-specific deletion of *Smad4*. As SMAD4 functions as a co-SMAD required for transcriptional responses to both TGF-β and BMP signaling pathways (102), this strategy enabled assessment of their combinatorial importance at SMAD-dependent regulatory elements. Clec4f-tdTomato expression was substantially reduced in Smad4 knockout Kupffer cells compared to Kupffer cells in Clec4f-Cre-tdTomato mice, suggesting the role of SMAD4 in *Clec4f* gene regulation and/or impaired survival of $Clec4f^{Pos}$ KCs after SMAD4 deletion (**Figure 2.S4C**). However, efficient *Smad4* knockout in both Clec4f-tdTomato-positive and negative populations were confirmed by qPCR targeting a floxed exon 8 (**Figure 2.S4B**). Flow cytometry of Smad4 knockout Kupffer cells also indicated that a subset of mice

exhibited a substantial reduction of Tim4 expression, similar to the effects of loss of function of LXRα (**Figure 2.S4C**). However this phenotype was variable, with $Tim4^{Pos}$ cells being the predominant population in most Kupffer cell specific Smad4 KO mice (**Figure 2.S4C**). RNA-seq analysis of $Tim4^{Neg}$ and $Tim4^{Pos}$ Smad4 KO cells indicated a quantitatively greater effect of the KO on the $Tim4^{Neg}$ population (**Figure 2.4C, 2.S4D**), with ~240 mRNAs differentially expressed in $Tim4^{Neg}$ Smad4 KO KCs compared to ~120 mRNAs in $Tim4^{Pos}$ Smad4 KO KCs (Fold change >2, adjusted p value <0.05). Significantly down-regulated genes included *Clec4f*, *Id3* and LXRα (*Nr1h3*) (**Figure 2.4D**, **2.S4E**). Interestingly, *Spic* was significantly upregulated in Smad4 KO KCs. In addition, *Cx3cr1,* which is strongly down-regulated in recruited liver macrophages following KC depletion, was strikingly upregulated in the Smad4 KO cells (**Figure 2.4D**, **2.S4E**). These results provide evidence that signaling through the TGF-β/BMP pathway is required for maintenance of Kupffer cell identity and that SMADs may also function to negatively regulate monocyte gene expression.

To investigate the molecular functions of SMAD4, we performed ATAC-seq experiments comparing control and Smad4 KO Kupffer cells. In comparison to the consequences of deletion of LXRα, deletion of Smad4 had a more modest effect on open chromatin (**Figure 2.4E**). However, loss of Smad4 was associated with marked reductions in ATAC-seq peak amplitude at several of the most strongly down-regulated Kupffer cell-specific genes, exemplified for *Clec4f* and the leptin receptor *Lepr* (Blue shading, **Figure 2.4F**). To relate changes in open chromatin to DNA binding of SMAD4,

we isolated Kupffer cell nuclei (Clec4f-Cre-tdTomato-positive) and performed ChIP-Seq of SMAD4 in a manner analogous to that described for LXRs. These studies identified more than 15,000 reproducible SMAD4 binding sites in Kupffer cells (**Figure 2.4G**), including binding sites within putative regulatory elements of the *Nr1h3* and *Id3* genes (**Figure 2.S4F**). Parallel ChIP-Seq experiments in TGF-β-stimulated BMDMs identified more than 14,000 SMAD4 binding sites. Comparison of these binding profiles indicated that substantial fractions were specific for Kupffer cells or BMDMs, respectively (**Figure 2.4G**). In addition to binding sites for the general macrophage lineage-determining transcription factors PU.1 and C/EBPs, and the SMAD motif itself, motif analysis also recovered motifs for LXRs, FOXO and MAF transcription factors among Kupffer cell-specific binding sites (**Figure 2.4H**), suggesting that SMAD4 collaborates with these factors to achieve a Kupffer cell specific binding pattern. Consistent with this, more than two thirds of the SMAD4 binding sites in Kupffer cells co-localized with LXR ChIP-seq peaks (**Figure 2.4I**), exemplified at the *Clec4f* and *Lepr* loci (**Figure 2.4F**). Overall, SMAD4 binding sites overlapped with 40% of the ATAC-seq peaks lost in Smad4 knockout Kupffer cells (**Figure 2.4J**), suggesting direct roles in establishing a small but significant component of the Kupffer cell transcriptional regulatory landscape.

Notch signaling induces expression of Kupffer cell lineage-determining transcription factors

We next investigated the potential of TGF-β and BMP2 to activate Kupffer cell lineage-determining transcription factors in vitro. Bone marrow cells were plated in the

presence of M-CSF for three days to promote the proliferation and differentiation of macrophage progenitors. After three days, TGF-β or BMP2 were added and gene expression was evaluated by RNA-Seq one day later. Despite the ability of TGF-β to induce expression of known target genes, such as *Tgfbi*, no induction of *Nr1h3* or *Id3* was observed (**Figure 2.5A**), despite high levels of SMAD4 binding at the putative regulatory elements associated with these genes (**Figure 2.S4F**). Similarly, no induction of these genes was observed in response to BMP2 treatment (not shown).

Based on the enrichment of binding sites for RBPJ in Kupffer cell specific enhancers, we next considered possible roles of Notch signaling in the induction of Kupffer cell lineage-determining factors. Among Notch ligands, DLL4 was found to be highly expressed in liver sinusoidal endothelial cells (STAB2 intermediate and high endothelial cells, **Figure 2.5B**). Conversely, *Notch1* and *Notch2* were highly expressed in Kupffer cells (**Figure 2.5C**). We therefore modified the bone marrow cell experimental system described for TGF-β and BMP2 by culturing cells in M-CSF for three days and then transferring to tissue culture plates in which the surface was coated with DLL4. Cells were harvested for RNA-seq analysis one day later. In contrast to TGF-β, DLL4 strongly induced the expression of *Nr1h3* and *Spic* and had lesser stimulatory effects on *Tfec* (**Figure 2.5D**). Induction of these genes was completely blocked by co-treatment with DAPT, an inhibitor of gamma secretase, consistent with a requirement for cleavage of the Notch intracellular domain for induction of gene expression (**Figure 2.5D**).

At a global scale, exposure of bone marrow progenitor cells to DLL4 for 24h led to significant up-regulation of 259 mRNAs, 38 of which correspond to KC identity genes (**Figure 2.5E**). Of the induced genes, 105 are upregulated in repopulating liver macrophages 24h after KC depletion (**Figure 2.S5A**). Examples of genes that are coordinately upregulated by DLL4 in bone marrow progenitor cells and in repopulating liver macrophages 24h after KC depletion include *Abcg3*, *Slc40a1*, *C1qa*, *Acp5* and *P2ry13* (**Figure 2.5F** and **2.S5B**). Collectively, these findings indicate that DLL4 is capable of rapidly inducing a subset of Kupffer cell lineage determining factors and other KC signature genes in bone marrow progenitor cells.

DLL4 induces KC lineage-determining factors through a pre-existing enhancer landscape

To investigate the molecular mechanisms responsible for DLL4 activation of Kupffer cell lineage-determining factors, we performed ChIP-Seq for RBPJ in conventional BMDMs, in bone marrow progenitor cells treated with DLL4 and in sorted nuclei isolated from Kupffer cells as described for LXRs and SMAD4. We identified >60,000 reproducible RBPJ binding sites in BMDMs and DLL4-treated bone marrow progenitor cells, whereas slightly less than 7000 reproducible binding sites were identified in Kupffer cell nuclei (**Figure 2.6A**). The lower number of binding sites in Kupffer cells is consistent with lower levels of *Rbpj* expression in these cells in comparison to BMDMs (not shown). This difference is also consistent with an ~4-fold down-regulation of *Rbpj* expression in monocytes following their recruitment into the

liver (**Figure 2.6B**). In contrast to LXR and SMAD4, relatively few RBPJ bindings sites were identified that are specific to Kupffer cells (**Figure 2.6B**), suggesting that the impact of Notch signaling becomes progressively restricted following entry of monocytes into the KC-depleted liver. Significantly enriched motifs within the set of RBPJ peaks common to Kupffer cells and BMDMs include the binding sites recognized by the general macrophage lineage-determining factors PU.1, AP-1, C/EBP and RUNX family members as well as binding sites for motifs recognized by IRF factors and TFEB/C, which are also present in Kupffer cell-specific enhancers (**Figure 2.S6A**).

ATAC-Seq experiments in bone marrow progenitor cells treated with DLL4 indicated fewer than 100 significant changes in open chromatin (**Figure 2.6C**), consistent with RBPJ being able to bind to its genomic targets in the presence or absence of Notch signaling (93). In contrast, ChIP-seq for H3K27ac identified more than 2500 sites of increased and more than 900 sites of decreased H3K27acetylation (**Figure 2.6D**). In addition to strong enrichment for the RBPJ motif, regions gaining H3K27ac following DLL4 treatment are also significantly enriched for binding sites for IRF factors, MAF factors, TFE factors, SMADs and LXRs (**Figure 2.6E**), all of which are also present in Kupffer cell-specific enhancers (**Figure 2.S2C**). Examples of the relationships of RBPJ binding sites to putative regulatory elements for *Nr1h3* and *Spic* exhibiting rapid increases in H3K27ac are illustrated in **Figure 2.6F**. Of interest, genomic regions exhibiting loss of H3K27ac are not enriched for RBPJ binding sites or motifs for Kupffer cell lineage-determining factors. Instead, these regions are enriched

for AP-1, KLF and HLF motifs (**Figure 2.S6B**) that are present in H3K27ac regions of circulating monocytes, but not in Kupffer cells (**Figure 2.S2F**). Collectively, these findings provide evidence that Notch signaling induced by DLL4 directly activates a pre-existing enhancer landscape to induce expression of *Nr1h3, Spic* and other genes that promote Kupffer cell differentiation and indirectly suppresses activities of transcription factors that specify monocytic gene expression.

Combinatorial interactions of liver environmental factors

Comparisons of the genome wide binding patterns of LXRs, SMAD4 and RBPJ indicate substantial overlap of these factors within Kupffer cells (**Figure 2.S7A**), suggesting the potential for combinatorial interactions of the signaling pathways that regulate their activities. Examples of overlapping and distinct binding patterns in the vicinities of genes that are highly upregulated in recruited liver monocytes are illustrated for *Abca1* and *C1qa* in **Figure 2.S7B**. To investigate functional consequences of simultaneous activation of SMAD and RBPJ, control and Smad4 KO bone marrow progenitor cells were treated with TGF-β and DLL4 alone or in combination and RNA-seq analysis was performed 24h later (**Figure 2.7A**). DLL4 alone induced expression of *Nr1h3* and *Clec4f*, whereas TGF-β alone had almost no effect. The combination of DLL4 and TGF-β had little additional effect on *Nr1h3* expression, but significantly increased expression of *Clec4f* over that observed in response to DLL4 treatment alone. Notably, the TGF-β effect on *Clec4f* expression was abolished in Smad4 KO bone marrow progenitor cells and the ability of DLL4 to induce *Nr1h3* expression was also

significantly reduced in Smad4 KO cells (**Figure 2.7A**). At a global level, the combination of TGF-β and DLL4 promoted a transition in the gene expression profile of bone marrow progenitor cells towards that of Kupffer cells to a greater extent than TGF-β or DLL4 alone (**Figure 2.7B**).

In addition to the TGF-β/BMP and Notch signaling pathways that regulate the activities of SMAD and RBPJ transcription factors, LXRα is also a signal-dependent transcription factor that regulates gene expression in response to changes in sterol/oxysterol concentrations (98, 99). Examination of genes involved in cholesterol homeostasis indicated marked upregulation of LXR target genes such as *Abca*1 (**Figure 2.7C**) and *Scd1* (**Figure 2.S7C**), and coordinate down-regulation of genes in the SREBP pathway, such as the genes encoding the LDL receptor (*Ldlr*) (**Figure 2.7C**) and HMG CoA reductase (*Hmgcr*) (**Figure 2.S7C**), in repopulating liver macrophages, which converged towards the expression levels of these genes observed in Kupffer cells (**Figure 2.7C**, **2.S7C**). This pattern of gene expression could represent a cell-autonomous response to elevated intracellular cholesterol levels (103), which in macrophages occurs following phagocytosis of apoptotic cells or uptake of modified lipoproteins. However, an alternative possibility is that Kupffer cells and repopulating liver macrophages sense one or more liver-derived molecules that coordinately regulate the LXR and SREBP pathways. Naturally occurring molecules that function as LXR agonists and also suppress the SREBP pathway by binding to INSIGs or SCAP include 24-, 25- and 27-hydroxy cholesterol (24-OHC, 25-OHC, and 27-OHC, respectively),

24,25-epoxy cholesterol (24,25-EC), and desmosterol (103-106). To investigate the potential of these species to function as endogenous regulators of the LXR and SREBP pathways, the abundance of relevant oxysterols and unesterified sterols was quantified by targeted mass spectroscopy using deuterated internal standards. These studies identified desmosterol as the most abundant species in intact liver, being present at a concentration of ~5uM (**Figure 2.7D**). This concentration is close to the EC50 for coordinate LXR activation and SREBP repression (106-108) and is about ~10-times higher than plasma levels (107). Desmosterol thus represents a potential hepatocyte-derived environmental signal that could function in concert with TGF-β/BMP ligands and DLL4 to promote the Kupffer cell phenotype.

Although exogenous desmosterol acutely activates LXR and suppresses SREBP in macrophages in vitro, it is also directly converted to cholesterol by the enzyme Dhcr24, limiting its duration of action. To reduce metabolic clearance as a confounding factor in time course experiments exceeding 12-16h, we used the synthetic LXR agonist DMHCA (109), which is a structural and functional mimetic of desmosterol (107) that cannot be converted to cholesterol. Bone marrow progenitor cells were treated with TGF-β, DMHCA, TGF-β+DLL4 or TGF-β+DLL4+DMHCA for 24h or 72h followed by RNA-seq analysis (**Figure 2.7E**). These experiments revealed two classes of LXR target genes. The first class largely consisted of prototypic LXR target genes, such as *Abca1*, which were rapidly induced by DMHCA and were only modestly affected by DLL4 and/or TGF-β (**Figure 2.7E** and **Figure 2.S7D**). Of note, some of these genes,

such as *Abca1*, were not affected by deletion of LXRα, suggesting compensation by LXRβ. LXR binding sites for these genes in Kupffer cells were largely at pre-existing regions of open chromatin (e.g., **Figure 2.3G**). The second class of target genes, exemplified by *Il18bp* and *Arg2*, consisted of genes that were induced late following recruitment into liver (**Figure 2.S7D**) and were defined as LXRα target genes based on reduced expression in KC-specific LXRα KO Kupffer cells (**Figure 2.3B**). These genes exhibited progressive activation by DLL4 and TGF-β from 24h to 72h and were less dependent on DMHCA for expression (**Figure 2.7E**). LXR binding sites in the vicinity of these genes were largely KC-specific and associated with induced enhancer like elements (**Figure 2.S7E**).

D. Discussion

The transcriptional mechanisms that enable myeloid progenitor cells to acquire the distinct functional characteristics of tissue resident macrophages are largely unknown. Here, we exploited the ability to rapidly and specifically deplete the Kupffer cell population and characterize the transcriptomes and epigenetic landscapes of repopulating liver macrophages as a function of time. We observed the transcriptomes of RLMs to progressively converge towards that of resident Kupffer cells over a 14d time frame. These findings are consistent with previous studies (42) and support the validity of this approach as a model system for investigation of Kupffer cell differentiation. A remarkable feature of this system is the exquisite sensitivity of the liver to loss of its resident Kupffer cell population. While very few monocyte-like cells are found in the perfused liver of control animals, substantial numbers of adherent liver monocytes are already observed by 12 hours following DT treatment. The window for recruitment may be quite transient, as we observe a strong transcriptional signature of proliferation in RLMs at 2-3 days following DT depletion, suggesting that cell division is a significant contributor to repopulation from this point onward. A major unanswered question is the mechanism employed by the liver to sense its Kupffer cell population and determine access to circulating monocytes when the niche is opened following KC depletion.

Integration of global patterns of gene expression, open chromatin, H3K27ac and transcription factor binding provides evidence for a combinatorial and sequential model

of differentiation of myeloid progenitor to Kupffer cell differentiation involving the LXR, DLL4/Notch and TGF-β/BMP signaling pathways. Our findings suggest that a critical initial step is provided by the interaction of recruited monocytes with DLL4 expressed on sinusoidal endothelium. DLL4 activation of Notch signaling converts RBPJ from a repressor to an activator as a consequence of the Notch intracellular domain mediating the exchange of co-repressor complexes associated with histone deacetylase activity for co-activator complexes associated with histone acetyl transferases (110). Consistent with this mechanism, we observe that sites of RBPJ binding at pre-existing regions of open chromatin exhibit increases in H3K27ac in repopulating liver macrophages by 24h after DT treatment. Treatment of bone marrow derived macrophages with DLL4 for 24h is sufficient to induce H3K27ac at many of these regions and to induce nearby gene expression in a manner that is blocked by an inhibitor of Notch cleavage. Importantly, *Nr1h3, Spic* and mRNAs encoding other Kupffer cell lineage-determining factors are among the genes that are rapidly induced both in recruited liver macrophages and DLL4-treated bone marrow derived macrophages. In addition, DLL4 treatment of bone marrow progenitor cells resulted in down-regulation of monocyte specific genes. Suppressive effects of DLL4 on H3K27ac were not associated with local enrichment of RBPJ recognition motifs, but instead were associated with motifs associated with monocyte-specific enhancers, including AP-1 motifs. Reduced H3K27ac at genomic regions enriched for AP-1 motifs is consistent with prior evidence Notch signaling inhibits AP-1 activity in a manner involving the Notch intracellular domain (111, 112). Thus, Notch signaling appears to simultaneously

initiate a program of Kupffer cell gene expression and suppress the expression of monocyte-specific genes.

Unlike circulating monocytes and BMDMs in vitro, tissue macrophages are always interacting with various types of cells in the organ. As Notch signaling is generally activated by direct cell-to-cell contact, our findings suggest that the expression of DLL4 by sinusoidal endothelial cells provides critical position-specific information necessary for triggering monocyte to Kupffer cell differentiation. These studies also imply that sinusoidal endothelial cells restrict access of circulating monocytes to DLL4 unless the resident KC niche is depleted. Previously, Notch-RBPJ has been reported as an essential pathway for tumor-associated macrophage differentiation (113). It has also been reported that Notch ligand DLL1 expressed in mammary gland stem cells activates Notch signaling in stromal macrophages to induce Wnt family ligands (114). Different consequences of Notch activation in macrophages might be caused by other tissue-specific signals. In fact, stimulation of bone marrow progenitor cells with TGF-β in addition to DLL4 can induce more Kupffer cell-specific genes. Given that Notch ligands DLL1 and DLL4 activate distinct targets by pulsatile or sustained Notch activation dynamics (115), different expression pattern of Notch ligands in adjacent cells might affect each tissue macrophage character.

Enrichment of SMAD motifs in Kupffer cell-specific enhancers and induced enhancers in repopulating liver macrophages provides evidence for roles of TGF-β/BMP

signaling in Kupffer cell differentiation and maintenance. Sinusoidal endothelial cells express high levels of and *Tgfb1*, and corresponding receptors are highly expressed on Kupffer cells. In contrast to RBPJ, which exhibited a reduced and largely overlapping binding pattern in Kupffer cells compared to BMDMs, SMAD4 acquired a large cell-specific cistrome in Kupffer cells that overlapped extensively with the Kupffer cell-specific LXR cistrome, consistent with genomic location of SMADs being influenced by specific combinations of lineage determining transcription factors (116). Evidence that TGF-β/BMP signaling is required for maintenance of Kupffer cell identity was provided by transcriptomic and epigenetic consequences of Kupffer cell-specific deletion of *Smad4*. In addition to functioning as a signal-dependent transcription factor that regulates pre-existing enhancers, our findings also indicate essential roles of SMAD4 in maintaining the open chromatin environment of a subset of Kupffer cell identity genes. As SMAD4 is an essential co-SMAD for both TGF-β and BMP signaling pathways, our findings thus far do not allow conclusions to be made regarding the relative roles of each pathway. While *Bmp2* is the more highly expressed mRNA on sinusoidal endothelial cells, *Tgfbr2* is the most highly expressed receptor mRNA on Kupffer cells. In addition, the interactions of TGF-β/BMP ligands with their receptors is highly influenced by co-expressed cell surface molecules and cellular context required for their processing and activity (117, 118). Cell specific deletions of these ligand/receptor combinations will be required to resolve their specific roles. Intriguingly, TGF-β alone was unable to induce *Nr1h3* or many other KC-specific genes in BMDMs, but could

stimulate expression of these genes in the presence of DLL4, suggesting that Notch signaling is permissive for a KC-specific differentiation role the TGF-β pathway.

SPI-C is a transcription factor expressed in iron-recycling macrophages induced by heme (26). In this research, we report the novel pathway, *Spic* induction by Notch signaling. Furthermore, *Spic* expression is up-regulated contrary to *Nr1h3* in Smad4 knockout Kupffer cells. BMP2 and BMP6 secreted by LSECs are important for iron-regulated hepcidin expression (119). Therefore, BMPs might regulate serum iron concentration though *Spic* suppression via SMAD signaling in Kupffer cells.

LXRα has recently emerged as a putative Kupffer cell lineage-determining factor based on its rapid induction in embryonic Kupffer cells (37), the presence of LXR recognition motifs in KC enhancers (38), and consequences of KC-specific deletion (42). Here we confirm the requirement of LXRα for expression of a subset of KC identity genes and establish that it is also required for shaping the Kupffer cell enhancer landscape. Previous studies of bone marrow derived macrophages indicated that genetic deletion of both LXRα and LXRβ had no impact on binding of the macrophage lineage-determining factor PU.1, whereas PU.1 was required for the binding of LXRs at a subset of their genomic locations (16). These observations suggested a hierarchical relationship in which PU.1 and other macrophage lineage-determining transcription factors primed cis-regulatory elements, providing access to signal-dependent factors such as nuclear receptors. Here, deletion of LXRα had no impact on open chromatin in

bone marrow derived macrophages, consistent with these prior studies, but resulted in reduced chromatin access at a significant fraction of Kupffer cell specific enhancers. Whether this result is simply a consequence of higher levels of LXRα expression or reflects an acquired chromatin remodeling function in KCs remains to be established. Liver environmental signals, TGF-β/BMP and Notch pathways are supporting this LXRα function, but it remains to be elucidated that they are necessary to recruit LXRα to Kupffer cell specific binding sites in addition to LXRα induction in Kupffer cells.

In addition to LXRα driving the selection of Kupffer cell enhancers through collaborative interactions with other KC lineage-determining factors, these studies also provide evidence that LXRα and LXRβ activity is regulated in an environment-dependent manner. The very rapid (within 12h) upregulation of LXR target genes and down-regulation of SREBP target genes in recruited cells, and the convergence of their expression patterns in RLMs to those of resident Kupffer cells, strongly implies the presence of endogenous sterol and/or oxysterol regulators of these pathways. It will be of particular interest to determine whether the coordinate regulation of LXRs and SREBPs in Kupffer cells is a cell-autonomous response to accumulation of intracellular cholesterol or results from uptake of sterols/oxysterols generated by other cell types in the liver. Based on lipidomic analysis, desmosterol is the most abundant lipid species that has the potential to both induce LXR target genes and repress the SREBP pathway. We recently reported the unexpected finding that while desmosterol and DMHCA effectively regulate both the LXR and SREBP pathways in macrophages, they

have almost no activity in hepatocytes (107). Mechanisms responsible for cell-specific discrimination of desmosterol and desmosterol mimetics remain to be established. Notably, desmosterol levels are highly dependent on the expression of *Dhcr24* (107, 120), which is a direct target gene of SREBP (108). Based on lipidomic analysis indicating that desmosterol is by far the most abundant LXR ligand in ex vivo hepatocytes, we speculate that it could function as a signal to other cell types in the liver reporting on the status of the SREBP pathway in hepatocytes.

Using molecules which mimic liver environment signals, we show that it is possible to partially induce Kupffer cell-specific genes in mouse bone marrow derived macrophages. This technology will provide improved in vitro systems for modeling pathological features of Kupffer cells in metabolic and inflammatory liver diseases. However, BMDMs treated with DLL4, TGF-β and DMCA do not come nearly as close to Kupffer cells as repopulating liver macrophages, indicating limitations of the in vitro system. There are likely to be many contributing factors to the remaining differences, including a requirement for additional liver-derived factors and inhibitory effects of the in vitro environment.

The present studies focused on a subset of dynamic regulatory elements to infer roles of Notch, TGF-β/BMP receptors, and LXR signaling pathways as mediators of the effects of liver environmental factors on Kupffer cell differentiation and homeostasis. Several additional pathways are suggested by our studies, including signaling systems

that converge on NFκB, IRF, and MAF transcription factors as well as additional nuclear receptors. For example, the enrichment of NFκB motifs in KC-specific enhancer may reflect exposure of Kupffer cells to gut-derived LPS present in portal blood. In conclusion, the ascertainment of transcriptomes and epigenetic landscapes of repopulating tissue macrophages provides a framework for understanding how a common macrophage progenitor cell acquires tissue specific phenotypes.

Figure 2.1: Recruited monocytes rapidly acquire expression of KC lineage-determining TFs followed by expression of a subset of KC-specific genes in KC-depleted livers

A. Experimental scheme: Clec4f-Cre-tdTomato x Rosa26 LSL DTR +/- diphtheria toxin (DT)
B. FACS analysis of cell populations as a function of time following DT treatment
C. MA plot analysis of RNA transcripts expressed in circulating Ly6C^{Hi} monocytes and repopulating liver macrophages at 24 hours. Each dot represents a gene, and the size of dots shows the significance as p-value in the comparison.
D. Genome-wide representation of differential gene expression from 12h to 14 days in comparison to circulating monocytes and resident Kupffer cells. Differentially-expressed 3101 genes are selected by DESeq2 (FDR < 0.05).
E. Principle component analysis of 9568 detectable genes (at least 8 TPM in at least two samples) in circulating monocytes, recruited liver monocytes, repopulating liver macrophages and resident Kupffer cells.
F. Bar plots for expression of *Nr1h3, Id3, Spic, Ccr2, Clec4f* and *Timd4*.The significance symbols represent the FDR from DESeq2 comparing to circulating monocytes respectively. ***p-adj < 0.001.

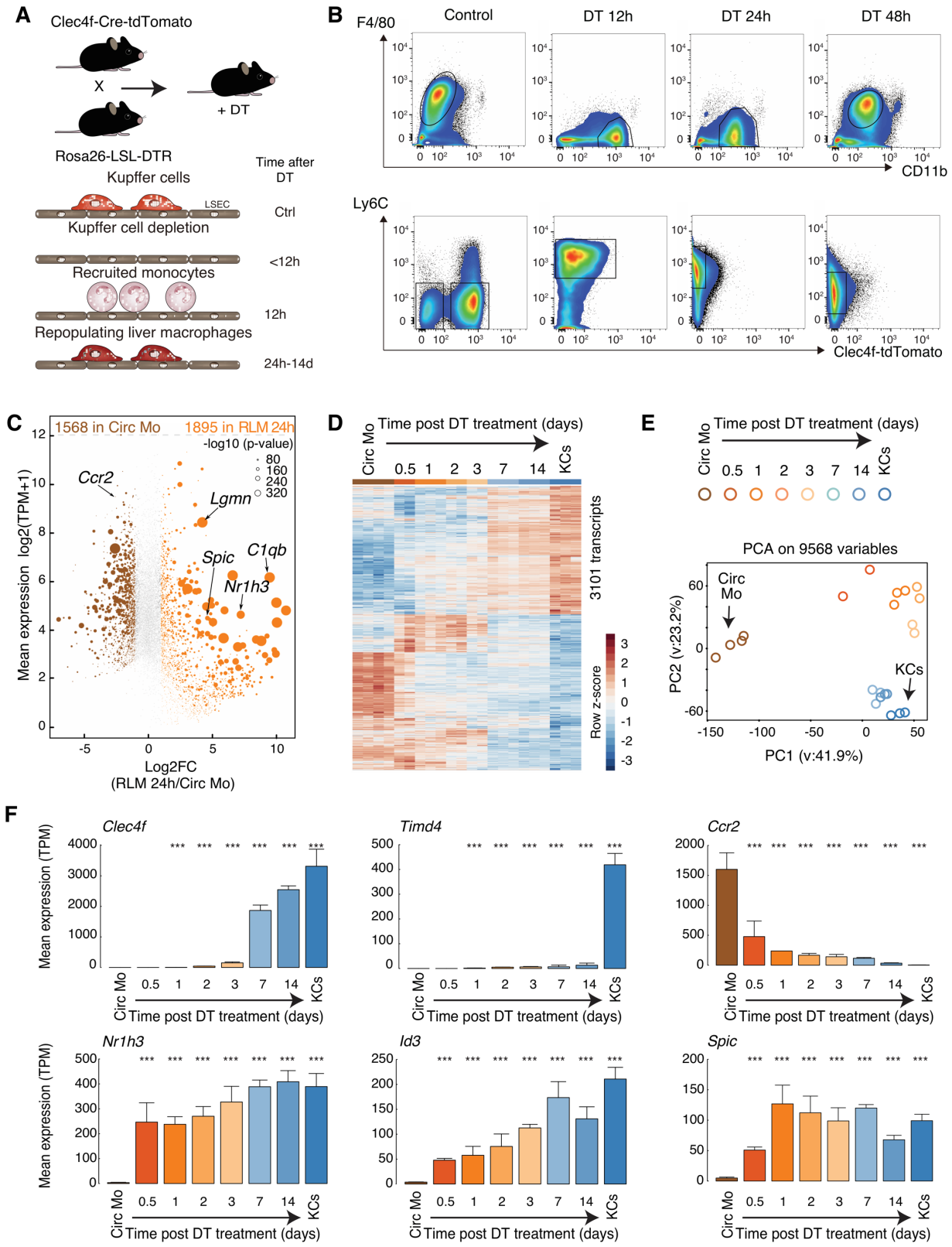
A
Clec4f-Cre-tdTomato
X
+ DT
Rosa26-LSL-DTR
Kupffer cells
Time after DT
LSEC
Kupffer cell depletion
Ctrl
Recruited monocytes
<12h
Repopulating liver macrophages
12h
24h-14d
B
F4/80
Control
DT 12h
DT 24h
DT 48h
CD11b
Ly6C
Clec4f-tdTomato
C
1568 in Circ Mo
1895 in RLM 24h
-log10 (p-value)
80
160
240
320
Ccr2
Lgmn
Spic
C1qb
Nr1h3
Mean expression log2(TPM+1)
Log2FC
(RLM 24h/Circ Mo)
D
Time post DT treatment (days)
Circ Mo
0.5 1 2 3 7 14
KCs
3101 transcripts
Row z-score
E
PCA on 9568 variables
Circ Mo
KCs
PC2 (v:23.2%)
PC1 (v:41.9%)
F
Clec4f
Timd4
Ccr2
Nr1h3
Id3
Spic
Mean expression (TPM)
Time post DT treatment (days)

Figure 2.2: Rapid reprogramming of the repopulating liver macrophage epigenetic landscape

A. Heat map of distal accessible chromatin regions defined by ATAC-seq in circulating monocytes, repopulating liver macrophages at 24 and 48 hours, and Kupffer cells. Each row is Z-score normalized tag counts for a peak. Distal regions are defined as 3kbp away from known transcription starting sites (TSS).
B. Enriched motifs in distal accessible chromatin regions defined by ATAC-seq of repopulating liver macrophages at 48 hours using GC-matched genomic background.
C. Bar plots for expression of Maf, Mafb, and Tfec in circulating monocytes (Circ Mo), repopulating liver macrophages as a function of time after DT treatment, and resident Kupffer cells (KCs). The significance markers represent the FDR from DESeq2 comparing to circulating monocytes respectively. *p-adj < 0.05; ***p-adj < 0.001.
D. Scatter plot of distal ATAC-associated H3K27ac in repopulating liver macrophages at 24h post DT treatment vs circulating monocytes. Color codes indicate significant changes (FDR < 0.05 & FC > 2) in H3K27ac signal with or without significant changes in ATAC-seq peaks.
E. Genome browser tracks of ATAC-seq and H3K27ac ChIP peaks in the vicinity of the Nr1h3, Mafb, Clec4f, and Cd5l loci in blood monocytes (Circ Mono), repopulating liver macrophages (RLM) at 24 and 48 hours and Kupffer cells. Yellow shading; pre-existing ATAC-seq peaks in circulating monocytes. Blue shading; regions of open chromatin acquired during RLM differentiation.

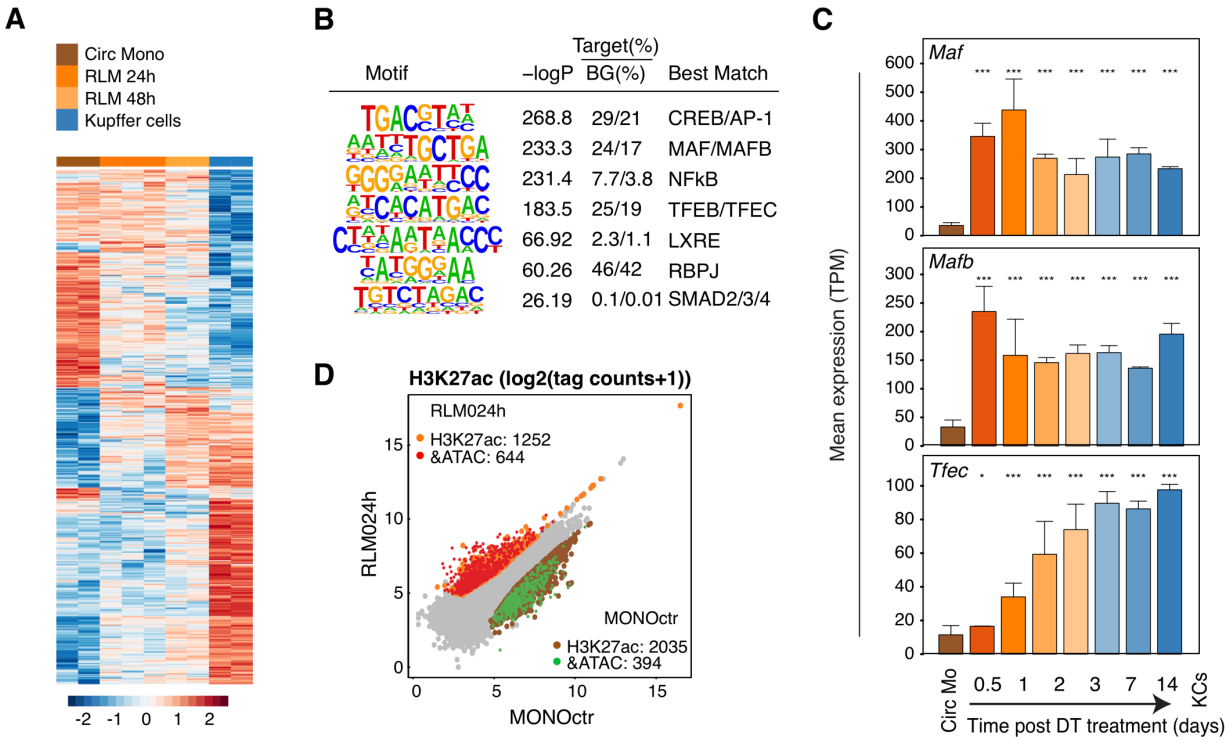
A
Circ Mono
RLM 24h
RLM 48h
Kupffer cells
-2 -1 0 1 2
B
Target(%)
Motif
–logP
BG(%)
Best Match
268.8 29/21 CREB/AP-1
233.3 24/17 MAF/MAFB
231.4 7.7/3.8 NFkB
183.5 25/19 TFEB/TFEC
66.92 2.3/1.1 LXRE
60.26 46/42 RBPJ
26.19 0.1/0.01 SMAD2/3/4
C
Maf
Mafb
Tfec
Mean expression (TPM)
Circ Mo
0.5 1 2 3 7 14
KCs
Time post DT treatment (days)
D
H3K27ac (log2(tag counts+1))
RLM024h
H3K27ac: 1252
&ATAC: 644
MONOctr
H3K27ac: 2035
&ATAC: 394
RLM024h
MONOctr

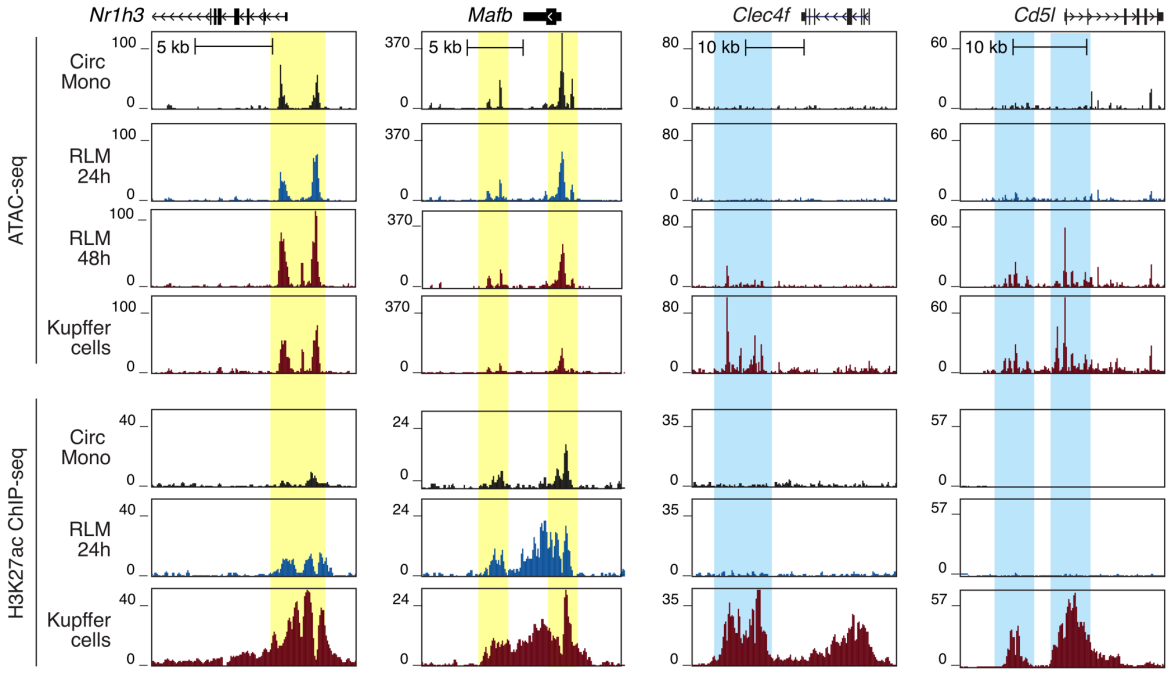
E
Nr1h3
Mafb
Clec4f
Cd5l
5 kb
10 kb
ATAC-seq
H3K27ac ChIP-seq
Circ Mono
RLM 24h
RLM 48h
Kupffer cells

Figure 2.3: LXRα is a Kupffer cell lineage-determining TF

A. Scatter plot of mRNA expression in Control Kupffer cells vs Tim4^{Neg} LXRα KO Kupffer cells. Significantly differentially-expressed genes are colored (blue: down-regulated in LXRα KO KC; purple: up-regulated in LXRα KO KC). Kupffer cell-specific genes are color-coded in red.
B. Bar plots of expression of the indicated genes in control or Tim4^{Neg} LXRα KO Kupffer cells. The significance symbols represent the FDR from DESeq2 comparing LXRα KO KC to Control KC. ***p-adj < 0.001.
C. Scatter plot of IDR-defined ATAC-seq peaks in Control Kupffer cells vs. Tim4^{Neg} LXRα KO Kupffer cells. Significantly-changed ATAC-peaks are color-coded (blue: significantly reduced in KC; purple: significantly gained in LXRα KO KC). KC-specific enhancers identified in **Figure 2.S2B** are color-coded in red.
D. Scatter plot of IDR-defined LXR ChIP-seq peaks in Kupffer cells against bone marrow derived macrophages. Differential LXR-ChIP peaks (FDR < 0.05 & FC > 2) are colored (Blue: KC-specific; Orange: BMDM-specific).
E. De novo motif enrichment analysis of Kupffer cell-specific LXR peaks using a GC-matched genomic background
F. Overlaps of total and KC-specific LXR ChIP-seq peaks with lost ATAC-Seq peaks in Tim4^{Neg} LXRα KO Kupffer cells
G. Genome browser tracks of LXR ChIP-seq peaks in BMDMs and KCs aligned with ATAC-seq peaks in control and LXRα KO KCs at the indicated loci. Yellow shading: common ATAC-seq peaks and LXR binding sites in BMDMs and KCs. Blue shading: KC-specific LXR binding sites associated with loss of ATAC peaks in Tim4^{Neg} LXRα KO Kupffer cells

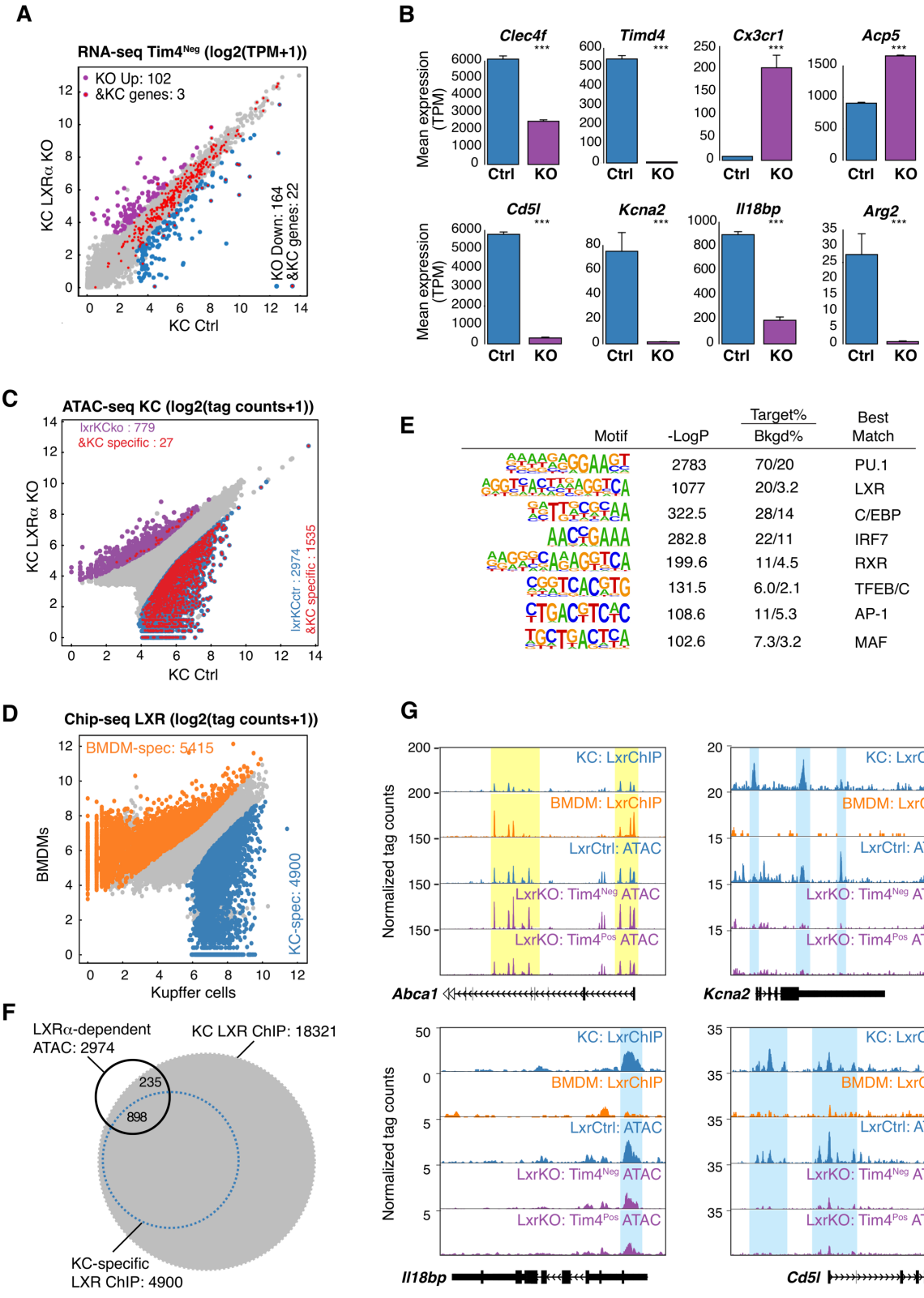
A
RNA-seq Tim4Neg (log2(TPM+1))
KO Up: 102
&KC genes: 3
KO Down: 164
&KC genes: 22
KC LXRα KO
KC Ctrl
B
Clec4f
Timd4
Cx3cr1
Acp5
Cd5l
Kcna2
Il18bp
Arg2
Mean expression (TPM)
Ctrl
KO
C
ATAC-seq KC (log2(tag counts+1))
lxrKCko : 779
&KC specific : 27
lxrKCctr : 2974
&KC specific : 1535
KC LXRα KO
KC Ctrl
D
Chip-seq LXR (log2(tag counts+1))
BMDM-spec: 5415
KC-spec: 4900
BMDMs
Kupffer cells
E
Motif
-LogP
Target%
Bkgd%
Best Match
2783 70/20 PU.1
1077 20/3.2 LXR
322.5 28/14 C/EBP
282.8 22/11 IRF7
199.6 11/4.5 RXR
131.5 6.0/2.1 TFEB/C
108.6 11/5.3 AP-1
102.6 7.3/3.2 MAF
F
LXRα-dependent ATAC: 2974
KC LXR ChIP: 18321
235
898
KC-specific LXR ChIP: 4900
G
Normalized tag counts
KC: LxrChIP
BMDM: LxrChIP
LxrCtrl: ATAC
LxrKO: Tim4Neg ATAC
LxrKO: Tim4Pos ATAC
Abca1
Kcna2
Il18bp
Cd5l

Figure 2.4: TGF-β/BMP signaling regulates KC identity

A. Expression of TGF-β/BMP family members in sinusoidal ECs.
B. Expression of TGF-β/BMP receptors in KCs.
C. Scatter plot of mRNA expression in control Kupffer cells vs Tim4Neg Smad4 KO Kupffer cells. Differentially-expressed genes are colored (blue: down-regulated in Smad4 KO KC; green: up-regulated in Smad4 KO KC) Kupffer cell-specific genes are color-coded in red.
D. Bar plots of expression of the indicated genes in control or Tim4Neg Smad4 KO Kupffer cells. The significance symbols represent the FDR from DESeq2 comparing Smad4 KO KC to Control KC. **p-adj < 0.01; ***p-adj < 0.001.
E. Scatter plot of IDR-defined ATAC-seq peaks in control or Smad4 KO Kupffer cells. Significantly-changed ATAC-peaks are colored (blue: reduced in Smad4 KO KC; green: gained in Smad4 KO KC).
F. Browser track examples of ATAC-seq in control and Smad4 KO KCs, Chip-seq for SMAD4 in KCs vs BMDMs and ChIP-seq for LXRs in KCs at the Clec4f and Lepr loci. Blue shading: Sites of SMAD4 binding exhibiting loss of corresponding ATAC-seq peak in Smad4 KO KCs.
G. Scatter plot of IDR-defined SMAD4 ChIP-seq peaks in Kupffer cells vs. bone marrow derived macrophages. Differential LXR-ChIP peaks (FDR < 0.05 & FC > 2) are colored (Blue: KC-specific; Orange: BMDM-specific).
H. De novo motif enrichment analysis of Kupffer cell-specific SMAD4 ChIP peaks using a GC-matched genomic background.
I. Overlap of LXR and SMAD4 binding sites in Kupffer cells.
J. Overlap of SMAD4 ChIP-seq peaks in Kupffer cells and KC-specific SMAD4 peaks with lost ATAC-seq peaks in Smad4 KO KCs.

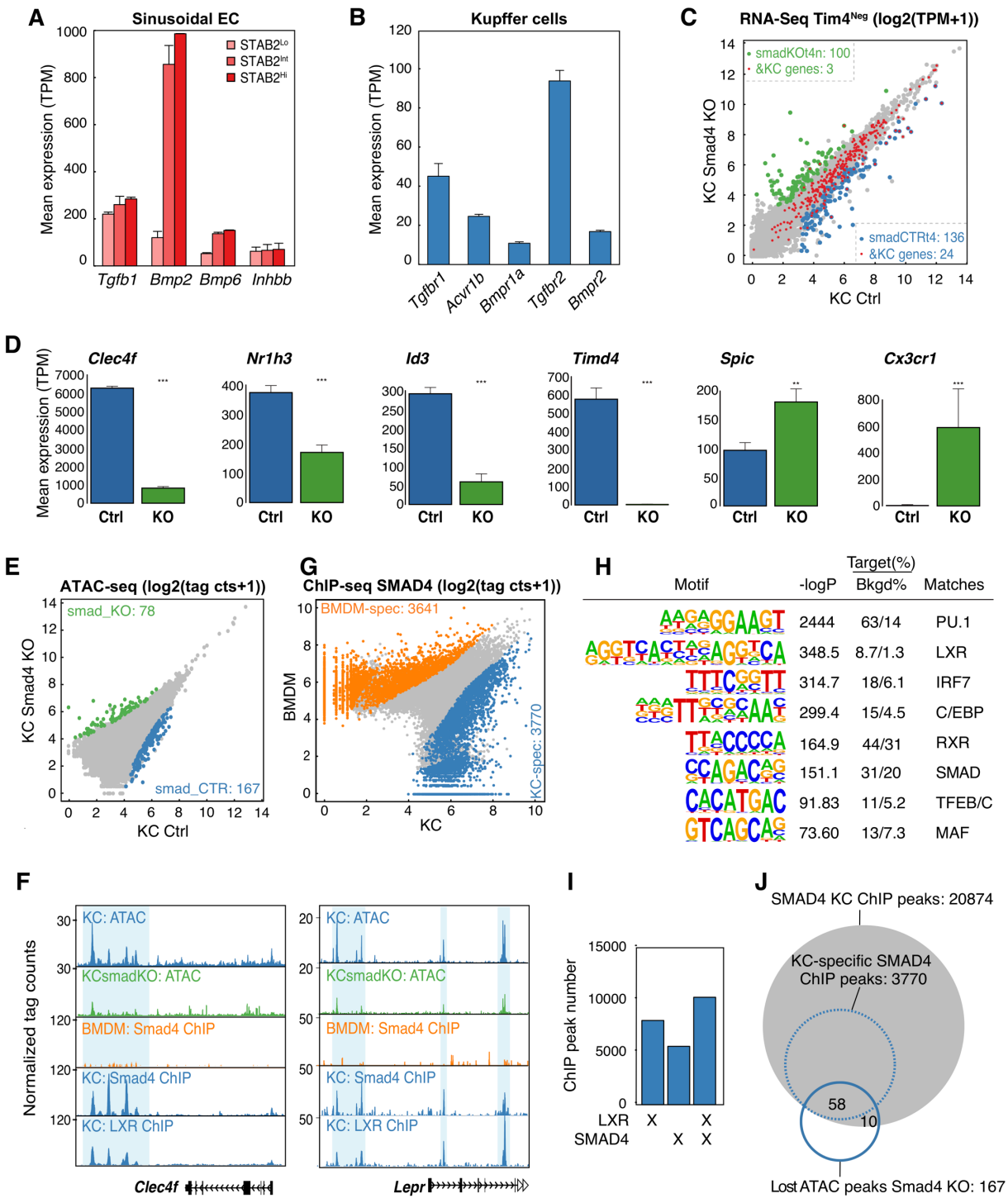
A
Sinusoidal EC
Mean expression (TPM)
STAB2Lo
STAB2Int
STAB2Hi
Tgfb1
Bmp2
Bmp6
Inhbb
B
Kupffer cells
Mean expression (TPM)
Tgfbr1
Acvr1b
Bmpr1a
Tgfbr2
Bmpr2
C
RNA-Seq Tim4Neg (log2(TPM+1))
smadKOt4n: 100
&KC genes: 3
smadCTRt4: 136
&KC genes: 24
KC Smad4 KO
KC Ctrl
D
Clec4f
Nr1h3
Id3
Timd4
Spic
Cx3cr1
Mean expression (TPM)
Ctrl
KO
E
ATAC-seq (log2(tag cts+1))
smad_KO: 78
smad_CTR: 167
KC Smad4 KO
KC Ctrl
G
ChIP-seq SMAD4 (log2(tag cts+1))
BMDM-spec: 3641
KC-spec: 3770
BMDM
KC
H
Motif
-logP
Target(%) Bkgd%
Matches
2444 63/14 PU.1
348.5 8.7/1.3 LXR
314.7 18/6.1 IRF7
299.4 15/4.5 C/EBP
164.9 44/31 RXR
151.1 31/20 SMAD
91.83 11/5.2 TFEB/C
73.60 13/7.3 MAF
F
Normalized tag counts
KC: ATAC
KCsmadKO: ATAC
BMDM: Smad4 ChIP
KC: Smad4 ChIP
KC: LXR ChIP
Clec4f
Lepr
I
ChIP peak number
LXR
SMAD4
J
SMAD4 KC ChIP peaks: 20874
KC-specific SMAD4 ChIP peaks: 3770
58
10
Lost ATAC peaks Smad4 KO: 167

Figure 2.5: Notch signaling activates KC lineage-determining factors in BMDMs

A. TGF-β induces *Tgfbi* expression in bone marrow derived macrophages, but does not induce expression of *Nr1h3* or *Id3*. The significance symbols represent the FDR from DESeq2 comparing TGF-β-stimulated BMDM to Control BMDM. ***p-adj < 0.001.
B. Expression of Notch ligands in sinusoidal ECs
C. Expression of Notch receptors in KCs
D. DLL4 induces *Nr1h3*, *Spic*, and *Tfec* gene expression in mouse BMDMs in a gamma secretase-dependent manner. The significance symbols represent the FDR from DESeq2 comparing BMDM stimulated with DLL4 alone or with DLL4 and DAPT to Control BMDM respectively. **p-adj < 0.01; ***p-adj < 0.001.
E. MA plot of RNA-seq data comparing control BMDMs and BMDMs treated with DLL4 for 24h. Each dot represents a gene, and the size of dots shows the significance as p-value in the comparison. Differentially-expressed genes are colored (purple: up-regulated in DLL4-stimulated BMDMs; Orange: down-regulated in DLL4-stimulated BMDMs) and Kupffer cell-specific genes are color-coded in red (up-regulated in DLL4-stimulated BMDMs) or black (not up-regulated in DLL4-stimulated BMDMs). Fisher's exact test was used to determine the odds ratio between DLL4 stimulation and KC-specific genes.
F. Bar plots for *Abcg3*, *Slc40a1*, *or C1qa* expression in circulating monocytes (Circ Mo), RLMs at 24 hours, and BMDMs with or without DLL4 stimulation. The significance symbols represent the FDR from DESeq2 comparing DLL4-treated BMDM to control BMDM, and RLMs at 24 hours to circulating monocytes respectively. ***p-adj < 0.001.

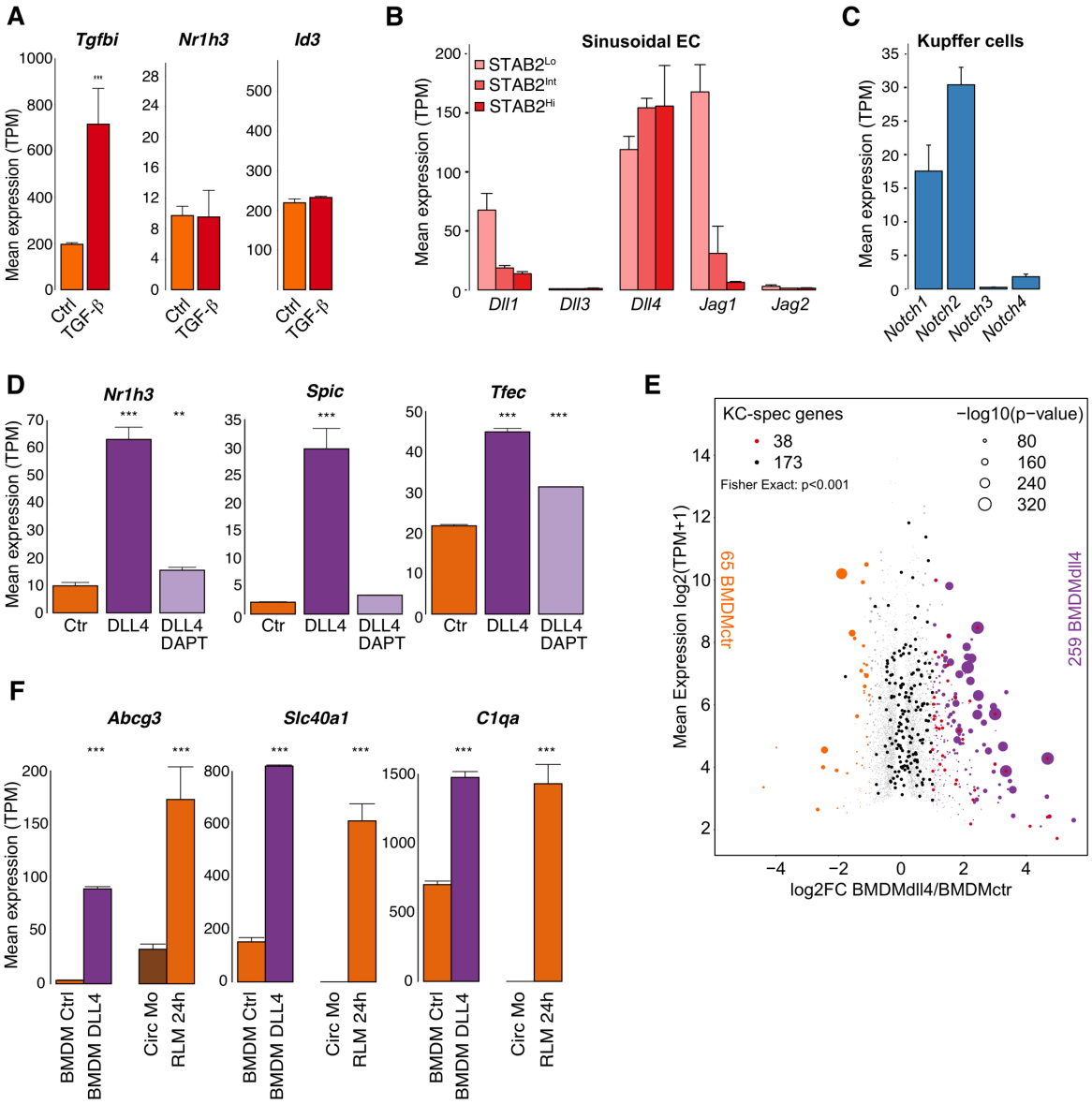
A
Tgfbi
Nr1h3
Id3
Mean expression (TPM)
Ctrl
TGF-β
B
Sinusoidal EC
STAB2Lo
STAB2Int
STAB2Hi
Dll1
Dll3
Dll4
Jag1
Jag2
C
Kupffer cells
Notch1
Notch2
Notch3
Notch4
D
Nr1h3
Spic
Tfec
Ctr
DLL4
DLL4 DAPT
E
KC-spec genes
38
173
Fisher Exact: p<0.001
−log10(p−value)
80
160
240
320
Mean Expression log2(TPM+1)
65 BMDMctr
259 BMDMdll4
log2FC BMDMdll4/BMDMctr
F
Abcg3
Slc40a1
C1qa
BMDM Ctrl
BMDM DLL4
Circ Mo
RLM 24h

Figure 2.6: Notch signaling activates a pre-existing enhancer landscape in bone marrow progenitor cells

A. Overlap of reproducible RBPJ ChIP-Seq peaks in Kupffer cells and bone marrow progenitor cells
B. Bar plot for *Rbpj* expression in circulating monocytes (Circ Mo), repopulating liver macrophages as a function of time after DT treatment, and resident Kupffer cells (KCs). The significance symbols represent the FDR from DESeq2 comparing to circulating monocytes respectively. ***p-adj < 0.001.
C. Scatter plot of IDR-defined distal ATAC-peaks in DLL4-treated BMDMs vs. control BMDMs. Significantly-changed ATAC-peaks (FDR < 0.05 & FC > 2) are colored (orange: reduced in control BMDMs; purple: gained in DLL4-treated BMDM).
D. Scatter plot of distal ATAC-associated H3K27ac in DLL4-treated BMDMs vs control BMDMs. Color codes indicate significant changes (FDR < 0.05 & FC > 2) in H3K27ac.
E. Motif enrichment analysis of distal ATAC-seq peaks in DLL4-treated BMDMs that gain H3K27ac.
F. Browser tracks of ATAC-Seq, H3K27ac ChIP-seq and RBPJ ChIP-seq peaks in the vicinities of putative regulatory elements for the *Nr1h3* and *Spic* genes (Yellow shading). Bar graphs illustrate H3K27ac normalized tag counts for the indicated genomic regions.

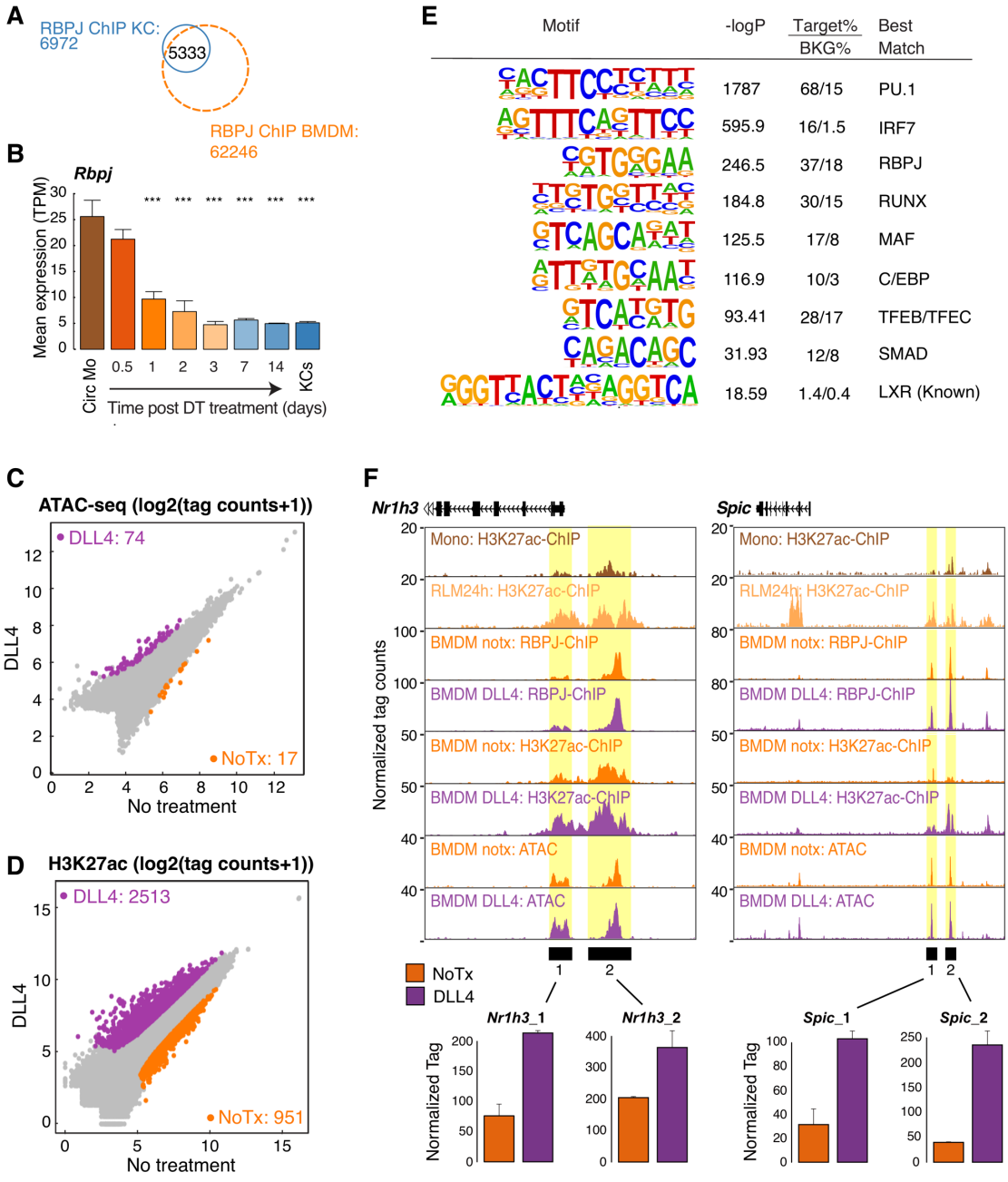
A
RBPJ ChIP KC: 6972
5333
RBPJ ChIP BMDM: 62246
B
Rbpj
Mean expression (TPM)
Circ Mo
0.5
1
2
3
7
14
KCs
Time post DT treatment (days)
E
Motif
-logP
Target%
BKG%
Best Match
1787
68/15
PU.1
595.9
16/1.5
IRF7
246.5
37/18
RBPJ
184.8
30/15
RUNX
125.5
17/8
MAF
116.9
10/3
C/EBP
93.41
28/17
TFEB/TFEC
31.93
12/8
SMAD
18.59
1.4/0.4
LXR (Known)
C
ATAC-seq (log2(tag counts+1))
DLL4: 74
NoTx: 17
DLL4
No treatment
D
H3K27ac (log2(tag counts+1))
DLL4: 2513
NoTx: 951
DLL4
No treatment
F
Nr1h3
Spic
Mono: H3K27ac-ChIP
RLM24h: H3K27ac-ChIP
BMDM notx: RBPJ-ChIP
BMDM DLL4: RBPJ-ChIP
BMDM notx: H3K27ac-ChIP
BMDM DLL4: H3K27ac-ChIP
BMDM notx: ATAC
BMDM DLL4: ATAC
Normalized tag counts
NoTx
DLL4
Nr1h3_1
Nr1h3_2
Spic_1
Spic_2
Normalized Tag

Figure 2.7: Combinatorial interactions of liver environmental signals

A. Effect of the combination of DLL4 and TGF-β on *Nr1h3* and *Clec4f* expression in control and Smad4 KO BMDMs. The significance symbols represent the FDR from DESeq2 comparing to control samples without stimulation in control and Smad4 KO respectively. ***p-adj < 0.001.
B. PCA analysis of overall gene expression in bone marrow progenitor cells stimulated with or without DLL4 and/or TGF-β, circulating monocytes (Circ Mo), repopulating liver macrophages (RLM) as a function of time after DT treatment, and resident Kupffer cells (KC).
C. Bar plots for expression of *Abca1* and *Ldlr* in circulating monocytes (Circ Mo), repopulating liver macrophages as a function of time after DT treatment, and resident Kupffer cells (KCs). The significance markers represent the FDR from DESeq2 comparing to circulating monocytes respectively. ***p-adj < 0.001.
D. Quantification of desmosterol, 24-, 25- and 27-OHC and 24,25-EC in mouse liver (left) and primary mouse hepatocytes (right).
E. Effects of the indicated combinations of DLL4, TGF-β and/or DMHCA on *Abca1, Il18bp* and *Arg2* expression in BMDMs.

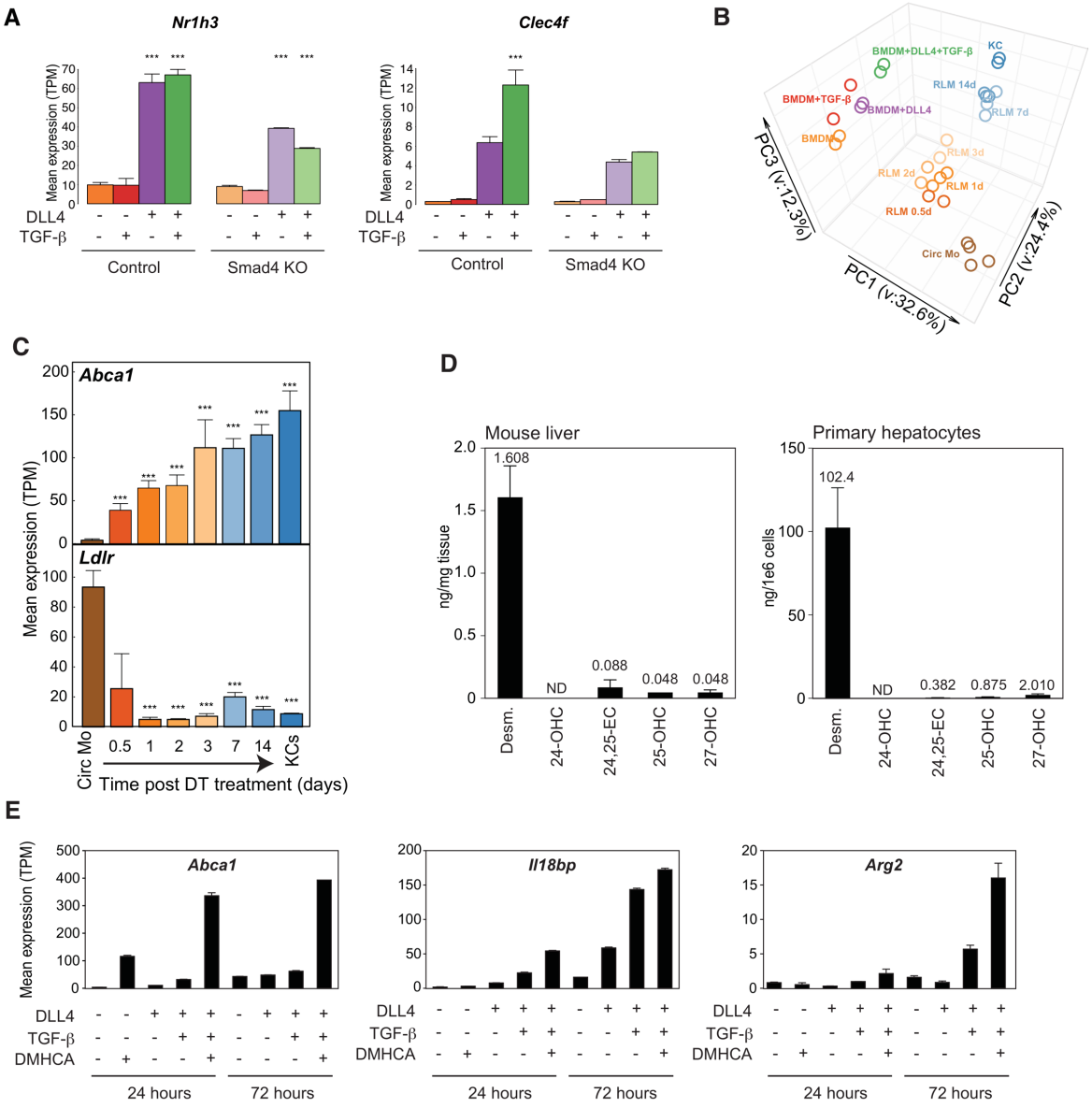
A
Nr1h3
Clec4f
Mean expression (TPM)
DLL4
TGF-β
Control
Smad4 KO
B
BMDM+DLL4+TGF-β
KC
RLM 14d
BMDM+TGF-β
BMDM+DLL4
RLM 7d
BMDM
RLM 3d
RLM 2d
RLM 1d
RLM 0.5d
Circ Mo
PC1 (v:32.6%)
PC2 (v:24.4%)
PC3 (v:12.3%)
C
Abca1
Ldlr
Circ Mo
0.5
1
2
3
7
14
KCs
Time post DT treatment (days)
D
Mouse liver
Primary hepatocytes
ng/mg tissue
ng/1e6 cells
1.608
ND
0.088
0.048
0.048
102.4
ND
0.382
0.875
2.010
Desm.
24-OHC
24,25-EC
25-OHC
27-OHC
E
Abca1
Il18bp
Arg2
DLL4
TGF-β
DMHCA
24 hours
72 hours

Figure 2.S1: Supplement to Figure 2.1

A. Targeting strategy for knock-in of IRES-Cre-T2A-tdTomato-NLS into the 3'-untranslated region of *Clec4f* and primers used for genotyping. L-HA, left homology arm; R-HA, right homology arm; IF, internal forward primer; IR, internal reverse primer; LF, left forward primer; LR, left reverse primer; RF, right forward primer; RR, right reverse primer
B. PCR screening of F0 mice derived from pronuclear injection of Cas9 protein, *Clec4f*-crRNA, tracrRNA, and targeting vector (TV)
C. Flow cytometry panels showing ZsGreen and Clec4f-tdTomato expressions in Kupffer cells (left) or hepatic $CD11b^{Hi}F4/80^{Lo}$ cells (right) from Rosa26 Lox-Stop-Lox ZsGreen Clec4f-Cre-tdTomato+/– or Rosa26 Lox-Stop-Lox ZsGreen LysM-Cre+/– mice
D. Clustering of replicate RNA-seq data for circulating monocytes (Circ Mo), repopulating liver macrophages as a function of time after DT treatment, and resident Kupffer cells (KCs)
E. MA plot of RNA-seq data comparing RLMs at 24 hours to circulating monocytes color-coded for KC-specific genes significantly up-regulated in RLMs (red) or not up-regulated (black). Fisher's exact test was used to determine the odds ratio between RLM24h and KC-specific genes.
F. Ingenuity pathway analysis of differentially-expressed genes in RLMs at 48 hours compared to RLMs at 24 hours
G. Bar plot for expression of *Mki67* in circulating monocytes (Circ Mo), repopulating liver macrophages as a function of time after DT treatment, and resident Kupffer cells (KCs). The significance symbols represent the FDR from DESeq2 comparing to circulating monocytes respectively. *p-adj < 0.05, **p-adj < 0.01; ***p-adj < 0.001.

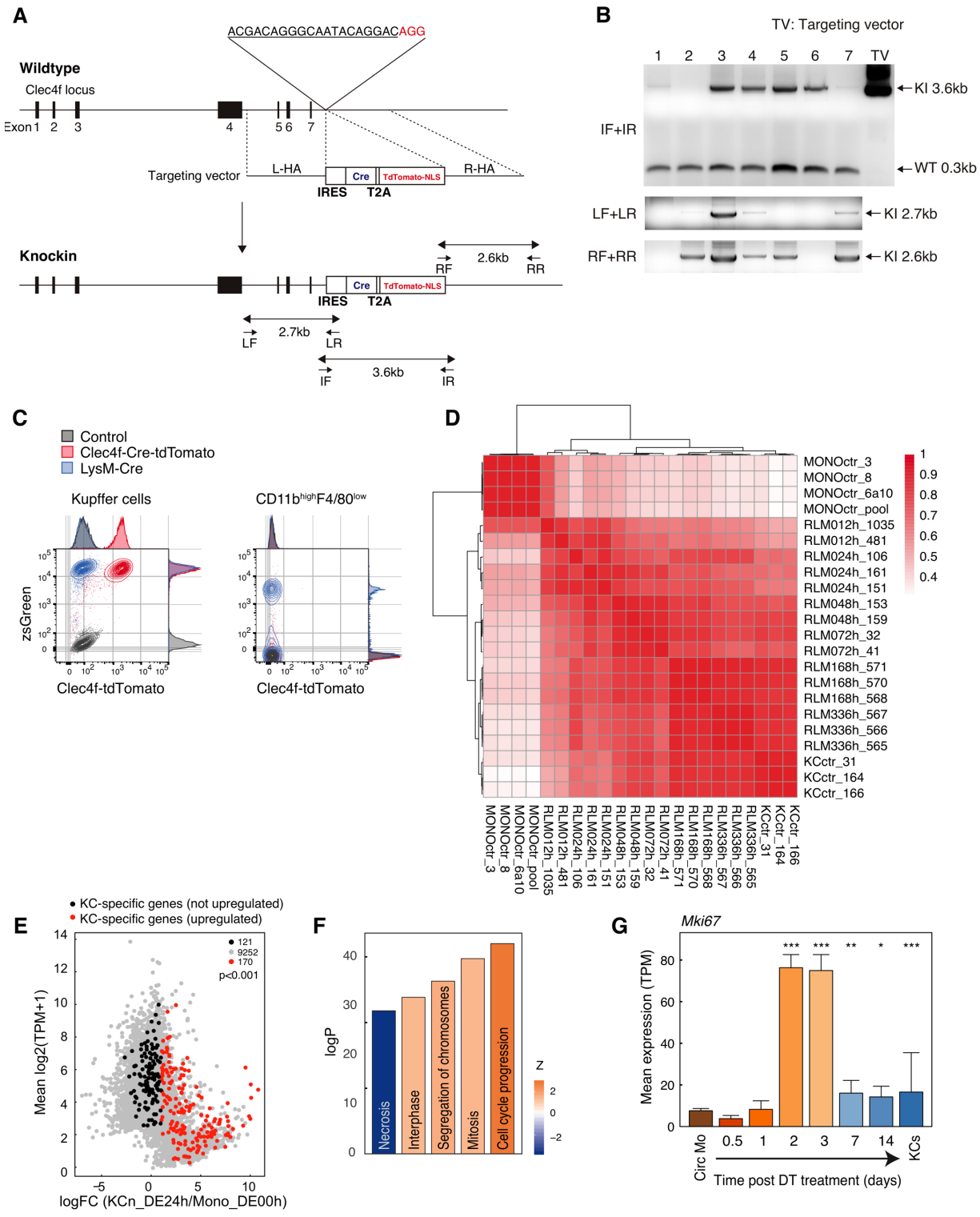
A
ACGACAGGGCAATACAGGACAGG
Wildtype
Clec4f locus
Exon 1 2 3 4 5 6 7
Targeting vector
L-HA
Cre
TdTomato-NLS
R-HA
IRES
T2A
Knockin
RF
2.6kb
RR
LF
2.7kb
LR
IF
3.6kb
IR
B
TV: Targeting vector
1 2 3 4 5 6 7 TV
KI 3.6kb
IF+IR
WT 0.3kb
LF+LR
KI 2.7kb
RF+RR
KI 2.6kb
C
Control
Clec4f-Cre-tdTomato
LysM-Cre
Kupffer cells
CD11b^highF4/80^low
zsGreen
Clec4f-tdTomato
Clec4f-tdTomato
D
MONOctr_3
MONOctr_8
MONOctr_6a10
MONOctr_pool
RLM012h_1035
RLM012h_481
RLM024h_106
RLM024h_161
RLM024h_151
RLM048h_153
RLM048h_159
RLM072h_32
RLM072h_41
RLM168h_571
RLM168h_570
RLM168h_568
RLM336h_567
RLM336h_566
RLM336h_565
KCctr_31
KCctr_164
KCctr_166
1
0.9
0.8
0.7
0.6
0.5
0.4
E
KC-specific genes (not upregulated)
KC-specific genes (upregulated)
121
9252
170
p<0.001
Mean log2(TPM+1)
logFC (KCn_DE24h/Mono_DE00h)
F
logP
Necrosis
Interphase
Segregation of chromosomes
Mitosis
Cell cycle progression
Z
G
Mki67
Mean expression (TPM)
Circ Mo
0.5
1
2
3
7
14
KCs
Time post DT treatment (days)

Figure 2.S2: Supplement to Figure 2.2

A. Clustering of correlation among replicate ATAC-seq data for circulating monocytes, repopulating liver macrophages (RLM) at 24 and 48h and Kupffer cells.
B. Heat map of distal ATAC-seq peaks exhibiting differential H3K27ac in BMDMs, Kupffer cells (KCs), Large Resident Peritoneal Macrophages (RPMs), Microglia (MG) and Circulating Monocytes (Mono). Peaks were filed to identify regions exhibiting >log2 fold change, p-adj <0.05 in at least 3 of the 4 comparisons with other cell types.
C. De novo motif enrichment analysis of distal accessible chromatin regions in Kupffer cells with > 2-fold increase in H3K27ac in at least 3/4 comparisons with other macrophages
D. Expression of *Irf7* in circulating monocytes (Circ Mo), repopulating liver macrophages as a function of time after DT treatment, and resident Kupffer cells (KCs). *** p-adj < 0.05.
E. Expression of *Jdp2*, *Fosl2*, *Junb* and *Jund* in circulating monocytes (Circ Mo), repopulating liver macrophages as a function of time after DT treatment, and resident Kupffer cells (KCs). D&E: The significance markers represent the FDR from DESeq2 comparing to circulating monocytes respectively. **p-adj < 0.05, **p-adj < 0.01; ***p-adj < 0.001.
F. Motif enrichment analysis for known motifs associated with distal ATAC-associated H3K27ac in circulating monocytes, RLMs at 24h and Kupffer cells.

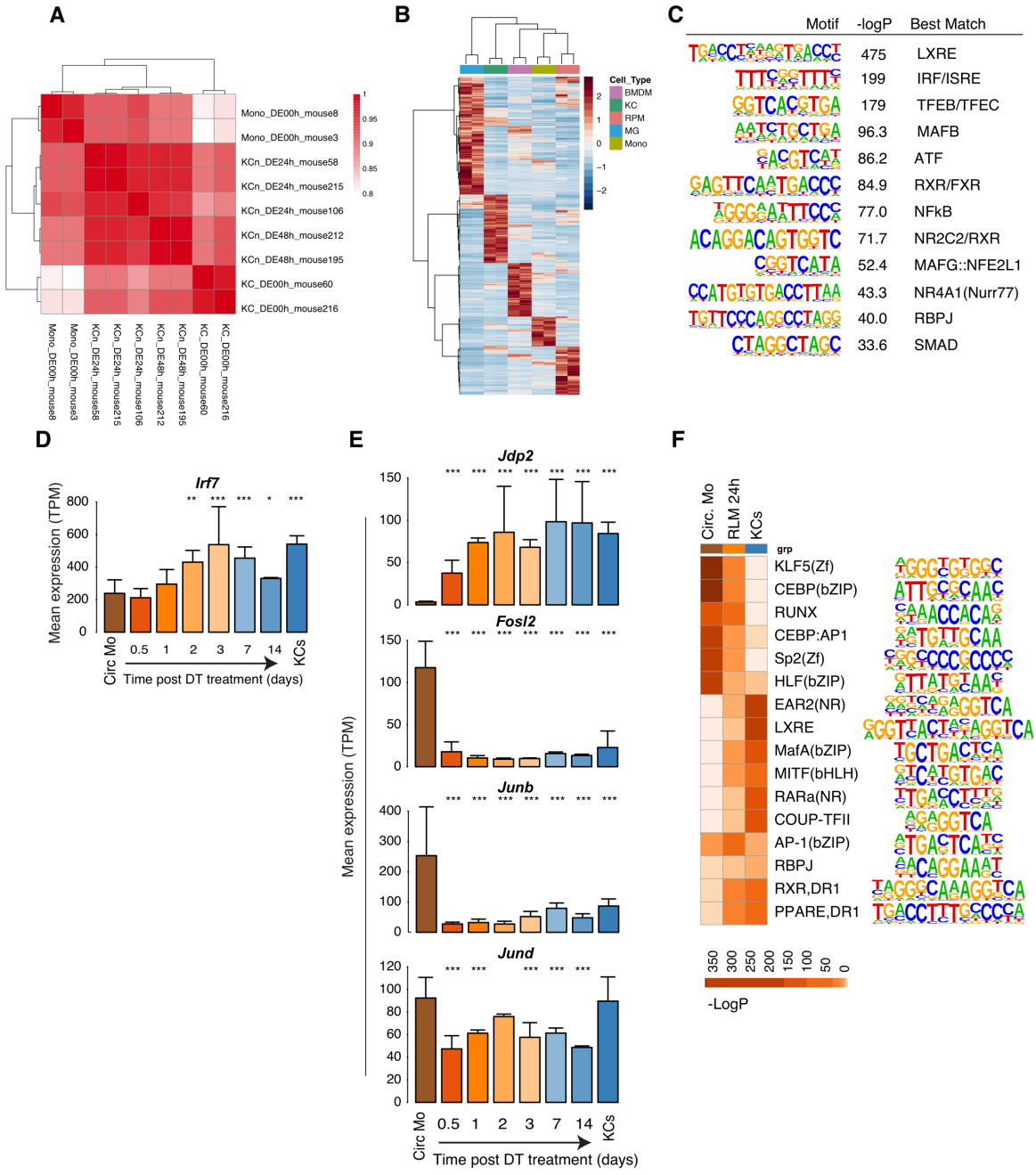
A
Mono_DE00h_mouse8
Mono_DE00h_mouse3
KCn_DE24h_mouse58
KCn_DE24h_mouse215
KCn_DE24h_mouse106
KCn_DE48h_mouse212
KCn_DE48h_mouse195
KC_DE00h_mouse60
KC_DE00h_mouse216
B
Cell_Type
BMDM
KC
RPM
MG
Mono
C
Motif
-logP
Best Match
475 LXRE
199 IRF/ISRE
179 TFEB/TFEC
96.3 MAFB
86.2 ATF
84.9 RXR/FXR
77.0 NFkB
71.7 NR2C2/RXR
52.4 MAFG::NFE2L1
43.3 NR4A1(Nurr77)
40.0 RBPJ
33.6 SMAD
D
Irf7
Mean expression (TPM)
Circ Mo
0.5 1 2 3 7 14
KCs
Time post DT treatment (days)
E
Jdp2
Fosl2
Junb
Jund
Mean expression (TPM)
Circ Mo
0.5 1 2 3 7 14
KCs
Time post DT treatment (days)
F
Circ. Mo
RLM 24h
KCs
grp
KLF5(Zf)
CEBP(bZIP)
RUNX
CEBP:AP1
Sp2(Zf)
HLF(bZIP)
EAR2(NR)
LXRE
MafA(bZIP)
MITF(bHLH)
RARa(NR)
COUP-TFII
AP-1(bZIP)
RBPJ
RXR,DR1
PPARE,DR1
-LogP

Figure 2.S3: Supplement to Figure 2.3

A. Flow cytometry of LXR $\alpha^{fl/fl}$ and LXRα$^{fl/fl}$ x Clec4f-Cre-tdTomato mice, indicating presence of Tim4^{Neg} populations in the Clec4f-Cre-tdTomato-positive mice
B. Genome browser image of RNA-seq data at the *Nr1h3* locus of LXRα$^{fl/fl}$ and LXRα$^{fl/fl}$ x Clec4f-Cre-tdTomato mice, indicating efficient excision of exons 4-7 in Cre-positive mice
C. Scatter plot of mRNA expression in control Kupffer cells vs. Tim4^{Pos} LXRα KO Kupffer cells. Differentially-expressed genes are colored (blue: down-regulated in Tim4^{Pos} LXRα KO KC; purple: up-regulated in Tim4^{Pos} LXRα KO KC). Kupffer cell-specific genes are color-coded in red.
D. Bar plots of expression of the indicated genes in control or Tim4^{Pos} LXRα KO Kupffer cells. ***p-adj < 0.001.
E. Scatter plot of mRNA expression in control BMDMs vs LXRα KO BMDMs. Differentially-expressed genes are colored (orange: down-regulated in LXRα KO BMDM; green: up-regulated in LXRα KO BMDM)
F. Scatter plot of ATAC-seq peaks in control Kupffer cells vs Tim4^{Pos} LXRα KO Kupffer cells. Significantly-changed ATAC-peaks are colored (blue: reduced in KC; purple: gained in Tim4^{Pos} LXRα KO KC) and KC-specific enhancers identified in **Figure 2.S2B** are color-coded in red.
G. Sorting of tdTomato-positive nuclei from Clec4f-Cre-tdTomato mice for ChIP-seq experiments.
H. Overlaps of total and KC-specific LXR ChIP-Seq peaks with lost ATAC-Seq peaks in Tim4-positive LXRα KO Kupffer cells
I. De novo motif analysis of lost ATAC-Seq peaks in Tim4^{Pos} LXRα KO Kupffer cells overlapping with KC-specific LXR ChIP-seq peaks.

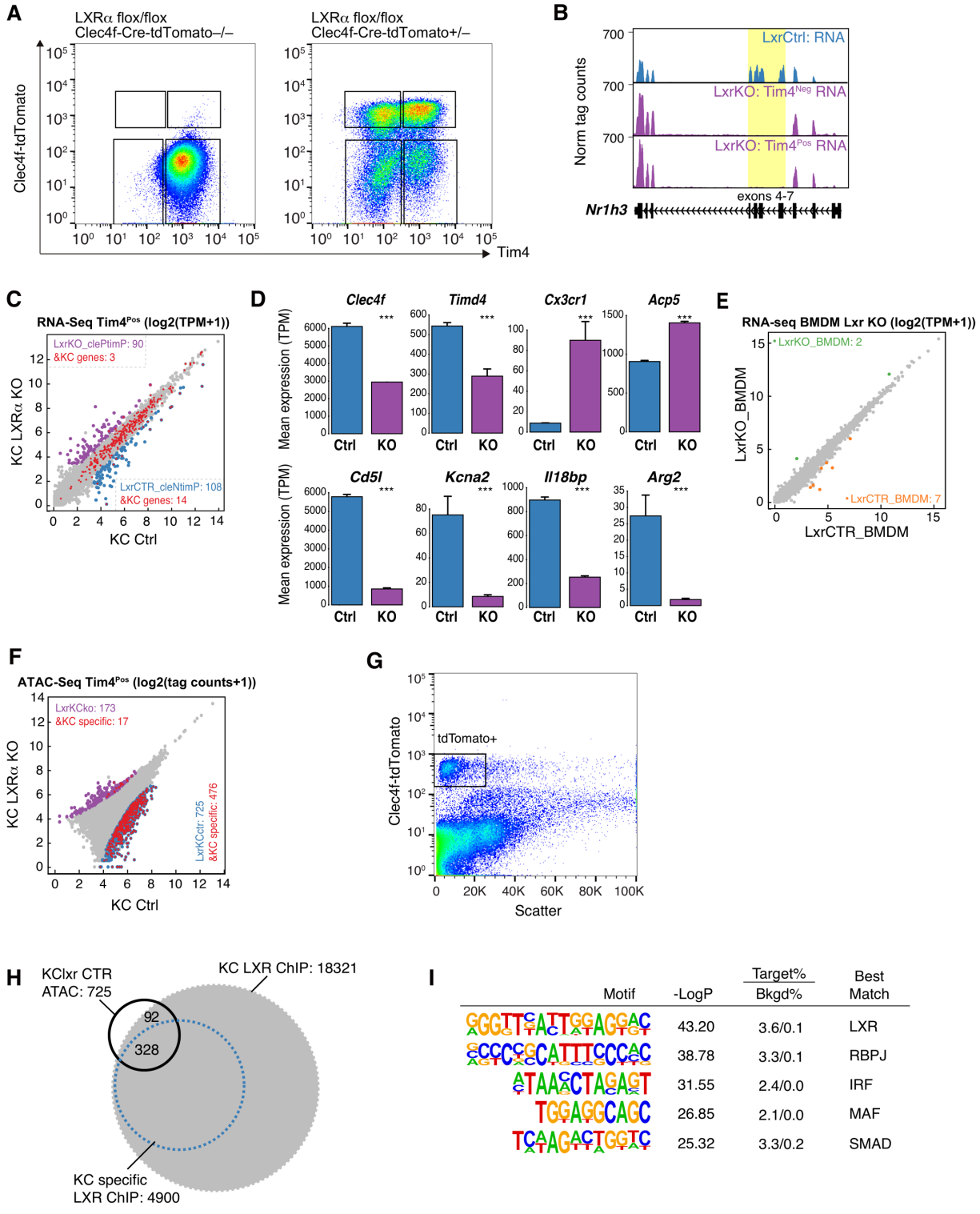
A
LXRα flox/flox
Clec4f-Cre-tdTomato–/–
LXRα flox/flox
Clec4f-Cre-tdTomato+/–
Clec4f-tdTomato
Tim4
B
LxrCtrl: RNA
LxrKO: Tim4Neg RNA
LxrKO: Tim4Pos RNA
Norm tag counts
exons 4-7
Nr1h3
C
RNA-Seq Tim4Pos (log2(TPM+1))
LxrKO_clePtimP: 90
&KC genes: 3
LxrCTR_cleNtimP: 108
&KC genes: 14
KC LXRα KO
KC Ctrl
D
Clec4f
Timd4
Cx3cr1
Acp5
Cd5l
Kcna2
Il18bp
Arg2
Mean expression (TPM)
Ctrl
KO
E
RNA-seq BMDM Lxr KO (log2(TPM+1))
LxrKO_BMDM: 2
LxrCTR_BMDM: 7
LxrKO_BMDM
LxrCTR_BMDM
F
ATAC-Seq Tim4Pos (log2(tag counts+1))
LxrKCko: 173
&KC specific: 17
LxrKCctr: 725
&KC specific: 476
KC LXRα KO
KC Ctrl
G
tdTomato+
Clec4f-tdTomato
Scatter
H
KClxr CTR
ATAC: 725
KC LXR ChIP: 18321
92
328
KC specific
LXR ChIP: 4900
I
Motif
-LogP
Target%
Bkgd%
Best
Match
43.20
3.6/0.1
LXR
38.78
3.3/0.1
RBPJ
31.55
2.4/0.0
IRF
26.85
2.1/0.0
MAF
25.32
3.3/0.2
SMAD

Figure 2.S4: Supplement to Figure 2.4

A. Flow cytometry of liver CD31^{Pos} endothelial cells sorted according to STAB2^{Lo}, STAB2^{Int} or STAB2^{Hi} levels.
B. Efficient deletion of a floxed *Smad4* exon 8 assessed by qPCR in Clec4f^{Pos} and Clec4f^{Neg} Smad4 KO Kupffer cells.
C. Flow cytometry of Smad4$^{fl/fl}$ and Smad4$^{fl/fl}$ x Clec4f-Cre-tdTomato mice, indicating variable presence of Tim4^{Neg} populations in the Clec4f-Cre-tdTomato-positive mice
D. Scatter plot of mRNA expression in control Kupffer cells vs Tim4^{Pos} Smad4 KO Kupffer cells. Differentially expressed genes are colored (blue: down-regulated in Tim4^{Pos} Smad4 KO KC; green: up-regulated in Tim4^{Pos} Smad4 KO KC). Kupffer cell-specific genes are color-coded in red.
E. Bar plots of expression of the indicated genes in control or Tim4^{Pos} Smad4 KO Kupffer cells. The significance markers represent the FDR from DESeq2 comparing Tim4^{Pos} Smad4 KO KC to control KC. **p-adj < 0.01; ***p-adj < 0.001.
F. Browser track examples of ATAC-seq in control and Smad4 KO KCs and ChIP-seq for SMAD4 in KCs vs BMDMs at the *Nr1h3* and *Id3* loci.

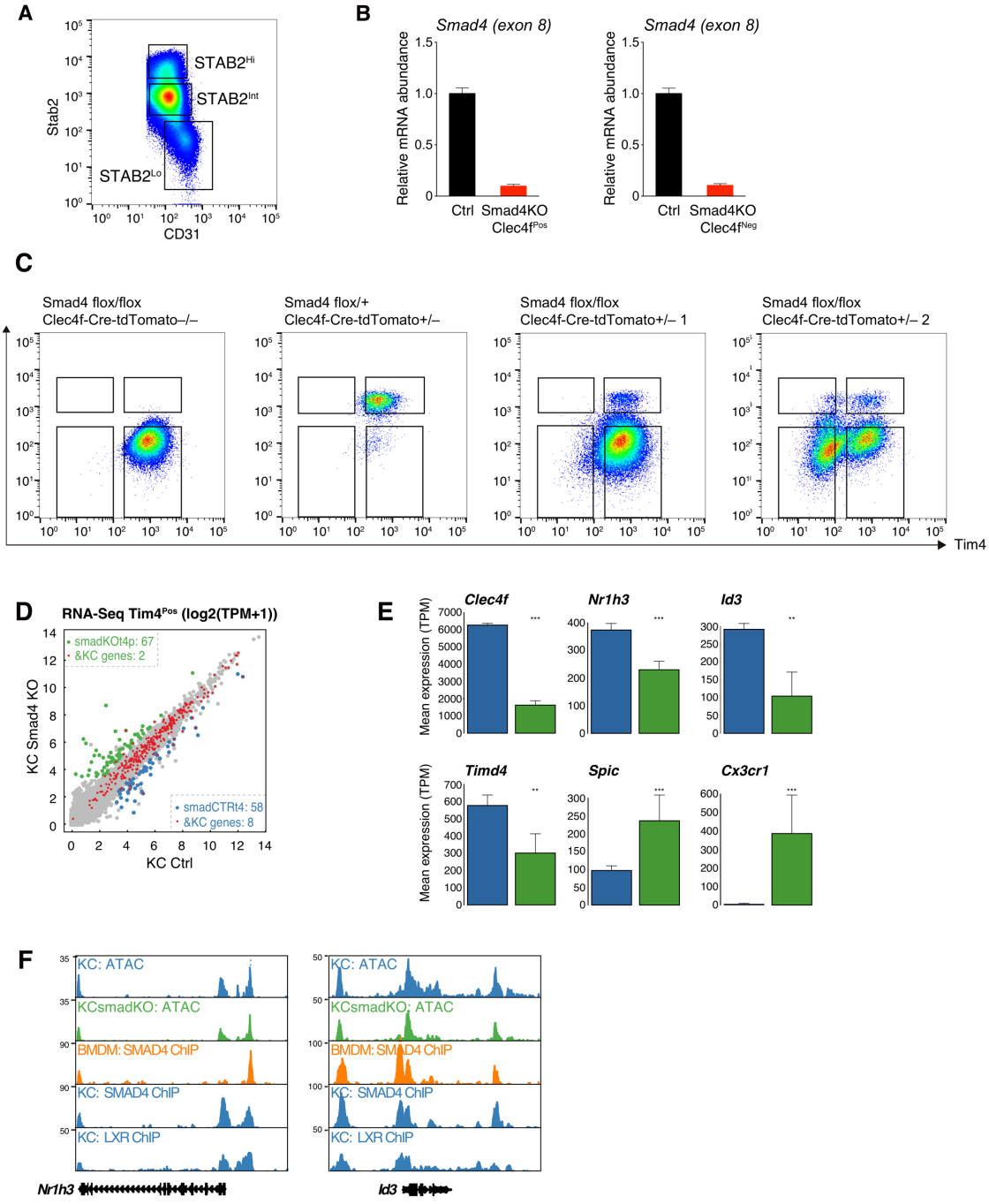
A
Stab2
CD31
STAB2Hi
STAB2Int
STAB2Lo
B
Smad4 (exon 8)
Relative mRNA abundance
Ctrl
Smad4KO Clec4fPos
Smad4 (exon 8)
Relative mRNA abundance
Ctrl
Smad4KO Clec4fNeg
C
Smad4 flox/flox Clec4f-Cre-tdTomato–/–
Smad4 flox/+ Clec4f-Cre-tdTomato+/–
Smad4 flox/flox Clec4f-Cre-tdTomato+/– 1
Smad4 flox/flox Clec4f-Cre-tdTomato+/– 2
Clec4f-tdTomato
Tim4
D
RNA-Seq Tim4Pos (log2(TPM+1))
smadKOt4p: 67
&KC genes: 2
smadCTRt4: 58
&KC genes: 8
KC Smad4 KO
KC Ctrl
E
Clec4f
Nr1h3
Id3
Timd4
Spic
Cx3cr1
Mean expression (TPM)
F
KC: ATAC
KCsmadKO: ATAC
BMDM: SMAD4 ChIP
KC: SMAD4 ChIP
KC: LXR ChIP
Nr1h3
Id3

Figure 2.S5: Supplement to Figure 2.5

A. MA plot of RNA-seq data comparing control BMDMs and BMDMs treated with DLL4 for 24h. Each dot represents a gene, and the size of dots shows the significance as p-value in the comparison. Differentially-expressed genes are colored (purple: up-regulated in DLL4-stimulated BMDMs; Orange: down-regulated in DLL4-stimulated BMDM) and genes up-regulated in RLM 24h compared to circulating monocytes are color-coded in red (up-regulated in DLL4-stimulated BMDMs) or black (not up-regulated in DLL4-stimulated BMDMs). Fisher's exact test was used to determine the odds ratio between DLL4 stimulation and genes induced in RLM 24h.
B. Bar plots for expression of indicated genes in circulating monocytes (Circ Mo), RLMs at 24 hours, and BMDMs with or without DLL4 stimulation. The significance symbols represent the FDR from DESeq2 comparing DLL4-treated BMDM to control BMDM, and RLMs at 24 hours to circulating monocytes respectively. ***p-adj < 0.001.

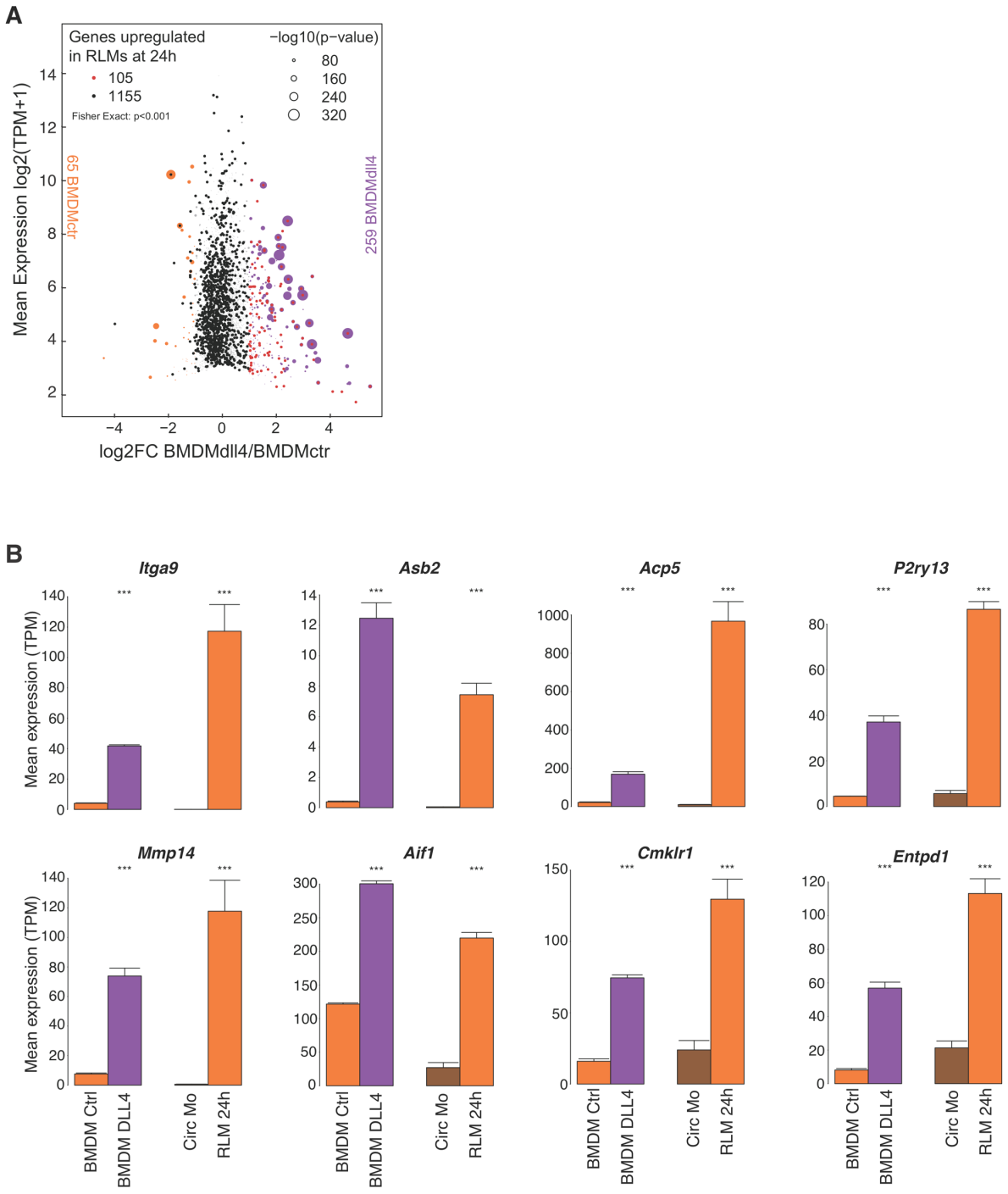
A
Genes upregulated
in RLMs at 24h
105
1155
Fisher Exact: p<0.001
−log10(p−value)
80
160
240
320
65 BMDMctr
259 BMDMdll4
Mean Expression log2(TPM+1)
log2FC BMDMdll4/BMDMctr
B
Itga9
Asb2
Acp5
P2ry13
Mmp14
Aif1
Cmklr1
Entpd1
Mean expression (TPM)
BMDM Ctrl
BMDM DLL4
Circ Mo
RLM 24h

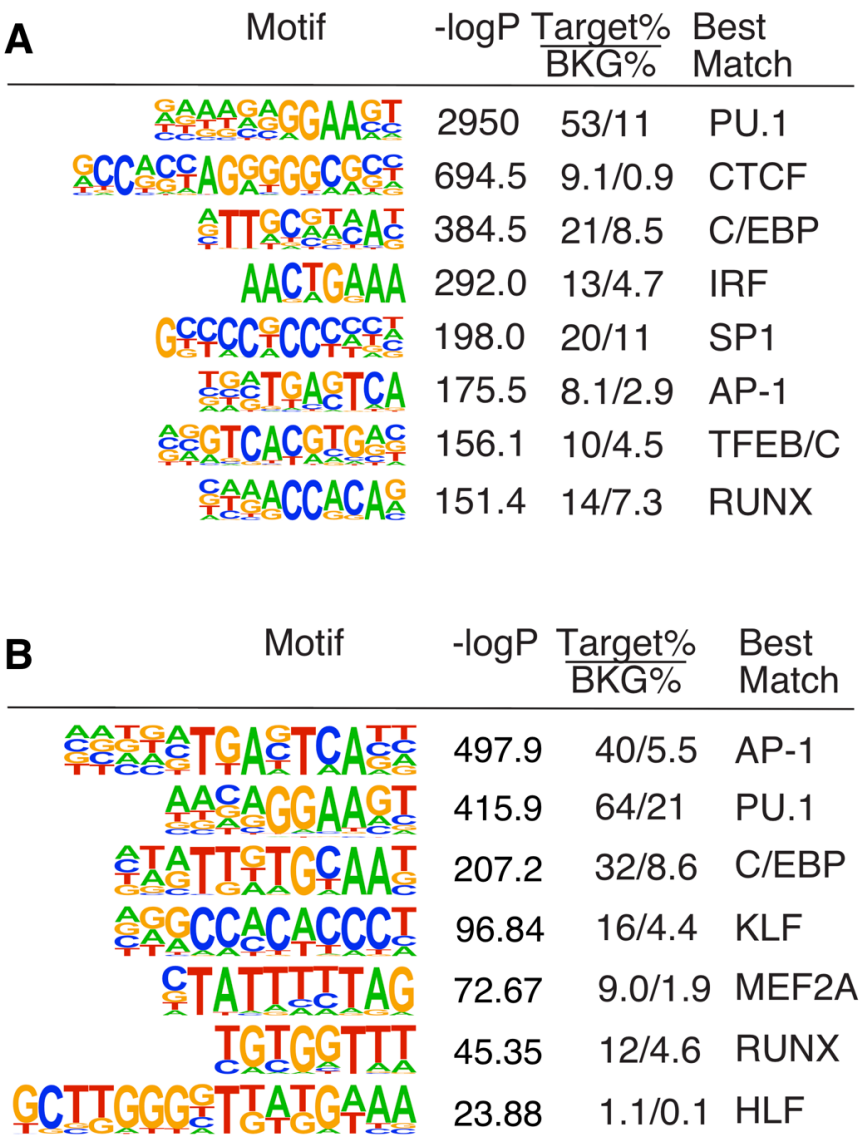

Figure 2.S6: Supplement to Figure 2.6

A. Motif enrichment analysis of distal RBPJ peaks common to Kupffer cells and DLL4-treated BMDMs.
B. Motif enrichment analysis of distal accessible ATAC-seq peaks in DLL4-treated BMDMs that lose H3K27ac.

Figure 2.S7: Supplement to Figure 2.7

A. Overlaps of LXR, SMAD4 and RBPJ binding sites in Kupffer cells
B. Browser tracks in the vicinity of *Abca1* and *C1qa* indicating H3K27ac in circulating monocytes (Circ Mono), repopulating liver macrophages at 24 hours (RLMs), and Kupffer cells (KCs) and ChIP-seq data for LXR, SMAD4 and RBPJ in KCs
C. Expression of *Scd1* and *Hmgcr* in circulating monocytes (Circ Mo), repopulating liver macrophages as a function of time after DT treatment, and resident Kupffer cells (KCs). ***p-adj < 0.001.
D. Expression of *Il18bp* and *Arg2* in circulating monocytes (Circ Mo), repopulating liver macrophages as a function of time after DT treatment, and resident Kupffer cells (KCs). ***p-adj < 0.001.
E. Browser tracks in the vicinity of *Il18bp* and *Arg2* indicating H3K27ac in circulating monocytes (Circ Mono), repopulating liver macrophages at 24 hours (RLMs), and Kupffer cells (KCs) and ChIP-seq data for LXR in KCs and BMDMs. ***p-adj < 0.001.

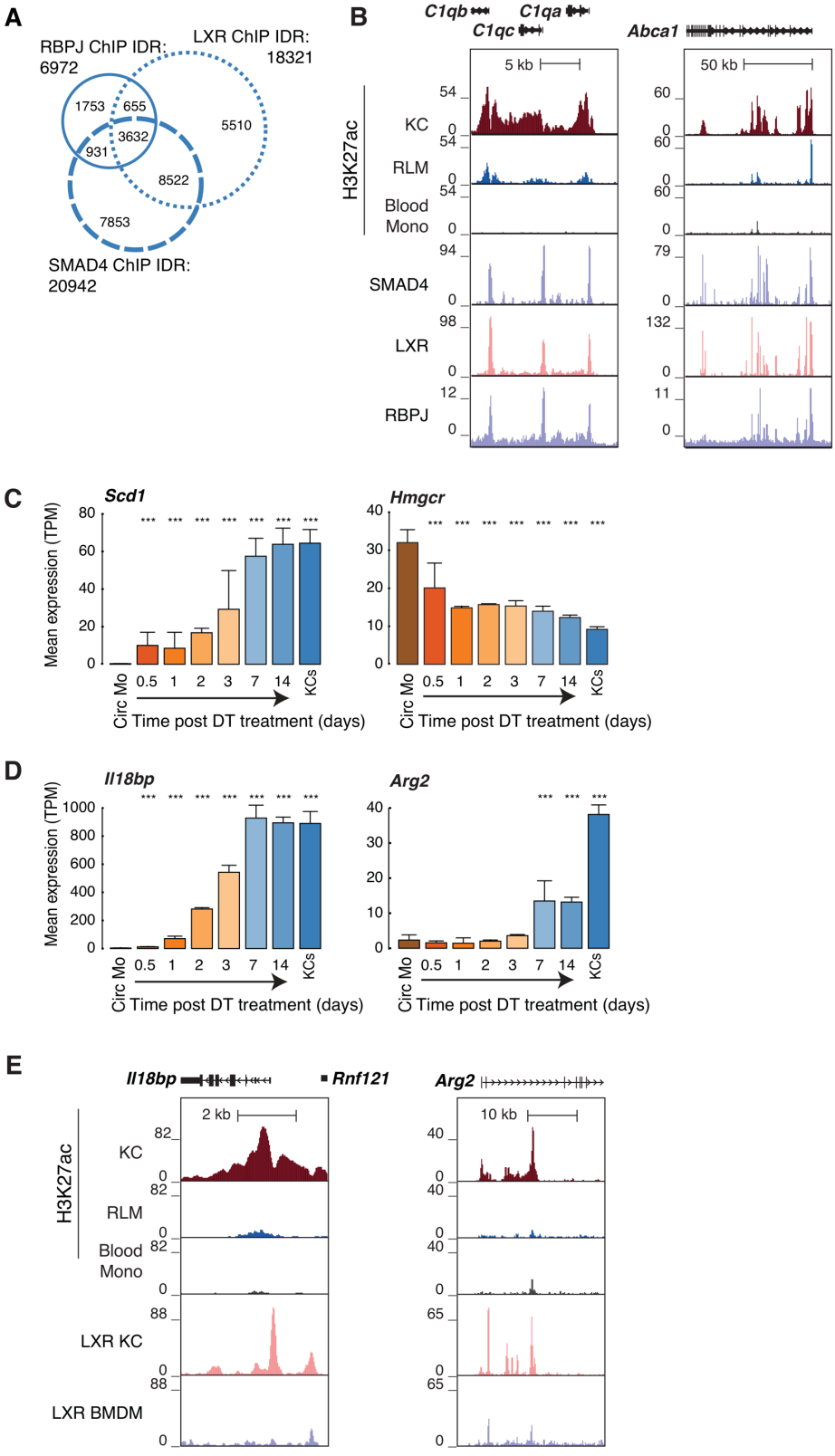
A
RBPJ ChIP IDR:
6972
LXR ChIP IDR:
18321
1753
655
5510
3632
931
8522
7853
SMAD4 ChIP IDR:
20942
B
C1qb
C1qa
C1qc
Abca1
5 kb
50 kb
H3K27ac
KC
RLM
Blood Mono
SMAD4
LXR
RBPJ
C
Scd1
Hmgcr
Mean expression (TPM)
Circ Mo
0.5
1
2
3
7
14
KCs
Time post DT treatment (days)
D
Il18bp
Arg2
E
Il18bp
Rnf121
Arg2
2 kb
10 kb
LXR KC
LXR BMDM

E. Methods

Mice

All animal procedures were approved by the University of California San Diego Institutional Animal Care and Use Committee in accordance with University of California San Diego research guidelines for the care and use of laboratory animals. The following mice were used in this study; C57BL/6J (The Jackson Laboratory, Stock No.000664), Clec4f-cre-tdTomato (generated by Glass Lab and transgenic core facility, University of California, San Diego) (The Jackson Laboratory, Stock No.033296), Rosa26-Lox-Stop-Lox-DTR mice (90)(The Jackson Laboratory, Stock No.007900), Rosa26-Lox-Stop-Lox-ZsGreen mice (The Jackson Laboratory, Stock No.007906), $Rosa^{nT\text{-}nG}$ mouse (121)(The Jackson Laboratory, Stock No.023035), LysM-cre (122)(The Jackson Laboratory, Stock No.004781), $Nr1h3^{fl/fl}$ (developed by Chambon Lab), Nr1h3 knockout (123)(The Jackson Laboratory, Stock No. 013763), and $Smad4^{fl/fl}$ (124)(The Jackson Laboratory, Stock No.017462). Mice were used between 8 and 12 weeks of age.

Cloning of the *Clec4f* targeting vector

The *Clec4f* targeting vector was cloned by modifying a pUC19 vector (NEB) using the In-Fusion HD Cloning Kit (Clontech). First, IRES-Cre-T2A was amplified from a pLV[Exp]-SYN1>mCherry:IRES:Cre:T2A:EGFP vector (VectorBuilder) with the forward primer IRES_Cre_T2A_F (5'-ATGCCTGCAGGTCGACCCCCTCTCCCTCCCCCCCCCCTAA-3') and the reverse primer IRES_Cre_T2A_R (5'-

GTGAATTCGAGCTCGGTACCGGGGCCGGGATTTTCCTCCACGTC-3') and inserted into the pUC19 at the SalI/KpnI site. Second, a nuclear localization signal-tagged tdTomato (tdTomato-NLS) was amplified from the genomic DNA of a Rosa$^{nT\text{-}nG}$ mouse (The Jackson Laboratory, Stock No.023035) (121) with the forward primer tdTomato_F (5'-CTAGAGGATCCCCGGGTACCATGGTGAGCAAGGGAGAGGAGGTC-3') and the reverse primer tdTomato_R (5'-GTGAATTCGAGCTCGTTATGAACGTCTTCGTCGCCTATC-3') and inserted into the KpnI site of pUC19-IRES-Cre-T2A. Third, a 2.5 kb left homology arm (LHA) was amplified from genomic DNA of a C57BL/6J mouse (The Jackson Laboratory) with the forward primer LHA_F (5'-ATGCCTGCAGGTCGACATGCTGAGAATCCCTGCTTCGCACAC-3') and the reverse primer LHA_R (5'-ATCCTCTAGAGTCGACGACAGGAAGCCCTGAAGTGAGATCAAGG-3') and inserted into the SalI site of the pUC19-IRES-Cre-T2A-tdTomato-NLS vector. Finally, a 2.5 kb right homology arm (RHA) was amplified from genomic DNA of a C57BL/6J mouse (The Jackson Laboratory) with the forward primer RHA_F (5'-TACCGAGCTCGAATTCCTGTATTGCCCTGTCGTTCTGCTATTT-3') and the reverse primer RHA_R (5'-GACGGCCAGTGAATTCGCTGCGGCTGAGGACCATTCTGAGTT-3') and inserted into the EcoRI site of the pUC19-LHA-IRES-Cre-T2A-tdTomato-NLS vector to make the *Clec4f* targeting vector, pUC19-LHA-IRES-Cre-T2A-tdTomato-NLS-RHA.

Generation of Clec4f-Cre-tdTomato mouse

30 ng/µl Cas9 protein (IDT), 0.61 pmol/µl *Clec4f*-crRNA (protospacer, ACGACAGGGCAATACAGGAC) (IDT), 0.61 pmol/µl tracrRNA (IDT), and 12ng/µl Clec4f targeting vector in IDTE pH7.5 (IDT) were injected into pronuclei of C57BL/6J one cell stage zygotes (125). Knock-in mice were screened by PCR with KOD Xtreme Hot Start DNA polymerase (EMD Millipore) using three different pairs of primers, internal forward primer (Clec4f_IF, 5'-ACTGGAGACATAGGAACGGAGAGCG-3') and internal reverse primer (Clec4f_IR, 5'-GTGCTGAGGGGACTCCAATGCAG-3'), left forward primer (Clec4f_LF, 5'-GCCAGGTCCAGTTTCCTGGTGATG-3') and left reverse primer (Clec4f_LR, 5'-TCCAAGCGGCTTCGGCCAGTAAC-3'), and right forward primer (Clec4f_RF, 5'-GCCAGATAGGCGACGAAGACGTTCA-3') and right reverse primer (Clec4f_RR, 5'-AGCCATTCCTGATACCTGGGGCC-3'). Clec4f_IF + Clec4f_IR amplified a 277-bp band from the WT allele and a 3652-bp band from the Clec4f-Cre-tdTomato allele. Clec4f_LF + Clec4f_LR amplified a 2668-bp band while Clec4f_RF + Clec4f_RR amplified a 2584-bp band from the Clec4f-Cre-tdTomato allele. Clec4f-Cre-tdTomato+/– mice were then crossed to C57BL/6J WT mice for at least for three generations.

Diphtheria toxin (DT)-mediated depletion of Kupffer cells

Mice expressing diphtheria toxin receptors (DTR) in Kupffer cells were produced by crossing Clec4f-cre-tdTomato mice to Rosa26-Lox-Stop-Lox-DTR mice

(Rosa26iDTR, The Jackson Laboratory, Stock No.007900) (90). Rosa26-Lox-Stop-Lox-DTR +/– Clec4f-Cre-tdTomato +/– mice were depleted of Kupffer cells by a single intraperitoneal administration of 200ng DT (Sigma).

Gene expression analysis by quantitative RT-PCR

Total RNA was isolated from sorted Kupffer cells with the use of a Direct-zol RNA MicroPrep Kit (Zymo Research). For quantitative RT-PCR analysis of *Smad4*, cDNA was synthesized from the total RNA extracted from sorted Kupffer cells with the use of a SuperScript III First-Strand Synthesis System (Thermo Fisher Scientific) and PCR was then performed with the use of a StepOnePlus Real-Time PCR System (Thermo Fisher Scientific), KAPA SYBR FAST qPCR Master Mix (2X) (Kapa Biosystems), and primers Smad4_qF1 (5'-CAGCCTCCCATTTCCAATCATC-3') and Smad4_qR1 (5'-CGAAGGATCCACATAGCCATCC-3'). Relative mRNA abundance was calculated by the standard curve method and was normalized by the corresponding amount of 18s rRNA using primers 18s_qF (5'-AATTCCCAGTAAGTGCGGGTCA-3') and 18s_qR (5'-GATCCGAGGGCCTCACTAAACC-3').

Sorting liver non-parenchymal cells

Mice were humanely euthanized by exposure to CO_2 and whole liver pieces saved and liver non-parenchymal cells processed for fluorescence-activated cell sorting of Kupffer cells, liver recruited monocytes, repopulating liver macrophages (RLMs), and liver sinusoidal endothelial cells (LSECs) with modifications from published

methodology (55, 126). Livers were perfused in a retrograde fashion for 3 minutes at a rate of 5 ml/min through the inferior vena cava with HBSS without Ca or Mg (Gibco) supplemented with 1 μM flavopiridol (Sigma), 0.5 mM EGTA, 0.5 mM EDTA, and 20 mM HEPES (Gibco). Perfusions were then switched to 40 ml of digestion buffer comprised of HBSS with Ca and Mg (Gibco) supplemented with 0.033 mg/ml of Liberase TM (Roche), 20 μg/ml DNase I, 1 μM flavopiridol, and 20 mM HEPES. Livers were then excised, minced, and digested for an additional 20 minutes in vitro at 37°C with gentle rotation in 20 ml of fresh digestion buffer. After tissue digestion, cells were passed through a 70 µm cell strainer, and hepatocytes were removed by two low-speed centrifugation steps at 50 X G for 2 minutes. Non-parenchymal cells in the supernatant were further separated from debris by pelleting for 15 minutes at 600 X G in 50 ml of 20% isotonic Percoll (Sigma) at room temperature. Next, cells were washed from Percoll containing buffer and resuspended in 10 ml 28% OptiPrep (Sigma) and carefully underlaid beneath 3 ml of wash buffer. The resulting gradient was centrifuged at 1,400 X G for 25 minutes at 4°C with no brake and cells enriched at the interface were saved and subjected to RBC lysis (eBioscience). Enriched non-parenchymal cells were washed, suspended in PBS, then stained for 10 minutes with Zombie NIR (BioLegend) and purified anti-CD16/32 (93, BioLegend) to label dead cells and block Fc receptors. After that, cells were stained in wash buffer for an additional 20 minutes with the antibodies of interest. Stained cells were washed twice and strained through a 30 µm strainer, then subjected to cell sorting using a Beckman Coulter MoFlo Astrios EQ configured with 355 nm, 405 nm, 488 nm, 561 nm, and 642 nm lasers. Each cell

population was hierarchically gated using Beckman Coulter Summit software. Kupffer cells were defined as $CD45^{Pos}F4/80^{Hi}CD11b^{Int}CD115^{Pos}$Clec4f-$tdTomato^{Pos}Ly6C^{Lo}CD31^{Neg}CD146^{Neg}$. Liver recruited monocytes were defined as $CD45^{Pos}F4/80^{Lo}CD11b^{Hi}CD115^{Pos}$Clec4f-$tdTomato^{Neg}Ly6C^{Hi}CD31^{Neg}CD146^{Neg}$ while RLMs at 24 hours, 48 hours, and 72 hours were defined as $CD45^{Pos}F4/80^{Int\sim Hi}CD11b^{Int}CD115^{Pos}$Clec4f-$tdTomato^{Neg}Ly6C^{Int\sim Lo}CD31^{Neg}CD146^{Neg}$. RLMs at day 7 and day 14 were defined as $CD45^{Pos}F4/80^{Hi}CD11b^{Int}Tim4^{Neg}$Clec4f-$tdTomato^{Pos}CD146^{Neg}$. $Tim4^{Neg}$ or $Tim4^{Pos}$ Kupffer cells were sorted as $CD45^{Pos}F4/80^{Hi}CD11b^{Int}Tim4^{Neg\ or\ Pos}$Clec4f-$tdTomato^{Neg\ or\ Pos}CD146^{Neg}$. LSECs were defined as $CD45^{Neg}F4/80^{Neg}CD11b^{Neg}CD31^{Pos}CD146^{Pos}STAB2^{Int\sim Hi}$. Each cell population was further restricted to single particles by comparing height and area side scatter pulses, and dead cells were excluded by detecting the integration of the live/dead dye (Zombie NIR).

Sorting blood monocytes

Mice were humanely euthanized by exposure to CO2. Blood was collected from mice via cardiac puncture into K3EDTA tubes and subjected to RBC lysis (eBioscience). Cells were pelleted by centrifugation at 350 X G for 10 minutes at 4°C and washed, suspended in PBS, then stained for 10 minutes with Zombie NIR (BioLegend) and purified anti-CD16/32 (93, BioLegend) to label dead cells and block Fc receptors. Next, cells were stained in wash buffer for an additional 20 minutes with the antibodies of interest. Stained cells were washed twice and strained through a 30 µm strainer, then

subjected to cell sorting using a Beckman Coulter MoFlo Astrios EQ configured with 355 nm, 405 nm, 488 nm, 561 nm, and 642 nm lasers. Each cell population was hierarchically gated using Beckman Coulter Summit software. Ly6C^{Hi} monocytes were defined as CD45^{Pos}CD11b^{Hi}CD115^{Pos}CD19^{Neg}CD90.2^{Neg}Ly6G^{Neg}Ly6C^{Hi}. Ly6C^{Hi} monocytes were further restricted to single particles by comparing height and area side scatter pulses, and dead cells were excluded by detecting the integration of the live/dead dye (Zombie NIR).

Sorting crosslinked Kupffer cell nuclei

Livers of Clec4f-Cre-tdTomato mice were perfused in a retrograde fashion using a Masterflex multichannel peristaltic pump (Cole-Parmer) briefly at a rate of 5ml/min through the inferior vena cava with HBSS without Ca or Mg (Gibco) supplemented with 0.5mM EGTA, 0.5mM EDTA, and 20mM HEPES. Subsequently, they were fixed by perfusion with 3mM DSG (ProteoChem) in PBS for 30 minutes, and 1% formaldehyde for 10 minutes at a rate of 5ml/min. The reaction was quenched by perfusion with 20ml 0.125M glycine. After fixation, livers were excised, minced and washed twice with 20ml ice-cold NF1 buffer (10mM Tris-HCl pH8.0, 1mM EDTA, 5mM MgCl2, 0.1M Sucrose, 0.5% Triton X-100) and pelleted by centrifugation for 7 minutes at 1,200 X G at 4°C. Livers were resuspended in NF1 buffer and homogenized with 10 strokes using the loose pestle of a Dounce homogenizer and incubated on ice for 30 minutes, and then homogenized with 50-70 strokes using the tight pestle with periodic assessment for released nuclei by microscopy. The homogenized liver was then filtered with a 70 µm

strainer into 50 ml tube and pelleted at 1,200g for 7 minutes at 4°C. Crude nuclei were then washed with 10ml PBS supplemented with 2mM EDTA and pelleted by centrifugation at 1,100 X G at 4°C for 5 minutes. The pellet was resuspended in PBS with 2mM EDTA and strained with a 40 µm strainer. Nuclei were purified by FACS using a Sony SH800 or Sony MA900 based on TdTomato expression and forward scatter. After sorting, nuclei were pelleted by centrifugation at 1,100 X G at 4°C for 5 minutes, and snap-frozen in liquid nitrogen and stored at –80°C until ready for ChIP-seq library preparation.

Bone marrow-derived macrophages (BMDM) culture

Femur, tibia and iliac bones from C57BL/6J mice, LXRα knockout mice, Smad4$^{fl/fl}$ mice, and Smad4 $^{fl/fl}$ LysM-Cre+/– mice were flushed with DMEM high glucose (Corning), and red blood cells were lysed using red blood cell lysis buffer (eBioscience).

For RNA-seq and ATAC-seq of LXRα wild-type and knockout mice, 20 million bone marrow cells were seeded per 15cm non-tissue culture plates in DMEM high glucose (60%) with 10% FBS (Biowest), 30% L929-cell conditioned laboratory-made media (as source of M-CSF), 100 U/ml penicillin-streptomycin (Thermo Fisher Scientific) and 2.5µg/ml Amphotericin B (Thermo Fisher Scientific). After 4 days of differentiation, 16.7 ng/ml mouse M-CSF (Shenandoah Biotechnology) was added to the media. After an additional 2 days of culture, non-adherent cells were washed off with room temperature DMEM and macrophages were obtained as a homogeneous population of adherent cells which were scraped and subsequently seeded onto tissue culture-treated

Petri dishes overnight in DMEM containing 10% FBS, 100 U/ml penicillin/streptomycin, 2.5µg/ml Amphotericin B and 16.7 ng/ml M-CSF.

For RNA-seq, ATAC-seq, and ChIP-seq of bone marrow progenitor cells from C57BL/6J mice, $Smad4^{fl/fl}$ mice, or $Smad4^{fl/fl}$ LysM-Cre mice, 20 million bone marrow cells were seeded per 15cm non-tissue culture plates in MEM (90%) with 10% FBS (Biowest), 10ng/ml M-CSF (Shenandoah Biotechnology), 100 U/ml penicillin/streptomycin+L-glutamine (Thermo Fisher Scientific) and 2.5µg/ml Amphotericin B (Thermo Fisher Scientific). For DLL4 stimulation, tissue culture-treated plates were coated with 1 µg/ml human recombinant DLL4 (R&D systems) overnight at 4°C. After 3 days of differentiation, non-adherent cells were washed off with room temperature DMEM and adherent cells were scraped and subsequently seeded onto tissue culture-treated plates in which the surface was coated with or without DLL4, and cultured with or without 2ng/ml human recombinant TGF-β1 (Cell Signaling Technology) and/or 1 µM DMHCA, for 24 hours or 72 hours in DMEM containing 10% FBS, 100 U/ml penicillin/streptomycin, 2.5µg/ml Amphotericin B, and 10 ng/ml M-CSF. Where indicated, cells were exposed to 10 µM DAPT (Cell Signaling Technology) for 24 hours.

Isolation and culture of mouse primary hepatocytes

Primary hepatocytes were isolated from 8- to 12-week-old male C57BL/6J mice as described previously (127). Mice were humanely euthanized by exposure to CO_2. Livers were perfused in a retrograde fashion for 3 minutes at a rate of 5 ml/min through the inferior vena cava with HBSS with Ca or Mg (Gibco) supplemented with 10 mM

HEPES (Gibco), then for 18 minutes with the same solution containing collagenase type I (32 mg per 100 ml, Worthington) and Protease Inhibitor Cocktail Complete–EDTA Free (Roche). The hepatocytes were harvested and purified by density gradient centrifugation with Percoll (Sigma) and plated on type I collagen–coated six-well plates (1 million cells per well) in Medium 199 (Gibco) supplemented with 5% FBS and 100 U/ml penicillin/streptomycin (Thermo Fisher Scientific).

Lipid Measurements

Livers and primary hepatocytes were processed at the University of Texas Southwestern Medical Center for oxysterol and lipid metabolite analysis by LC-MS as previously described in full (www.lipidmaps.org/protocols/index.html).

ATAC-seq library preparation

Approximately 50,000 sorted cells were washed once with PBS and once with cold lysis buffer (10 mM Tris-HCl, pH 7.4, 10 mM NaCl, 3 mM MgCl2, 0.1% IGEPAL CA-630). Cells were then suspended in 50 μl 1X reaction buffer (25µl Tagment DNA Buffer, 2.5µl Tagment DNA enzyme I, and 22.5µl water) (Nextera DNA Library Preparation Kit, Illumina) as previously described (128). Transposase reactions were carried out at 37°C for 30 minutes and immediately DNA was purified using ChIP DNA Clean & Concentrator kits (Zymo Research). DNA was amplified using the Nextera primer Ad1 and a unique Ad2.n barcoding primer using NEBNext High-Fidelity 2XPCR Master Mix (NEB) for 14 cycles. Resulting libraries were size selected by gel excision to

175-225 bp, purified, and single end sequenced using a HiSeq 4000 or a NextSeq 500 (Illumina) for 51 cycles according to the manufacturer's instructions.

RNA-seq library preparation

Total RNA was isolated from *in vitro* culture cells and purified using a Direct-zol RNA MicroPrep Kit (Zymo Research) according to the manufacturer's instructions (Zymo Research). FACS purified cells were pelleted and put into 150 µl lysis/Oligo d(T) Magnetic Beads binding buffer (100mM Tris-HCl pH7.5, 500mM LiCl, 10mM EDTA pH8.0, 1% LiDS, 5mM DTT) and stored at –80°C until processing. mRNAs were enriched by incubation with Oligo d(T) Magnetic Beads (NEB, S1419S). Poly A enriched mRNA was fragmented, in 2x Superscript III first-strand buffer with 10mM DTT (Thermo Fisher Scientific), by incubation at 94°C for 9 minutes, then immediately chilled on ice before the next step. The 10 μL of fragmented mRNA, 0.5 μL of Random primers (3 μg/μL) (Thermo Fisher Scientific), 0.5 μL of Oligo dT primer (50 μM) (Thermo Fisher Scientific), 0.5 μL of SUPERase-In (Ambion), 1 μL of dNTPs (10 mM) and 1 μL of DTT (10 mM) were heated at 50°C for one minute. At the end of incubation, 5.8 μL of water, 1 μL of DTT (100 mM), 0.1 μL Actinomycin D (2 μg/μL), 0.2 μL of 1% Tween-20 (Sigma) and 0.5 μL of Superscript III (Thermo Fisher Scientific) were added and incubated in a PCR machine using the following conditions: 25°C for 10 minutes, 50°C for 50 minutes, and a 4°C hold. The product was then purified with RNAClean XP beads (Beckman Coulter) according to manufacturer's instruction and eluted with 10 μL nuclease-free water. The RNA/cDNA double-stranded hybrid was then added to 1.5 μL of Blue Buffer

(Enzymatics), 1.1 μL of dUTP mix (10 mM dATP, dCTP, dGTP and 20 mM dUTP), 0.2 μL of RNAse H (5 U/μL), 1.05 μL of water, 1 μL of DNA polymerase I (Enzymatics) and 0.15 μL of 1% Tween-20. The mixture was incubated at 16°C for 2.5 hours. The resulting dUTP-marked dsDNA was purified using 28 μL of SpeedBeads (GE Healthcare), diluted with 20% PEG8000, 2.5M NaCl to final of 13% PEG, eluted with 40 μL EB buffer (10 mM Tris-Cl, pH 8.5) and frozen at -80°C. The purified dsDNA (40 μL) underwent end repair by blunting, A-tailing and adapter ligation as previously described (16) using barcoded adapters (NextFlex, Bioo Scientific). Libraries were PCR-amplified for 16 cycles, size selected by gel extraction, quantified using a Qubit dsDNA HS Assay Kit (Thermo Fisher Scientific) and sequenced on a HiSeq 4000 or a NextSeq 500 (Illumina) for 51 cycles according to the manufacturer's instructions.

Crosslinking *in vitro* culture cells for ChIP-seq

For H3K27ac ChIP-seq, culture media was removed and plates were washed once with PBS and then fixed with 1% formaldehyde (Thermo Fisher Scientific) in PBS for 10 minutes at room temperature. The reaction was quenched by adding glycine (Thermo Fisher Scientific) to 0.125M. For LXR, SMAD4, and RBPJ ChIP-seq, cells were crosslinked with 3mM DSG (ProteoChem) in PBS for 30 minutes at room temperature, and then fixed with 1% formaldehyde (Thermo Fisher Scientific) in PBS for 10 minutes at room temperature. The reaction was quenched by adding glycine (Thermo Fisher Scientific) to 0.125M. After fixation, cells were washed once with cold PBS and then

pelleted at 700 X G for 5 minutes at 4°C. Crosslinked cells were stored at –80°C until ready for ChIP-seq library preparation.

ChIP-seq library preparation

Chromatin immunoprecipitation (ChIP) was performed in biological replicates as previously described (129). Fixed cells were thawed on ice, resuspended in either ice-cold LB3 (10 mM Tris/HCl pH 7.5, 100 mM NaCl, 1mM EDTA, 0.5mM EGTA, 0.1% Na-deoxycholate, 0.5% N-lauroylsarcosine, 1 X protease inhibitor cocktail, 1mM Na-Butyrate, for H3K27ac ChIP) or ice-cold RIPA-NR lysis buffer (20 mM Tris-HCl, pH 7.5, 150 mM NaCl, 1 mM EDTA, 0.5 mM EGTA, 0.4% Na-Deoxycholate, 0.1% SDS, 1% NP-40, 1x protease inhibitors, for LXR, SMAD4, and RBPJ ChIP). Frozen crosslinked nuclei were resuspended in wash buffer (10mM HEPES/KOH pH7.9, 85mM KCl, 1mM EDTA, 0.2% IGEPAL CA-630, 1x protease inhibitor cocktail (Sigma), 1 mM PMSF) for 5minutes on ice. Nuclei were spun down and then resuspended in RIPA-NR lysis buffer. Chromatin was sheared by sonication. Samples were sonicated in a 96 Place microTUBE Rack (Covaris cat#500282) using a Covaris E220 for 12 cycles (samples in LB3) or 18 cycles (samples in RIPA-NR buffer) with the following setting: time, 60 seconds; duty, 5.0; PIP, 140; cycles, 200; amplitude, 0.0; velocity, 0.0; dwell, 0.0. Samples were recovered and spun down at max speed, 4°C for 10 minutes. The LB3 lysate was diluted 1.1-fold with ice-cold 10% Triton X-100 after sonication. One percent of the lysate was kept as ChIP input. For each immunoprecipitation, aliquots of diluted lysate equivalent to 500,000 cells (for H3K27ac ChIP) or 2-3 million cells or

nuclei (for LXR, SMAD4, or RBPJ ChIP), 30 μl of Dynabeads Protein A (for rabbit polyclonal antibodies) or Dynabeads protein A/G (for LXR ChIP) bound to specific antibodies for H3K27ac (2 μg, Active Motif, 39133), LXR (2 μg each of the indicated LXR specific antibodies, Santa Cruz Biotechnology: sc-1000X, sc-133221X, sc-271064X)), SMAD4 (1 μg each of Cell Signaling technology 46535 and 38454) or RBPJ (2 μg, Abcam, ab25949) were combined and rotated overnight at 4°C. For H3K27ac ChIP, beads were collected on a magnet and washed three times each with wash buffer I (20 mM Tris/HCl pH 7.5, 150 mM NaCl, 1% Triton X-100, 0.1% SDS, 2 mM EDTA), wash buffer III (10 mM Tris/HCl pH 7.4, 250 mM LiCl, 1% Triton X-100, 0.7% Na-Deoxycholate, 1 mM EDTA) and twice with ice-cold TET (10 mM Tris/HCl pH7.5, 1 mM EDTA, 0.2% Tween-20). For LXR, SMAD4, or RBPJ ChIP, beads were washed three times with RIPA-NR buffer (20 mM Tris-HCl/pH7.5, 150 mM NaCl, 0.1% SDS, 1% NP-40, 0.4 % Na-Deoxycholate, 1 mM EDTA, 0.5mM EGTA, 0.5mM DTT), six times with RIPA-LiCl buffer (10 mM Tris-HCl/pH 7.5, 250 mM LiCl, 1% NP-40, 0.7% Na-Deoxycholate, 1 mM EDTA), three times with ice-cold TET (10 mM Tris/HCl pH7.5, 1 mM EDTA, 0.2% Tween-20), and one time with IDTE (10mM Tris-HCl pH 8.0, 0.1mM EDTA). Libraries were prepared with NEBNext Ultra II DNA library prep kit (NEB) reagents according to the manufacturer's protocol on the beads suspended in 25 μL TT (10mM Tris/HCl pH7.5, 0.05% Tween-20), with reagent volumes reduced by half. DNA was eluted and crosslinks reversed by adding 4 μl 10% SDS, 4.5 μl 5 M NaCl, 3 μl EDTA, 1 μl proteinase K (20 mg/ml), 20 μl water, incubating for 1 h at 55°C , then 30 minutes to overnight at 65°C . DNA was purified using 2 μL of SpeedBeads (GE

Healthcare), diluted with 20% PEG8000, 1.5M NaCl to final of 12% PEG, eluted with 25 μl TT. DNA contained in the eluate was then amplified for 12 cycles in 50 μl PCR reactions using NEBNext High-Fidelity 2X PCR Master Mix (NEB) and 0.5 mM each of primers Solexa 1GA and Solexa 1GB. ChIP input material (1 percent of sheared DNA) was treated with RNase for 15 minutes at 37°C in EB buffer (10 mM Tris pH 8, 0.5% SDS, 5 mM EDTA, 280 mM NaCl), then digested with Proteinase K for 1 h at 55°C and crosslinks reversed at 65°C for 30 minutes to overnight. DNA was purified using 2 μL of SpeedBeads (GE Healthcare), diluted with 20% PEG8000, 1.5M NaCl to final of 12% PEG, eluted with 25 μl TT and library prep and amplification were performed as described for ChIP samples. Resulting libraries were size selected by gel excision to 225-325 bp, purified, and single-end sequenced using a HiSeq 4000 or a NextSeq 500 (Illumina).

Data mapping

Libraries were sequenced either on a HiSeq 4000 (Illumina) or a NextSeq 500 (Illumina). Raw sequences/fastqs were obtained from Illumina Studio pipeline, and then some of them were trimmed according to their qualities. RNA-seq data was mapped to mm10 genome using STAR (130) with default parameters. ChIP-seq and ATAC-seq data were mapped to custom genomes using bowtie2 (Langmead and Salzberg, 2012) with default parameters. Finally, HOMER (Heinz et al., 2010) tag directories were created for mapped samples.

RNA-seq analysis

The gene expression raw counts were quantified by HOMER's analyzeRepeats with the option "-condenseGenes -count exons -noadj". All genes shorted than 250bp were removed, and the TPM (transcript per kilobase million) were quantified for all genes matching accession number to the raw counts. Differentially expressed genes were assessed with DESeq2 (Love et al., 2014) at FDR < 0.05 (False Discovery Rate) and FC > 2 (Fold Change).

IDR analysis

ChIP-seq experiments were performed in two replicates with corresponding input experiments. Peaks were called with HOMER for each tag directory with relaxed peak finding parameters "-L 0 -C 0 -fdr 0.9") against the corresponding input directory. For ATAC-seq, no inputs were used, but the size was set to 200bp "-L 0 -C 0 -fdr 0.9 -minDist 200 -size 200". IDR (Li et al., 2011) was used to test for reproducibility between replicates, and only peaks with IDR < 0.05 were used for downstream analysis. The pooled tag directory from two replicates was used for track visualization.

ATAC-seq and ChIP-seq analysis

To quantify the TF binding and chromatin accessibility, the raw tag counts at merged IDR peaks of different conditions by HOMER's mergePeaks, were extracted by HOMER's annotatePeaks with "-noadj", "-size 200" for ATAC-Seq and TF ChIP-Seq, but "-size 2000" for H3K27ac ChIP on ATAC-associated peaks. Subsequently, DESeq2

(Love et al., 2014) was used to identify the differentially bound TF binding distal sites (3000bp away from known TSS/transcription starting sites) or the differential distal chromatin accessibilities with FDR < 0.05 and FC > 2.

Motif analysis

To identify motifs enriched in peak regions over the background, HOMER's motif analysis (findMotifsGenome.pl) including known default motifs and de novo motifs was used (16). The background peaks used either from random genome sequences or from peaks in comparing condition were indicated throughout the main text and in the figure legends.

Data visualization

Heatmap of RNA expression or tags of ATAC-Seq peaks were generated by pheatmap, an R package. Significance indicated by "*" in bar-plot represents the FDR (after multiple-testing correction). MA-plot was used to demonstrate the differentially expressed genes for RNA-Seq data with log2fold change against expression value TPM, additionally with the sizes of dots representing the significant p-values. Scatter plots were used for direct comparison of two conditions, either the gene TPM or normalized tag counts were used for RNA-Seq, ChIP-/ATAC-Seq respectively. Browser tracks for ATAC-Seq and ChIP-Seq were generated by open source pygbrowse (https://github.com/phageghost/python-genome-browser).

F. Acknowledgements

Chapter 2, in full, is adapted from a manuscript currently in review at *Immunity*. The dissertation author was the co-primary author of this paper along with Ty D. Troutman and Mashito Sakai. Other authors include Zhengyu Ouyang, Nathanael J. Spann, Yohei Abe, Kaori M. Ego, Cassi M. Bruni, Johannes C. M Schlachetzki, Alexi, Nott, Hunter Bennett, Jonathan Chang, BaoChau T. Vu, Martina P. Pasillas, Verena M. Link, Bonne M. Thompson, Jeffrey G. McDonald, and Christopher K. Glass.

These studies were supported by NIH grants DK091183, HL088083 and GM085764. MS was supported by the Manpei Suzuki Diabetes Foundation of Tokyo, Japan, and the Osamu Hayaishi Memorial Scholarship for Study Abroad, Japan. TDT was supported by P30 DK063491, T32DK007044, and NRSA T32CA009523. JSS was supported by American Heart Association Fellowship 16PRE30980030 and NIH Predoctoral Training Grant 5T32DK007541. YA was supported by Japan Society for the Promotion of Science Overseas Research Fellowship.

Chapter 3. Niche-Specific Re-Programming of Epigenetic Landscapes Drives Myeloid Cell Diversity in NASH

A. Abstract

Tissue resident macrophages and recruited monocyte-derived macrophages contribute to host defense but also play pathological roles in a diverse range of human diseases. Multiple macrophage phenotypes are often represented in a diseased tissue, but we lack a deep understanding of the mechanisms that control diversification. Here we use a combination of genetic, genomic, and imaging approaches to investigate the origins and epigenetic trajectories of hepatic myeloid cells during a diet-induced model of non-alcoholic steatohepatitis (NASH). We provide evidence that distinct micro-environments within the NASH liver induce strikingly divergent transcriptomes of resident and infiltrating cells. Myeloid cell diversification results from both remodeling open chromatin landscapes of recruited monocytes and altering activities of pre-existing enhancers of resident Kupffer cells. These findings provide evidence that niche-specific combinations of disease-associated environmental signals instruct resident and recruited macrophages to acquire distinct programs of gene expression and corresponding phenotypes.

B. Introduction

Tissue resident macrophages function as essential components of the innate immune system by serving as sensors and responders to infection and injury (45, 79). Functional and transcriptomic studies further indicate that macrophages residing within different tissues are phenotypically distinct and exhibit correspondingly different programs of gene expression that enable tissue-specific functions (37, 38, 40, 83), with notable examples provided by bone resorption by osteoclasts and neuronal synaptic remodeling by microglia (131, 132). Most tissues acquire resident macrophage populations early in development from yolk sac or fetal liver erythromyeloid progenitor (EMP) cells (32-35). In some cases, such as brain microglia and liver Kupffer cells, the initial EMP-derived macrophages continue as exclusive, self-renewing populations. In other tissues, such as the gut, EMP-derived macrophages are partially or completely replaced over time by hematopoietic stem cell (HSC) derived cells (43, 133-135).

The ultimate gene expression profile obtained by a particular adult resident macrophage is determined to a variable extent by the combination of origin (EMP or HSC) and tissue environment. HSC-derived cells that engraft the brains of microglia-depleted mice acquire many features of embryonically-derived microglia, but also exhibit substantial differences even after residing within the CNS for months (86, 87, 136). In contrast, following depletion of resident Kupffer cells, HSC-derived cells that repopulate the empty niche acquire transcriptomes that are very similar to EMP-derived Kupffer cells (42). Studies of microglia and resident macrophages in the peritoneal cavity and lung indicate that tissue environmental signals exert effects on transcription

factor expression and function that drive alterations in transcriptional regulatory elements underlying specialized programs of gene expression (38, 40, 89).

In addition to their immune and homeostatic functions, resident macrophages and infiltrating monocyte-derived cells contribute to a diverse array of metabolic and degenerative human diseases (137-139). The relative contributions of tissue resident macrophages and monocyte-derived cells appear to differ in a disease specific manner. Dichotomous examples are provided by atherosclerosis (140, 141), in which the majority of pathogenic myeloid lineage cells that contribute to lesion formation are derived from circulating monocytes, and by Alzheimer's disease, in which microglia promote disease in the absence of infiltrating monocytes (139).

In contrast to signals associated with infection and acute injury, in which responses are ultimately self-limited, signals associated with chronic diseases do not resolve and thus have a sustained impact on both resident and recruited cells (142). Inducers of pathological macrophage phenotypes include damage-associated molecular patterns, lipotoxic molecules, cytokines and microbial products (45, 143-146). Responses to disease-associated signals typically include production of cytokines, chemokines, and reactive oxygen species that contribute to a feed-forward loop that sustains and often accelerates inflammation and tissue damage. However, different combinations of pathogenic molecules are associated with different diseases and result in varying effects on resident and recruited macrophage phenotypes.

In most cases, diseased tissues exhibit multiple macrophage phenotypes, as particularly exemplified by non-alcoholic steatohepatitis (NASH) (147). Nonalcoholic

fatty liver disease (NAFLD) is a spectrum of liver conditions strongly coupled with obesity, insulin resistance, cardiovascular disease, and type-2 diabetes mellitus (148-153). NASH develops through combinatorial actions of steatosis resulting from fatty liver disease, and growing inflammation in response to cellular stresses of the perturbed environment existing within the fatty liver. During development of NASH, or following acute liver injury, new macrophages are derived from circulating monocytes (47, 154-157). These recruited monocyte-derived cells can have both detrimental and supportive roles, contributing to increases in pathology during fibrosis onset, but hastening recovery when the damage-evoking agent is removed (147, 154-158).

These observations raise questions as to the mechanisms underlying the phenotypic diversity of disease-associated macrophages. Multiple macrophage phenotypes could result from differences in macrophage origin (i.e., EMP versus HSC), from local environmental factors, or a combination of both factors. Ontological differences might determine cell responses to pathological signaling molecules while microanatomical differences in the combinations/concentrations of such molecules and/or from differences in the time of exposure of newly recruited cells to these environmental factors could induce other changes in cell state. Mouse models of diet-induced NASH provide powerful experimental systems to address these general questions because of the relatively large numbers of myeloid cells that can be obtained from healthy and diseased liver and the availability of genetic tools for tracing and genetically targeting these cells.

Here, we use a combination of single cell RNA-sequencing, lineage tracing and multiplex quantitative immunofluorescence imaging (histo-cytometry) to first define the developmental origins and micro-anatomic locations of the major myeloid populations of the healthy liver and following the response to a NASH-inducing diet. We then go on to sort each of these cell populations and perform deep transcriptomic and genomic analysis. By integrating these data, we provide evidence for combinatorial effects of diet, developmental origin, and anatomic location on regulatory pathways and transcription factors that explain the emergence of distinct disease-associated macrophage phenotypes during NASH.

C. Results

Single-cell RNA-seq defines myeloid diversity during dietary NASH

To investigate immune cell heterogeneity during NASH, we performed single-cell RNA sequencing (scRNA-seq) on liver non-parenchymal cells from healthy mice fed a control diet or a model NASH diet. As noted in previous studies (159, 160), C57BL/6J mice exhibited rapid weight gain when fed the NASH diet (**Figure 3.S1A**) and developed hepatic steatosis, inflammation, and a modest degree of fibrosis **(Figure 3.S1B).** Non-parenchymal cells from duplicate healthy control mice and mice fed the NASH diet for 30 weeks were purified using fluorescence activated cell sorting (FACS) and minimally defined as $CD45^{Pos}CD146^{Neg}$LiveSinglets (**Figure 3.S1C)**. Importantly, livers were thoroughly cleared of blood by perfusion prior to tissue digestion, therefore all cells collected are presumed to be resident in the liver and not blood-derived. In

addition, an RNA polymerase II inhibitor was included in all buffers to minimize the impact of tissue digestion on gene expression. Using the 10X Genomics platform, over 6,000 scRNA-seq libraries that passed quality thresholds were created from these isolated cells.

The NASH diet induced qualitative differences in cell clustering, with the major population of immune cells in control livers having virtually no representation in the NASH liver, and the major populations of immune cells in the NASH liver having virtually no representation in the control liver (**Figure 3.1A left**, **Figure 3.1B**, and **Table 3.1**). At a finer grained level, 3 of 17 clusters identified were primarily derived from cells from control diet mice, 8 clusters were primarily derived from NASH diet mice, and 6 had substantial contribution (at least 1/3 from each group) from both control and NASH diet mice (**Figure 3.1A**, **Figure 3.S1D** and **Table 3.1**). Interrogation of the most abundant and most differentially expressed transcripts in each cluster allowed a cell type identity to readily be assigned to most clusters (**Table 3.1**). We focused on cell clusters with greater than one percent representation in the overall data set (clusters 0 to 12), selected “myeloid” cell clusters, including likely recruited macrophage (RM) clusters, based on expression of *Spi1*, *Csf1r*, and *Cd68*, and excluded clusters with indication of significant cell cycle activity, leaving 5 main myeloid clusters (clusters 0, 1, 2, 4, and 9) (**Table 3.1** and **Figure 3.S1E**).

The three most abundant clusters (0, 1 and 2, hereafter referred to as KC1, KC2 and KN-RM, named for being a recruited macrophage occupying the Kupffer cell niche, as described later) expressed high levels of *Adgre1*, encoding the tissue macrophage

marker F4/80 (also known as Emr1), and high levels of putative Kupffer cell lineage-determining factors *Mafb* and *Maf* (see **Chapter 2**), as well as low levels of *Itgam*, encoding CD11b (**Figure 3.1C** and **Figure 3.S1E)**. These clusters also displayed high expression of Kupffer cell-specific genes including *C1qa*, *Id3*, *Ptgs1*, *Scl40a1*, *Il18bp*, and *Cd5l* (**Figure 3.S1E**) (38). KC1 consisted almost entirely of cells from controls while KC2 and KN-RM consisted of cells from the NASH diet animals (**Figure 3.1A**, **Figure 3.1B**, and **Table 3.1**). The remaining two myeloid cell clusters (clusters 4 and 9) were predominantly found in NASH livers and had characteristic gene expression of previously described monocyte-derived liver macrophages, such as *Itgam*, *Ly6c2*, *Ccr2*, and *S100a4* (**Figure 3.1C** and **Figure 3.S1E**) (161). Cluster 4 (hereafter referred to as Ly6C^{Hi}-RM) expressed higher levels of transcripts typical of Ly6C^{Hi} monocytes such as *Ly6c2*, *Chil3*, *F13a1*, and *Fn1*, while cluster 9 (hereafter referred to as Ly6C^{Lo}-RM) expressed higher levels of *Cd209a*, *Cd7*, and *Itgax* (**Figure 3.S1E**).

Interestingly, while healthy animals had only one major population of Kupffer cells (KC1), animals on the NASH model diet almost completely lacked this population and instead formed two Kupffer cell-like clusters present in similar proportions (KC2 and KN-RM) (**Figure 3.1A** and **Figure 3.1B**). Directly comparing KC2 to KN-RM, we found that KN-RM had significantly lower expression of various typical Kupffer cell genes, including *Timd4*, *Vsig4*, *C6* and *Clec4f* compared to the KC2 cluster (**Figure 3.1C**, **Figure 3.S1E** and **Figure 3.S1F**). *Ccr2* and *Cx3cr1*, which are characteristic of monocytes, were amongst the genes with significantly higher expression in KN-RM compared to KC2 (**Figure 3.1C** and **Figure 3.S1F**). However, cluster KN-RM was

transcriptionally distinct from clusters corresponding to Ly6C^{Hi}-RM and Ly6C^{Lo}-RM (**Figure 3.1A**, **Figure 3.1F**, and **Figure 3.S1E**). KN-RM also expressed significantly higher levels of genes involved in MHC class II presentation such as *H2-Aa* and *Cd74* compared to KC2 (**Figure 3.S1F**). These data suggested that KC2 cells were in some ways more similar to steady-state KC1 than were the KN-RM, which had similarities to monocytes in their transcriptional state.

Using flow cytometry, we observed both Tim4^{Pos} and Tim4^{Neg} cells in the CD11b^{Lo}F4/80^{Hi} Kupffer cell gate during NASH in similar proportions to KC2 and KN-RM and collected them for bulk RNA-seq and epigenomic profiling (**Figure 3.1D**). These data are in agreement with a recently published study using a methionine and choline deficient diet NASH model (75). We also collected CD11b^{Hi}F4/80^{Lo}-Ly6C^{Hi}-RM and Ly6C^{Lo}-RM in sufficient quantities for RNA-seq and assay for transposase-accessible chromatin (ATAC-seq) (128) (**Figure 3.1E**). RNA-seq analysis of these sorted populations resulted in highly similar patterns of expression of the genes determining myeloid clusters of interest defined by scRNA-seq, indicating that we had appropriately isolated the corresponding major myeloid populations present in the livers of healthy and NASH mice defined by scRNA-seq analysis (**Figure 3.1F**).

Ontogeny and Environment of Myeloid Cells in NASH

Our analysis indicated that four major populations of myeloid cells exist in livers of mice during NASH: CD11b^{Lo}F4/80^{Hi}Tim4^{Pos} and Tim4^{Neg} Kupffer cell-like macrophages (KC2 and KN-RM, respectively) and CD11b^{Hi}F4/80^{Hi}Ly6C^{Hi} and Ly6C^{Lo}

recruited macrophages (Ly6C^{Hi}-RM and Ly6C^{Lo}-RM, respectively). We also detected neutrophils (PMN) in our single cell analysis and verified their presence by flow cytometry, but they comprised less than 1% of the cells (**Figure 3.1E**, **Figure 3.S1D** and **Table 3.1**). We hypothesized that similar to experimental Kupffer cell ablation (42) and damaged erythrocyte stress conditions (76), Tim4^{Neg} Kupffer cell-like macrophages that arise during NASH (KN-RM) may be ontogenically distinct from the Tim4^{Pos} Kupffer cells (KC2), which are described as repopulating largely independently from the peripheral mononuclear phagocyte system (36). To address this hypothesis, we performed formal lineage tracing experiments using Cx3cr1^{CreERT2};Rosa26$^{tdTomato/+}$ mice (**Figure 3.2A**) (76, 133). Tissue resident macrophage precursors are known to express *Cx3cr1* at sufficient levels to drive recombination if tamoxifen is administered during the perinatal period, while only certain macrophages such as microglia, but not Kupffer cells, express sufficient *Cx3cr1* to drive recombination during adulthood (76, 133, 162). In contrast, administering tamoxifen during adulthood labels monocytes and thus monocyte-derived macrophages.

Tamoxifen administration on day 1 and day 2 post-parturition resulted in approximately 50% labeling of embryonically-derived Kupffer cells (**Figure 3.2A**, top), consistent with previous studies in which tamoxifen was administered at e13.5 and e15.5 (76), or at E18.5 (162). After 20 weeks on the NASH diet, nearly all tdTomato^{Pos} cells were Tim4^{Pos} Kupffer cells (KC2) (**Figure 3.2A**, top), indicating that Tim4^{Neg} Kupffer cell-like macrophages (KN-RM) are not long-lived daughters of embryonically-derived Kupffer cells. Conversely, when adult mice fed the NASH diet for 20 weeks

were administered tamoxifen 1 week prior to sacrifice, ~90% of circulating monocytes were TdTomato^{Pos} 2 days after the final tamoxifen injection **(data not shown)** and ~70% of CD11b^{Lo}F4/80^{Hi}Tim4^{Neg} Kupffer cell-like macrophages (KN-RM) were labeled 5 days after the final injection (**Figure 3.2A**, bottom). We also observed a small degree of labeling of Tim4^{Pos} Kupffer cells (**Figure 3.2A**, bottom), which could be due to low levels of expression of *Cx3cr1* in Tim4^{Pos} KC2 cells, or alternatively due to the gradual upregulation of Tim4 by recruited cells (42). Overall, these results indicate that embryonically-derived Kupffer cells remain in the liver during development of NASH and are Tim4^{Pos}, while most recruited CD11b^{Lo}F4/80^{Hi} macrophages are Tim4^{Neg}.

To determine the localization of myeloid cells in the liver during NASH, immunofluorescence microscopy was performed on livers from Cx3cr1^{CreERT2};Rosa26$^{tdTomato/+}$ mice pulsed with tamoxifen 7 and 5 days prior to tissue collection (**Figure 3.2B** and **Figure 3.2C**). As expected, tdTomato^{Pos} cells, indicative of cells derived from recruited monocytes, were abundant in NASH liver samples but nearly absent in control diet livers. Using multi-parameter imaging and histo-cytometry (163), we distinguished three subsets of myeloid cells (KC1/KC2, KN-RM and Ly6C$^{Hi/Lo}$-RM) in the control and NASH livers based on Tim4, F4/80 and tdTomato expression corresponding to what was previously observed using flow-cytometry and scRNA-seq (**Figure 3.2C-D** and **Figure 3.S2A**). Following *in situ* confirmation of these myeloid cell subsets, we assessed their spatial distribution using the positional data preserved in histo-cytometry (**Figure 3.2D**, right). The two subsets (KN-RM and Ly6C$^{Hi/Lo}$-RM) that are increased during NASH displayed significant differences in their spatial distributions.

By comparing nearest-neighbor distances from KC2, KN-RM cells were found to be distributed significantly closer to KC2 cells than Ly6C$^{Hi/Lo}$-RM cells (**Figure 3.2E**). In addition, the small number of F4/80^{Hi}Tim4^{Neg}tdTomato^{Pos} KN-RM cells observed in healthy control livers were also in close proximity to KC1 cells (**Figure 3.S2B**).

While Kupffer cells are known to reside within the hepatic sinusoids, the sub-anatomical organization of other liver macrophage subsets during NASH is less certain (147). High magnification imaging using Collagen IV to visualize the endothelial basement membrane demonstrated that KC2 and KN-RM cells reside within hepatic sinusoids in this model (**Figure 3.2F**). In contrast, Ly6C$^{Hi/Lo}$-RM cells were not found within the liver sinusoids, but were enriched around both portal and central vein vasculature identifiable by the large vessel diameter (15 μm or larger) (**Figure 3.2G** and **Figure 3.S2C**). These findings further supported Ly6C$^{Hi/Lo}$-RM cells as being positionally separated from KC2 and KN-RM cells based on measurements that were independent of anatomical landmarks. These results provide evidence that KC2 and KN-RM cells reside in a similar niche within the liver sinusoids, which is environmentally distinct from the anatomic positions occupied by Ly6C^{Hi}-RM and Ly6C^{Lo}-RM cells.

Effect of NASH-inducing Diet on Resident and Recruited Myeloid Cell Transcriptomes

The ability to sort distinct populations of hepatic myeloid cells defined by scRNA-seq analysis enabled deep transcriptomic profiling of each population. Unsupervised hierarchical clustering of 2,210 genes differentially expressed among KC1, KC2, KN-

RM, Ly6C^{Hi}-RM, and Ly6C^{Lo}-RM tightly grouped KC2 and KN-RM and distinguished KC1, KC2 and KN-RM cells from Ly6C^{Hi}-RM and Ly6C^{Lo}-RM cells (**Figure 3.3A**). With inclusion of genes differentially expressed in blood monocytes, principal component analysis also indicated that KC2 and KN-RM cells from NASH mice grouped most closely with KC1 cells from healthy mice (**Figure 3.3B**). After experimental induced Kupffer cell ablation, blood Ly6C^{Hi} monocytes are recruited to the liver and rapidly differentiate into Kupffer cell-like liver macrophages (42) (see **Chapter 2**). At 14 days after experimental Kupffer cell ablation, these repopulating liver macrophages (RLMs) also grouped closely with KC1, KC2 and KN-RM (**Figure 3.3B**). Approximately 65% of the variation existed along PC1, which primarily separated cells residing in the liver from those in the blood. PC2 explained approximately 18% of the total variation and primarily explained the variation between KC1, KC2, KN-RM and day 14 RLMs in healthy and NASH conditions and Ly6C$^{Hi/Lo}$-RM populations during NASH. Interestingly, PC2 also accounted for variation between control KC1 and NASH KC2 cells, with KC1 and KC2/KN-RM cells progressively closer to the Ly6C$^{Hi/Lo}$-RM.

Pairwise comparisons of KC1 and KC2 cells indicated that the NASH diet had a significant impact on resident Kupffer cell gene expression, consistent with scRNA-seq data. More than 800 genes exhibited differential expression (fold change > 2, p.adj < 0.05, log2(TPM+1) > 2) (**Figure 3.3C**). Notably, only 93 genes were identified as significantly altered when comparing KC2 and KN-RM Kupffer cells from mice with NASH (**Figure 3.3D**), despite their distinct origins (EMP versus HSC). In contrast, during NASH KN-RM cells exhibited more than 2,200 differentially expressed genes in

comparison to Ly6C^{Hi}-RM, despite both cells originating from an HSC precursor (**Figure 3.3E**). The divergent differentiation programs of KN-RM and Ly6C^{Hi}-RM are further reinforced by pairwise comparisons with gene expression in Ly6C^{Hi} circulating monocytes, indicating more than 2,000 differentially expressed genes in each case (**Figure 3.3F** and **Figure 3.S3A**). Although KN-RM and Ly6C^{Hi}-RM cells have a shared HSC origin, KN-RM are phenotypically more similar to KC2 (of EMP origin) than to Ly6C^{Hi}-RM cells. These findings provide evidence that distinct liver microenvironments may exert highly divergent effects on the differentiation programs and ultimate molecular phenotypes of recruited KN-RM and Ly6C$^{Hi/Lo}$-RM cells.

Prior studies defined a set of Kupffer cell identity genes that distinguish them from other tissue resident macrophages (38). Twenty-eight of the genes downregulated during the transition of KC1 cells to KC2 cells in the NASH model are among this set, exemplified by *Cd163* and *C6* (**Figure 3.3G** and **Figure 3.S3C**). However, many Kupffer cell-specific genes maintained similar levels of expression in cells from mice on the NASH model diet, including *C1qa*, *Cd5l*, *Id3*, and *Il18bp*, indicating that only a subset of the Kupffer cell-specific gene expression program is altered during NASH**.** Furthermore, classic Kupffer cell genes such as *Clec4f*, *Vsig4*, and *Cdh5* were expressed at high levels in KN-RM but neither Ly6C$^{Hi/Lo}$-RM population, suggesting that the Kupffer cell niche is necessary to promote induction of these genes (**Figure 3.S3C**). We observed significant overlap in the genes distinguishing KC2 from KN-RM cells during NASH and healthy Kupffer cells compared to day 14 RLMs (see **Chapter 2**) (**Figure 3.S3D**). Consistent with previous studies comparing embryonically derived Kupffer cells with

monocyte derived RLMs, we found that KC1 and KC2 expressed higher levels of *Sdc2*, *Snrpn*, *Bmpr1a*, *C2*, *Colec12*, *Xlr*, *Timd4*, and *Cd163* (42).

Gene ontology analyses of genes that distinguish KC1, KC2 and KN-RM cells from Ly6C^{Hi}-RM and Ly6C^{Lo}-RM, (Clusters 1 and 2, **Figure 3.3A**) are consistent with a stronger pro-inflammatory and wound repair phenotype of the Ly6C$^{Hi/Lo}$ recruited macrophage populations (**Figure 3.S3E**), in agreement with prior studies (164). Examples of differentially expressed genes associated with the functional categories of "ROS metabolism", "regulation of cell adhesion", "inflammatory response", "response to wounding", and "extracellular matrix organization" are illustrated in **Figure 3.3G**. Of interest, Ly6C^{Lo}-RM primarily express *Mgl2* (CD301b), a gene recently reported to be expressed in skin macrophages that activates a specific myofibroblast population implicated in tissue repair and aging (165). Collectively, these results indicate that the NASH inducing diet acts to reprogram the endogenous Kupffer cell population and induce micro-environment associated dichotomous programs of differentiation of KN-RM cells and Ly6C$^{Hi/Lo}$ recruited liver macrophages.

Niche-Specific Reprogramming of Epigenetic Landscapes

To investigate mechanisms responsible for environment-specific programs of gene expression, we identified accessible chromatin defined by ATAC-seq in five populations of cells from mice with NASH: KC2 and KN-RM cells, Ly6C^{Hi}-RM, Ly6C^{Lo}-RM, and Ly6C^{Hi} peripheral blood monocytes. Examples of ATAC-seq peaks in these five populations of cells from mice fed the NASH-inducing diet in the vicinity of the

Clec4f and *Itgam* genes, which are highly differentially expressed in Kupffer cells compared to Ly6C^{Hi}-RM and Ly6C^{Lo}-RM, are illustrated in **Figure 3.4A**. Genome wide comparisons of ATAC-seq peak tag counts for Ly6C^{Lo}-RM versus Ly6C^{Hi} blood monocytes are illustrated in **Figure 3.4B** and the same comparison for KN-RM and Ly6C^{Hi} blood monocytes is shown in **Figure 3.4C**. Statistically significant different regions (> 2-fold, p-adj < 0.05) of distal open chromatin (> 3 kb from the TSS) between cell types were identified through comparisons of replicate experiments using DESeq2 (differential genes color coded red and blue in each scatter plot). Differential regions from the five myeloid populations in NASH mice, as well as healthy KC1 cells and 24- and 48-hour RLMs after experimental Kupffer cell ablation (see **Chapter 2**) were used for principal component analysis illustrated in **Figure 3.4D**. PC1, accounting for ~65% of variance, primarily distinguished KC1, KC2 and KN-RM populations from Ly6C^{Hi} blood monocytes and Ly6C^{Hi}-RM and Ly6C^{Lo}-RM. RLMs 24 and 48 hours after experimental ablation became incrementally closer to Kupffer cells along PC1, reflecting chromatin remodeling after arriving at the Kupffer cell niche. PC2, accounting for ~13% of variance, primarily separated Ly6C^{Hi} blood monocytes from Ly6C^{Hi}-RM and Ly6C^{Lo}-RM. The intermediate position of liver Ly6C^{Hi}-RM between blood Ly6C^{Hi} monocytes and liver Ly6C^{Lo}-RM is consistent with the possibility that they represent a transition state between Ly6C^{Hi} blood monocytes and the Ly6C^{Lo}-RM cells(154, 166) (**Figure 3.4D**).

Hierarchical clustering of ATAC-seq data further support the relationships suggested by principal component analysis, with KC2 and KN-RM cells exhibiting highly similar patterns of open chromatin that are distinct from the transitional patterns

observed in Ly6C^{Hi}-RM and Ly6C^{Lo}-RM (**Figure 3.S4A**). Based on these findings and the results of lineage tracing experiments, we considered the open chromatin regions of KC2/KN-RM and Ly6C^{Lo}-RM populations as divergent endpoints of chromatin remodeling events following entry of Ly6C^{Hi} blood monocytes into the NASH liver. ATAC-seq peaks specific for KN-RM or Ly6C^{Lo}-RM in comparison to circulating Ly6C^{Hi} monocytes (red data points in **Figures 3.4B** and **3.4C**, respectively) indicated that approximately 75% of these peaks were specific to KN-RM or Ly6C^{Lo}-RM cells (**Figure 3.4E**). Peaks specific for KN-RM cells were highly enriched for motifs recognized by LXR and members of the MAF and TFE families of transcription factors (**Figure 3.4E**). In contrast, ATAC-seq peaks specific for Ly6C^{Lo}-RM cells were highly enriched for NF-κB motifs and motifs recognized by RUNX, ZEB and KLF transcription factors. Open chromatin regions lost from blood monocytes during acquisition of either the Kupffer cell or Ly6C$^{Hi/Lo}$-RM niche signatures (**Figures 3.4B** and **3.4C**, blue points) were enriched for KLF and CEBP motifs (**Figure 3.S4B** and **Figure 3.S4C**). The open chromatin regions lost during acquisition of the KC niche additionally included motifs for RUNX and CTCF (**Figure 3.S4B**).

The pattern of motif enrichment in KC2 and KN-RM cells implies that liver niche signals increase the expression and/or activities of transcription factors that bind to LXR, MAF and TFE motifs. Consistent with this possibility, *Nr1h3* (encoding LXRα), *Mafb*, and *Tfec* are among a set of Kupffer cell lineage-determining factors observed to be significantly more highly expressed in KC2 and KN-RM cells than in Ly6C$^{Hi/Lo}$-RM cells (**Figure 3.4F**). Importantly, studies of repopulating liver macrophages following

acute elimination of resident Kupffer cells indicate that these transcription factors are highly induced within 12 hours of entry into the open Kupffer cell niche of the liver (see **Chapter 2**) Additional Kupffer cell lineage-determining factors exhibiting this pattern include *Spic* (recognizing a motif similar to PU.1 and not distinguishable by motif analysis) and *Id3* (lacking a DNA binding domain and functioning as a dominant inhibitor of bHLH transcription factors) (37, 38) (**Figure 3.4F**). The rapid induction of these factors in repopulating liver macrophages following Kupffer cell depletion is linked to combinatorial effects of DLL4 and TGF-β/BMP provided by sinusoidal endothelial cells (see **Chapter 2**). These findings suggest that KN-RM cells largely follow the developmental program taken by repopulating liver macrophages following Kupffer cell depletion upon adherence to sinusoidal endothelial cells. In contrast, the lack of induction of KC lineage-determining factors in Ly6C^{Hi}-RM and Ly6C^{Lo}-RM cells is consistent with their location outside of the sinusoidal space. NF-κB motifs are enriched in Kupffer cell enhancers in comparison to other tissue resident macrophages (see **Chapter 2**), but the particularly strong enrichment for this motif in Ly6C^{Lo}-RM cells implies that the niche occupied by these cells provides additional signals that activate NF-κB. In addition, while RUNX factors are lower in KC2 and KN-RM cells in comparison to blood Ly6C^{Hi} monocytes, their expression is maintained or increased in Ly6C^{Hi}-RM and Ly6C^{Lo}-RM cells (**Figure 3.S4D**). In concert, analysis of open chromatin provides evidence that the divergent patterns of gene expression observed in HSC-derived KN-RM and Ly6C$^{Hi/Lo}$-RM cells are in part determined by whether or not they

receive niche-specific signals necessary to adequately induce Kupffer cell lineage-determining transcription factors.

NASH Diet Alters Function of a Pre-existing Kupffer Cell Enhancer Landscape

We next sought to understand the basis for the altered expression of more than 900 mRNAs during the transition of KC1 cells in the healthy liver to KC2 cells in the NASH liver (**Figure 3.3A**, **C**). Corresponding changes in the regulatory landscapes during this transition would potentially enable inference of transcription factors and upstream signaling pathways that mediate responses to pathogenic signals. In marked contrast to the striking changes in open chromatin observed in the transition of Ly6C^{Hi} blood monocytes to KN-RM cells (**Figure 3.4B**, **D**), relatively few differences in open chromatin were observed comparing KC1 and KC2 cells (**Figure 3.5A**). To investigate potential changes in the transcriptional functions of these regions, we performed chromatin immunoprecipitation sequencing (ChIP-seq) for acetylation of histone H3 lysine 27 (H3K27ac) in KC1 cells in the healthy liver and KC2 cells in the NASH liver. H3K27ac is deposited by histone acetyltransferases associated with transcriptional co-activators and is highly correlated with regulatory element activity (92). ChIP-seq experiments demonstrated that the NASH diet both positively and negatively affected H3K27 acetylation. Induction of H3K27ac at the promoter and a putative upstream regulatory element of the positively regulated *Pdgfb* gene and reduced acetylation for corresponding elements associated with the negatively regulated *Cd163* gene are illustrated in **Figure 3.5B**.

To associate the relatively broad H3K27ac peaks with specific regulatory elements, we overlapped H3K27ac with ATAC-seq peaks by assigning each ATAC-seq peak the H3K27ac signal residing within a 1,000 bp window surrounding the ATAC-seq peak center in both directions. Differential acetylation of these ATAC-seq regions was determined by statistical analysis of biological replicates using DESeq2 (> 2-fold, p-adj < 0.05). Out of 43,352 total distal open chromatin regions, the NASH inducing diet resulted in significantly increased H3K27ac at 4,201 putative enhancers and significantly decreased H3K27ac at 3,583 putative enhancers (**Figure 3.5C**). Changes in H3K27ac ChIP-seq signal at open chromatin were strongly correlated with changes in expression of the nearest mRNA (R=0.70, **Figure 3.5D**). The relatively modest alterations in open chromatin, coupled with substantial changes in histone acetylation, suggest the NASH-inducing diet primarily alters Kupffer cell gene expression by altering the function of a pre-existing enhancer landscape.

The NASH model diet increased expression of transcripts associated with functional annotations including “cell adhesion” (e.g. *Mmp2*, *Mmp12*, *Mmp14*, and *Adam15*), “hemostasis and wound healing” (e.g. *Pdgfa*, *Pdgfb*, *Cxcr4, Hgf*, *Tgfb3*, and *Vegfa*), “lipid localization” (e.g. *Abca1*, *Stard10*, *Srebf1*, *Pltp*, *Abcg1*, *Cd36*, *ApoE*, *Ldlr, Apoa1,* and *Pparg*), and “cytokine production” (e.g. *Slamf8*, *Ccl3*, *Ccl5*, *Il1rn*, *Ccl9*, *Ccl22*, *Ccl4*, *Chil3*, *Cxcl14*, and *Cxcl2*) (**Figure 3.5E** and **Figure 3.S5B**). Protein-protein Interaction Enrichment Analysis also showed enrichment of genes related to “positive regulation of apoptotic process” (e.g. *Anxa1*, *Egr1*, *Bcl6*, *Fbxo32*, *Bcl2l11*, *Sort1*, *Cdkn2a*, and *Psen2*). These findings are consistent with known roles of Kupffer cells as

orchestrating inflammation and tissue repair during NASH, and additionally suggest that the Kupffer cells may be more prone to apoptosis during NASH (46-48).

A comparison of H3K27ac associated with ATAC-seq peaks in KC1 cells with other macrophage populations enabled definition of a set of 10,452 putative KC1-signature enhancers (**Figure 3.S5A** and **Chapter 2**). A profound overlap was observed between Kupffer cell signature enhancers and enhancers downregulated by the NASH diet, in total identifying 2,553 Kupffer cell signature downregulated enhancers (24% of Kupffer cell signature enhancers, 71% of all downregulated enhancers) (**Figure 3.5C**, purple points). Conversely, only 365 Kupffer cell signature enhancers were upregulated by NASH diet (3.5% of Kupffer cell signature enhancers, 8.7% of all upregulated enhancers) (**Figure 3.5C**, orange points). These findings suggest a preferential suppressive effect of the NASH-inducing diet on gene regulatory networks governing the function of Kupffer cell enhancers and are in line with the corresponding down-regulation of KC identity genes (**Figure 3.S3C**). Consistent with this possibility, motif enrichment analysis of regions of open chromatin exhibiting loss of H3K27ac signal in response to the NASH-inducing diet were significantly enriched for binding sites recognized by LXR, MAF and IRF transcription factors (**Figure 3.5F** lower). Each of these motifs are found preferentially in Kupffer cell enhancers in comparison to other macrophage populations, and are recognized by transcription factors that are established or proposed to drive Kupffer cell identity (37-39) (and **Chapter 2**). In contrast, regions of open chromatin exhibiting gain of H3K27ac signal were enriched for

de novo motifs matching AP1, NFAT, RUNX and EGR transcription factors (**Figure 3.5F**).

By RNA-seq of KC1 to KC2 cells, we observed significant induction of *Atf3*, *Fos, Jun*, *Egr2*, and *Runx1* (**Figure 3.5G** and **Figure 3.S5C**), suggesting that increased expression of these transcription factors during NASH may contribute to activation of enhancers with corresponding DNA binding elements (**Figure 3.5F**). In contrast, expression of *Nr1h3*, encoding LXRα, was not significantly affected by the NASH diet, and expression of *Nr1h2*, encoding LXRβ, was slightly increased. In addition, many canonical LXR target genes such as *Abca1*, *Abcg1*, *Mylip*, and *Srebf1*, were unchanged or even upregulated in response to the NASH diet (**Figure 3.5H**). Targeted lipidomic analysis of all known LXR ligands (105) in liver indicated that the concentration of desmosterol, which is the most highly abundant endogenous LXR ligand in the liver (and **Chapter 2**)(106) was significantly increased in NASH model diet mice compared to controls (**Figure 3.5I**). This result is consistent with the up-regulation of general LXR target genes involved in cholesterol homeostasis and suggests that the decreased activity of enhancers with LXRE binding sites during NASH is not due to reduced availability of LXR ligands. Instead, these findings suggest that the NASH diet affects LXR function in a gene-specific manner. Overall, analysis of the epigenetic landscapes of KC1 and KC2 cells suggests that the NASH-inducing diet alters resident Kupffer cell gene expression by altering the expression and activities of transcription factors that control the functions of Kupffer cell-specific enhancers.

NASH Impairs LXR Regulation of Kupffer Cell Identity Genes

A possible explanation for the apparent paradox that the LXR recognition element is highly enriched in the global set of down-regulated enhancers but that conventional LXR target genes are not affected is that in Kupffer cells, LXRα functions as a lineage-determining factor to control expression of a large set of KC-specific genes (and **Chapter 2**) (39). A selective effect of the NASH-inducing diet on the Kupffer cell-specific functions of LXR would resolve this apparent paradox. To investigate this hypothesis, we performed RNA-seq analysis of Kupffer cells isolated from mice in which LXRα and LXRβ were globally deleted (LXR DKO), LXRα alone was globally deleted (LXRα KO) or LXRα was selectively deleted from Kupffer cells using a Clec4f-Cre-tdTomato deleter line (and **Chapter 2**).

We observed a significant correlation ($p < 2.2e-16$) of the effect of the NASH inducing diet and the LXR DKO on Kupffer cell gene expression, with 184 genes being coordinately up-regulated and 104 genes coordinately down-regulated (**Figure 3.6A**). The coordinately upregulated genes were associated with functional annotations related to “regulation of cell adhesion”, “hemostasis”, “angiogenesis”, “inflammatory response”, “extracellular matrix organization”, and “leukocyte migration” (**Figure 3.6B**). Only 51 genes exhibited divergent patterns of regulation, including the canonical LXR target genes *Abca1*, *Abcg1*, *Arg2*, *Apoe*, *Pltp*, and *Scd1*, which were induced by the NASH diet but down-regulated in LXR DKO Kupffer cells (**Figure 3.6A** and **Figure 3.6C**). Coordinately regulated examples of strikingly up-regulated genes associated with leukocyte migration and extracellular matrix organization are provided by *Cx3cr1* and

Mmp13, and strongly down-regulated genes associated with the complement cascade and phagocytosis of apoptotic cells are provided by *C6* and *Timd4,* respectively (**Figure 3.6C**). Several other Kupffer cell identity genes such as *Pcolce2*, *Kcna2*, *Lbp*, *Cdh5*, *Il18bp*, *Icos* and *Vsig4* were down-regulated by both NASH and LXR deletion, suggesting that NASH impairs the function of LXR at these loci.

Overlapping but distinct relationships were observed for the global LXRα KO and the Kupffer cell-specific LXRα KO (**Figure 3.6C**), indicating both non-redundant and redundant roles of LXRα and LXRβ in the Kupffer cell. For example, *Abca1* and *Abcg1* expression is significantly induced in KC2 cells and the Kupffer cell-specific LXRα KO, but is strongly downregulated in LXR DKO Kupffer cells. In contrast, *C6* expression is almost completely dependent on LXRα (**Figure 3.6C**). Notably, *Cd5l*, which is also almost completely dependent on LXRα for expression, is not significantly altered by the NASH-inducing diet (**Figure 3.6C**).

The maintained expression of a subset of LXR target genes, such as *Abca1* and *Cd5l*, and the loss of others suggest that the NASH-inducing diet does not affect the intrinsic transcriptional activity of LXR, but rather its ability to function in a gene-specific manner. To test the importance of LXRα in controlling the activity of Kupffer cell-specific enhancers, we performed H3K27ac ChIP-seq on healthy global LXRα KO mice. Changes in enhancer activity caused by deletion of LXRα or the NASH diet were strikingly similar (**Figure 3.S6A**, R = 0.74 for purple points representing enhancers differentially regulated in both comparisons). Of the 1,369 enhancers downregulated due to both loss of LXRα and the NASH diet, 1,178 of these regions corresponded to

Kupffer cell signature enhancers (**Figure 3.S6A**, black points), indicating that a major effect of NASH is to reduce enhancer activity at LXRα-dependent regulatory regions important for Kupffer cell identity. The acquisition of the genome wide locations of LXRα and LXRβ in Kupffer cells (**Chapter 2** and **Figure 3.S6B**), enabled their alignment with H3K27ac under control and NASH diet conditions. This analysis indicated a dramatic and highly preferential reduction of H3K27ac signal at LXR binding sites (1069/1565, or 68% of LXR peaks with significantly reduced H3K27ac signal due to NASH model diet) that overlapped with Kupffer cell-specific enhancers (**Figure 3.6D**, purple and blue points).

To investigate whether changes in gene expression and H3K27ac are associated with corresponding changes in LXR binding, we performed ChIP-seq for LXRα + LXRβ in the combination of KC2 and KN-RM cells marked by nuclear Clec4f-tdTomato expression in the NASH liver. These studies indicated that the NASH diet induced dramatic remodeling of the LXRα + LXRβ cistromes. While similar numbers of LXR binding sites were observed under control and NASH diet conditions, only about a half of the binding sites were shared (**Figure 3.6E**). Notably, DNA binding was relatively unchanged at most of the LXR binding sites associated with canonical LXR activity (e.g., *Abca1* and *Cd5l*), which are highly LXRα-dependent but are not affected at the mRNA level by the NASH-inducing diet (**Figure 3.6F**). In contrast, LXR binding in the vicinity of *C6* and *Timd4* was markedly reduced. Motif analysis of genomic regions at which LXR is lost (KC1-specific) indicates enrichment for motifs recognized by Kupffer cell lineage-determining factors, whereas genomic regions at which LXR binding is

gained (KC2-specific) are not enriched for these motifs (**Figure 3.S6C** and **Figure 3.S6D**). Further, LXR ChIP-seq peaks were preferentially depleted from Kupffer cell signature enhancers (584/1565, or 37% of total downregulated LXR peaks in enhancers, blue and purple points) compared to LXR signal gained at Kupffer cell signature enhancers (65/2071, or 3.1% of total upregulated LXR peaks in enhancers, orange and red points) (**Figure 3.S6E**). Tag density LXR ChIP-seq signal was approximately equivalent across an average of all LXR peaks in control and NASH but was reduced at Kupffer cell signature enhancers during NASH (**Figure 3.S6F**) Together, these findings indicate that the NASH-inducing diet reduces LXR binding and function in a selective manner at a large fraction of Kupffer cell-specific genes.

NASH Model Diet Induces Kupffer Cell Apoptosis and Replacement

Kupffer cells are considered to represent a self-renewing population that is normally closed to HSC-derived cells (36). However, we found that the NASH-inducing diet resulted in a subset of HSC-derived KN-RM cells that exhibited a transcriptomic signature and anatomic location that converged with EMP-derived KC2 cells. Notably, a population of $Tim4^{Neg}$ cells is observed in LXRα KO Kupffer cells, which partially phenocopy the effects of the NASH-inducing diet. Further, recent studies suggest an important pro-survival role of LXRα in Kupffer cells and splenic marginal zone and metallophilic macrophages (24, 39), and Protein-Protein Interaction Enrichment analysis identified “positive regulation of apoptotic process” as the top term for genes enriched in Kupffer cells during NASH (**Figure 3.5E**) . Collectively, these observations raise the

question of whether the NASH diet induces loss of embryonically-derived Kupffer cells, which would provide an open niche and enable the recruitment of monocytic precursors.

TUNEL staining of NASH livers showed apoptosis of Tim4^{Pos} Kupffer cells (KC2) during NASH diet but not of KC1 cells from age matched mice fed a healthy control diet (**Figure 3.7A** and **Figure 3.7B**). In both NASH and control diet livers, TUNEL^{Pos} KN-RM and Ly6C$^{Hi/Lo}$-RM cells were rare. By performing a nearest-neighbor analysis of TUNEL^{Pos} cells, we found that KN-RM cells were significantly enriched in nearby areas as compared to Ly6C$^{Hi/Lo}$-RM and KC2 cells (**Figure 3.7C**). Time course experiments indicate that KN-RM cells are detected by ten weeks after initiation of the NASH inducing diet, and progressively accumulate to account for more than 50% of the Kupffer cell population at 30 weeks (**Figure 3.7D**). These results indicate that Tim4^{Pos} Kupffer cells undergo cell death during NASH and may suggest that this process results in partial opening of the KC2 niche, enabling repopulation by HSC-derived KN-RM cells.

D. Discussion

Tissue resident macrophages and recruited monocyte-derived cells play pathological roles in a diverse range of human diseases (45). How the evolutionarily-derived protective and homeostatic functions of these cells are subverted to promote tissue damage and dysfunction remains to be explained at a deep mechanistic level. In particular, discerning the precise roles in disease of each of the diverse macrophage subtypes found in affected tissue requires more precise analysis of the genomic, topological, and phenotypic properties of these cells. The need for this combination of

studies follows from the exquisite ability of macrophages to sense and respond to environmental signals, which suggests that pathological phenotypes are acquired as the consequence of exposure to various combinations of disease-associated molecules, analogous to how distinct combinations of environmental signals play instructive roles in promoting the acquisition of tissue-specific resident macrophage phenotypes during development (e.g., **Chapter 2**). Here, we used a combination of approaches to investigate the genomic and anatomic relationships among phenotypically distinct macrophage populations in a mouse model of NASH. Our data reveal a strong association of niche occupancy with the transcriptional / phenotypic state of different EMP- and HSC-derived myeloid cells, providing evidence that the loss of classical Kupffer cell transcripts in EMP-derived KCs is strongly associated with locus-specific alteration in the action of LXR proteins, and reveal the ability of blood monocytic cells to acquire a KC-like state only upon entry into the liver sinusoids.

It is recognized that many mouse NASH models only partially capture features of NASH observed in humans (167, 168). The widely used model chosen for these studies (169, 170) resulted in marked infiltration of monocyte-derived cells, steatosis and a mild degree of fibrosis, enabling general questions regarding origin and niche to be addressed. The combination of lineage tracing, histo-cytometry, RNA-seq and epigenetic analyses suggests that HSC-derived macrophages observed in this model of NASH reside in at least two distinct microanatomical niches that drive divergent pathways of differentiation. One pathway corresponds to the development of Ly6C^{Hi}-RM and Ly6C^{Lo}-RM recruited macrophages in contact with conventional (but most likely

inflamed) vascular endothelium. These monocyte-derived cells have been extensively studied previously (154, 155, 166). The two populations cannot at present be readily distinguished by confocal microscopy due to limitation in reagents reactive with Ly6C, but each reside proximal to large portal and central vein vessels in a distinct distribution from that occupied by KC2 and KN-RM cells inside the liver sinusoidal vasculature network. Principle component analysis of the alterations in open chromatin are consistent with a transition of blood Ly6C^{Hi} monocytes to Ly6C^{Hi}-RM to Ly6C^{Lo}-RM macrophages (154, 166). Whether the distinct transcriptomic profiles of these cells reflect further diversification of the hepatic niche or represent different tissue residence times will require further investigation.

The alternative differentiation pathway taken by recruited macrophages resulted in the accumulation of KN-RM cells, which colocalized with KC2 in contact with the liver sinusoidal endothelial cells (LSEC) and adopted a highly similar pattern of gene expression that may have been imposed by signals from this specialized endothelial population. It is unlikely that KN-RM cells are derived from the recruited Ly6C$^{Hi/Lo}$ macrophage population based both on the divergent paths of remodeling of their open chromatin profiles and the observation that repopulating liver macrophages initiate the Kupffer cell-specific program of differentiation within 12 hours of resident Kupffer cell depletion (see **Chapter 2**). Instead, the combined findings from these studies and prior work that KN-RM and Ly6C$^{Hi/Lo}$-RM cells are all derived from Ly6C^{Hi} blood monocytes (42, 76, 154, 166). The striking differences in their chromatin landscapes and gene expression provides strong evidence that these differences arise from responses to

spatially distinct environmental signals. The absence of extensive fibrosis and ballooning (apoptotic/necrotic) in hepatocytes in the relatively mild model of NASH studied here suggests that additional myeloid phenotypes might be observed in more severe forms of NASH in which, for example, myeloid cells surround dying hepatocytes to form crown-like structures (171).

The ability to specifically isolate embryonic KCs in the healthy liver and following the NASH-inducing diet further provided the opportunity to investigate effects of this environmental perturbation on the resident cell population. In contrast to HSC-derived KN-RM cells, which exhibited extensive remodeling of open chromatin in comparison to their progenitor Ly6C^{Hi} blood monocytes, the transition of KC1 to KC2 cells was associated with relatively few changes in open chromatin, despite significant changes in the expression of nearly 1,000 genes. Instead, substantial changes in H3K27ac were observed, suggesting that the NASH liver environment primarily reprogrammed resident KC1 gene expression by altering the activity states of pre-existing enhancers. Motifs recognized by KC lineage-determining transcription factors, including LXRα, were enriched in enhancers exhibiting loss of H3K27ac, suggesting down-regulation of their activities. However, LXRα expression was not altered, nor were many general LXR target genes involved in cholesterol homeostasis. Instead, the Kupffer cell-specific functions of LXRα were significantly altered, resulting in changes in gene expression that overlapped significantly with consequences of genetic deletion of LXRα. Conversely, the enrichment of motifs for AP-1 and EGR transcription factors in regulatory elements gaining H3K27ac in the context of the NASH diet suggest activation

of upstream signaling pathways that regulate their activities. It will be of considerable interest to identify NASH diet-induced signaling molecules that are responsible for these effects.

Overall, these studies provide evidence that distinct microenvironments within the NASH liver drive strikingly divergent patterns of differentiation of resident and infiltrating cells by remodeling the open chromatin landscapes of recruited monocytes and altering the activities of pre-existing enhancers of the resident Kupffer cell population. The inference of transcription factors and upstream signaling pathways associated with these distinct cell populations provides a basis for understanding how disease-promoting environmental signals instruct resident and recruited macrophages to acquire distinct pathogenic programs of gene expression. Application of the methods utilized in concert in this study should prove valuable in gaining a better understanding how distinct myeloid phenotypes are established in other disease contexts.

Figure 3.1: Transcriptional diversity of hepatic macrophages during NASH

A. tSNE projections of identified graph-based cell clusters from 10X Genomics scRNA-seq data derived from hepatic $CD45^{Pos}CD146^{Neg}$ cells from healthy control mice or mice fed a model NASH diet for 30 weeks. Left panel: cells are color coded based on dietary condition. Right panel: cells are color coded based on cell identity of the five major myeloid cells identified. Data represent two independent cell donor mice per group.
B. Pie charts depicting macrophage proportions from **A** for control mice (left) or mice with NASH (right).
C. Gene expression of normalized scRNA-seq data of selected genes supporting cluster identities.
D. Representative terminal FACS gates for purification of Kupffer cells from healthy control mice (left), or $CD11b^{Lo}F4/80^{Hi}Tim4^{Pos}$ and $Tim4^{Neg}$ cells from mice with NASH (right).
E. Representative terminal FACS gates for purification of $Ly6C^{Hi}$ and $Ly6C^{Lo}$ $CD11b^{Hi}F4/80^{Lo}Ly6G^{Neg}CX3CR1^{Pos}$ recruited hepatic macrophages (RM). Neutrophils are depicted as "PMN."
F. Comparison of myeloid clusters defined by scRNA-seq (left) and bulk RNA-seq (right) for the corresponding sorted populations. Left heatmap depicts normalized and scaled expression values for marker genes identified in the Seurat R package. Each column of data represents an individual cell, showing 100 cells per cluster. Marker genes were statistically identified using a Wilcoxon rank sum test. Right heatmap shows z-normalized expression of each gene for RNA-seq from bulk purified cell populations from independent biological duplicates.

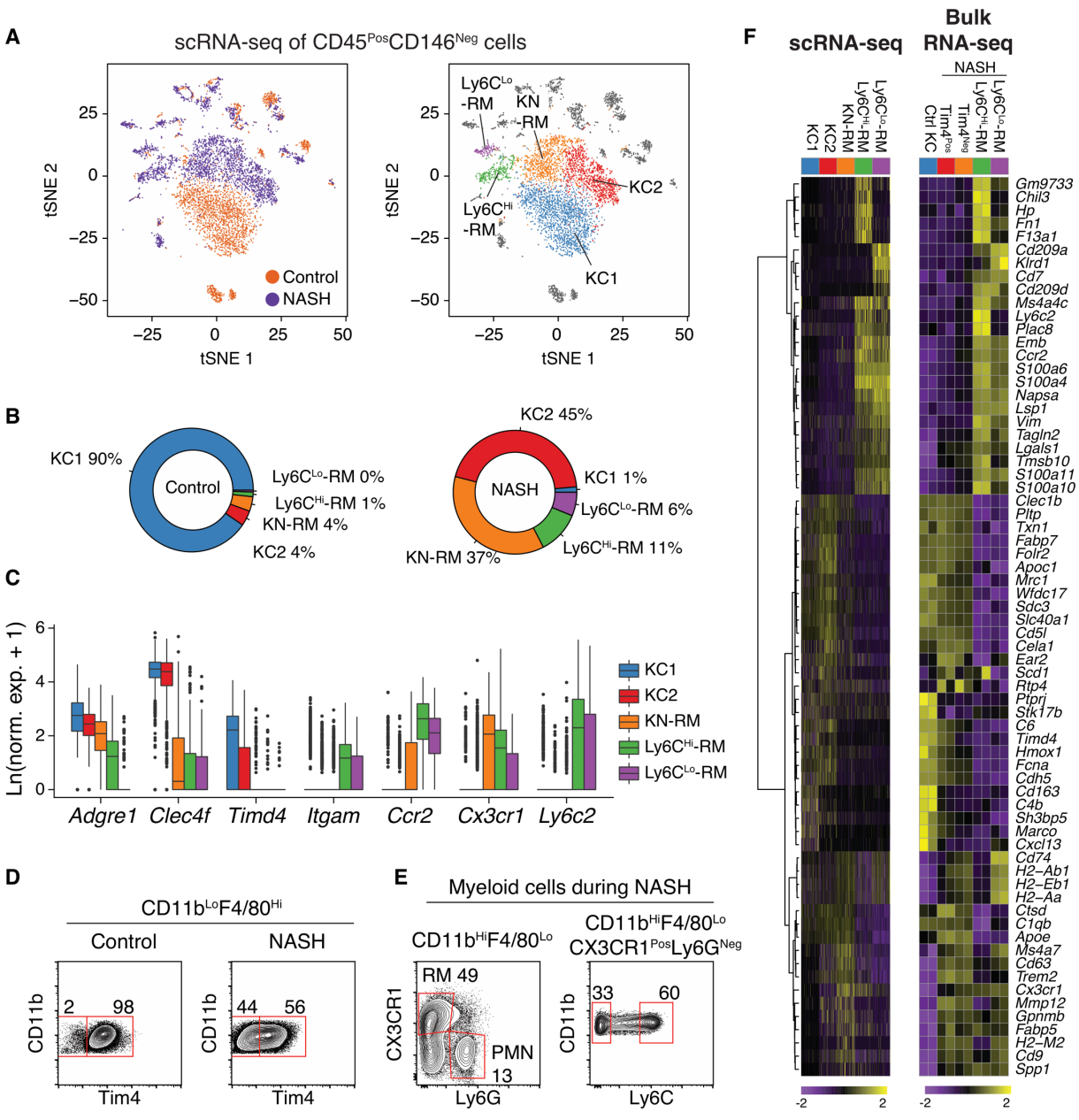
A
scRNA-seq of CD45PosCD146Neg cells
tSNE 2
tSNE 1
Control
NASH
Ly6CLo -RM
KN -RM
Ly6CHi -RM
KC2
KC1
B
KC1 90%
Control
Ly6CLo-RM 0%
Ly6CHi-RM 1%
KN-RM 4%
KC2 4%
KC2 45%
NASH
KC1 1%
Ly6CLo-RM 6%
Ly6CHi-RM 11%
KN-RM 37%
C
Ln(norm. exp. + 1)
KC1
KC2
KN-RM
Ly6CHi-RM
Ly6CLo-RM
Adgre1
Clec4f
Timd4
Itgam
Ccr2
Cx3cr1
Ly6c2
D
CD11bLoF4/80Hi
Control
NASH
CD11b
Tim4
2
98
44
56
E
Myeloid cells during NASH
CD11bHiF4/80Lo
CD11bHiF4/80Lo
CX3CR1PosLy6GNeg
CX3CR1
Ly6G
RM 49
PMN
13
CD11b
Ly6C
33
60
F
scRNA-seq
Bulk RNA-seq
NASH
KC1
KC2
KN-RM
Ly6CHi-RM
Ly6CLo-RM
Ctrl KC
Tim4Pos
Tim4Neg
Gm9733
Chil3
Hp
Fn1
F13a1
Cd209a
Klrd1
Cd7
Cd209d
Ms4a4c
Ly6c2
Plac8
Emb
Ccr2
S100a6
S100a4
Napsa
Lsp1
Vim
Tagln2
Lgals1
Tmsb10
S100a11
S100a10
Clec1b
Pltp
Txn1
Fabp7
Folr2
Apoc1
Mrc1
Wfdc17
Sdc3
Slc40a1
Cd5l
Cela1
Ear2
Scd1
Rtp4
Ptprj
Stk17b
C6
Timd4
Hmox1
Fcna
Cdh5
Cd163
C4b
Sh3bp5
Marco
Cxcl13
Cd74
H2-Ab1
H2-Eb1
H2-Aa
Ctsd
C1qb
Apoe
Ms4a7
Cd63
Trem2
Cx3cr1
Mmp12
Gpnmb
Fabp5
H2-M2
Cd9
Spp1
-2
2

Figure 3.2: Expanded macrophage diversity during NASH is supported by monocyte recruitment and occupancy of unique anatomical niches

A. (Left) Experiment timeline for tracing ontogeny of Tim4^{Pos} Kupffer cells during NASH. (Right) Representative flow cytometry result assessing co-expression of Tim4 and tamoxifen-induced tdTomato expression in Kupffer cells from mice with perinatal labeling (top) or adult labeling with tamoxifen administered 1 week prior to the study conclusion (bottom).
B. Representative multi-parameter microscopy images of liver sections of animals as in **A, bottom** assessing expression of CD138 (sinusoidal vasculature), F4/80, Tim4, and tdTomato. tdTomato^{Pos} cells are shown enriched in NASH diet animals. Representative image from n=4 mice/condition; maximum intensity projection (MIP) of a 20 µm z-stack. "Ctrl" denotes tissue section from a healthy control.
C. Enlarged panels corresponding to boxes 1 and 2 in NASH diet samples from panel **B**, showing composite and single-color panels. Highlighted are Ly6C$^{Hi/Lo}$-RM, KC2, and KN-RM cells.
D. Representative histo-cytometry analysis of NASH liver sample. Statistical information of segmented objects (F4/80^{Pos} tdTomato^{Pos} surfaces) was imported into FlowJo and subsequently gated on F4/80 and tdTomato expression to quantify KC2, KN-RM, and Ly6C$^{Hi/Lo}$-RM cells. Tim4 mean fluorescence intensity (MFI) and x/y positioning for each gated population are shown in the middle and right-hand panels, respectively.
E. Distance and phenotype (KN-RM or Ly6C$^{Hi/Lo}$-RM) of closest neighbor to KC2 cells in NASH livers. Data pooled from n=4 mice. Wilcox Two-sided test; $p<0.0001$(****).
F. Two representative multi-parameter immunofluorescence (IF) microscopy image (composite and single-color panels) for liver section from NASH animals prepared as in **A, bottom** assessing expression of Collagen IV, F4/80, Tim4, and tdTomato. Highlighted are KN-RM and Ly6C$^{Hi/Lo}$-RM cells. Representative image from n=4 mice/condition; maximum intensity projection (MIP) of a 20-µm z-stack.
G. Distance to nearest portal or central vein vasculature (large diameter vessels defined to be greater than 15 μm in diameter) of KC2, KN-RM, and Ly6C$^{Hi/Lo}$-RM cells. One-Way ANOVA with Tukey HSD test; $p<0.0001$(****), $p<0.001$(***), not significant (ns).

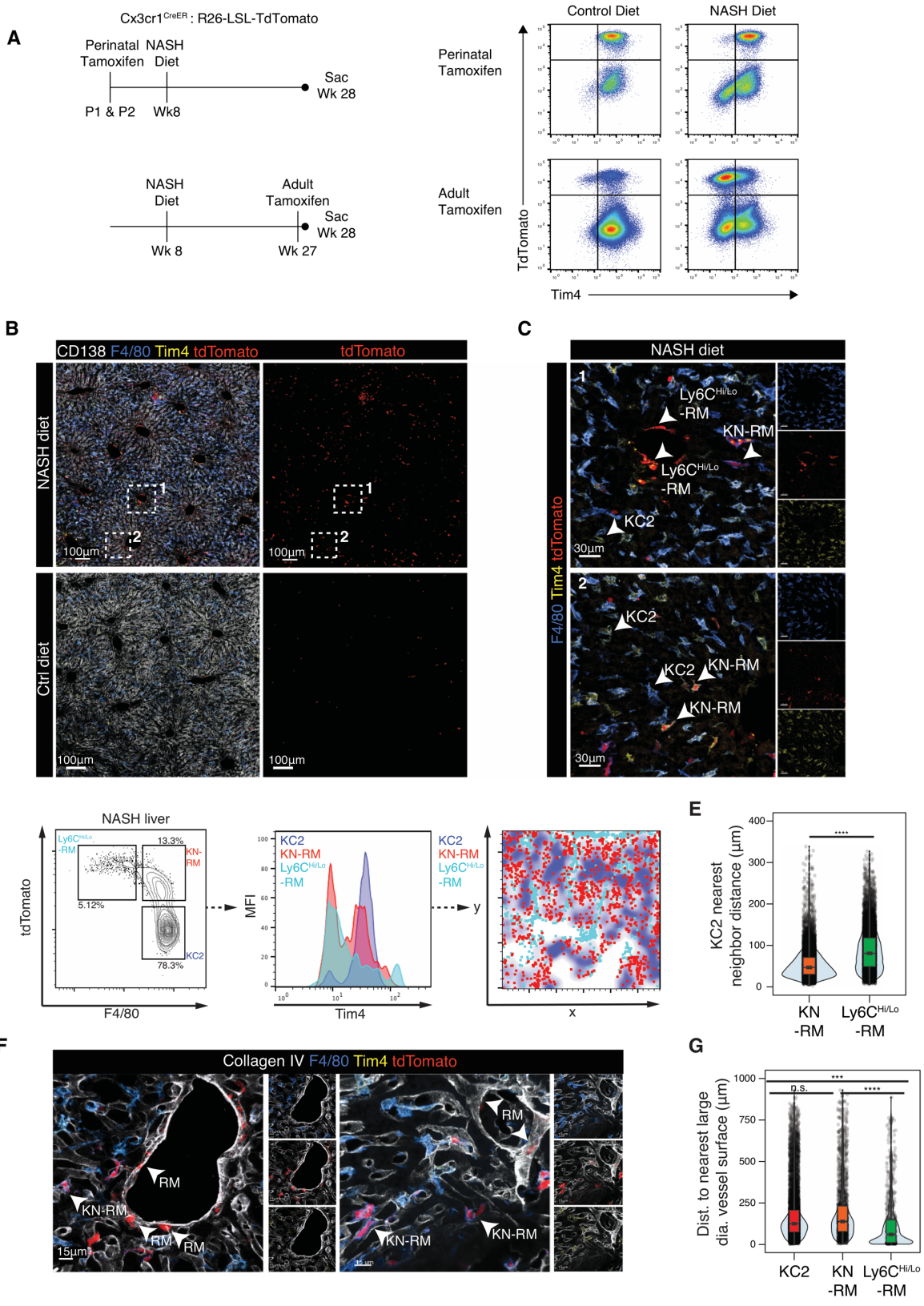
A
Cx3cr1CreER : R26-LSL-TdTomato
Perinatal Tamoxifen
NASH Diet
Sac Wk 28
P1 & P2
Wk8
NASH Diet
Adult Tamoxifen
Sac Wk 28
Wk 8
Wk 27
Control Diet
NASH Diet
Perinatal Tamoxifen
Adult Tamoxifen
TdTomato
Tim4
B
CD138 F4/80 Tim4 tdTomato
tdTomato
NASH diet
Ctrl diet
100µm
C
NASH diet
Ly6CHi/Lo -RM
KN-RM
KC2
30µm
F4/80 Tim4 tdTomato
D
NASH liver
tdTomato
F4/80
13.3%
5.12%
78.3%
MFI
Tim4
KC2
KN-RM
Ly6CHi/Lo -RM
x
y
E
KC2 nearest neighbor distance (µm)
KN -RM
Ly6CHi/Lo -RM
F
Collagen IV F4/80 Tim4 tdTomato
RM
KN-RM
15µm
G
Dist. to nearest large dia. vessel surface (µm)
n.s.
KC2
KN -RM
Ly6CHi/Lo -RM

Figure 3.3: Highly divergent gene expression patterns across myeloid populations in NASH

A. Unsupervised hierarchical clustering of differentially expressed genes in the indicated cell types in control and NASH liver.
B. Principal component analysis of 2,000 most variable genes in RNA-seq data from myeloid cells in liver and blood from healthy and NASH model diet fed mice (n = 2 per group).
C. Scatterplot of RNA-seq data in healthy (KC1) or NASH model diet (KC2) $Tim4^{Pos}$ Kupffer cells. Differentially expressed genes identified by DESeq2 (> 2-fold, p-adj < 0.05) are colored in red.
D. Comparison of NASH model diet $Tim4^{Pos}$ Kupffer cells (KC2) and $Tim4^{Neg}$ Kupffer niche recruited macrophages (KN-RM).
E. Comparison of NASH model diet $Tim4^{Neg}$ Kupffer niche recruited macrophages (KN-RM) and $Ly6C^{Hi}$-RM.
F. Comparison of NASH model diet peripheral blood $Ly6C^{Hi}$ monocytes and $Ly6C^{Hi}$-RM.
G. RNA-seq expression (mean TPM +/- SD) of representative genes. TPM = transcripts per kilobase million).

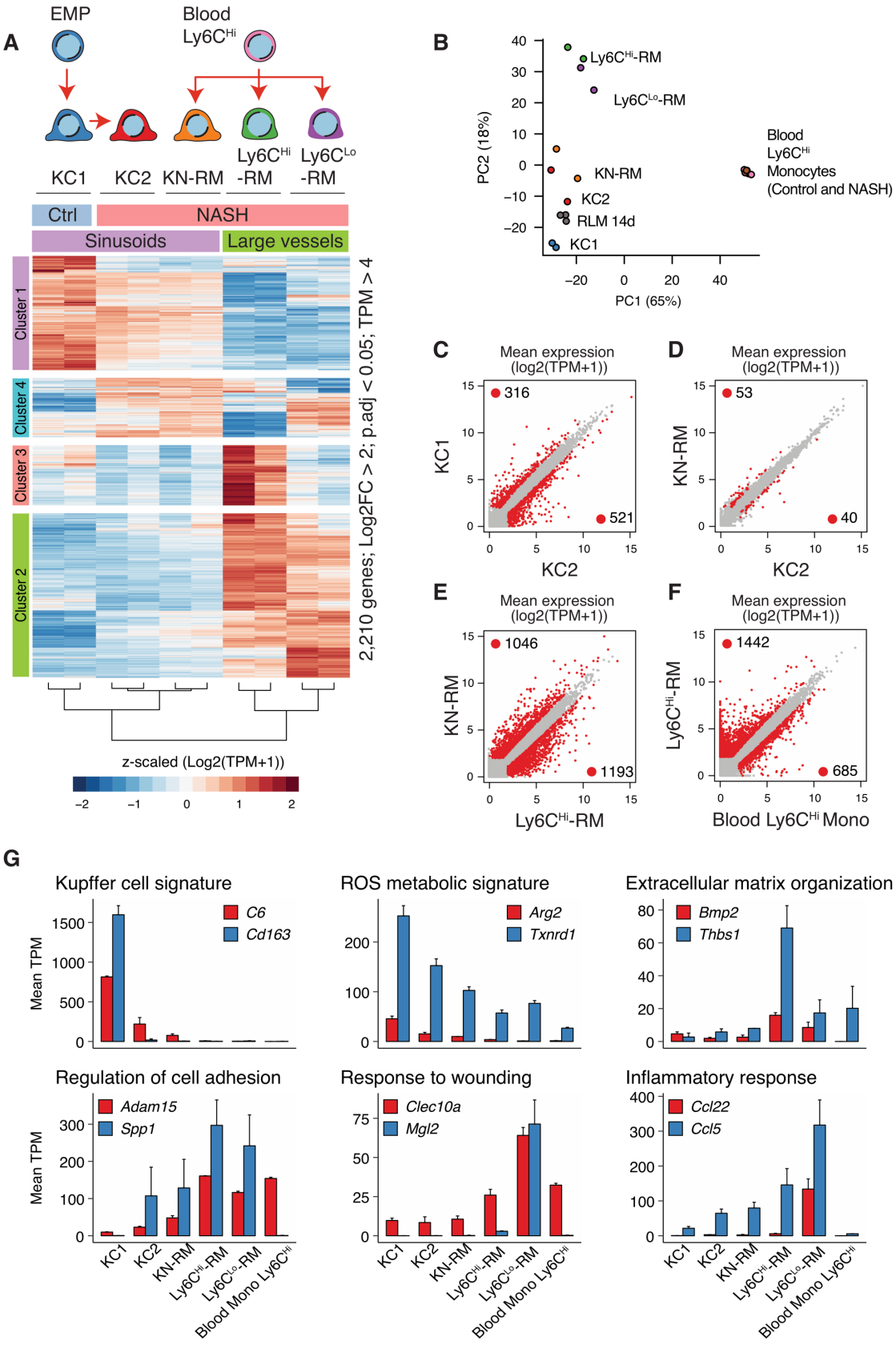
A
EMP
Blood Ly6C^Hi
KC1
KC2
KN-RM
Ly6C^Hi -RM
Ly6C^Lo -RM
Ctrl
NASH
Sinusoids
Large vessels
Cluster 1
Cluster 4
Cluster 3
Cluster 2
2,210 genes; Log2FC > 2; p.adj < 0.05; TPM > 4
z-scaled (Log2(TPM+1))
B
Ly6C^Hi-RM
Ly6C^Lo-RM
KN-RM
KC2
RLM 14d
KC1
Blood Ly6C^Hi Monocytes (Control and NASH)
PC2 (18%)
PC1 (65%)
C
Mean expression (log2(TPM+1))
316
521
KC1
KC2
D
Mean expression (log2(TPM+1))
53
40
KN-RM
KC2
E
Mean expression (log2(TPM+1))
1046
1193
KN-RM
Ly6C^Hi-RM
F
Mean expression (log2(TPM+1))
1442
685
Ly6C^Hi-RM
Blood Ly6C^Hi Mono
G
Kupffer cell signature
C6
Cd163
ROS metabolic signature
Arg2
Txnrd1
Extracellular matrix organization
Bmp2
Thbs1
Regulation of cell adhesion
Adam15
Spp1
Response to wounding
Clec10a
Mgl2
Inflammatory response
Ccl22
Ccl5
Mean TPM
KC1
KC2
KN-RM
Ly6C^Hi-RM
Ly6C^Lo-RM
Blood Mono Ly6C^Hi

Figure 3.4: Niche-specific reprogramming of epigenetic landscapes

A. UCSC genome browser tracks of ATAC-seq signals in the vicinities of the *Clec4f* and *Itgam* genes in the indicated cell types. Bar plots to the right of each track represent the RNA-seq gene expression (mean TPM) +/- SD in each population
B. Genome-wide comparison of normalized ATAC-seq peak tags at enhancer like regions (>3kb removed from TSS) comparing Ly6C^{Hi} peripheral blood monocytes and Ly6C^{Lo}-RM during NASH. Differential regions were identified using DESeq2 (> 2-fold and p-adj < 0.05 using independent biological duplicates).
C. Genome-wide comparison of normalized ATAC-seq peak tags at enhancer-like regions (>3kb removed from TSS) comparing open chromatin in Ly6C^{Hi} peripheral blood monocytes and KN-RM.
D. Principal component analysis of ATAC-seq data sets (N = 2-3) for the top 10,000 most variable distal (>3kb from TSS) regions in myeloid cell populations during NASH. Transparent arrows suggest divergent developmental trajectories of Ly6C^{Hi} blood monocytes entering the Kupffer cell or Ly6C$^{Hi/Lo}$ recruited macrophage niche. Summaries of changes in motif enrichment in regions gained or lost during niche acquisition (**Figure 3.4E**, **Figure 3.S4B** and **Figure 3.S4C**) are overlaid on the plot.
E. De novo motifs enriched in distal open chromatin regions (>3kb from TSS) enriched in KN-RM (top), Ly6C^{Lo}-RM (bottom), or enriched in both populations (middle) compared to Ly6C^{Hi} peripheral blood monocytes during NASH. The background for motif enrichment analysis is the distal open chromatin (ATAC-seq) from Ly6C^{Hi} peripheral blood monocytes.
F. Expression levels (mean TPM +/- SD) of Kupffer cell lineage-determining transcription factors in the indicated cell types.

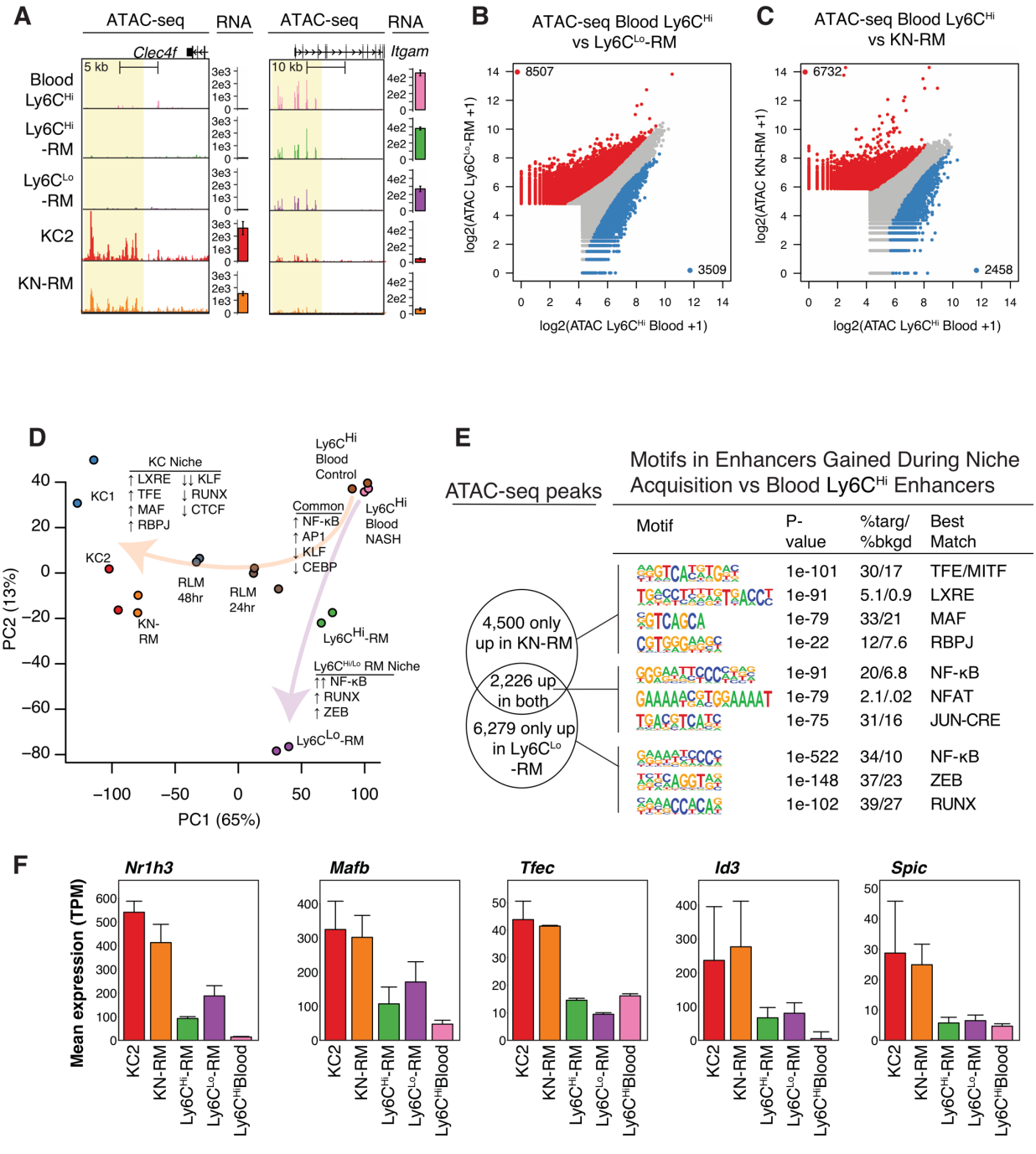
A
ATAC-seq
RNA
ATAC-seq
RNA
Clec4f
Itgam
5 kb
10 kb
Blood Ly6C^Hi
Ly6C^Hi -RM
Ly6C^Lo -RM
KC2
KN-RM
B
ATAC-seq Blood Ly6C^Hi vs Ly6C^Lo-RM
8507
3509
log2(ATAC Ly6C^Lo-RM +1)
log2(ATAC Ly6C^Hi Blood +1)
C
ATAC-seq Blood Ly6C^Hi vs KN-RM
6732
2458
log2(ATAC KN-RM +1)
log2(ATAC Ly6C^Hi Blood +1)
D
KC Niche
↑ LXRE ↓↓ KLF
↑ TFE ↓ RUNX
↑ MAF ↓ CTCF
↑ RBPJ
KC1
KC2
RLM 48hr
RLM 24hr
KN-RM
Ly6C^Hi Blood Control
Common
↑ NF-κB
↑ AP1
↓ KLF
↓ CEBP
Ly6C^Hi Blood NASH
Ly6C^Hi-RM
Ly6C^Hi/Lo RM Niche
↑↑ NF-κB
↑ RUNX
↑ ZEB
Ly6C^Lo-RM
PC2 (13%)
PC1 (65%)
E
ATAC-seq peaks
Motifs in Enhancers Gained During Niche Acquisition vs Blood Ly6C^Hi Enhancers
4,500 only up in KN-RM
2,226 up in both
6,279 only up in Ly6C^Lo -RM
Motif
P-value
%targ/%bkgd
Best Match
1e-101 30/17 TFE/MITF
1e-91 5.1/0.9 LXRE
1e-79 33/21 MAF
1e-22 12/7.6 RBPJ
1e-91 20/6.8 NF-κB
1e-79 2.1/.02 NFAT
1e-75 31/16 JUN-CRE
1e-522 34/10 NF-κB
1e-148 37/23 ZEB
1e-102 39/27 RUNX
F
Nr1h3
Mafb
Tfec
Id3
Spic
Mean expression (TPM)
KC2
KN-RM
Ly6C^Hi-RM
Ly6C^Lo-RM
Ly6C^HiBlood

Figure 3.5: The NASH-inducing diet alters the activity states of resident KC enhancers

A. Scatterplot of normalized ATAC-seq signal at all distal open chromatin regions (> 3kb from TSS) in Tim4^{Pos} Kupffer cells from healthy mice (KC1) or Tim4^{Pos} Kupffer cells from mice on NASH mode diet (KC2). Regions with significantly more chromatin accessibility during NASH are colored in **red** while regions with less accessibility during NASH are colored **blue**.
B. Genome browser tracks (left) showing ATAC-seq and H3K27ac ChIP-seq signal in the vicinity of *Pdgfb* or *Cd163* in KC1 cells (blue) or KC2 cells (red). RNA-seq expression data shown at right represents the mean TPM +/- SD.
C. Scatterplot of H3K27ac ChIP-seq signal around distal (> 3kb from TSS) ATAC-seq peaks in 2,000 bp window. Differentially acetylated regions were determined using DESeq2 (> 2-fold, p-adj < 0.05). Regions overlapping with Kupffer cell signature enhancers (**Figure 3.S5A**) are colored **green**. Enhancers with more acetylation during NASH are colored **red,** or colored **orange** if also a Kupffer cell signature enhancer. Enhancers with less activity during NASH are colored **blue,** or **purple** if also a Kupffer cell signature enhancer. Pie charts (top) depict percentage of upregulated and downregulated total enhancers (left) or Kupffer cell signature enhancers (right).
D. Ratio-ratio plot depicting fold change in H3K27ac ChIP-seq signal at enhancers (2,000 bp window centered on ATAC-seq peaks > 3kb from TSS) compared to fold change in mRNA expression of closest gene annotated to enhancer region in Tim4^{Pos} Kupffer cells in NASH diet mice (KC2) versus healthy mice (KC1). Points colored in **blue** are differentially expressed (> 2-fold, p-adj < 0.05) for both H3K27ac ChIP-seq signal at enhancers and closest mRNA. Pearson correlation = 0.70 for blue points.
E. Gene ontology of transcripts significantly upregulated (Fold change > 2, p-adj < 0.05, TPM > 4) in Kupffer cells from mice on the NASH model diet (KC2) compared to Kupffer cells from healthy mice (KC1).
F. De novo motif analysis of ATAC-seq peaks with significant gain of H3K27ac (red or orange points in **C**, top) or ATAC-seq peaks exhibiting significant loss of H3K27ac (purple or blue points in **C**, bottom).
G. Log_2 fold-change of candidate transcription factors known to bind DNA elements found enriched in (**E**) for Kupffer cells from healthy mice (KC1) and NASH mice (KC2). * = p-adj < 0.05, ** = p-adj < 0.01, and *** = p-adj < 0.001 using DESeq2.
H. Mean expression levels (TPM +/- SD) of the indicated genes in KC1 (control) and KC2 (NASH) Kupffer cells.
I. Quantification of desmosterol, 24-, 25- and 27-OHC and 24,25-EC in livers from control or NASH model diet mice.

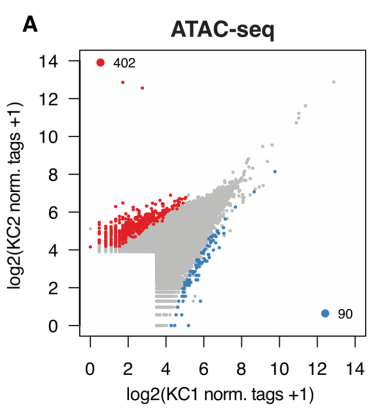

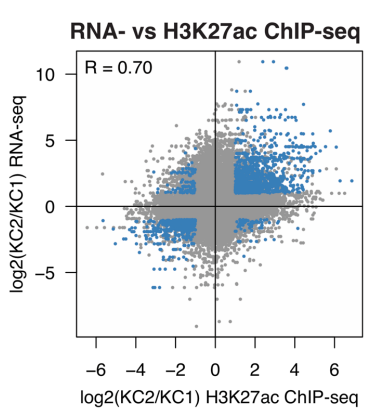

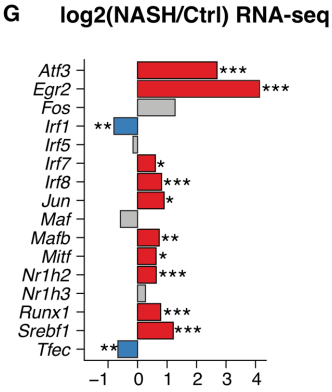

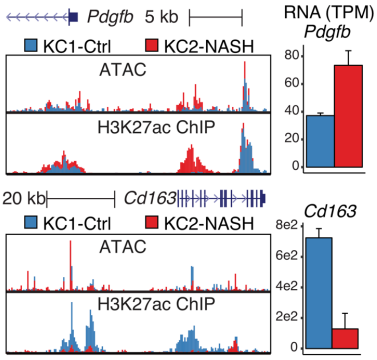

E

Gene Annotation Analysis of mRNAs Induced by NASH Diet

Pathway and Process Enrichment

Term	Log10(q)
Neutrophil degran.	-16.9
Cell adhesion	-16.9
Hemostasis (wound healing)	-13.0
Lipid localization	-10.6
Cytokine production	-10.6
HDL remodeling	-8.2
Reg. lipid met. process	-7.9
MAPK cascade	-6.4

Protein-protein Interaction Enrichment

Term	Log10(q)
Pos. reg. of apoptotic proc.	-8.0
Cell. resp. to toxic substance	-5.1

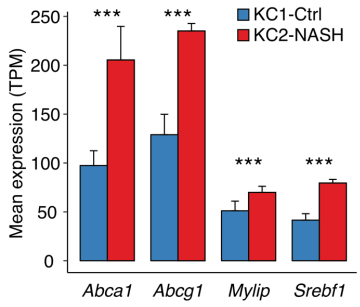

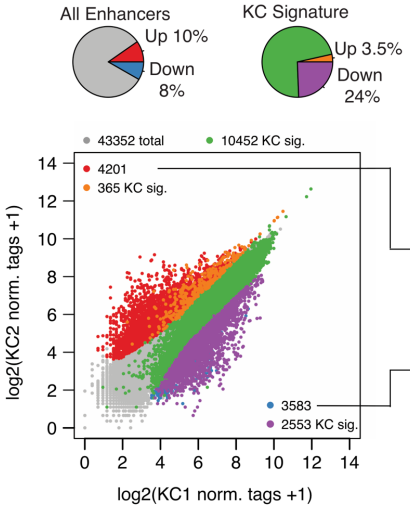

F

Differential Kupffer cell enhancers

Motif	P-value	%targ/ %bkgd	Best Match
	1e-137	35/19	AP1
	1e-25	0.7/.04	NFAT
	1e-20	11/7.3	RUNX
	1e-19	16/11	EGR
	1e-33	49/39	NR half-site
	1e-25	0.4/0.0	MITF
	1e-19	0.3/0.0	MAF
	1e-17	0.3/0.0	IRF
	1e-15	3.5/1.6	LXRE (known)

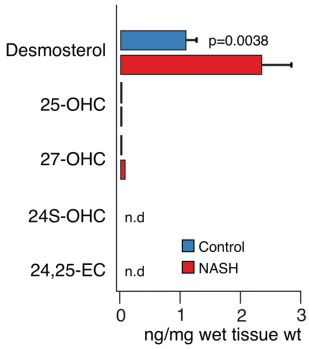

Figure 3.6: Genome wide occupancy of LXR binding in Kupffer cells during NASH

A. Ratio-ratio comparison of RNA-seq data of Kupffer cells from NASH mice versus controls (x-axis) compared to RNA-seq data of Kupffer cells from global LXRα/β DKO Kupffer cells versus controls (y-axis). DESeq2 identified gene expression differences (> 2-fold, p-adj < 0.05) are indicated in each quadrant and color coded as indicated. **Blue** points indicate genes differentially expressed due to NASH. **Red** points indicate genes differentially expressed due to LXRα/β DKO. **Purple** points indicate genes differentially expressed in both conditions. Pearson correlation = 0.69 for purple points; p < 2.2e-16 using "cor.test" in R.
B. Gene ontology of transcripts significantly upregulated (Fold change > 2, p-adj < 0.05, TPM > 4) by both NASH model diet and LXR DKO.
C. Heatmaps of $\log_2$ fold-change values comparing indicated population to the control Kupffer cell data set: NASH diet Tim4^{Pos} Kupffer cells (KC2), NASH diet Tim4^{Neg} Kupffer niche recruited macrophages (KN-RM), global LXR α/β DKO Kupffer cells, global LXR α KO Tim4^{Pos} and Tim4^{Neg} Kupffer cells, KC-specific LXR α KO (Clec4f-Cre Nr1h3-fl/fl) Tim4^{Pos} and Tim4^{Neg} Kupffer cells. Fold change values with p-adj > 0.05 are not considered significant and set to be colored white.
D. Scatterplot of H3K27ac ChIP-seq signal around distal (> 3kb from TSS) LXR ChIP-seq peaks in 2,000 bp window. Differentially acetylated regions were determined using DESeq2 (> 2-fold, p-adj < 0.05). Regions overlapping with Kupffer cell signature enhancers (**Figure 3.S5A**) are colored **green**. Enhancers with more activity during NASH are colored **red,** or **orange** if also a Kupffer cell signature enhancer. Enhancers with less activity during NASH are colored **blue,** or **purple** if also a Kupffer cell signature enhancer. Pie charts depict percentage of upregulated and downregulated total enhancers (left) or Kupffer cell signature enhancers (right).
E. Comparison of data intersection for LXR ChIP-seq peaks (>16 normalized tag counts in at least one condition) in KC1 (Healthy) and KC2 (NASH) Kupffer cells.
F. UCSC genome browser tracks for H3K27ac or LXR ChIP-seq under control (**blue**) or NASH (**red**) conditions for the indicated loci.

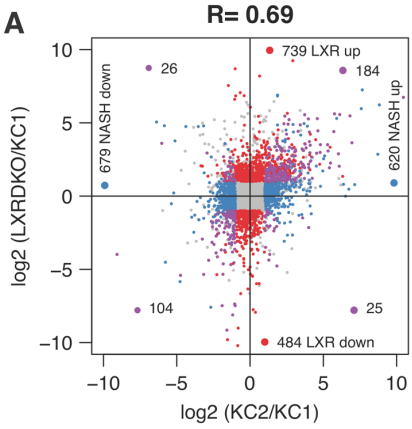

B

GO terms Up in KC2 and LXR DKO

Term	Log(q-val)
Reg. of cell adhesion	-11.8
Hemostasis	-9.7
Angiogenesis	-8.3
Inflammatory response	-7.1
Extracellular matrix org.	-5.8
Leukocyte migration	-5.7

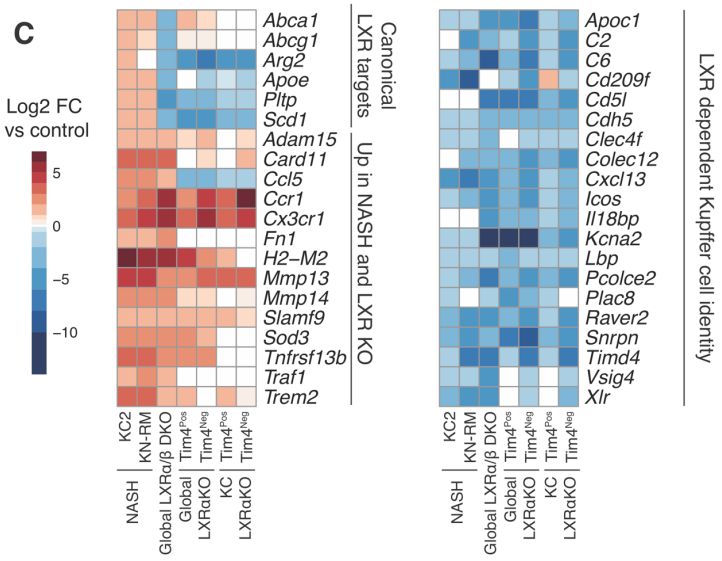

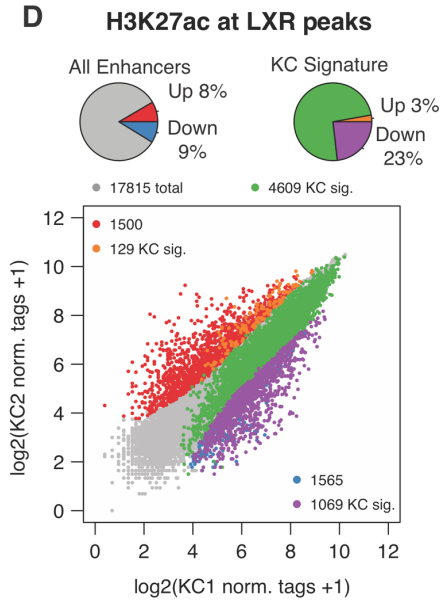

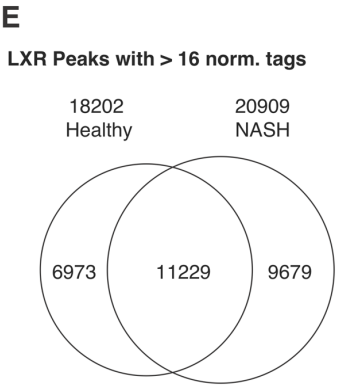

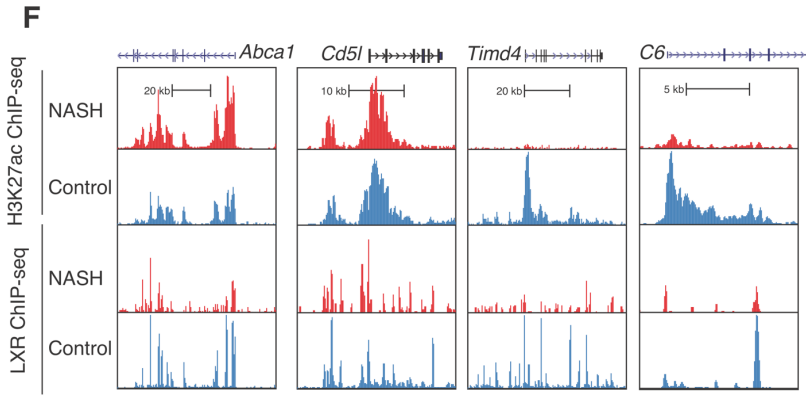

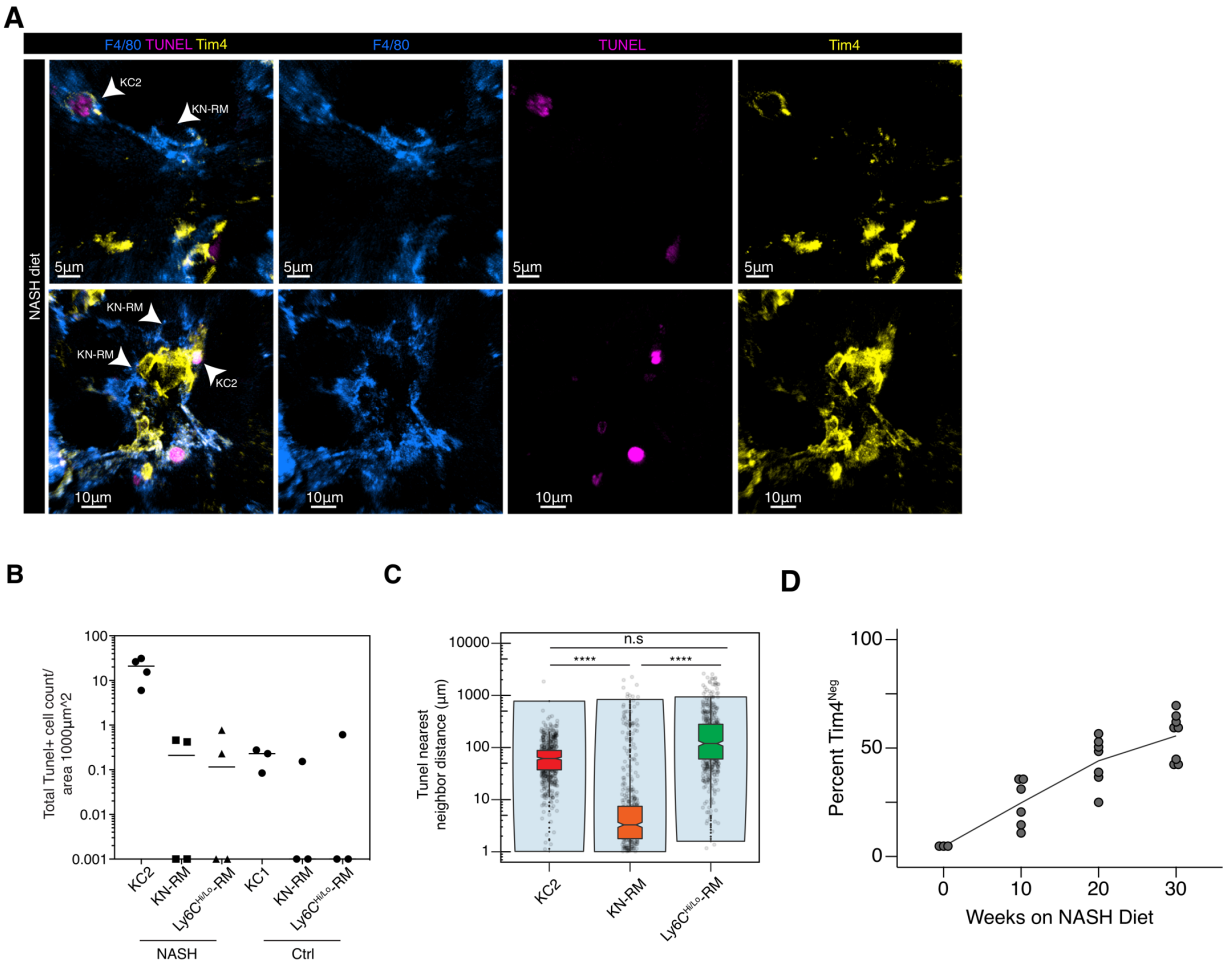

Figure 3.7: Apoptosis and replacement of embryonically derived KCs during NASH

A. Representative immunofluorescence (IF) image assessing *in situ* cell death via TUNEL staining in addition to Tim4, and F4/80 staining. Representative image from n=4 mice/condition; maximum intensity projection (MIP) of a 20-µm z-stack.
B. Quantification of total TUNEL^{Pos} hepatic macrophages per area (100 μm^2) in Ctrl and NASH mouse livers, n=3-4 mice/condition.
C. Nearest neighbor distance of all TUNEL^{Pos} cells to KN-RM, Ly6C$^{Hi/Lo}$-RM and KC2 cells in NASH livers, data pooled from n=4 mice. One-Way ANOVA with Tukey HSD test; p<0.0001(****), not significant (ns).
D. Temporal assessment of Tim4 expression by flow cytometry of CD11b^{Lo}F4/80^{Pos}CD146^{Neg} Kupffer cells from mice fed a NASH-inducing diet as indicated.

Figure 3.S1: Supplement to Figure 3.1

A. Weight gain (g) over 30 weeks of mice fed NASH model diet or healthy control diet.
B. Example hematoxylin and eosin or picrosirius red staining of liver sections from mice fed a healthy control diet (left) or NASH model diet for 30 weeks (right).
C. Representative FACS gates for purification of $CD45^{Pos}CD146^{Neg}$LiveSinglets from healthy or NASH model diet fed mice for single-cell RNA-seq experiments.
D. tSNE projections of identified graph-based cell clusters from 10X Genomics scRNA-seq data using cells purified as in **C** from healthy control mice, or from mice fed a model NASH diet for 30 weeks. Clusters are labeled based on interrogation of top marker genes (**Table 3.1**).
E. Heatmap of single cell RNA-seq gene normalized expression (unscaled) at genes of interest used to identify KC1, KC2, KN-RM, $Ly6C^{Lo}$-RM and $Ly6C^{Hi}$-RM. Data represent 100 cells per cluster.
F. Volcano plot of differentially expressed genes (> 1.5-fold change, p-adj < 0.05) between KC2 and KN-RM identified by Seurat's "FindAllMarkers" function. **Red** points indicate Kupffer cell-specific genes (38) with higher expression in KC2. **Orange** points indicate Kupffer cell specific genes with higher expression in KN-RM.

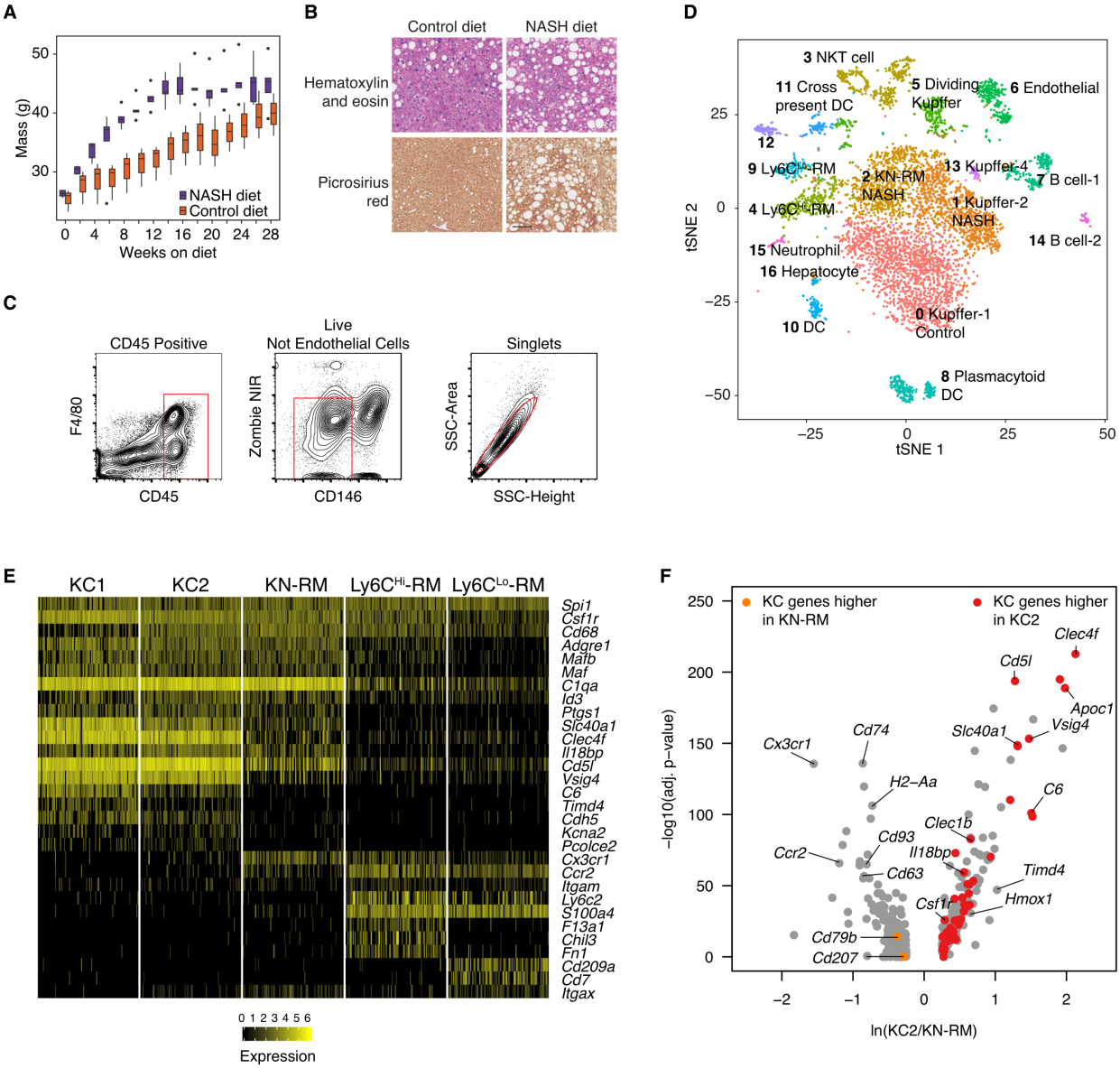
A
Mass (g)
Weeks on diet
NASH diet
Control diet
B
Control diet
NASH diet
Hematoxylin and eosin
Picrosirius red
C
CD45 Positive
F4/80
CD45
Live
Not Endothelial Cells
Zombie NIR
CD146
Singlets
SSC-Area
SSC-Height
D
3 NKT cell
11 Cross present DC
5 Dividing Kupffer
6 Endothelial
12
9 Ly6C^Lo-RM
2 KN-RM NASH
13 Kupffer-4
7 B cell-1
4 Ly6C^Hi-RM
1 Kupffer-2 NASH
14 B cell-2
15 Neutrophil
16 Hepatocyte
0 Kupffer-1 Control
10 DC
8 Plasmacytoid DC
tSNE 1
tSNE 2
E
KC1
KC2
KN-RM
Ly6C^Hi-RM
Ly6C^Lo-RM
Spi1
Csf1r
Cd68
Adgre1
Mafb
Maf
C1qa
Id3
Ptgs1
Slc40a1
Clec4f
Il18bp
Cd5l
Vsig4
C6
Timd4
Cdh5
Kcna2
Pcolce2
Cx3cr1
Ccr2
Itgam
Ly6c2
S100a4
F13a1
Chil3
Fn1
Cd209a
Cd7
Itgax
0 1 2 3 4 5 6
Expression
F
KC genes higher in KN-RM
KC genes higher in KC2
−log10(adj. p−value)
ln(KC2/KN-RM)
Clec4f
Cd5l
Apoc1
Vsig4
Slc40a1
Cd74
Cx3cr1
H2−Aa
C6
Clec1b
Cd93
Ccr2
Il18bp
Cd63
Timd4
Hmox1
Csf1r
Cd79b
Cd207

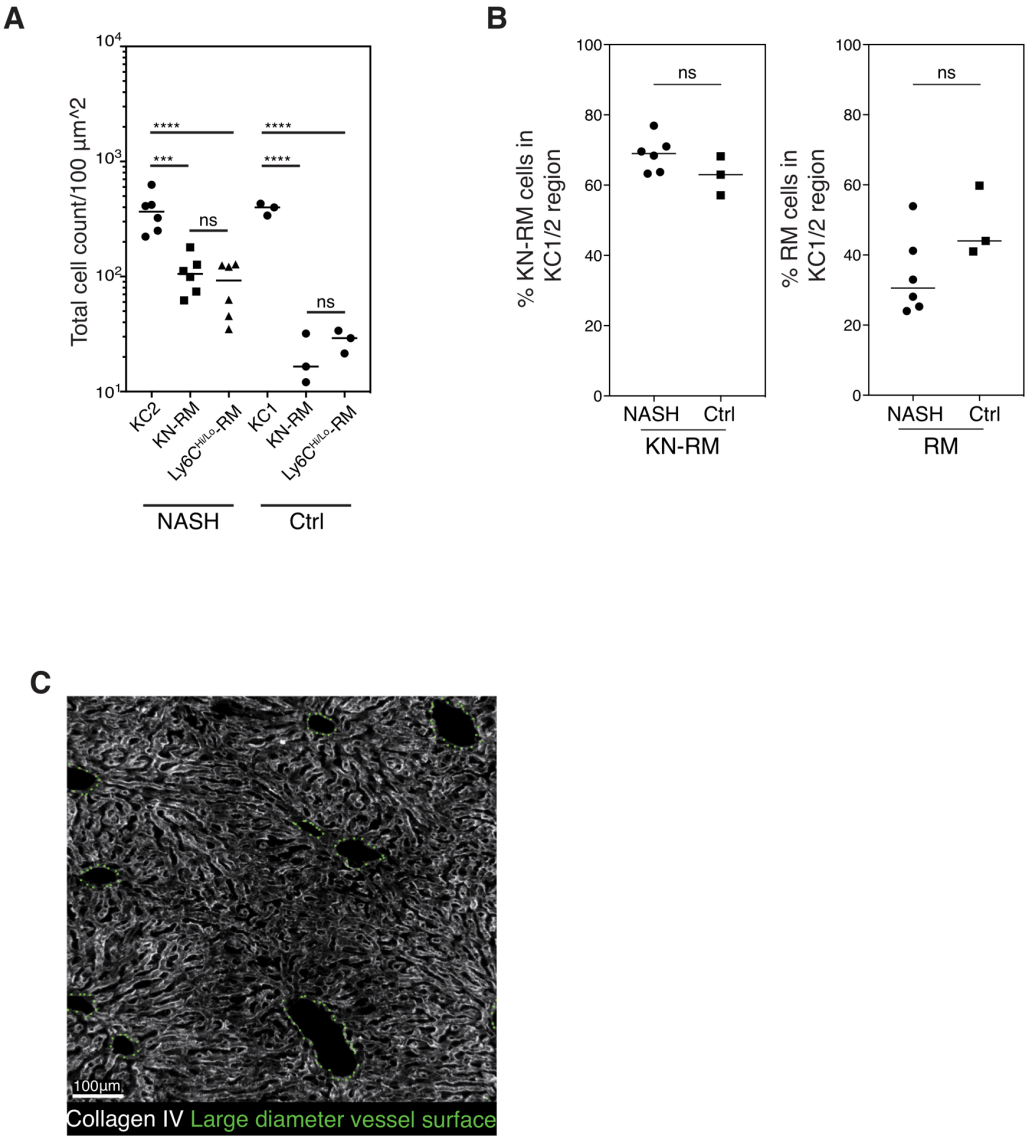

Figure 3.S2: Supplement to Figure 3.2

A. Quantification of immunofluorescence images. Total cell count per 100 μm^2 area for KC2, KN-RM, and Ly6C$^{Hi/Lo}$-RM cells in NASH and control livers. Note KC1/KC2 have the same surface markers, but KC1 corresponds to livers from animals fed a control diet while KC2 corresponds to livers from animals fed the NASH model diet. Two-way ANOVA with Bonferroni multiple comparison; $p<0.0001$(****), $p<0.001$(***), not significant (ns).

B. Percent of KN-RM or Ly6C$^{Hi/Lo}$-RM cells within the region of Tim4^{Pos} Kupffer cells in control (KC1) or NASH model diet fed (KC2) mice.

C. Representative IF image showing Collagen IV staining (lining the basement membrane of all blood vessels) and Imaris surface around portal and central vein vasculature (large diameter vessels, greater than 15-μm in diameter).

Figure 3.S3: Supplement to Figure 3.3

A. Scatterplot of RNA-seq data in NASH model diet peripheral blood Ly6C^{Hi} monocytes and NASH Tim4^{Neg} (KN-RM) Kupffer niche recruited macrophages. Differentially expressed genes identified by DESeq2 (>2-fold, p-adj < 0.05) are colored in red.
B. Scatterplot of RNA-seq data for KC1 and KN-RM. Differentially expressed genes identified by DESeq2 (> 2-fold, p-adj < 0.05) are colored in red.
C. Heatmap of selected Kupffer cell-specific genes (38) induced in macrophages from control and NASH livers versus NASH blood Ly6C^{Hi} monocytes (> 2-fold, p-adj < 0.05, TPM > 4). Genes labeled with "*" were not identified as Kupffer cell-specific genes (38) but were found to be specific to embryonically-derived Kupffer cells (42).
D. Heatmap of differentially expressed genes (> 2-fold, p-adj < 0.05, TPM > 4) similarly regulating when comparing control Kupffer cells versus day 14 RLMs and KC2 versus KN-RM. Genes labeled with "*" were found to be specific to embryonically-derived Kupffer cells (42).
E. Gene ontology of selected enriched terms from cluster 1 (KC1, KC2 and KN-RM-specific) and cluster 2 (Ly6C^{Hi}-RM Ly6C^{Lo}-RM specific) from **Figure 3.3A.**

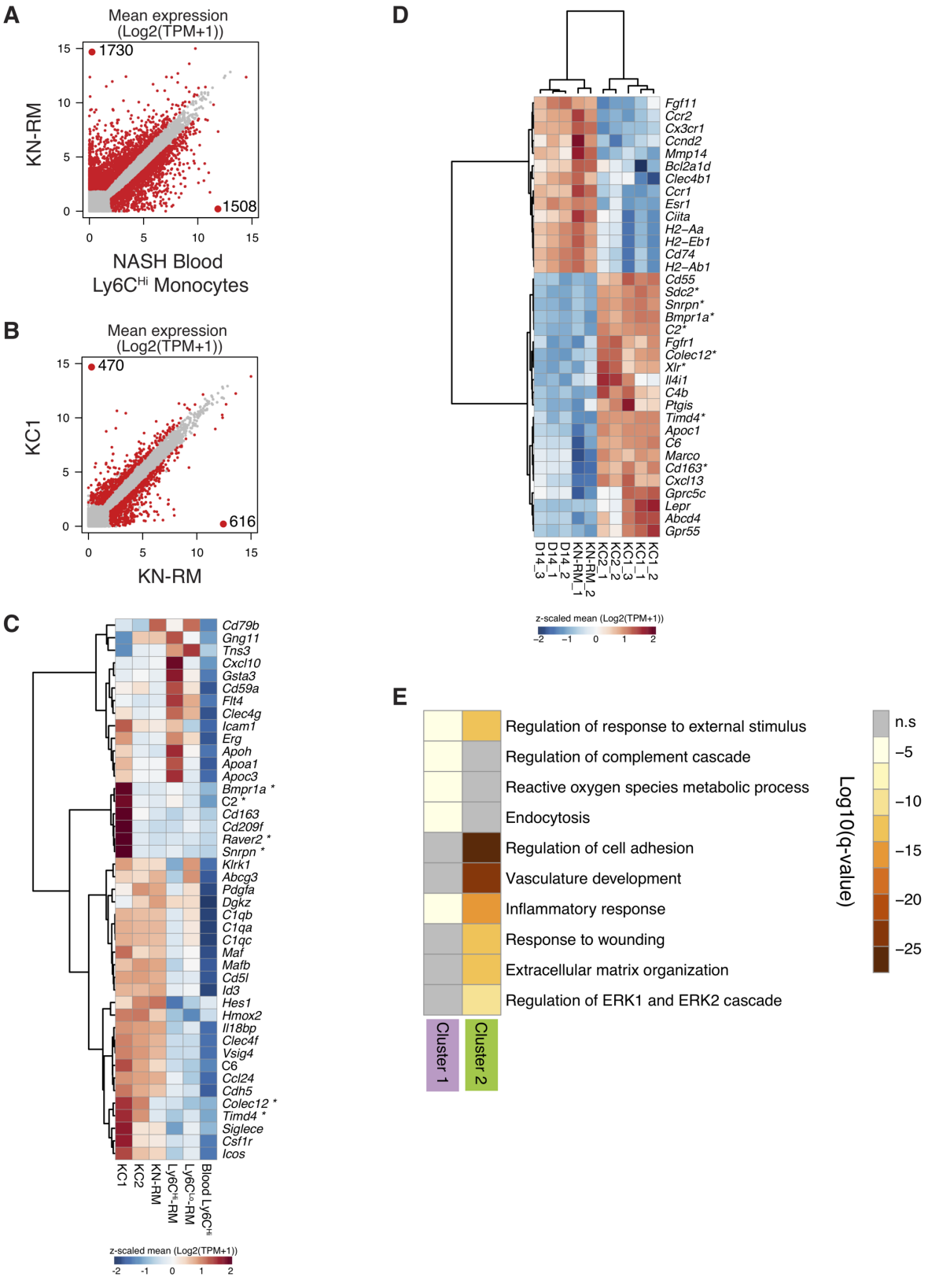
A
Mean expression
(Log2(TPM+1))
1730
1508
KN-RM
NASH Blood
Ly6C^Hi Monocytes
B
Mean expression
(Log2(TPM+1))
470
616
KC1
KN-RM
C
Cd79b
Gng11
Tns3
Cxcl10
Gsta3
Cd59a
Flt4
Clec4g
Icam1
Erg
Apoh
Apoa1
Apoc3
Bmpr1a *
C2 *
Cd163
Cd209f
Raver2 *
Snrpn *
Klrk1
Abcg3
Pdgfa
Dgkz
C1qb
C1qa
C1qc
Maf
Mafb
Cd5l
Id3
Hes1
Hmox2
Il18bp
Clec4f
Vsig4
C6
Ccl24
Cdh5
Colec12 *
Timd4 *
Siglece
Csf1r
Icos
KC1
KC2
KN-RM
Ly6C^Hi-RM
Ly6C^Lo-RM
Blood Ly6C^Hi
z-scaled mean (Log2(TPM+1))
D
Fgf11
Ccr2
Cx3cr1
Ccnd2
Mmp14
Bcl2a1d
Clec4b1
Ccr1
Esr1
Ciita
H2-Aa
H2-Eb1
Cd74
H2-Ab1
Cd55
Sdc2*
Snrpn*
Bmpr1a*
C2*
Fgfr1
Colec12*
Xlr*
Il4i1
C4b
Ptgis
Timd4*
Apoc1
C6
Marco
Cd163*
Cxcl13
Gprc5c
Lepr
Abcd4
Gpr55
KC1_2
KC1_1
KC1_3
KC2_2
KC2_1
KN-RM_2
KN-RM_1
D14_2
D14_1
D14_3
z-scaled mean (Log2(TPM+1))
E
Regulation of response to external stimulus
Regulation of complement cascade
Reactive oxygen species metabolic process
Endocytosis
Regulation of cell adhesion
Vasculature development
Inflammatory response
Response to wounding
Extracellular matrix organization
Regulation of ERK1 and ERK2 cascade
Cluster 1
Cluster 2
Log10(q-value)
n.s
−5
−10
−15
−20
−25

Figure 3.S4: Supplement to Figure 3.4

A. Heatmap of all ATAC-seq distal open chromatin regions (>3kb from TSS) differentially enriched (as in **3.4B** and **3.4C**) in any pairwise comparison between populations. Values are Z-scaled rLog normalized tag counts calculated using DESeq2.
B. *De novo* motifs enriched in distal open chromatin regions (>3kb from TSS) enriched in Ly6C^{Hi} peripheral blood monocytes compared to Tim4^{Neg} Kupffer niche recruited macrophages (KN-RM). The background for motif enrichment analysis is all distal open chromatin in KN-RM.
C. *De novo* motifs enriched in distal open chromatin regions (>3kb from TSS) enriched in Ly6C^{Hi} peripheral blood monocytes compared to Ly6C^{Lo}-RM. The background for motif enrichment analysis is all distal open chromatin in Ly6C^{Lo}-RM.
D. Bar plots of mean gene expression (TPM) +/- SD of RUNX family transcription factors important in myeloid populations during NASH.

A

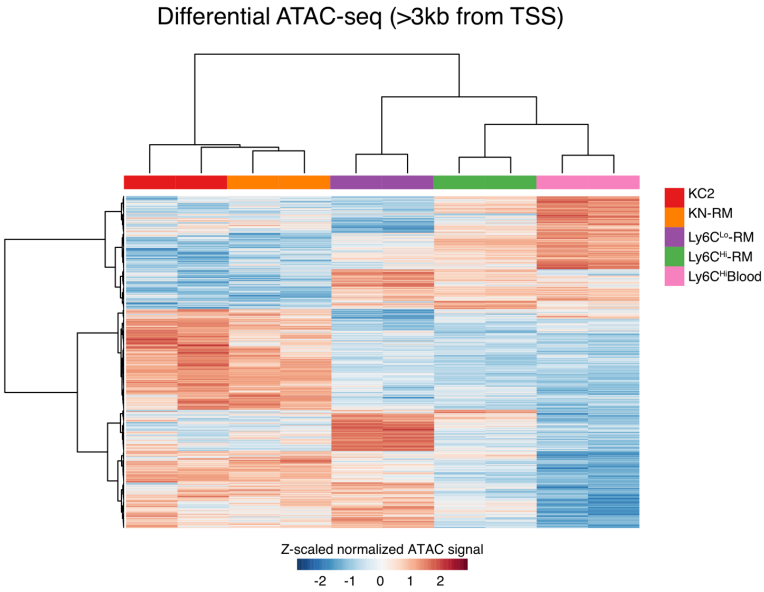

B

Motifs in Blood Ly6C^{Hi} Enhancers Lost During Transition to KN-RM vs KN-RM Enhancers

Motif	P-value	%targ/%bkgd	Best Match
	1e-119	25/8.8	KLF
	1e-41	35/23	CEBPA
	1e-29	15/8.4	CTCF
	1e-22	4.1/1.3	RUNX

C

Motifs in Blood Ly6C^{Hi} Enhancers Lost During Transition to Ly6C^{Lo}-RM vs Ly6C^{Lo}-RM Enhancers

Motif	P-value	%targ/%bkgd	Best Match
	1e-338	44/16	CEBPA
	1e-78	32/19	KLF
	1e-22	2.2/0.5	CEBP:AP1

D

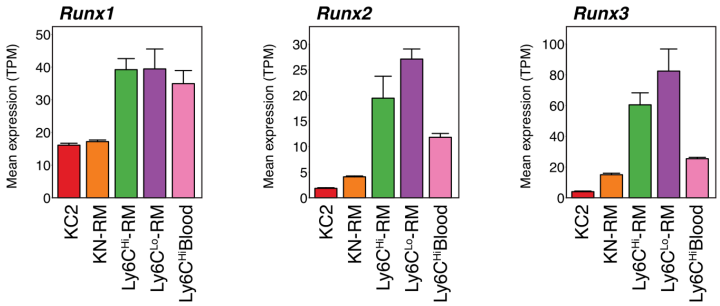

Figure 3.S5: Supplement to Figure 3.5

A. Heatmap showing clustering of enhancer regions (2kb window of H3K27ac centered at ATAC-seq peaks >3 kb from TSS) specific to microglia, Kupffer cells, bone marrow-derived macrophages, blood Ly6C^{Hi} monocytes, and large peritoneal macrophages. Regions displayed on the plot are enriched in at least 3 out of 4 comparisons with other macrophage populations (using DESeq2 on biological duplicates, > 2-fold, p-adj < 0.05).
B. Selected genes from GO terms in **3.5E**. Heatmap indicates whether or not each gene is a member of each category. The log2 fold change between NASH (KC2) and healthy control (KC1) Kupffer cells is depicted on the barplot, along with the expression level (mean TPM) of each gene during NASH. * = p-adj < 0.05; ** = p-adj < 0.01; and *** = p-adj < 0.001 using DESeq2.
C. Mean expression (TPM +/- SD) of transcription factors in **3.5G** in Kupffer cells from healthy (KC1) or NASH (KC2) livers. * = p-adj < 0.05; ** = p-adj < 0.01; and *** = p-adj < 0.001 using DESeq2.

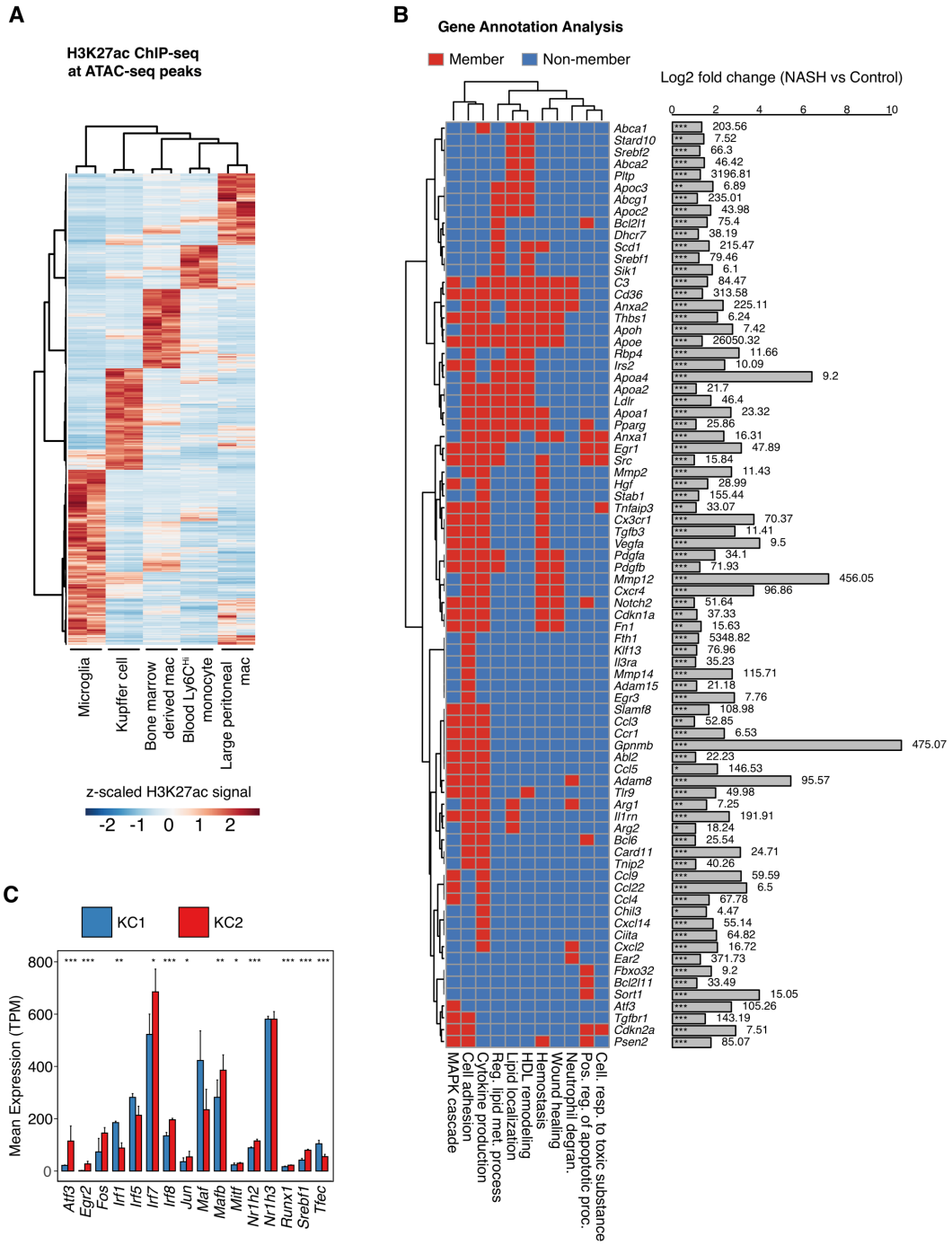
A
H3K27ac ChIP-seq
at ATAC-seq peaks
Microglia
Kupffer cell
Bone marrow derived mac
Blood Ly6C^{Hi} monocyte
Large peritoneal mac
z-scaled H3K27ac signal
-2 -1 0 1 2
B
Gene Annotation Analysis
Member
Non-member
Log2 fold change (NASH vs Control)
0 2 4 6 8 10
Abca1 *** 203.56
Stard10 ** 7.52
Srebf2 *** 66.3
Abca2 *** 46.42
Pltp *** 3196.81
Apoc3 ** 6.89
Abcg1 *** 235.01
Apoc2 *** 43.98
Bcl2l1 *** 75.4
Dhcr7 *** 38.19
Scd1 *** 215.47
Srebf1 *** 79.46
Sik1 *** 6.1
C3 *** 84.47
Cd36 *** 313.58
Anxa2 *** 225.11
Thbs1 *** 6.24
Apoh *** 7.42
Apoe *** 26050.32
Rbp4 *** 11.66
Irs2 *** 10.09
Apoa4 *** 9.2
Apoa2 *** 21.7
Ldlr *** 46.4
Apoa1 *** 23.32
Pparg *** 25.86
Anxa1 *** 16.31
Egr1 *** 47.89
Src *** 15.84
Mmp2 *** 11.43
Hgf *** 28.99
Stab1 *** 155.44
Tnfaip3 ** 33.07
Cx3cr1 *** 70.37
Tgfb3 *** 11.41
Vegfa *** 9.5
Pdgfa *** 34.1
Pdgfb *** 71.93
Mmp12 *** 456.05
Cxcr4 *** 96.86
Notch2 *** 51.64
Cdkn1a ** 37.33
Fn1 ** 15.63
Fth1 *** 5348.82
Klf13 *** 76.96
Il3ra *** 35.23
Mmp14 *** 115.71
Adam15 *** 21.18
Egr3 *** 7.76
Slamf8 *** 108.98
Ccl3 ** 52.85
Ccr1 *** 6.53
Gpnmb *** 475.07
Abl2 *** 22.23
Ccl5 * 146.53
Adam8 *** 95.57
Tlr9 *** 49.98
Arg1 ** 7.25
Il1rn *** 191.91
Arg2 * 18.24
Bcl6 *** 25.54
Card11 *** 24.71
Tnip2 *** 40.26
Ccl9 *** 59.59
Ccl22 *** 6.5
Ccl4 *** 67.78
Chil3 * 4.47
Cxcl14 *** 55.14
Ciita *** 64.82
Cxcl2 *** 16.72
Ear2 *** 371.73
Fbxo32 *** 9.2
Bcl2l11 *** 33.49
Sort1 *** 15.05
Atf3 *** 105.26
Tgfbr1 *** 143.19
Cdkn2a *** 7.51
Psen2 *** 85.07
MAPK cascade
Cell adhesion
Cytokine production
Reg. lipid met. process
Lipid localization
HDL remodeling
Hemostasis
Wound healing
Neutrophil degran.
Pos. reg. of apoptotic proc.
Cell. resp. to toxic substance
C
KC1
KC2
Mean Expression (TPM)
0 200 400 600 800
*** *** ** * *** * ** * *** *** *** ***
Atf3 Egr2 Fos Irf1 Irf5 Irf7 Irf8 Jun Maf Mafb Mitf Nr1h2 Nr1h3 Runx1 Srebf1 Tfec

Figure 3.S6: Supplement to Figure 3.6

A. Ratio-ratio plot of H3K27ac ChIP-seq signal from Kupffer cells from NASH mice versus controls (x-axis) compared with data resulting from Kupffer cells from global LXRα KO Kupffer cells versus controls (y-axis). DESeq2 identified changes in H3K27ac signal (2kb window centered at ATAC-seq peaks > 3kb from TSS, > 2-fold, p-adj < 0.05) are indicated in each quadrant and color coded as indicated. **Blue** indicates regions differentially enriched due to NASH. **Red** indicates regions differentially enriched due to LXRα KO. **Purple** indicates regions differentially enriched in both conditions. Pearson correlation = 0.74 for purple points; p < 2.2e-16 using "cor.test" in R. **Black** indicates regions differentially enriched in both conditions that intersect with Kupffer cell signature enhancers **(Figure 3.S5A**).
B. Representative initial FACS gate for sorting of tdTomato-positive nuclei from Clec4f-Cre-tdTomato mice for LXR ChIP-seq experiments.
C. Scatterplot of LXR ChIP-seq signal at all peaks with > 16 tags (normalized to 1e7) in at least one condition in Kupffer cells from healthy mice and Tim4^{Pos} Kupffer cells from mice on NASH model diet. Differentially bound peaks are identified using HOMER's "getDifferentialPeaks" function (Fold change > 4, Poisson p-value < 1e-4) and are colored in **red** if increased during NASH and **blue** if decreased during NASH.
D. *De novo* motif enrichment using repeat masked mm10 genome of differentially bound LXR ChIP-seq peaks from **C** using upregulated or downregulated peaks set as foreground and the other as background.
E. Scatterplot of LXR ChIP-seq signal as in **C**, showing only distal (> 3,000 bp from TSS) LXR ChIP-seq peaks. Differentially bound peaks were determined as in **C**. Peaks overlapping with Kupffer cell signature enhancers (**Figure 3.S5A**) are denoted in **green**. Peaks are denoted in **red** if increased during NASH and **blue** if decreased during NASH. Peaks colored in **orange** are gained during NASH and lie within Kupffer cell signature enhancers, while peaks colored in **purple** are lost during NASH and lie within Kupffer cell signature enhancers. Pie charts depict percentage of peaks with increased binding at all distal LXR peaks (top) or within Kupffer cell signature enhancer regions (bottom).
F. Distribution of LXR ChIP-seq tag densities in at LXR peaks located in all enhancers (> 3 kb from TSS) or within Kupffer cell signature enhancers (**Figure 3.S5A)** in healthy or control Kupffer cells.

A

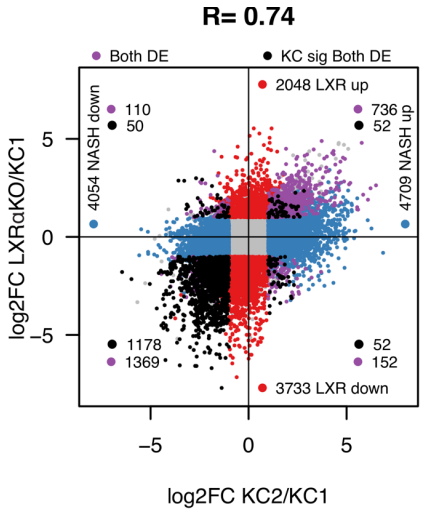

B

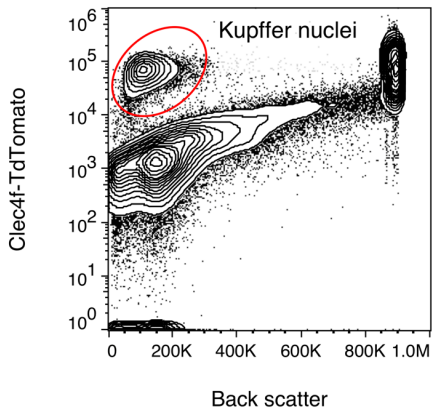

C

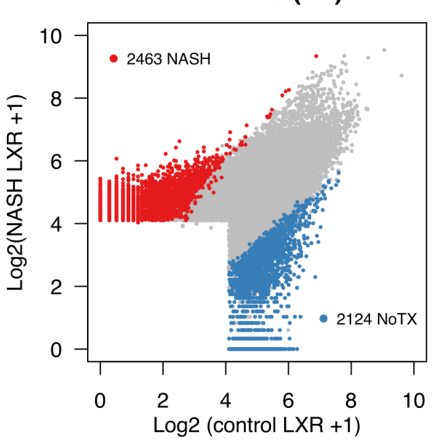

D

Enriched in LXR Peaks Gained During NASH versus Lost

Motif	P-value	%targ/ %bkgd	Best Match
	1e-53	2.3/.09	RUNX (GFY?)
	1e-51	2.3/.11	MADS/SRF
	1e-39	1.8/0.1	CTCF
	1e-17	9.5/4.8	ZEB1 (known)

Enriched in LXR Peaks Lost During NASH versus Gained

Motif	P-value	%targ/ %bkgd	Best Match
	1e-108	47/24	NR Half-Site
	1e-101	48/24	PU.1
	1e-70	2.9/.09	IRF
	1e-46	2.1/.08	SMAD
	1e-30	14/6.6	CEBPE
	1e-29	3.8/.67	LXRE (Known)

E

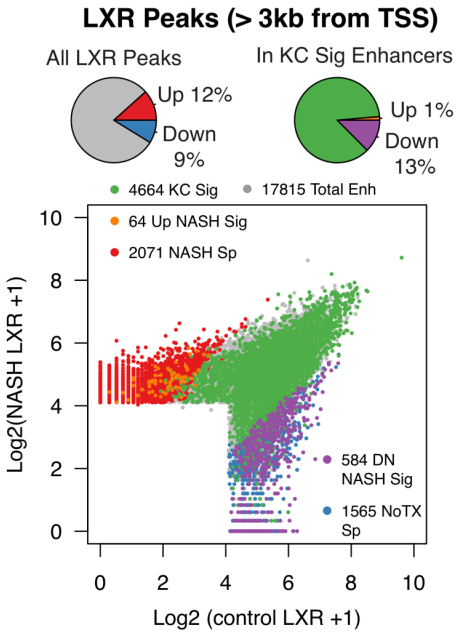

F

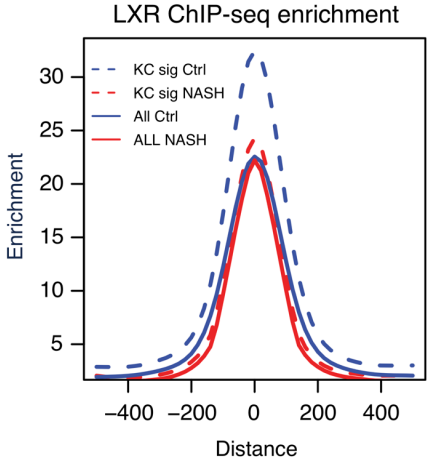

Table 3.1 Cluster identities for scRNA-seq

Cluster identities identified by single cell RNA-seq, along with cell type abundance, % representation in the data set, and marker genes for each cluster.

Identity	Cluster	#Ctrl	#NASH	% total data set	Cluster identity genes
KC1-Control	0	1667	31	27.5%	*Cd163, Marco, C6, Hmox1, Fcna, Slc40a1, Sdc3, C4b, Timd4, Tnfaip2, Mrc1, Ptprj, Adgre4, Itgal, BC005537, Vcam1, Cd44, Cxcl13, Paqr9, Atp1b3*
KC2-NASH	1	74	976	17.0%	*Folr2, Cd5l, Ear2, Apoc1, Clec1b, C1qb, Ctsd, Fabp7, Il18bp, Pltp, Aif1, Apoe, Wfdc17, Igf1, Trem2, Clec4n, Lpl, Clec4f, Mmp12, Ccl24*
KN-RM-NASH	2	70	804	14.1%	*Cx3cr1, Ms4a7, Trem2, Cd63, Apoe, H2-Eb1, Cd74, H2-Ab1, H2-Aa, Gpnmb, Hexb, Cd9, Clec4b1, Bcl2a1b, H2-M2, Cxcl14, Pf4, Mmp12, Fabp5, Cd207*
NK/NKT	3	88	313	6.5%	*Nkg7, Ms4a4b, Xcl1, Cd3g, Cd3d, Ctsw, Thy1, Gimap3, Lck, Lat, Skap1, Ltb, Klre1, Klrb1c, Gimap4, Ptprcap, Ccl5, Bcl2, Tmsb10, Cd7*
Ly6CHi-RM	4	23	346	6.0%	*Chil3, Fn1, S100a4, Hp, F13a1, Gm9733, F10, Emb, Ccr2, S100a6, Mcemp1, Sirpb1c, Ms4a4c, Lyz2, Ly6c2, Coro1a, Ms4a6b, Ccl9, Ifitm6, Plac8*
Proliferating KC	5	127	180	5.0%	*Stmn1, Top2a, Ube2c, Birc5, 2810417H13Rik, Ccnb2, Mki67, Cdca3, Lockd, Cdk1, Smc2, Cenpa, Cks2, Cks1b, Hmgb2, H2afx, Hist1h2ap, Smc4, Tubb5, Tuba1b*
LSEC	6	185	118	4.9%	*Igfbp7, Aqp1, Ptprb, Gpihbp1, Clec4g, Kdr, Ehd3, Eng, Egfl7, Adgrf5, Timp3, Bgn, Bmp2, Il6st, Tinagl1, Sdpr, Fabp4, Rspo3, Fcgr2b, Dnase1l3*
B cell	7	108	140	4.0%	*Cd79a, Ms4a1, Ebf1, Fcmr, Cd19, Cd79b, Mzb1, Ly6d, Siglecg, H2-DMb2, H2-Ob, Ltb, Cd2, Gm43603, Ralgps2, Ptprcap, Cd37, Napsa, Cd24a, Foxp1*
PDC-Control	8	246	0	4.0%	*Siglech, Cox6a2, Ly6d, Klk1, Cd209d, Cd300c, Smim5, Ccr9, D13Ertd608e, Atp1b1, Klk1b27, Sell, Ly6c2, Rpgrip1, Rnase6, Dnajc7, Tcf4, Lgals1, Bst2, Irf8*
Ly6CLo-RM	9	9	136	2.3%	*Cd209a, Klrd1, S100a4, Flt3, Cbfa2t3, Napsa, S100a6, Lsp1, Cd7, Tppp3, S100a11, Vim, Gm2a, Crip1, H2-Oa, Coro1a, Fxyd5, S100a10, Lgals1, Tagln2*
PDC-NASH	10	23	116	2.2%	*Siglech, Ccr9, Atp1b1, Cd300c, Cox6a2, Upb1, Pacsin1, Smim5, Klk1, Sell, Ly6d, Cd209d, Ly6c2, Rnase6, Tsc22d1, Irf8, Dnajc7, Bst2, Lgals1, Plac8*
DC-1	11	21	94	1.9%	*Xcr1, Cd24a, Ifi205, Flt3, Tnni2, Amica1, Naaa, Septin5, H2-Oa, Wdfy4, Cxx1a, Ppt1, Cst3, Plbd1, Tmsb10, Irf8, Lsp1, H2-Aa, H2-Ab1, Gm2a*
DC-2	12	4	98	1.6%	*Fscn1, Ccr7, Ccl22, Tbc1d4, Il12b, Il4i1, Traf1, Eno3, Zmynd15, Serpinb6b, Gadd45b, Relb, Rogdi, Tspan3, Ccl5, Bcl2a1d, Tmem123, Gyg, Fabp5, Epsti1*
KC3-Control	13	54	1	0.9%	*Cxcl13, Wfdc17, Marco, Ifitm2, Gm10116, Vsig4, Apoc1, Timd4, Fabp7, Cfp, Folr2, Ccl6, Aif1, AW112010, Blvrb, Clec1b, Fcgr4, Ninj1, Cd302, Ctla2b*
B cell	14	29	25	0.9%	*Derl3, Fkbp11, Eaf2, Tnfrsf17, Pou2af1, Gm43291, Mzb1, Jchain, Creld2, Txndc5, Pdia4, Edem1, Slpi, Xbp1, Sec11c, H13, Sdf2l1, Ssr4, Manf, Hsp90b1*
Neutrophil	15	16	32	0.8%	*Retnlg, Lcn2, Mmp9, Hdc, Wfdc21, S100a9, Pglyrp1, Lrg1, S100a8, Mmp8, Mcemp1, Gda, Camp, Ngp, Hp, Slpi, Chil3, S100a11, Anxa1, Ifitm6*
Hepatocyte	16	13	17	0.5%	*Ambp, Clu, Serpina1c, Ttr, Serpina1a, Serpina1e, Mup7, Rbp4, Serpina1b, Alb, Bhmt, Mup11, Apoc3, Spp1, Serpina3k, Mup3, Fabp1, Mup20, Apoa1, Apoa2*

E. Methods

Microscopy and Histo-Cytometry

Livers were perfused with 2% PFA and fixed using 0.5% BD fix/perm buffer for 12 hours, dehydrated in 30% sucrose, and subsequently embedded in OCT freezing media (Sakura Finetek). 20 µm sections were made with a Leica cryostat and blocked with a blocking buffer containing 1% Fc-Block (anti-CD16/32), 1% BSA, and 0.3% Triton X-100 for 3 hours. Sections were stained with directly conjugated antibodies or appropriate primary and secondary antibodies for 5 hours at room temperature or overnight at 4 °C, in a humidified chamber. The following antibodies were used for staining: anti-F4/80 (BM8), anti-Collagen IV (Rabbit), anti-Tim4, anti-CD138. The following secondaries were used: goat anti-rabbit (Invitrogen). Sections were mounted with Flouromount G (Southern Biotech, Cat# 0100-01) and images were acquired on a Leica SP8 confocal microscope (40x objective), and subsequent analysis performed using Imaris software (Bitplane), and R-studio (spatstat package used for nearest neighbor analyses) (172). Histo-cytometry analysis was performed as previously described (163). In short, surfaces were created for F4/80 and tdTomato^{Pos} cells and mean fluorescence intensity (MFI) for all channels were obtained using Imaris. Objects were then exported into FlowJo 10.3 (TreeStar Inc.) and later analyzed with Prism (Graphpad). For detection of *in situ* cell death (TUNEL staining), staining was performed using the supplier's protocol (Sigma-Roche). In brief, the tissue was blocked and stained with primary and secondary antibodies (as outlined above). Cells were

permeabilized with 0.1% Triton for 20 min at 4C. Tissue sections then were washed gently three times with PBS (5min each) and dried briefly. The enzyme-probe buffer solution was then added for 1hr at 37C in dark. The tissue was subsequently washed gently three times with PBS (5min each) and mounted, then imaged.

Nuclei Sorting

Mice were humanely euthanized by exposure to CO_2, then briefly perfused with HBSS without Ca^{++} or Mg^{++} supplemented with 0.5mM EGTA, 0.5mM EDTA, and 20mM HEPES. Perfusions were then switched sequentially to 1 mg/ml disuccinimidyl glutarate in PBS for 30 minutes, then 1% formaldehyde in PBS for 10 minutes. Finally, the fixation was quenched by perfusion with 20 ml 0.125M glycine. Livers were excised, finely minced with a razor, and washed twice with 20 ml ice cold NF1 buffer (10mM Tris pH 8.0, 5mM $MgCl_2$, 0.1M sucrose, 0.5% Triton X-100) followed by centrifugation 1,200 XG for 7 minutes at 4C. Liver pellets were next suspended in NF1 buffer and homogenized using the “loose” pestle of a Dounce homogenizer for 10 strokes, followed by incubation on ice for 30 minutes. Samples were finally homogenized using the “tight” pestle of a Dounce homogenizer for an additional 50-70 strokes, with periodic assessment for released nuclei by microscopy. The homogenized liver was then strained through a 70-micron mesh strainer, centrifuged at 1,200 XG for 7 minutes at 4C, then washed once more in PBS. Finally, the homogenized liver was suspended in PBS with 2mM EDTA and passed through a 40-micron mesh strainer. Nuclei were purified by FACS using a Sony SH800 based on TdTomato expression and forward

scatter. Acquired nuclei were snap frozen in a dry ice ethanol bath and stored at -80C prior to use in ChIP-seq experiments.

Cell Sorting and Flow Cytometry

Mice were humanely euthanized by exposure to CO_2 and liver non-parenchymal cells processed for fluorescence activated cell sorting of Kupffer cells, with modifications from published methodology (55, 107, 173). In brief, livers were retrograde perfused for 3 min at a rate of 5-7 ml/min through the inferior vena cava with HBSS without Ca^{++} or Mg^{++} supplemented with 0.5 mM EGTA, 0.5 mM EDTA, and 20 mM HEPES. Perfusions were then switched to 40 ml of a digestion buffer, held at 37C, comprised of HBSS with Ca^{++} and Mg^{++} supplemented with 0.033 mg/ml of Liberase TM (Roche), 20 μg/ml DNaseI (Worthington), and 20 mM HEPES. Livers were then excised, minced, and digested for an additional 20 minutes in vitro at 37C with gentle rotation in 20 ml of fresh digestion buffer. The perfusion and digestion steps were performed in the presence of 1 μM flavopiridol to offset transcriptional changes associated with digestion. After tissue digestion, cells were passed through a 70-micron cell strainer and hepatocytes removed by 2 low-speed centrifugation steps at 50 X G for 2 min. Non-parenchymal cells in the supernatant were further separated from debris by pelleting for 15 min at 600 X G in 50 ml of 20% isotonic Percoll (Sigma Aldrich) at room temperature. Cells were then washed from Percoll containing buffer and suspended in 10 ml 28% OptiPrep (Sigma Aldrich) and carefully underlaid beneath 3 ml of wash buffer. The resulting gradient was centrifuged at 1,400 X G for 25 minutes at 4C with no break and cells enriched at the

interface were saved and subjected to isotonic erythrocyte lysis. Enriched non-parenchymal cells were then washed, suspended in PBS, then stained for 10 minutes with Zombie NIR (BioLegend) and purified anti-CD16/32 (93, BioLegend) to label dead cells and block Fc receptors. Cells were then immunolabeled with specific antibodies of interest, washed, and sorted using a Beckman Coulter MoFlo Astrios EQ configured with spatially separated 355 nm, 405 nm, 488 nm, 561 nm, and 642 nm lasers.

NASH-Model Diet

Mice are fed for up to 30 weeks with a NASH-model diet (Research Diets, D09100301) composed of 40 kcal% fat from vegetable shortening, 20 kcal% from fructose, and 2% cholesterol by mass, or a custom defined control diet (Research Diet, D15100601) composed of 10% kcal from fat with 50 g inulin (a dietary fiber) per 4,057 kcal.

Single-Cell RNA-Seq

Liver Liver non-parenchymal cells were isolated as above and sorted using FACS on the basis of $CD45^{Pos}$, $CD146^{Neg}$ (to exclude endothelial cells) and viability (negative for the live/dead dye Zombie NIR). The resulting purified cell preparations were washed twice with PBS and suspended in PBS supplemented with 400 μg/ml non-acetylated bovine serum albumin (Sigma Aldrich, B6917). Individual cells were then coupled to beads using the 10X Genomics Chromium controller. Single-cell sequencing libraries were prepared following the 10X Genomics Protocol using v2 chemistry and

sequenced to a median depth of approximately 50,000 reads per cell using an Illumina HiSeq 2500 on rapid run. Data was mapped using Cell Ranger (10X Genomics) to mm10 and analyzed using the Seurat R toolkit for single cell genomics (174).

ATAC-Seq

Approximately 50,000 sorted cells were washed once with PBS and once with 10mM Tris pH 7.4, 10 mM NaCl, 3 mM MgCl2, and 0.1% Igepal by centrifugation at 500 X G at 4C. Cells were then suspended in 50 μl reaction buffer comprised of 25 μl Tagment DNA buffer, 2.5 μl Tagment DNA enzyme, and 22.5 μl nuclease free water, using reagents sourced from Illumina Nextera DNA Library Prep Kit (128). Transposase reactions were carried out at 37C for 30 minutes and immediately DNA was purified using Zymo ChIP Clean & Concentrate columns. Resulting DNA was PCR amplified for 14 cycles using barcoding primers and resulting libraries were size selected by gel excision to 175-225 bp as described in (175). Library DNA was purified, and single end sequenced using a HiSeq 4000 or a NextSeq 500.

Poly A RNA-Seq

Performed as published previously (89, 176)**.** Isolated cells were pelleted and put into 150 µl lysis/Oligo d(T) Magnetic Beads binding buffer and stored at -80°C until processing. mRNAs were enriched by incubation with Oligo d(T) Magnetic Beads (NEB, S1419S) and then fragmented/eluted by incubation at 94°C for 9 min. Poly A enriched mRNA was fragmented, in 2x Superscript III first-strand buffer with 10mM DTT

(Invitrogen), by incubation at 94°C for 9 minutes, then immediately chilled on ice before the next step. The 10 μL of fragmented mRNA, 0.5 μL of Random primer (Invitrogen), 0.5 μL of Oligo dT primer (Invitrogen), 0.5 μL of SUPERase-In (Ambion), 1 μL of dNTPs (10 mM) and 1 μL of DTT (10 mM) were heated at 50°C for three minutes. At the end of incubation, 5.8 μL of water, 1 μL of DTT (100 mM), 0.1 μL Actinomycin D (2 μg/μL), 0.2 μL of 1% Tween-20 (Sigma) and 0.2 μL of Superscript III (Invitrogen) were added and incubated in a PCR machine using the following conditions: 25°C for 10 minutes, 50°C for 50 minutes, and a 4°C hold. The product was then purified with RNAClean XP beads according to manufacturer's instruction and eluted with 10 μL nuclease-free water. The RNA/cDNA double-stranded hybrid was then added to 1.5 μL of Blue Buffer (Enzymatics), 1.1 μL of dUTP mix (10 mM dATP, dCTP, dGTP and 20 mM dUTP), 0.2 μL of RNAse H (5 U/μL), 1.05 μL of water, 1 μL of DNA polymerase I (Enzymatics) and 0.15 μL of 1% Tween-20. The mixture was incubated at 16°C for 1 hour. The resulting dUTP-marked dsDNA was purified using 28 μL of Sera-Mag Speedbeads (Thermo Fisher Scientific), diluted with 20% PEG8000, 2.5M NaCl to final of 13% PEG, eluted with 40 μL EB buffer (10 mM Tris-Cl, pH 8.5) and frozen at -80°C. The purified dsDNA (40 μL) underwent end repair by blunting, A-tailing and adapter ligation as previously described (16) using barcoded adapters (NextFlex, Bioo Scientific). Libraries were PCR-amplified for 9-14 cycles, size selected by gel extraction, quantified using a Qubit dsDNA HS Assay Kit (Thermo Fisher Scientific) and sequenced on a Hi-seq 4000 or a NextSeq 500 (Illumina, San Diego, CA) according to the manufacturer's instructions.

Chromatin Immunoprecipitation

ChIP for H3K27ac was performed essentially as describe previously (177). In brief, FACS purified cells were fixed with 1% paraformaldehyde for 10 minutes at room temperature. Next, 2.625 M glycine was added to 125 mM to quench fixation and cells were collected by centrifugation with the addition of 0.01% Tween-20 at 1,200 X G for 10 minutes at 4C. Cells were washed once with 0.01 % Tween-20 in PBS and collected by centrifugation at 1,200 X G for 10 minutes at 4C. Cell pellets were then snap frozen and stored at -80C. For ChIP reactions, cell pellets were thawed on ice and lysed in 80 μl LB3 (10 mM Tris/HCl pH 7.5, 100 mM NaCl, 1 mM EDTA, 0.5mM EGTA, 0.1% deoxcycholate, 0.5% sarkosyl, 1 × protease inhibitor cocktail, and 1 mM sodium butyrate). Lysate was sonicated using a Covaris for 12 cycles with the following setting: time, 60 seconds; duty, 5.0; PIP, 140; cycles, 200; amplitude, 0.0; velocity, 0.0; dwell, 0.0. Samples were collected and 10% Triton X-100 was added to 1% final concentration. One percent of the sonicated lysate was saved as a ChIP input. For each chromatin immunoprecipitation, aliquots of ~500,000 cells were added to 20 μl Dynabeads Protein A with 2 μg anti-H3K27ac (Active Motif) and incubated with slow rotation at 4C overnight. The following day, beads were collected using a magnet and washed three times each with wash buffer I (20 mM Tris/HCl pH 7.5, 150 mM NaCl, 1% Triton X-100, 0.1% SDS, 2 mM EDTA, and 1 × protease inhibitor cocktail) and wash buffer III (10 mM Tris/HCl pH 7.5, 250 mM LiCl, 1% Triton X-100, 0.7% Deoxycholate, 1 mM EDTA, and 1 × protease inhibitor cocktail). Beads were then washed twice with ice cold 10 mM Tris/HCl pH 7.5, 1 mM EDTA, 0.2% Tween-20. Sequencing libraries were

prepared for ChIP products while bound to the Dynabeads Protein A initially suspended in 25 μl 10 mM Tris/HCl pH 8.0 and 0.05% Tween-20.

For LXR ChIP-seq, FACS purified Kupffer cell nuclei were resuspended in wash buffer (10mM HEPES/KOH pH7.9, 85mM KCl, 1mM EDTA, 0.2% IGEPAL CA-630, 1x protease inhibitor cocktail (Sigma), 1 mM PMSF) for 5 minutes on ice. Nuclei were spun down and resuspended in 130 μl RIPA-NR1 lysis buffer (20 mM Tris/HCl pH7.5, 1 mM EDTA, 0.5 mM EGTA, 0.1% SDS, 0.4% Na-Deoxycholate, 1% NP-40 alternative, 0.5 mM DTT, 1x protease inhibitor cocktail (Sigma), 1 mM PMSF) and chromatin was sheared by sonication. Samples were sonicated in a 96 Place microTUBE Rack (Covaris cat#500282) using a Covaris E220 for 18 cycles with the following setting: time, 60 seconds; duty, 5.0; PIP, 140; cycles, 200; amplitude, 0.0; velocity, 0.0; dwell, 0.0. Samples were recovered and spun down at max speed, 4°C for 10 minutes. 1% supernatant was taken as input DNA and remaining supernatant was transferred to PCR strips and brought up to a volume of 200 μl using RIPA-NR1 lysis buffer (20 mM Tris/HCl pH7.5, 1 mM EDTA, 0.5 mM EGTA, 0.1% SDS, 0.4% Na-Deoxycholate, 1% NP-40 alternative, 0.5 mM DTT, 1x protease inhibitor cocktail (Sigma), 1 mM PMSF). 30 μl Dynabeads Protein A/G coated with 2 μg each of the indicated LXR specific antibodies (Santa Cruz Biotechnology: sc-1000X, sc-133221X, sc-271064X) was added to the sample, and immunoprecipitation was carried out with slow rotation at 4°C overnight. Beads were then collected using a magnet and washed with 175 μl ice cold buffer as indicated by incubating samples on ice for 3 minutes: 3 times RIPA-NR1 lysis buffer (20 mM Tris/HCl pH7.5, 1 mM EDTA, 0.5 mM EGTA, 0.1%

SDS, 0.4% Na-Deoxycholate, 1% NP-40 alternative, 0.5 mM DTT, 1x protease inhibitor cocktail (Sigma), 1 mM PMSF), 6 times LiCl-NR1 buffer (10 mM Tris/HCl pH7.5, 250mM LiCl, 1 mM EDTA, 0.7% Na-Deoxycholate, 1% NP-40 alternative, 1x protease inhibitor cocktail (Sigma), 1 mM PMSF), 3 times TET (10 mM Tris/HCl pH 8.0, 1 mM EDTA, 0.2% Tween-20, 1x protease inhibitor cocktail (Sigma), 1 mM PMSF), and 1 time IDTE (10 mM Tris/HCl pH 8.0, 0.1 mM EDTA, 1x protease inhibitor cocktail (Sigma), 1 mM PMSF). Bead complexes were resuspended in 25 μl TT (10 mM Tris/HCl pH 8.0, 0.05% Tween-20, 1x protease inhibitor cocktail) and sequencing libraries were prepared on-bead as described below.

ChIP-Seq Library Preparation

ChIP libraries were prepared while bound to Dynabeads using NEBNext Ultra II Library preparation kit with reaction volumes reduced by half, essentially as previously described (129). Libraries were eluted and crosslinks reversed by adding to the 46.5 μl NEB reaction 20 μl water, 4 μl 10% SDS, 4.5 μl 5M NaCl, 3 μl 0.5 M EDTA, and 1 μl 20 mg/ml proteinase K, followed by incubation at 55C for 1 hour and 65C for 30 minutes to overnight in a thermal cycler. Dynabeads were removed from the library using a magnet and libraries cleaned by adding 2 μl SpeedBeads 3 EDAC in 61 μl 20% PEG 8000/1.5 M NaCl, mixing well, then incubating at room temperature for 10 minutes. SpeedBeads were collected on a magnet and washed two times with 150 μl 80% ethanol for 30 seconds. Beads were collected and ethanol removed following each wash. After the second ethanol wash, beads were air dried and DNA eluted in 25 μl 10 mM Tris/HCl pH

8.0 and 0.05% Tween-20. DNA was amplified by PCR for 14 cycles in a 50 μl reaction volume using NEBNext Ultra II PCR master mix and 0.5 μM each Solexa 1GA and Solexa 1GB primers. Libraries were cleaned up with SpeedBeads as above using 36.5 μl 20% PEG 8000/1.5 M NaCl and 2 μl SpeedBeads. After ethanol washing and drying, PCR amplified libraries were eluted from the SpeedBeads using 20 μl 10 mM Tris/HCl pH 8.0 and 0.05% Tween-20. Next, libraries were size selected 250-500 bp using gel extraction using 10% TBE acrylamide gels. Libraries were single-end sequenced using either a HiSeq 4000 or a NextSeq 500 to a depth of 10-20 million reads.

Lipid Measurements

Livers were processed at the University of Texas Southwestern Medical Center for oxysterol and lipid metabolite analysis by LC-MS as previously described in full (www.lipidmaps.org/protocols/index.html).

Mice

Mice used in this study were bred and maintained in the Glass laboratory vivarium on the C57BL/6J background or were C57BL/6J sourced directly from Jackson laboratories. Creation and validation of the Clec4f-Cre-tdTomato mice, which express a T2A cleavable polypeptide of Cre coupled to TdTomato with a nuclear localization sequence in the 3'UTR of *Clec4f*, was describe elsewhere (Sakai, et al., accompanying manuscript). The Clec4f-cre mice will be available at The Jackson Laboratory as Stock No. 033296**.** Cx3cr1 driven inducible lineage tracing was performed by crossing

B6.129P2(Cg)-Cx3cr1tm2.1(cre/ERT2)Litt/WganJ (Jackson stock no. 021160) mice to B6.Cg-Gt(ROSA)26Sortm14(CAG-tdTomato)Hze/J (Jackson stock no. 007914) mice. Progeny were injected on days 1 and 2 of life with 50 μg then 75 μg tamoxifen dissolved in corn oil and ethanol. To label monocyte lineage cells, adult mice were injected via the intraperitoneal route 1 week prior to euthanasia for 5 consecutive days with 75 mg/kg tamoxifen dissolved in corn oil and ethanol. All animals were maintained and all procedures performed in accordance with an approval animal study protocol meeting AALAC standards.

Sequencing Data Analysis

Preprocessing: FASTQ files from sequencing experiments were mapped to the mouse mm10 genome. STAR with default parameters was used to map RNA-seq experiments (130). Bowtie2 with default parameters was used to map ATAC-seq and ChIP-seq experiments (178). HOMER was used to convert aligned reads into “tag directories” for further analysis (16).

RNA-seq: Each experiment was quantified using the “analyzeRepeats” script of HOMER. To generate a table of raw read counts, the parameters -count exons -condenseGenes -noadj were used. To generate a table of TPM values, the parameters -count exons -condenseGenes -tpm were used. The TPM values were further processed by log2(TPM+1). Differentially expressed genes were identified using raw sequencing read counts by DESeq2 (179) analysis through the

"getDifferentialExpression" HOMER command. Gene ontology analysis was performed using Metascape (180).

IDR analysis: ChIP-seq experiments were performed in replicate with corresponding input experiments. Peaks were called with HOMER for each tag directory with relaxed peak finding parameters -L 0 -C 0 -fdr 0.9 against the corresponding input directory. For ATAC-seq, no inputs were used and peaks were called with parameters -L 0 -C 0 -fdr 0.9 -minDist 200 -size 200. IDR (181) was used to test for reproducibility between replicates, and only peaks with IDR < 0.05 were used for downstream analysis. The pooled tag directory from two replicates was used for track visualization.

ATAC-seq and ChIP-seq analysis: To quantify transcription factor (TF) binding and chromatin accessibility, peak files were merged with HOMER's mergePeaks and annotated with raw tag counts with HOMER's annotatePeaks using parameters -noadj, -size given. To annotate H3K27ac signal around ATAC-seq peaks the parameter -size 2000 was used. Subsequently, DESeq2 (179) was used to identify the differentially bound TF, H3K27ac signal or chromatin accessibility with > 2 fold-change and p-adj < 0.05, unless stated otherwise in the text.

Motif enrichment: To identify motifs enriched in peak regions over the background, HOMER's motif analysis (findMotifsGenome.pl) including known default motifs and de novo motifs was used. The background sequences were either from

random genome sequences or from peaks from the comparing condition indicated in the main text and in the figure legends.

Data visualization: The UCSC genome browser (182) was used to visualize ChIP-seq and ATAC-seq data.

F. Acknowledgements

Chapter 3, in full, is adapted from a manuscript currently in review at *Cell*. The dissertation author was the co-primary author of this paper along with Ty D. Troutman and Mashito Sakai. Other authors include Anita Gola, Zhengyu Ouyang, Nathanael J. Spann, Cassi M. Bruni, Hunter Bennett, Xiaoli Sun, BaoChau T. Vu, Martina P. Pasillas, Kaori M. Ego , David Gosselin, Verena M. Link, Bonne M. Thompson, Jeffery G. McDonald, Joseph L. Witztum, Ronald N. Germain, and Christopher K. Glass.

These studies were supported by NIH grants DK091183, HL088083 and GM085764. JSS was supported by American Heart Association Fellowship 16PRE30980030 and NIH Predoctoral Training Grant 5T32DK007541. TDT was supported by P30 DK063491, T32DK007044, and NRSA T32CA009523. M.S. was supported by the Manpei Suzuki Diabetes Foundation of Tokyo, Japan, and the Osamu Hayaishi Memorial Scholarship for Study Abroad, Japan. X.S was supported by The American Heart Association Grant 18POST34060088. This work as also supported in part by the Intramural Research program of NIAID, NIH.

Chapter 4. Conclusions and Future Directions

The findings presented here lead to several important conclusions about how distinct liver niches regulate gene expression in hepatic macrophages during homeostasis and liver disease. Macrophage mediated inflammation is linked to a multitude of chronic disease states, and inflammation often leads to increased complexity of the myeloid population structure due to recruitment and differentiation of inflammatory monocytes as well as cell intrinsic changes in the tissue resident cells. Studying how environmental signals are sensed and integrated to produce specific patterns of gene expression will allow us to better understand the mechanisms controlling macrophage behavior and opens new possibilities for therapeutic interventions that target macrophages.

A. A two-step model of tissue macrophage niche specification

In **Chapter 2**, using an experimental model of Kupffer cell ablation and repopulation, we performed high sensitivity transcriptomic and enhancer profiling as monocytes colonized the empty Kupffer cell niche and differentiated into Kupffer cell-like hepatic macrophages. We found that many genes, including key Kupffer cell lineage determining factors such as *Nr1h3*, *Spic*, and *Id3* are induced within only 12 hours of Kupffer cell ablation. We found that these rapidly induced genes tended to have associated pre-existing open chromatin regions in blood monocytes, and that enhancer activity assed by H3K27ac signal rapidly increased at these regions. TGF/SMAD and NOTCH/RBPJ signaling were found to be important environmental signaling pathways originating in liver sinusoidal endothelial cells, while hepatocyte derived desmosterol is

present at sufficient concentrations to drive LXR signaling. While many Kupffer cell genes were rapidly induced upon niche colonization by monocytes, much of the Kupffer cell gene program was not fully engaged until 7 to 14 days. In contrast to the early-activated genes, these late-activated genes tended to lack associated pre-existing open chromatin regions; rather, chromatin accessibility and enhancer activation appeared later in the time course. These observations are consistent with a two-step model where upon engraftment within the available niche, environmental signals rapidly induce tissue specificity of the developing macrophage by directing transcription factors to bind to and activate latent enhancers (**Figure 4.1**). Once the resident macrophage lineage factors are induced, they then work to differentiate the recruited macrophage closer to the resident macrophage phenotype by establishing cell type specific enhancers.

The collaborative hierarchical model of enhancer selection posits that lineage determining transcription factors establish a cell type specific enhancer landscape by working together with collaborating transcription factors. Using this novel system of Kupffer cell ablation and monocyte recruitment, we found supporting evidence of the collaborative hierarchical model *in vivo*, and gained new insights into how environmental signals influence both lineage and signal dependent transcription factors. Monocytes express general macrophage LDTFs, including PU.1, C/EBP and AP-1, and share many core macrophage enhancers that are also present in tissue macrophages, but they lack expression of certain transcription factors and activated enhancers that are present in specific tissue macrophage subsets. In the Kupffer cell repopulation system, environmentally derived signals such as TGF-β/BMP family members and notch ligands

rapidly induce expression of important Kupffer cell specific LDTFs (*Nr1h3*, *Spic*, *Id3*, *Tfec*, *Mafb*), which can then act to open chromatin, as evidenced by the enrichment of the associated motifs for these factors in newly acquired (48 hours after DT administration) open chromatin regions in recruited liver macrophages. We also found that SMADs and RBPJ act at many Kupffer cell niche specific enhancers to directly regulate expression of Kupffer cell identity genes. SMAD4 was required for establishment or maintenance of a small subset of open chromatin regions, indicating it may induce de novo enhancer formation in response to TGF signaling, while RBPJ marked regions that gained H3K27 acetylation signal during differentiation, consistent with NOTCH signaling inducing coactivator/corepressor exchange (110). Further, liver derived desmosterol appears to serve as an environmental signal to induce expression of both canonical LXR target genes and LXR dependent Kupffer cell identity genes, and LXRα was found to be required for the formation of several thousand open chromatin regions in Kupffer cells. Thus, in addition to tissue macrophage specific LDTFs early in differentiation, environmentally derived signals also act through signal dependent transcription factors to both induce de novo enhancer formation and activate latent enhancers.

B. Biological relevance of the Kupffer cell ablation/repopulation system

The main advantages to this DTR-system are that the nearly complete and rapid ablation of the Kupffer cell niche permits the recruitment of a large pool of HSC-derived monocyte progenitors to rapidly colonize the niche and differentiate into Kupffer cell-like macrophages in a synchronized fashion. This allows a sufficient number of cells to be

obtained for transcriptomic and enhancer profiling, permitting inference of temporally dependent developmental processes. The main drawbacks and criticism of this model are that it is highly artificial. Indeed, it is hard to image an situation in which the entire Kupffer cell population is lost and replaced by monocytes, although it has been reported that certain pathological conditions such as infection with listeria monocytogenes, triggers massive KC death within hours of infection and subsequently leads to monocyte recruitment (183). Kupffer cell necroptosis in this model lead to production of IL33 by hepatocytes, which was identified as an important alarmin initiating the inflammatory response that recruited and fostered monocyte differentiation. The context of diphtheria-toxin mediated Kupffer cell death may provide its own unique set of signals, and it is unclear to what extent those signals are similar to normal biological processes in which Kupffer cells might be replaced by monocyte derived precursors. Thus, it is possible that in other biological contexts, different sets of environmentally derived signals could instruct monocytes to adopt a Kupffer cell-like phenotype through separate pathways. Further, we cannot say with certainty whether erythromyeloid progenitors follow the same path when differentiating into Kupffer cells during embryogenesis, where the liver environment likely has important differences from adult animals such as microbial products in portal blood. With current technology, it is not possible to perform the high sensitivity temporally based enhancer profiling studies we carried out using our model system during embryogenesis or on very small numbers of monocytes gradually filling the Kupffer cell niche during a normal biological process like aging. Rather, the findings

from this model system may better apply to various types of chronic liver disease if monocytes are recruited to the Kupffer cell niche.

In **Chapter 3**, we studied myeloid cell diversification in the liver in a mouse model of NASH and were able to confirm many of the findings from our Kupffer cell replacement/repopulation model. We found that monocytes are recruited to distinct niches during NASH, the Kupffer cell niche in liver sinusoids and a distinct niche outside of the sinusoids near large diameter vessels. The transcriptomes and open chromatin landscapes of recruited macrophages depended on niche. This supports the findings from **Chapter 2** in two important ways: 1) It provides a biologically relevant context in which monocytes follow the same developmental trajectory we observed in the experimental Kupffer cell ablation and repopulation system in **Chapter 2**, and 2) It demonstrates the necessity of specific micro-anatomic niche within the liver to provide the appropriate context of signals that instruct the Kupffer cell phenotype. In particular, the findings in **Chapter 2** heavily concentrated on sinusoidal endothelia derived Notch and TGF-family ligands. The expression of these ligands was found to be specific to the liver sinusoidal endothelial cells marked by expression of STAB2 (101). Thus, lack of sinusoidal endothelia derived-signals could represent an important reason why large-diameter vessel associated Ly6C^{Hi}- and Ly6C^{Lo}-RM do not display a Kupffer cell-like phenotype.

C. Regulation of recruited macrophages outside of the Kupffer cell niche

The NF-κB motif is enriched in all liver macrophages, including healthy Kupffer cells compared to other tissue resident macrophages (**Figure 2.S2C**). Intestinally

derived microbial products such as lipopolysaccharide (LPS) entering from the portal circulation could thus be an important signal that instructs normal Kupffer cell behavior. However, the enrichment for NF-κB is much stronger in distal open chromatin regions specifically gained in Ly6C^{Lo}-RM compared to macrophages in the Kupffer cell niche (**Figure 3.4E**), indicating pro-inflammatory signaling through this pathway has even greater importance in these recruited macrophages. Possible explanations for this result include: 1) These cells may sense higher concentrations of LPS than Kupffer cells during NASH (e.g. if they are positioned closer to the portal vein), 2) They may be less tolerant of LPS than Kupffer cells, and 3) They may be localized closer to disease active areas and are responding to tissue damage signals. Enrichment of the NF-κB in Ly6C^{Lo}-RM indicates that this macrophage subset may be play a more pro-inflammatory or disease active role compared to cells in the liver sinusoid. Indeed, genes more highly expressed in Ly6C^{Hi}- and Ly6C^{Lo}-RM had functional annotations such as Inflammatory response, Response to wounding and Extracellular matrix organization (**Figure 3.3A** and **Figure 3.S3E**).

To our knowledge, this is the first study that showed subset specific RNA-seq data of CD11b^{Hi} F4/80^{Lo} Ly6C^{Hi} and Ly6C^{Lo} recruited macrophages during NASH. A recent study was the first to publish the transcriptomes of CD11b^{Hi} recruited macrophages in a methionine and choline deficient murine model of NASH, but did not subset with Ly6C expression (161). Further analysis of these data and comparison with previous literature should allow better understanding of the importance of each of these subsets during progression of NASH. By histo-cytometry, we were able to determine

that Ly6C^{Hi} and Ly6C^{Lo}-RM exist in a niche that is anatomically distinct from the sinusoidal Kupffer cell niche and is closer to large vessels. Further microscopy studies will be aimed to determine if these cells have a more peri-portal versus peri-central distribution, if they are located near areas of fibrosis or apoptotic hepatocytes, and if there is a difference between the localization of Ly6C^{Hi} and Ly6C^{Lo}-RM. Although we were unable to visualize Ly6C by immunofluorescence in these studies, alternative approaches such as using Gr1 or an alternative epitope highly expressed in a subset specific manner, such as Mgl2 for Ly6C^{Lo}-RM, could help us understand address this question. By linking positional information with gene expression data, we will be better able to understand the roles of these recruited macrophages during NASH.

D. Niche dependent reprogramming of resident Kupffer cells during NASH

In addition to monocyte recruitment to inflamed liver niches, embryonically derived Kupffer cells undergo cell intrinsic changes in response to changes in the liver environment during NASH. NASH caused profound changes to the Kupffer cell enhancer landscape, with approximately 20% of all Kupffer cell enhancers undergoing significant up- or downregulation (**Figure 3.5C**). This represents the first evidence of changes in active chromatin marks in a highly specific resident macrophage population during a disease model. Interestingly, while nearly 8,000 regions displayed differences in active histone mark H3K27ac, the open chromatin landscape was much more stable, with less than 500 regions changing (**Figure 3.5A**). In contrast, monocyte differentiation into either KN-RM or Ly6C^{Lo}-RM was associated with significant changes of approximately 9,000 and 12,000 open chromatin regions, respectively (**Figure 3.4B** and

Figure 3.4C). This may relate to the fact that Kupffer cells are a fully differentiated tissue macrophage, while circulating monocytes must possess greater plasticity in order to respond to signals present in a wide variety of bodily tissues. Alternatively, the environmental change in healthy versus diseased liver may simply be of much lower magnitude compared to monocytes being recruited to a tissue niche.

The most dramatic effect of the NASH diet on the Kupffer cell enhancer landscape appears to be the overwhelmingly asymmetric reduced activity of Kupffer cell signature enhancers (**Figure 3.5C**). Motif analysis indicated that LXRs normally regulate these regions that are important for normal Kupffer cell identity and homeostasis, and genetic loss of LXRα confirmed it is required for the activity of these enhancers (**Figure 3.S6A**) as well as in the expression of LXR target genes (**Figure 3.6C**). Further, LXR ChIP-seq revealed specific loss of LXRs from Kupffer cell signature enhancers (**Figure 3.S6E**,**F**).

What causes the loss of LXR binding specifically at enhancers that control Kupffer cell identity? The increase in canonical LXR targets such as *Abca1*, *Abcg1*, *Mylip,* and *Srebf1* during NASH (**Figure 3.5H**) argues that this is a specific rather than generalized effect on LXR activity. SMAD motifs were enriched in the LXR peaks lost during NASH (**Figure 3.S6D**). Thus, collaborative interactions with SMADs may be required to maintain LXR binding at the specific regions lost during NASH, similar to how PU.1 requires collaborative interactions with other transcription factors such as AP1 ad C/EBP to maintain many macrophage enhancers (16). Preliminary RNA-seq data suggests *Bmp2* and *Bmp6*, which appear to be the most highly expressed TGF

family members specifically expressed in STAB2 positive sinusoidal endothelial cells (**Figure 2.4A**), are significantly downregulated during NASH (**Figure 4.2**). Furthermore, *Bmpr1a* is strongly downregulated in Kupffer cells in response to NASH, and is one of the few genes not induced in repopulating liver macrophages in the experimentally induced Kupffer cell ablation model system even after 30 days (**Figure 3.S3C**, **D**) (42). Preliminary data also showed downregulation of NOTCH ligand *Dll4* (see **Chapter 2**). Thus, NASH may indirectly affect LXR signaling in Kupffer cells by disrupting the binding of collaborating transcription factors that act downstream of sinusoidal endothelia derived niche signals that are required for normal Kupffer cell gene expression. Liver sinusoidal endothelial cells are known to lose morphological and functional characteristics during NASH in a process referred to as “capillarization” (184), which is thought to contribute to NASH progression through multiple mechanisms including activation of hepatic stellate cells and increased resistance to blood flow. Our findings suggest that this process of sinusoidal endothelial dysfunction may also dysregulate Kupffer cell homeostasis by altering the production of paracrine signals that support normal Kupffer cell phenotype.

There are several other possibilities that could lead to the dysregulation of LXR signaling in Kupffer cells during NASH. LXRs have traditionally been considered signal dependent transcription factors involved in cholesterol homeostasis, lipid biosynthesis and regulation of inflammation (98, 99). As type II nuclear receptors, LXRs are thought to be constantly bound to DNA as heterodimers with RXR, and ligand binding is thought to induce coactivator/corepressor exchange rather than new binding events. How LXRs

may act as lineage determining transcription factors in certain cell types, such as Kupffer cells and marginal zone and metallophilic macrophage (24, 38), is less well understood. Previous comparisons of different tissue macrophages have shown *Nr1h3* is more highly expressed in these macrophage populations (38), indicating that the lineage determining functions may simply require higher concentrations of nuclear LXRs. Although we did not observe decreased expression of *Nr1h3* or *Nr1h2* during NASH (**Figure 3.5G**), we did not measure changes in LXR protein levels, which could be decreased through reduced protein synthesis or increased proteasomal degradation.

LXRs can be posttranslationally modified through ubiquitination, SUMOylation and phosphorylation, acetylation, and O-GlcNacylation which can have different effects on protein degradation and function (185). LXRα can be phosphorylated on S196 in mouse (S198 in human) by cysteine kinase 2, PKA and other kinases (186, 187). This modification appears to have gene specific modulatory effects on LXR target genes. While the effects of LXRα S196 phosphorylation have not yet been studied in Kupffer cells, LXRα is highly expressed in Kupffer cells, and we observed downregulation of *Ccl24* in Kupffer cells during NASH (data not shown), which was previously shown to be negatively regulated by phosphorylation in a macrophage cell line (188). A mouse with an LXRα S196A mutation was recently studied in a murine model of NASH (189) and could serve as a valuable research tool to study the effect of LXRα S196 phosphorylation in Kupffer cells.

E. Potential functional consequences of myeloid diversification during NASH

Macrophage recruitment contributes to the pathogenesis of acute liver injury and chronic inflammatory disease such as NASH. However, different macrophage populations are thought to acquire specific functions during liver disease (48, 166). In **Chapter 3**, which showed that the high fat, high fructose, high cholesterol NASH model diet lead to recruitment of monocytes to the Kupffer cell niche, where they adopted a similar transcriptional program as Kupffer cells and could be identified as $CD11b^{Lo}F4/80^{Hi}Tim4^{Neg}$. At the latest time point analyzed, approximately half of $CD11b^{Lo}F4/80^{Hi}$ cells isolated from the liver are these Kupffer niche recruited macrophages. To our knowledge, only one other study, which was recently published and used a methionine and choline deficient dietary NASH model (75), has demonstrated that $CD11b^{Lo}F4/80^{Hi}$ macrophages can be monocyte derived during chronic liver disease. Thus, the functional roles of Kupffer niche recruited macrophages have not been studied. Our RNA-seq data from these studies indicate that several while these Kupffer niche recruited macrophages are similar to Kupffer cells, there are several important molecular differences, such as lower expression of Kupffer cell identity genes with potential important homeostatic functions including *Timd4*, *Vsig4*, *Il18bp*, *Cd163* and *Hmox1* (**Figure 3.S1F** and **Figure 3.S3D**). These recruited macrophages also had higher expression of a many genes involved in antigen presentation through class II MHC, such as *Ciita*, *Cd74* and *H2-Aa*. Kupffer niche recruited macrophages also appear to be transcriptionally similar to the repopulating liver macrophages studied in the Kupffer cell ablation/repopulation model described in **Chapter 2** (**Figure 3.S3D**),

indicating ontogeny may be primarily responsible for the differences between recruited and embryonically derived macrophages in both model systems. Thus, the KC-DTR system described in **Chapter 2** could be used to replace embryonically derived Kupffer with monocyte derived Kupffer niche recruited macrophages prior to the onset of NASH or any other studies, allowing us to study the functional differences between these cell types. Specifically blocking recruitment of these cells without affecting $Ly6C^{Hi}$ or $Ly6C^{Lo}$ recruited macrophages does not seem possible at present. A two-component system to specifically act only on cells that are both monocyte-derived and in the Kupffer cell niche could be devised to target this subset of recruited macrophages.

Interestingly, preliminary data from other studies performed in our laboratory have shown that these macrophages also accumulate during repeated carbon tetrachloride (CCl_4) injection and have similar transcriptional differences compared to $Tim4^{Pos}$ Kupffer cells as is observed during our NASH model (**data not shown**). Further, BALB/c mice do not display prominent steatosis, inflammation, fibrosis or $Tim4^{Neg}$ macrophage recruitment in response to the AMLN NASH model, but develop fibrosis and accumulate $Tim4^{Neg}$ recruited macrophages in response to CCl_4 (**data not shown**). These observations indicate that accumulation of $Tim4^{Neg}$ recruited macrophages may be a generalized phenomenon in any chronic injury model that causes Kupffer cell apoptosis. Furthermore, we have observed that up to 20% of $F4/80^{Hi}$ hepatic macrophages are $Tim4^{Neg}$ in chow or healthy control diet fed 40-week-old C57BL/6 mice (**data not shown**). This suggests that embryonically derived Kupffer cells may normally undergo replacement with monocyte derived macrophages with age.

It should be noted that most lineage tracing experiments are performed on relatively young mice and typically do not follow mice past early adulthood. Lineage tracing studies are not feasible in humans, and it is important to consider that we live more than two orders of magnitude longer than the duration of typical mouse studies. Further, chronic inflammatory diseases such as NAFLD and those caused by alcohol or viral hepatitis are quite common in humans and could accelerate this replacement of embryonically derived Kupffer cells with monocyte derived macrophages. Thus, in a typical adult human, what proportion of Kupffer cells are monocyte rather than embryonically derived, and how does this impact human health and susceptibility to disease as we age? If there are functional differences between embryonically derived and monocyte derived macrophages living in the Kupffer cell niche, then variability in the composition of these cells could impact health and susceptibility to a variety of diseases including diabetes, NASH and hepatocellular carcinoma.

F. Closing thoughts

The disruption of the Kupffer cell homeostatic program during NASH suggests that continuous input from environmental signals is required to maintain normal tissue macrophage phenotypes, and that these signals may be altered during chronic disease. Absent or abnormal function of tissue macrophages can induce tissue pathology (18, 190). For example, osteoclast deficiency or dysfunction leads to osteopetrosis (191), mice with deficiency of SPI-C do not develop normal splenic red pulp macrophages and display an iron overload disorder (25), and alveolar macrophage deficiency causes insufficient clearance of surfactant and leads to alveolar pulmonary proteinosis(192,

193). In the context of chronic inflammation, continually suppressed homeostatic functions of macrophages may thus have detrimental consequences that contribute to organ dysfunction. Genetic tools to manipulate specific populations such as the Clec4f-Cre we generated to target Kupffer cells in these studies will be helpful for future research into this topic. For example, by chronically administering diphtheria toxin to the Clec4f-Cre Rosa26-LSL-DTR mice we used in **Chapter 2**, we assess the effects of Kupffer cell deficiency in otherwise healthy animals or during disease models.

The multi-level genomics approach we used to understand how niche signals affect macrophage gene expression identified pathways that are potential actionable therapeutic targets during NASH. For example, motif analysis of differentially regulated enhancers during NASH suggests bolstering LXR function may allow Kupffer cells to maintain expression of homeostatic genes during NASH. This could be done by either directly activating LXR by supplying LXR agonists or by activating SMAD or Notch/RBPJ signaling pathways that collaborate with LXR. AP-1 is the top motif enriched in Kupffer cell enhancers upregulated during NASH, indicating that inhibiting signaling pathways upstream of AP-1, or targeting transcription factors induced during NASH such as ATF3, could help control pro-fibrotic and pro-inflammatory gene expression. Ideally, these pathways would be targeted in a selective or even cell type specific fashion. Considerable interest exists in targeting macrophages, and approaches leveraging their high phagocytic activity such as using liposomes or nanoparticles as delivery agents are promising (194). Virally delivered CRISPR/Cas9 systems expressed

under control of macrophage specific promoters offers another strategy to target these cells.

Translating the findings presented here to humans will require both greater understanding of the myeloid diversity during human NASH as well as careful comparisons between human and mouse liver macrophages. While much is conserved between human and mouse, important functional differences may exist. A recent study from the Glass Lab compared human to mouse microglia and identified sets of genes that were similarly expressed, as well as gene sets with species specific expression (89). Understanding these similarities and differences could help design of future mouse studies focused on pathways of increased applicability to human disease. Performing human to mouse comparisons during NASH will be more challenging due to increased macrophage complexity during NASH. Using human postmortem samples from patients with NASH, we performed a preliminary scRNA-seq experiment to capture the myeloid diversity of macrophages and have started experimenting with flow cytometry strategies to capture and profile the various populations we identified. Understanding the relationships between mice and humans at the cellular and genetic levels will serve as a valuable resource in interpreting basic liver fibrosis research done in mice and applying findings to humans.

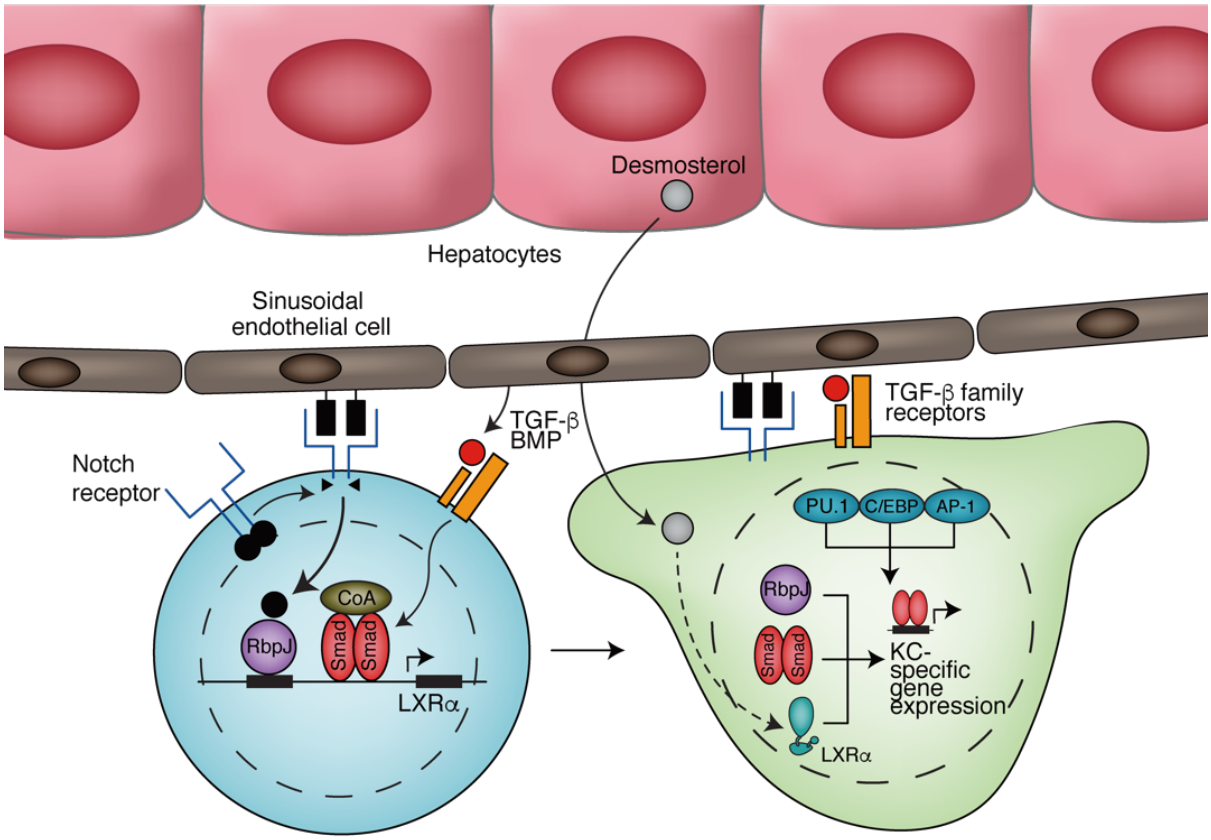

Figure 4.1: A two-step model for establishing niche specific gene regulator landscapes

Step1: Within hours of monocyte recruitment to the Kupffer cell niche, environmentally derived signals such as TGF-β/BMPs and Notch ligands activate pre-existing open chromatin regions to activate transcription of key Kupffer cell lineage determining transcription factors (LDTFs) such LXRα, and other "early" Kupffer cell genes. Step 2: Newly induced Kupffer cell LDTFs collaborate with other macrophage LDTFs such as PU.1, C/EBP and AP-1 to establish Kupffer cell specific enhancers and induce the expression of other Kupffer cell specific genes. Environmentally derived signals, including desmosterol produced from hepatocytes, continue to drive expression of these "late" Kupffer cell genes.

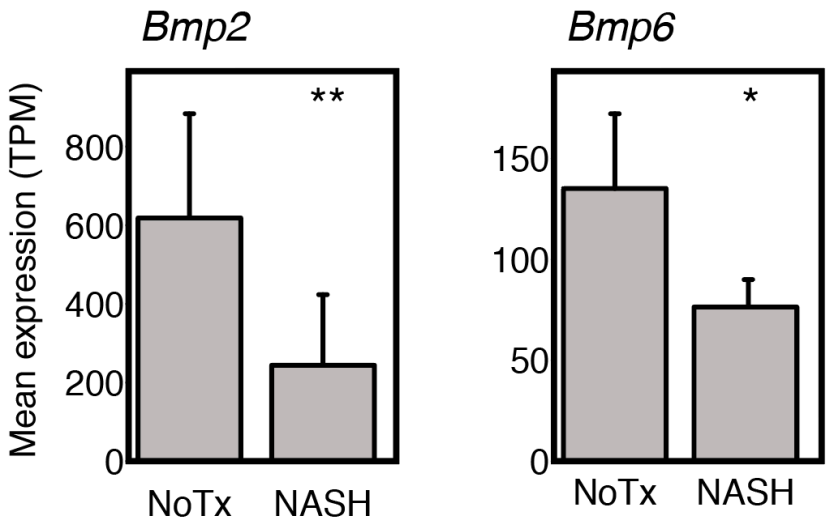

Figure 4.2: Expression of BMPs in liver sinusoidal endothelial cells during NASH

Mean expression (TPM) of *Bmp2* and *Bmp6* in liver sinusoidal endothelial cells isolated from healthy mice or mice on NASH model diet. * = p-adj < 0.05, ** = p-adj < 0.01.

References

1. Bloom K & Joglekar A (2010) Towards building a chromosome segregation machine. *Nature* 463(7280):446-456.

2. Clapier CR, Iwasa J, Cairns BR, & Peterson CL (2017) Mechanisms of action and regulation of ATP-dependent chromatin-remodelling complexes. *Nat Rev Mol Cell Biol* 18(7):407-422.

3. Kouzarides T (2007) Chromatin modifications and their function. *Cell* 128(4):693-705.

4. Lawrence M, Daujat S, & Schneider R (2016) Lateral Thinking: How Histone Modifications Regulate Gene Expression. *Trends Genet* 32(1):42-56.

5. Schwartz YB & Pirrotta V (2008) Polycomb complexes and epigenetic states. *Curr Opin Cell Biol* 20(3):266-273.

6. Heintzman ND, Stuart RK, Hon G, Fu Y, Ching CW, Hawkins RD, Barrera LO, Van Calcar S, Qu C, Ching KA, Wang W, Weng Z, Green RD, Crawford GE, & Ren B (2007) Distinct and predictive chromatin signatures of transcriptional promoters and enhancers in the human genome. *Nature genetics* 39:311-318.

7. Kim TK & Shiekhattar R (2015) Architectural and Functional Commonalities between Enhancers and Promoters. *Cell* 162(5):948-959.

8. Heintzman ND, Hon GC, Hawkins RD, Kheradpour P, Stark A, Harp LF, Ye Z, Lee LK, Stuart RK, Ching CW, Ching Ka, Antosiewicz-Bourget JE, Liu H, Zhang X, Green RD, Lobanenkov VV, Stewart R, Thomson Ja, Crawford GE, Kellis M, & Ren B (2009) Histone modifications at human enhancers reflect global cell-type-specific gene expression. *Nature* 459:108-112.

9. Murray PJ & Wynn TA (2011) Protective and pathogenic functions of macrophage subsets. *Nat Rev Immunol* 11(11):723-737.

10. Wynn TA & Vannella KM (2016) Macrophages in Tissue Repair, Regeneration, and Fibrosis. *Immunity* 44(3):450-462.

11. Glass CK & Saijo K (2010) Nuclear receptor transrepression pathways that regulate inflammation in macrophages and T cells. *Nature reviews. Immunology* 10(5):365-376.

12. Olefsky JM & Glass CK (2010) Macrophages, inflammation, and insulin resistance. *Annu Rev Physiol* 72:219-246.

13. Moore KJ & Tabas I (2011) Macrophages in the pathogenesis of atherosclerosis. *Cell* 145(3):341-355.

14. Medzhitov R & Horng T (2009) Transcriptional control of the inflammatory response. *Nat Rev Immunol* 9(10):692-703.

15. Scott EW, Simon MC, Anastasi J, & Singh H (1994) Requirement of transcription factor PU.1 in the development of multiple hematopoietic lineages. *Science* 265(5178):1573-1577.

16. Heinz S, Benner C, Spann N, Bertolino E, Lin YC, Laslo P, Cheng JX, Murre C, Singh H, & Glass CK (2010) Simple Combinations of Lineage-Determining Transcription Factors Prime cis-Regulatory Elements Required for Macrophage and B Cell Identities. *Molecular Cell* 38:576-589.

17. Heinz S, Romanoski CE, Benner C, & Glass CK (2015) The selection and function of cell type-specific enhancers. *Nat Rev Mol Cell Biol*.

18. T'Jonck W, Guilliams M, & Bonnardel J (2018) Niche signals and transcription factors involved in tissue-resident macrophage development. *Cell Immunol* 330:43-53.

19. Alfaqeeh S, Oralova V, Foxworthy M, Matalova E, Grigoriadis AE, & Tucker AS (2015) Root and Eruption Defects in c-Fos Mice Are Driven by Loss of Osteoclasts. *J Dent Res* 94(12):1724-1731.

20. Johnson RS, Spiegelman BM, & Papaioannou V (1992) Pleiotropic effects of a null mutation in the c-fos proto-oncogene. *Cell* 71(4):577-586.

21. Grigoriadis AE, Wang ZQ, Cecchini MG, Hofstetter W, Felix R, Fleisch HA, & Wagner EF (1994) c-Fos: a key regulator of osteoclast-macrophage lineage determination and bone remodeling. *Science* 266(5184):443-448.

22. Wang ZQ, Ovitt C, Grigoriadis AE, Mohle-Steinlein U, Ruther U, & Wagner EF (1992) Bone and haematopoietic defects in mice lacking c-fos. *Nature* 360(6406):741-745.

23. Schneider C, Nobs SP, Kurrer M, Rehrauer H, Thiele C, & Kopf M (2014) Induction of the nuclear receptor PPAR-gamma by the cytokine GM-CSF is critical for the

differentiation of fetal monocytes into alveolar macrophages. *Nat Immunol* 15(11):1026-1037.

24. A. Gonzalez N, Guillen JA, Gallardo G, Diaz M, de la Rosa JV, Hernandez IH, Casanova-Acebes M, Lopez F, Tabraue C, Beceiro S, Hong C, Lara PC, Andujar M, Arai S, Miyazaki T, Li S, Corbi AL, Tontonoz P, Hidalgo A, & Castrillo A (2013) The nuclear receptor LXRalpha controls the functional specialization of splenic macrophages. *Nat Immunol* 14(8):831-839.

25. Kohyama M, Ise W, Edelson BT, Wilker PR, Hildner K, Mejia C, Frazier WA, Murphy TL, & Murphy KM (2009) Role for Spi-C in the development of red pulp macrophages and splenic iron homeostasis. *Nature* 457(7227):318-321.

26. Haldar M, Kohyama M, So AY, Kc W, Wu X, Briseno CG, Satpathy AT, Kretzer NM, Arase H, Rajasekaran NS, Wang L, Egawa T, Igarashi K, Baltimore D, Murphy TL, & Murphy KM (2014) Heme-mediated SPI-C induction promotes monocyte differentiation into iron-recycling macrophages. *Cell* 156(6):1223-1234.

27. Wada T, Nakashima T, Hiroshi N, & Penninger JM (2006) RANKL-RANK signaling in osteoclastogenesis and bone disease. *Trends Mol Med* 12(1):17-25.

28. Yasui T, Hirose J, Aburatani H, & Tanaka S (2011) Epigenetic regulation of osteoclast differentiation. *Ann N Y Acad Sci* 1240:7-13.

29. Macian F, Lopez-Rodriguez C, & Rao A (2001) Partners in transcription: NFAT and AP-1. *Oncogene* 20(19):2476-2489.

30. Crotti TN, Sharma SM, Fleming JD, Flannery MR, Ostrowski MC, Goldring SR, & McHugh KP (2008) PU.1 and NFATc1 mediate osteoclastic induction of the mouse beta3 integrin promoter. *J Cell Physiol* 215(3):636-644.

31. Okabe Y & Medzhitov R (2014) Tissue-specific signals control reversible program of localization and functional polarization of macrophages. *Cell* 157(4):832-844.

32. Gomez Perdiguero E, Klapproth K, Schulz C, Busch K, Azzoni E, Crozet L, Garner H, Trouillet C, de Bruijn MF, Geissmann F, & Rodewald HR (2015) Tissue-resident macrophages originate from yolk-sac-derived erythro-myeloid progenitors. *Nature* 518(7540):547-551.

33. McGrath KE, Frame JM, Fegan KH, Bowen JR, Conway SJ, Catherman SC, Kingsley PD, Koniski AD, & Palis J (2015) Distinct Sources of Hematopoietic Progenitors Emerge

before HSCs and Provide Functional Blood Cells in the Mammalian Embryo. *Cell Rep* 11(12):1892-1904.

34. Schulz C, Gomez Perdiguero E, Chorro L, Szabo-Rogers H, Cagnard N, Kierdorf K, Prinz M, Wu B, Jacobsen SEW, Pollard JW, Frampton J, Liu KJ, & Geissmann F (2012) A lineage of myeloid cells independent of Myb and hematopoietic stem cells. *Science (New York, N.Y.)* 336:86-90.

35. Ginhoux F, Greter M, Leboeuf M, Nandi S, See P, Gokhan S, Mehler MF, Conway SJ, Ng LG, Stanley ER, Samokhvalov IM, & Merad M (2010) Fate mapping analysis reveals that adult microglia derive from primitive macrophages. *Science* 330(6005):841-845.

36. Perdiguero EG & Geissmann F (2015) The development and maintenance of resident macrophages. *Nature immunology* 17:2-8.

37. Mass E, Ballesteros I, Farlik M, Halbritter F, Günther P, Crozet L, Jacome-galarza CE, Händler K, Klughammer J, Kobayashi Y, Gomez- E, Schultze JL, Beyer M, Bock C, & Geissmann F (2016) Specification of tissue-resident macrophages during organogenesis. *Science* 4238:epub.

38. Lavin Y, Winter D, Blecher-Gonen R, David E, Keren-Shaul H, Merad M, Jung S, & Amit I (2014) Tissue-Resident Macrophage Enhancer Landscapes Are Shaped by the Local Microenvironment. *Cell* 159:1312-1326.

39. Scott CL, T'Jonck W, Martens L, Todorov H, Sichien D, Soen B, Bonnardel J, De Prijck S, Vandamme N, Cannoodt R, Saelens W, Vanneste B, Toussaint W, De Bleser P, Takahashi N, Vandenabeele P, Henri S, Pridans C, Hume DA, Lambrecht BN, De Baetselier P, Milling SWF, Van Ginderachter JA, Malissen B, Berx G, Beschin A, Saeys Y, & Guilliams M (2018) The Transcription Factor ZEB2 Is Required to Maintain the Tissue-Specific Identities of Macrophages. *Immunity* 49(2):312-325 e315.

40. Gosselin D, Link VM, Romanoski CE, Fonseca GJ, Eichenfield DZ, Spann NJ, Stender JD, Chun HB, Garner H, Geissmann F, & Glass CK (2014) Environment drives selection and function of enhancers controlling tissue-specific macrophage identities. *Cell* 159:1327-1340.

41. Beattie L, Sawtell A, Mann J, Frame TCM, Teal B, de Labastida Rivera F, Brown N, Walwyn-Brown K, Moore JWJ, MacDonald S, Lim E-K, Dalton JE, Engwerda CR, MacDonald KP, & Kaye PM (2016) Bone marrow-derived and resident liver macrophages display unique transcriptomic signatures but similar biological functions. *Journal of hepatology* 65:758-768.

42. Scott CL, Zheng F, De Baetselier P, Martens L, Saeys Y, De Prijck S, Lippens S, Abels C, Schoonooghe S, Raes G, Devoogdt N, Lambrecht BN, Beschin A, & Guilliams M (2016) Bone marrow-derived monocytes give rise to self-renewing and fully differentiated Kupffer cells. *Nat Commun* 7:10321.

43. Shaw TN, Houston SA, Wemyss K, Bridgeman HM, Barbera TA, Zangerle-Murray T, Strangward P, Ridley AJL, Wang P, Tamoutounour S, Allen JE, Konkel JE, & Grainger JR (2018) Tissue-resident macrophages in the intestine are long lived and defined by Tim-4 and CD4 expression. *J Exp Med* 215(6):1507-1518.

44. Ginhoux F & Jung S (2014) Monocytes and macrophages: developmental pathways and tissue homeostasis. *Nat Rev Immunol* 14(6):392-404.

45. Wynn TA, Chawla A, & Pollard JW (2013) Macrophage biology in development, homeostasis and disease. *Nature* 496(7446):445-455.

46. Ritz T, Krenkel O, & Tacke F (2018) Dynamic plasticity of macrophage functions in diseased liver. *Cell Immunol* 330:175-182.

47. Tacke F & Zimmermann HW (2014) Macrophage heterogeneity in liver injury and fibrosis. in *Journal of Hepatology*, pp 1090-1096.

48. Pellicoro A, Ramachandran P, Iredale JP, & Fallowfield JA (2014) Liver fibrosis and repair: immune regulation of wound healing in a solid organ. *Nat Rev Immunol* 14(3):181-194.

49. Hardy T, Oakley F, Anstee QM, & Day CP (2016) Nonalcoholic Fatty Liver Disease: Pathogenesis and Disease Spectrum. *Annu Rev Pathol* 11:451-496.

50. Haas JT, Francque S, & Staels B (2016) Pathophysiology and Mechanisms of Nonalcoholic Fatty Liver Disease. *Annual review of physiology* 78:181-205.

51. Buzzetti E, Pinzani M, & Tsochatzis EA (2016) The multiple-hit pathogenesis of non-alcoholic fatty liver disease (NAFLD). *Metabolism* 65(8):1038-1048.

52. Tilg H & Moschen AR (2010) Evolution of inflammation in nonalcoholic fatty liver disease: The multiple parallel hits hypothesis. *Hepatology* 52:1836-1846.

53. Perdiguero EG & Geissmann F (2016) The development and maintenance of resident macrophages. *Nat Immunol* 17(1):2-8.

54. Rivera CA, Adegboyega P, van Rooijen N, Tagalicud A, Allman M, & Wallace M (2007) Toll-like receptor-4 signaling and Kupffer cells play pivotal roles in the pathogenesis of non-alcoholic steatohepatitis. *J Hepatol* 47(4):571-579.

55. Seki E, De Minicis S, Osterreicher CH, Kluwe J, Osawa Y, Brenner DA, & Schwabe RF (2007) TLR4 enhances TGF-beta signaling and hepatic fibrosis. *Nat Med* 13(11):1324-1332.

56. Tu Z, Bozorgzadeh A, Pierce RH, Kurtis J, Crispe IN, & Orloff MS (2008) TLR-dependent cross talk between human Kupffer cells and NK cells. *The Journal of experimental medicine* 205(1):233-244.

57. Copple BL, Kaska S, & Wentling C (2012) Hypoxia-inducible factor activation in myeloid cells contributes to the development of liver fibrosis in cholestatic mice. *J Pharmacol Exp Ther* 341(2):307-316.

58. Miura K, Yang L, van Rooijen N, Ohnishi H, & Seki E (2012) Hepatic recruitment of macrophages promotes nonalcoholic steatohepatitis through CCR2. *Am J Physiol Gastrointest Liver Physiol* 302(11):G1310-1321.

59. Huang H, Shiffman ML, Friedman S, Venkatesh R, Bzowej N, Abar OT, Rowland CM, Catanese JJ, Leong DU, Sninsky JJ, Layden TJ, Wright TL, White T, & Cheung RC (2007) A 7 gene signature identifies the risk of developing cirrhosis in patients with chronic hepatitis C. *Hepatology* 46(2):297-306.

60. Guo J, Loke J, Zheng F, Hong F, Yea S, Fukata M, Tarocchi M, Abar OT, Huang H, Sninsky JJ, & Friedman SL (2009) Functional linkage of cirrhosis-predictive single nucleotide polymorphisms of Toll-like receptor 4 to hepatic stellate cell responses. *Hepatology* 49(3):960-968.

61. Arbour NC, Lorenz E, Schutte BC, Zabner J, Kline JN, Jones M, Frees K, Watt JL, & Schwartz DA (2000) TLR4 mutations are associated with endotoxin hyporesponsiveness in humans. *Nature genetics* 25(2):187-191.

62. Tacke F & Zimmermann HW (2014) Macrophage heterogeneity in liver injury and fibrosis. *J Hepatol* 60(5):1090-1096.

63. Karlmark KR, Weiskirchen R, Zimmermann HW, Gassler N, Ginhoux F, Weber C, Merad M, Luedde T, Trautwein C, & Tacke F (2009) Hepatic recruitment of the inflammatory Gr1+ monocyte subset upon liver injury promotes hepatic fibrosis. *Hepatology* 50(1):261-274.

64. Wynn TA & Barron L (2010) Macrophages: master regulators of inflammation and fibrosis. *Semin Liver Dis* 30(3):245-257.

65. Pradere JP, Kluwe J, De Minicis S, Jiao JJ, Gwak GY, Dapito DH, Jang MK, Guenther ND, Mederacke I, Friedman R, Dragomir AC, Aloman C, & Schwabe RF (2013) Hepatic macrophages but not dendritic cells contribute to liver fibrosis by promoting the survival of activated hepatic stellate cells in mice. *Hepatology* 58(4):1461-1473.

66. Ide M, Kuwamura M, Kotani T, Sawamoto O, & Yamate J (2005) Effects of gadolinium chloride (GdCl(3)) on the appearance of macrophage populations and fibrogenesis in thioacetamide-induced rat hepatic lesions. *J Comp Pathol* 133(2-3):92-102.

67. Sunami Y, Leithauser F, Gul S, Fiedler K, Guldiken N, Espenlaub S, Holzmann KH, Hipp N, Sindrilaru A, Luedde T, Baumann B, Wissel S, Kreppel F, Schneider M, Scharffetter-Kochanek K, Kochanek S, Strnad P, & Wirth T (2012) Hepatic activation of IKK/NFkappaB signaling induces liver fibrosis via macrophage-mediated chronic inflammation. *Hepatology* 56(3):1117-1128.

68. Duffield JS, Forbes SJ, Constandinou CM, Clay S, Partolina M, Vuthoori S, Wu S, Lang R, & Iredale JP (2005) Selective depletion of macrophages reveals distinct, opposing roles during liver injury and repair. *The Journal of clinical investigation* 115(1):56-65.

69. Ramachandran P, Pellicoro A, Vernon MA, Boulter L, Aucott RL, Ali A, Hartland SN, Snowdon VK, Cappon A, Gordon-Walker TT, Williams MJ, Dunbar DR, Manning JR, van Rooijen N, Fallowfield JA, Forbes SJ, & Iredale JP (2012) Differential Ly-6C expression identifies the recruited macrophage phenotype, which orchestrates the regression of murine liver fibrosis. *Proceedings of the National Academy of Sciences of the United States of America* 109(46):E3186-3195.

70. Popov Y, Sverdlov DY, Bhaskar KR, Sharma AK, Millonig G, Patsenker E, Krahenbuhl S, Krahenbuhl L, & Schuppan D (2010) Macrophage-mediated phagocytosis of apoptotic cholangiocytes contributes to reversal of experimental biliary fibrosis. *Am J Physiol Gastrointest Liver Physiol* 298(3):G323-334.

71. Fallowfield JA, Mizuno M, Kendall TJ, Constandinou CM, Benyon RC, Duffield JS, & Iredale JP (2007) Scar-associated macrophages are a major source of hepatic matrix metalloproteinase-13 and facilitate the resolution of murine hepatic fibrosis. *J Immunol* 178(8):5288-5295.

72. Pellicoro A, Aucott RL, Ramachandran P, Robson AJ, Fallowfield JA, Snowdon VK, Hartland SN, Vernon M, Duffield JS, Benyon RC, Forbes SJ, & Iredale JP (2012) Elastin accumulation is regulated at the level of degradation by macrophage metalloelastase (MMP-12) during experimental liver fibrosis. *Hepatology* 55(6):1965-1975.

73. Karlmark KR, Zimmermann HW, Roderburg C, Gassler N, Wasmuth HE, Luedde T, Trautwein C, & Tacke F (2010) The fractalkine receptor CX(3)CR1 protects against liver fibrosis by controlling differentiation and survival of infiltrating hepatic monocytes. *Hepatology* 52(5):1769-1782.

74. Aoyama T, Inokuchi S, Brenner DA, & Seki E (2010) CX3CL1-CX3CR1 interaction prevents carbon tetrachloride-induced liver inflammation and fibrosis in mice. *Hepatology* 52(4):1390-1400.

75. Devisscher L, Scott CL, Lefere S, Raevens S, Bogaerts E, Paridaens A, Verhelst X, Geerts A, Guilliams M, & Van Vlierberghe H (2017) Non-alcoholic steatohepatitis induces transient changes within the liver macrophage pool. *Cell Immunol* 322:74-83.

76. Theurl I, Hilgendorf I, Nairz M, Tymoszuk P, Haschka D, Asshoff M, He S, Gerhardt LMS, Holderried TAW, Seifert M, Sopper S, Fenn AM, Anzai A, Rattik S, McAlpine C, Theurl M, Wieghofer P, Iwamoto Y, Weber GF, Harder NK, Chousterman BG, Arvedson TL, McKee M, Wang F, Lutz OMD, Rezoagli E, Babitt JL, Berra L, Prinz M, Nahrendorf M, Weiss G, Weissleder R, Lin HY, & Swirski FK (2016) On-demand erythrocyte disposal and iron recycling requires transient macrophages in the liver. *Nature Medicine* 22:945-951.

77. Trapnell C (2015) Defining cell types and states with single-cell genomics. *Genome Res* 25(10):1491-1498.

78. Grun D & van Oudenaarden A (2015) Design and Analysis of Single-Cell Sequencing Experiments. *Cell* 163(4):799-810.

79. Gordon S, Pluddemann A, & Martinez Estrada F (2014) Macrophage heterogeneity in tissues: phenotypic diversity and functions. *Immunol Rev* 262(1):36-55.

80. Wu Y, Dissing-Olesen L, MacVicar BA, & Stevens B (2015) Microglia: Dynamic Mediators of Synapse Development and Plasticity. *Trends Immunol* 36(10):605-613.

81. Joshi N, Walter JM, & Misharin AV (2018) Alveolar Macrophages. *Cell Immunol* 330:86-90.

82. Krenkel O & Tacke F (2017) Liver macrophages in tissue homeostasis and disease. *Nat Rev Immunol* 17(5):306-321.

83. Gautier EL, Shay T, Miller J, Greter M, Jakubzick C, Ivanov S, Helft J, Chow A, Elpek KG, Gordonov S, Mazloom AR, Ma'ayan A, Chua WJ, Hansen TH, Turley SJ, Merad M, Randolph GJ, & Immunological Genome C (2012) Gene-expression profiles and

transcriptional regulatory pathways that underlie the identity and diversity of mouse tissue macrophages. *Nat Immunol* 13(11):1118-1128.

84. Ginhoux F & Guilliams M (2016) Tissue-Resident Macrophage Ontogeny and Homeostasis. *Immunity* 44(3):439-449.

85. Schulz C, Gomez Perdiguero E, Chorro L, Szabo-Rogers H, Cagnard N, Kierdorf K, Prinz M, Wu B, Jacobsen SE, Pollard JW, Frampton J, Liu KJ, & Geissmann F (2012) A lineage of myeloid cells independent of Myb and hematopoietic stem cells. *Science* 336(6077):86-90.

86. Bennett FC, Bennett ML, Yaqoob F, Mulinyawe SB, Grant GA, Hayden Gephart M, Plowey ED, & Barres BA (2018) A Combination of Ontogeny and CNS Environment Establishes Microglial Identity. *Neuron* 98(6):1170-1183 e1178.

87. Cronk JC, Filiano AJ, Louveau A, Marin I, Marsh R, Ji E, Goldman DH, Smirnov I, Geraci N, Acton S, Overall CC, & Kipnis J (2018) Peripherally derived macrophages can engraft the brain independent of irradiation and maintain an identity distinct from microglia. *J Exp Med* 215(6):1627-1647.

88. Shemer A, Grozovski J, Tay TL, Tao J, Volaski A, Suss P, Ardura-Fabregat A, Gross-Vered M, Kim JS, David E, Chappell-Maor L, Thielecke L, Glass CK, Cornils K, Prinz M, & Jung S (2018) Engrafted parenchymal brain macrophages differ from microglia in transcriptome, chromatin landscape and response to challenge. *Nat Commun* 9(1):5206.

89. Gosselin D, Skola D, Coufal NG, Holtman IR, Schlachetzki JCM, Sajti E, Jaeger BN, O'Connor C, Fitzpatrick C, Pasillas MP, Pena M, Adair A, Gonda DG, Levy ML, Ransohoff RM, Gage FH, & Glass CK (2017) An environment-dependent transcriptional network specifies human microglia identity. *Science*.

90. Buch T, Heppner FL, Tertilt C, Heinen TJ, Kremer M, Wunderlich FT, Jung S, & Waisman A (2005) A Cre-inducible diphtheria toxin receptor mediates cell lineage ablation after toxin administration. *Nat Methods* 2(6):419-426.

91. Bain CC, Hawley CA, Garner H, Scott CL, Schridde A, Steers NJ, Mack M, Joshi A, Guilliams M, Mowat AM, Geissmann F, & Jenkins SJ (2016) Long-lived self-renewing bone marrow-derived macrophages displace embryo-derived cells to inhabit adult serous cavities. *Nat Commun* 7:ncomms11852.

92. Creyghton MP, Cheng AW, Welstead GG, Kooistra T, Carey BW, Steine EJ, Hanna J, Lodato MA, Frampton GM, Sharp PA, Boyer LA, Young RA, & Jaenisch R (2010) Histone H3K27ac separates active from poised enhancers and predicts developmental state. *Proc Natl Acad Sci U S A* 107(50):21931-21936.

93. Bray SJ (2006) Notch signalling: a simple pathway becomes complex. *Nat Rev Mol Cell Biol* 7(9):678-689.

94. Heinz S, Romanoski CE, Benner C, & Glass CK (2015) The selection and function of cell type-specific enhancers. *Nature reviews. Molecular cell biology* 16:144-154.

95. Schmierer B & Hill CS (2007) TGFbeta-SMAD signal transduction: molecular specificity and functional flexibility. *Nat Rev Mol Cell Biol* 8(12):970-982.

96. Hess J, Angel P, & Schorpp-Kistner M (2004) AP-1 subunits: quarrel and harmony among siblings. *J Cell Sci* 117(Pt 25):5965-5973.

97. Tempe D, Vives E, Brockly F, Brooks H, De Rossi S, Piechaczyk M, & Bossis G (2014) SUMOylation of the inducible (c-Fos:c-Jun)/AP-1 transcription complex occurs on target promoters to limit transcriptional activation. *Oncogene* 33(7):921-927.

98. Calkin AC & Tontonoz P (2012) Transcriptional integration of metabolism by the nuclear sterol-activated receptors LXR and FXR. *Nat Rev Mol Cell Biol* 13(4):213-224.

99. Spann NJ & Glass CK (2013) Sterols and oxysterols in immune cell function. *Nat Immunol* 14(9):893-900.

100. Dixon LJ, Barnes M, Tang H, Pritchard MT, & Nagy LE (2013) Kupffer cells in the liver. *Compr Physiol* 3(2):785-797.

101. Geraud C, Koch PS, Zierow J, Klapproth K, Busch K, Olsavszky V, Leibing T, Demory A, Ulbrich F, Diett M, Singh S, Sticht C, Breitkopf-Heinlein K, Richter K, Karppinen SM, Pihlajaniemi T, Arnold B, Rodewald HR, Augustin HG, Schledzewski K, & Goerdt S (2017) GATA4-dependent organ-specific endothelial differentiation controls liver development and embryonic hematopoiesis. *J Clin Invest* 127(3):1099-1114.

102. Meng XM, Chung AC, & Lan HY (2013) Role of the TGF-beta/BMP-7/Smad pathways in renal diseases. *Clin Sci (Lond)* 124(4):243-254.

103. Brown MS & Goldstein JL (2009) Cholesterol feedback: from Schoenheimer's bottle to Scap's MELADL. *Journal of lipid research* 50 Suppl:S15-S27.

104. Radhakrishnan A, Sun LP, Kwon HJ, Brown MS, & Goldstein JL (2004) Direct binding of cholesterol to the purified membrane region of SCAP: mechanism for a sterol-sensing domain. *Mol Cell* 15(2):259-268.

105. Peet DJ, Janowski BA, & Mangelsdorf DJ (1998) The LXRs: a new class of oxysterol receptors. *Curr Opin Genet Dev* 8(5):571-575.

106. Yang C, McDonald JG, Patel A, Zhang Y, Umetani M, Xu F, Westover EJ, Covey DF, Mangelsdorf DJ, Cohen JC, & Hobbs HH (2006) Sterol intermediates from cholesterol biosynthetic pathway as liver X receptor ligands. *The Journal of biological chemistry* 281:27816-27826.

107. Muse ED, Yu S, Edillor CR, Tao J, Spann NJ, Troutman TD, Seidman JS, Henke A, Roland JT, Ozeki KA, Thompson BM, McDonald JG, Bahadorani J, Tsimikas S, Grossman TR, Tremblay MS, & Glass CK (2018) Cell-specific discrimination of desmosterol and desmosterol mimetics confers selective regulation of LXR and SREBP in macrophages. *Proc Natl Acad Sci U S A* 115(20):E4680-E4689.

108. Spann NJ, Garmire LX, McDonald JG, Myers DS, Milne SB, Shibata N, Reichart D, Fox JN, Shaked I, Heudobler D, Raetz CRH, Wang EW, Kelly SL, Sullards MC, Murphy RC, Merrill AH, Brown HA, Dennis Ea, Li AC, Ley K, Tsimikas S, Fahy E, Subramaniam S, Quehenberger O, Russell DW, & Glass CK (2012) Regulated accumulation of desmosterol integrates macrophage lipid metabolism and inflammatory responses. *Cell* 151:138-152.

109. Kratzer A, Buchebner M, Pfeifer T, Becker TM, Uray G, Miyazaki M, Miyazaki-Anzai S, Ebner B, Chandak PG, Kadam RS, Calayir E, Rathke N, Ahammer H, Radovic B, Trauner M, Hoefler G, Kompella UB, Fauler G, Levi M, Levak-Frank S, Kostner GM, & Kratky D (2009) Synthetic LXR agonist attenuates plaque formation in apoE-/- mice without inducing liver steatosis and hypertriglyceridemia. *J Lipid Res* 50(2):312-326.

110. Borggrefe T & Oswald F (2009) The Notch signaling pathway: transcriptional regulation at Notch target genes. *Cell Mol Life Sci* 66(10):1631-1646.

111. Chu J, Jeffries S, Norton JE, Capobianco AJ, & Bresnick EH (2002) Repression of activator protein-1-mediated transcriptional activation by the Notch-1 intracellular domain. *J Biol Chem* 277(9):7587-7597.

112. Nowell CS & Radtke F (2017) Notch as a tumour suppressor. *Nat Rev Cancer* 17(3):145-159.

113. Franklin RA, Liao W, Sarkar A, Kim MV, Bivona MR, Liu K, Pamer EG, & Li MO (2014) The cellular and molecular origin of tumor-associated macrophages. *Science* 344(6186):921-925.

114. Chakrabarti R, Celia-Terrassa T, Kumar S, Hang X, Wei Y, Choudhury A, Hwang J, Peng J, Nixon B, Grady JJ, DeCoste C, Gao J, van Es JH, Li MO, Aifantis I, Clevers H,

& Kang Y (2018) Notch ligand Dll1 mediates cross-talk between mammary stem cells and the macrophageal niche. *Science* 360(6396).

115. Nandagopal N, Santat LA, LeBon L, Sprinzak D, Bronner ME, & Elowitz MB (2018) Dynamic Ligand Discrimination in the Notch Signaling Pathway. *Cell* 172(4):869-880 e819.

116. Mullen AC, Orlando DA, Newman JJ, Loven J, Kumar RM, Bilodeau S, Reddy J, Guenther MG, DeKoter RP, & Young RA (2011) Master transcription factors determine cell-type-specific responses to TGF-beta signaling. *Cell* 147(3):565-576.

117. Travis MA & Sheppard D (2014) TGF-beta activation and function in immunity. *Annu Rev Immunol* 32:51-82.

118. Constam DB (2014) Regulation of TGFbeta and related signals by precursor processing. *Semin Cell Dev Biol* 32:85-97.

119. Parrow NL & Fleming RE (2017) Liver sinusoidal endothelial cells as iron sensors. *Blood* 129(4):397-398.

120. Avigan J, Steinberg D, Thompson MJ, & Mosettig E (1960) Mechanism of Action of MER-29, An inhibitor of cholesterol biosynthesis. *Biochemical and biophysical research communications* 2:63-65.

121. Prigge JR, Wiley JA, Talago EA, Young EM, Johns LL, Kundert JA, Sonsteng KM, Halford WP, Capecchi MR, & Schmidt EE (2013) Nuclear double-fluorescent reporter for in vivo and ex vivo analyses of biological transitions in mouse nuclei. *Mamm Genome*.

122. Clausen BE, Burkhardt C, Reith W, Renkawitz R, & Forster I (1999) Conditional gene targeting in macrophages and granulocytes using LysMcre mice. *Transgenic Res* 8(4):265-277.

123. Peet DJ, Turley SD, Ma W, Janowski BA, Lobaccaro JM, Hammer RE, & Mangelsdorf DJ (1998) Cholesterol and bile acid metabolism are impaired in mice lacking the nuclear oxysterol receptor LXR alpha. *Cell* 93(5):693-704.

124. Yang X, Li C, Herrera PL, & Deng CX (2002) Generation of Smad4/Dpc4 conditional knockout mice. *Genesis* 32(2):80-81.

125. Aida T, Chiyo K, Usami T, Ishikubo H, Imahashi R, Wada Y, Tanaka KF, Sakuma T, Yamamoto T, & Tanaka K (2015) Cloning-free CRISPR/Cas system facilitates functional cassette knock-in in mice. *Genome Biology* 16:87.

126. Mederacke I, Dapito DH, Affo S, Uchinami H, & Schwabe RF (2015) High-yield and high-purity isolation of hepatic stellate cells from normal and fibrotic mouse livers. *Nat Protoc* 10(2):305-315.

127. Sakai M, Matsumoto M, Tujimura T, Yongheng C, Noguchi T, Inagaki K, Inoue H, Hosooka T, Takazawa K, Kido Y, Yasuda K, Hiramatsu R, Matsuki Y, & Kasuga M (2012) CITED2 links hormonal signaling to PGC-1alpha acetylation in the regulation of gluconeogenesis. *Nat Med* 18(4):612-617.

128. Buenrostro JD, Giresi PG, Zaba LC, Chang HY, & Greenleaf WJ (2013) Transposition of native chromatin for fast and sensitive epigenomic profiling of open chromatin, DNA-binding proteins and nucleosome position. *Nat Methods* 10(12):1213-1218.

129. Heinz S, Texari L, Hayes MGB, Urbanowski M, Chang MW, Givarkes N, Rialdi A, White KM, Albrecht RA, Pache L, Marazzi I, Garcia-Sastre A, Shaw ML, & Benner C (2018) Transcription Elongation Can Affect Genome 3D Structure. *Cell* 174(6):1522-1536 e1522.

130. Dobin A, Davis CA, Schlesinger F, Drenkow J, Zaleski C, Jha S, Batut P, Chaisson M, & Gingeras TR (2013) STAR: Ultrafast universal RNA-seq aligner. *Bioinformatics* 29:15-21.

131. Davies LC, Jenkins SJ, Allen JE, & Taylor PR (2013) Tissue-resident macrophages. *Nature Immunology* 14:986-995.

132. Jakubzick C, Gautier EL, Gibbings SL, Sojka DK, Schlitzer A, Johnson TE, Ivanov S, Duan Q, Bala S, Condon T, van Rooijen N, Grainger JR, Belkaid Y, Ma'ayan A, Riches DW, Yokoyama WM, Ginhoux F, Henson PM, & Randolph GJ (2013) Minimal differentiation of classical monocytes as they survey steady-state tissues and transport antigen to lymph nodes. *Immunity* 39(3):599-610.

133. Yona S, Kim KW, Wolf Y, Mildner A, Varol D, Breker M, Strauss-Ayali D, Viukov S, Guilliams M, Misharin A, Hume DA, Perlman H, Malissen B, Zelzer E, & Jung S (2013) Fate Mapping Reveals Origins and Dynamics of Monocytes and Tissue Macrophages under Homeostasis. *Immunity* 38:79-91.

134. De Schepper S, Verheijden S, Aguilera-Lizarraga J, Viola MF, Boesmans W, Stakenborg N, Voytyuk I, Schmidt I, Boeckx B, Dierckx de Casterle I, Baekelandt V, Gonzalez Dominguez E, Mack M, Depoortere I, De Strooper B, Sprangers B, Himmelreich U,

Soenen S, Guilliams M, Vanden Berghe P, Jones E, Lambrechts D, & Boeckxstaens G (2018) Self-Maintaining Gut Macrophages Are Essential for Intestinal Homeostasis. *Cell* 175(2):400-415 e413.

135. Bain CC, Bravo-Blas A, Scott CL, Perdiguero EG, Geissmann F, Henri S, Malissen B, Osborne LC, Artis D, & Mowat AM (2014) Constant replenishment from circulating monocytes maintains the macrophage pool in the intestine of adult mice. *Nat Immunol* 15(10):929-937.

136. Bowman RL, Klemm F, Akkari L, Pyonteck SM, Sevenich L, Quail DF, Dhara S, Simpson K, Gardner EE, Iacobuzio-Donahue CA, Brennan CW, Tabar V, Gutin PH, & Joyce JA (2016) Macrophage Ontogeny Underlies Differences in Tumor-Specific Education in Brain Malignancies. *Cell Rep* 17(9):2445-2459.

137. Pirzgalska RM & Domingos AI (2018) Macrophages in obesity. *Cell Immunol* 330:183-187.

138. Kiss M, Van Gassen S, Movahedi K, Saeys Y, & Laoui D (2018) Myeloid cell heterogeneity in cancer: not a single cell alike. *Cell Immunol* 330:188-201.

139. Holtman IR, Skola D, & Glass CK (2017) Transcriptional control of microglia phenotypes in health and disease. *J Clin Invest* 127(9):3220-3229.

140. Geovanini GR & Libby P (2018) Atherosclerosis and inflammation: overview and updates. *Clin Sci (Lond)* 132(12):1243-1252.

141. Glass CK & Witztum JL (2001) Atherosclerosis. the road ahead. *Cell* 104(4):503-516.

142. Tabas I & Glass CK (2013) Anti-inflammatory therapy in chronic disease: challenges and opportunities. *Science* 339(6116):166-172.

143. Glass CK & Natoli G (2016) Molecular control of activation and priming in macrophages. *Nat Immunol* 17(1):26-33.

144. Pasare C & Medzhitov R (2005) Toll-like receptors: linking innate and adaptive immunity. *Adv Exp Med Biol* 560:11-18.

145. Franklin BS, Mangan MS, & Latz E (2016) Crystal Formation in Inflammation. *Annu Rev Immunol* 34:173-202.

146. Que X, Hung MY, Yeang C, Gonen A, Prohaska TA, Sun X, Diehl C, Maatta A, Gaddis DE, Bowden K, Pattison J, MacDonald JG, Yla-Herttuala S, Mellon PL, Hedrick CC, Ley K, Miller YI, Glass CK, Peterson KL, Binder CJ, Tsimikas S, & Witztum JL (2018) Oxidized phospholipids are proinflammatory and proatherogenic in hypercholesterolaemic mice. *Nature*.

147. Ju C & Tacke F (2016) Hepatic macrophages in homeostasis and liver diseases: from pathogenesis to novel therapeutic strategies. *Cellular and Molecular Immunology* 13:316-327.

148. Haas JT, Francque S, & Staels B (2016) Pathophysiology and Mechanisms of Nonalcoholic Fatty Liver Disease. *Annu. Rev. Physiol* 78:181-205.

149. Hardy T, Oakley F, Anstee QM, & Day CP (2016) Nonalcoholic Fatty Liver Disease: Pathogenesis and Disease Spectrum. *Annu. Rev. Pathol. Mech. Dis* 11:451-496.

150. MacHado MV & Diehl AM (2016) Pathogenesis of Nonalcoholic Steatohepatitis. *Gastroenterology* 150:1769-1777.

151. Musso G, Cassader M, & Gambino R (2016) Non-alcoholic steatohepatitis: emerging molecular targets and therapeutic strategies. *Nature Publishing Group* 15.

152. Rinella ME & Sanyal AJ (2016) Management of NAFLD: a stage-based approach. *Nature Reviews Gastroenterology and Hepatology* 13:196-205.

153. Younossi ZM, Blissett D, Blissett R, Henry L, Stepanova M, Younossi Y, Racila A, Hunt S, & Beckerman R (2016) The economic and clinical burden of nonalcoholic fatty liver disease in the United States and Europe. *Hepatology* 64:1577-1586.

154. Zigmond E, Samia-Grinberg S, Pasmanik-Chor M, Brazowski E, Shibolet O, Halpern Z, & Varol C (2014) Infiltrating Monocyte-Derived Macrophages and Resident Kupffer Cells Display Different Ontogeny and Functions in Acute Liver Injury. *The Journal of Immunology* 193:344-353.

155. Karlmark KR, Weiskirchen R, Zimmermann HW, Gassler N, Ginhoux F, Weber C, Merad M, Luedde T, Trautwein C, & Tacke F (2009) Hepatic recruitment of the inflammatory Gr1+ monocyte subset upon liver injury promotes hepatic fibrosis. *Hepatology* 50:261-274.

156. Seki E, De Minicis S, Gwak GY, Kluwe J, Inokuchi S, Bursill CA, Llovet JM, Brenner DA, & Schwabe RF (2009) CCR1 and CCR5 promote hepatic fibrosis in mice. *J Clin Invest* 119(7):1858-1870.

157. Seki E, de Minicis S, Inokuchi S, Taura K, Miyai K, van Rooijen N, Schwabe RF, & Brenner DA (2009) CCR2 promotes hepatic fibrosis in mice. *Hepatology* 50:185-197.

158. Mitchell C, Couton D, Couty J-P, Anson M, Crain A-M, Bizet V, Ré L, Pol S, Mallet V, Lè Ne Gilgenkrantz H, Rénia L, Pol S, Mallet V, & Gilgenkrantz H (2009) Dual Role of CCR2 in the Constitution and the Resolution of Liver Fibrosis in Mice. *The American Journal of Pathology* 174:1766-1775.

159. Hall D, Poussin C, Velagapudi VR, Empsen C, Joffraud M, Beckmann JS, Geerts AE, Ravussin Y, Ibberson M, Oresic M, & Thorens B (2010) Peroxisomal and microsomal lipid pathways associated with resistance to hepatic steatosis and reduced pro-inflammatory state. *Journal of Biological Chemistry* 285:31011-31023.

160. Poussin C, Ibberson M, Hall D, Ding J, Soto J, Abel ED, & Thorens B (2011) Oxidative phosphorylation flexibility in the liver of mice resistant to high-fat diet-induced hepatic steatosis. *Diabetes* 60:2216-2224.

161. Krenkel O, Puengel T, Govaere O, Abdallah AT, Mossanen JC, Kohlhepp M, Liepelt A, Lefebvre E, Luedde T, Hellerbrand C, Weiskirchen R, Longerich T, Costa IG, Anstee QM, Trautwein C, & Tacke F (2018) Therapeutic inhibition of inflammatory monocyte recruitment reduces steatohepatitis and liver fibrosis. *Hepatology* 67(4):1270-1283.

162. Dick SA, Macklin JA, Nejat S, Momen A, Clemente-Casares X, Althagafi MG, Chen J, Kantores C, Hosseinzadeh S, Aronoff L, Wong A, Zaman R, Barbu I, Besla R, Lavine KJ, Razani B, Ginhoux F, Husain M, Cybulsky MI, Robbins CS, & Epelman S (2019) Self-renewing resident cardiac macrophages limit adverse remodeling following myocardial infarction. *Nat Immunol* 20(1):29-39.

163. Gerner MY, Kastenmuller W, Ifrim I, Kabat J, & Germain RN (2012) Histo-cytometry: a method for highly multiplex quantitative tissue imaging analysis applied to dendritic cell subset microanatomy in lymph nodes. *Immunity* 37(2):364-376.

164. Heymann F & Tacke F (2016) Immunology in the liver - from homeostasis to disease. *Nature reviews. Gastroenterology & hepatology* 13:88-110.

165. Shook BA, Wasko RR, Rivera-Gonzalez GC, Salazar-Gatzimas E, Lopez-Giraldez F, Dash BC, Munoz-Rojas AR, Aultman KD, Zwick RK, Lei V, Arbiser JL, Miller-Jensen K, Clark DA, Hsia HC, & Horsley V (2018) Myofibroblast proliferation and heterogeneity are supported by macrophages during skin repair. *Science* 362(6417).

166. Ramachandran P, Pellicoro A, Vernon MA, Boulter L, Aucott RL, Ali A, Hartland SN, Snowdon VK, Cappon A, Gordon-Walker TT, Williams MJ, Dunbar DR, Manning JR, van Rooijen N, Fallowfield JA, Forbes SJ, & Iredale JP (2012) Differential Ly-6C expression

identifies the recruited macrophage phenotype, which orchestrates the regression of murine liver fibrosis. *P Natl Acad Sci USA* 109:E3186-3195.

167. Farrell G, Schattenberg JM, Leclercq I, Yeh MM, Goldin R, Teoh N, & Schuppan D (2018) Mouse models of nonalcoholic steatohepatitis Towards optimization of their relevance to human NASH. *Hepatology*.

168. Santhekadur PK, Kumar DP, & Sanyal AJ (2018) Preclinical models of non-alcoholic fatty liver disease. *J Hepatol* 68(2):230-237.

169. Clapper JR, Hendricks MD, Gu G, Wittmer C, Dolman CS, Herich J, Athanacio J, Villescaz C, Ghosh SS, Heilig JS, Lowe C, & Roth JD (2013) Diet-induced mouse model of fatty liver disease and nonalcoholic steatohepatitis reflecting clinical disease progression and methods of assessment. *Am J Physiol Gastrointest Liver Physiol* 305:G483-495.

170. Friedman SL, Neuschwander-Tetri BA, Rinella M, & Sanyal AJ (2018) Mechanisms of NAFLD development and therapeutic strategies. *Nat Med* 24(7):908-922.

171. Itoh M, Kato H, Suganami T, Konuma K, Marumoto Y, Terai S, Sakugawa H, Kanai S, Hamaguchi M, Fukaishi T, Aoe S, Akiyoshi K, Komohara Y, Takeya M, Sakaida I, & Ogawa Y (2013) Hepatic crown-like structure: a unique histological feature in non-alcoholic steatohepatitis in mice and humans. *PLoS One* 8(12):e82163.

172. Baddeley A, Rubak E, & Turner R (2016) *Spatial point patterns : methodology and applications with R* (CRC Press, Taylor & Francis Group, Boca Raton ; London ; New York) pp xvii, 810 pages.

173. Mederacke I, Dapito DH, Affò S, Uchinami H, & Schwabe RF (2015) High-yield and high-purity isolation of hepatic stellate cells from normal and fibrotic mouse livers. *Nature protocols* 10:305-315.

174. Satija R, Farrell JA, Gennert D, Schier AF, & Regev A (2015) Spatial reconstruction of single-cell gene expression data. *Nat Biotechnol* 33(5):495-502.

175. Link VM, Duttke SH, Chun HB, Holtman IR, Westin E, Hoeksema MA, Abe Y, Skola D, Romanoski CE, Tao J, Fonseca GJ, Troutman TD, Spann NJ, Strid T, Sakai M, Yu M, Hu R, Fang R, Metzler D, Ren B, & Glass CK (2018) Analysis of Genetically Diverse Macrophages Reveals Local and Domain-wide Mechanisms that Control Transcription Factor Binding and Function. *Cell* 173(7):1796-1809 e1717.

176. Oishi Y, Spann NJ, Link VM, Muse ED, Strid T, Edillor C, Kolar MJ, Matsuzaka T, Hayakawa S, Tao J, Kaikkonen MU, Carlin AF, Lam MT, Manabe I, Shimano H, Saghatelian A, & Glass CK (2016) SREBP1 Contributes to Resolution of Pro-inflammatory TLR4 Signaling by Reprogramming Fatty Acid Metabolism. *Cell Metabolism*:1-16.

177. Eichenfield DZ, Troutman TD, Link VM, Lam MT, Cho H, Gosselin D, Spann NJ, Lesch HP, Tao J, Muto J, Gallo RL, Evans RM, & Glass CK (2016) Tissue damage drives co-localization of NF-κB, Smad3, and Nrf2 to direct Rev-erb sensitive wound repair in mouse macrophages. *eLife* 5:554-562.

178. Langmead B & Salzberg SL (2012) Fast gapped-read alignment with Bowtie 2. *Nat Methods* 9:357-359.

179. Love MI, Huber W, & Anders S (2014) Moderated estimation of fold change and dispersion for RNA-seq data with DESeq2. *Genome Biol* 15(12):550.

180. Tripathi S, Pohl MO, Zhou Y, Rodriguez-Frandsen A, Wang G, Stein DA, Moulton HM, DeJesus P, Che J, Mulder LC, Yanguez E, Andenmatten D, Pache L, Manicassamy B, Albrecht RA, Gonzalez MG, Nguyen Q, Brass A, Elledge S, White M, Shapira S, Hacohen N, Karlas A, Meyer TF, Shales M, Gatorano A, Johnson JR, Jang G, Johnson T, Verschueren E, Sanders D, Krogan N, Shaw M, Konig R, Stertz S, Garcia-Sastre A, & Chanda SK (2015) Meta- and Orthogonal Integration of Influenza "OMICs" Data Defines a Role for UBR4 in Virus Budding. *Cell Host Microbe* 18(6):723-735.

181. Li Q, Brown JB, Huang H, & Bickel J (2011) Measuring reproducibility of high-throughput experiments. *The Annals of Applied Statistics* 5(3):1752-1779.

182. Kent WJ, Sugnet CW, Furey TS, Roskin KM, Pringle TH, Zahler AM, & Haussler D (2002) The human genome browser at UCSC. *Genome Res* 12(6):996-1006.

183. Bleriot C, Dupuis T, Jouvion G, Eberl G, Disson O, & Lecuit M (2015) Liver-resident macrophage necroptosis orchestrates type 1 microbicidal inflammation and type-2-mediated tissue repair during bacterial infection. *Immunity* 42(1):145-158.

184. Poisson J, Lemoinne S, Boulanger C, Durand F, Moreau R, Valla D, & Rautou PE (2017) Liver sinusoidal endothelial cells: Physiology and role in liver diseases. *J Hepatol* 66(1):212-227.

185. Becares N, Gage MC, & Pineda-Torra I (2017) Posttranslational Modifications of Lipid-Activated Nuclear Receptors: Focus on Metabolism. *Endocrinology* 158(2):213-225.

186. Yamamoto T, Shimano H, Inoue N, Nakagawa Y, Matsuzaka T, Takahashi A, Yahagi N, Sone H, Suzuki H, Toyoshima H, & Yamada N (2007) Protein kinase A suppresses sterol regulatory element-binding protein-1C expression via phosphorylation of liver X receptor in the liver. *J Biol Chem* 282(16):11687-11695.

187. Chen M, Bradley MN, Beaven SW, & Tontonoz P (2006) Phosphorylation of the liver X receptors. *FEBS Lett* 580(20):4835-4841.

188. Torra IP, Ismaili N, Feig JE, Xu CF, Cavasotto C, Pancratov R, Rogatsky I, Neubert TA, Fisher EA, & Garabedian MJ (2008) Phosphorylation of liver X receptor alpha selectively regulates target gene expression in macrophages. *Mol Cell Biol* 28(8):2626-2636.

189. Becares N, Gage MC, Voisin M, Shrestha E, Martin-Gutierrez L, Liang N, Louie R, Pourcet B, Pello OM, Luong TV, Goni S, Pichardo-Almarza C, Roberg-Larsen H, Diaz-Zuccarini V, Steffensen KR, O'Brien A, Garabedian MJ, Rombouts K, Treuter E, & Pineda-Torra I (2019) Impaired LXRalpha Phosphorylation Attenuates Progression of Fatty Liver Disease. *Cell Rep* 26(4):984-995 e986.

190. Okabe Y & Medzhitov R (2016) Tissue biology perspective on macrophages. *Nat Immunol* 17(1):9-17.

191. Boyle WJ, Simonet WS, & Lacey DL (2003) Osteoclast differentiation and activation. *Nature* 423:337-342.

192. Suzuki T, Arumugam P, Sakagami T, Lachmann N, Chalk C, Sallese A, Abe S, Trapnell C, Carey B, Moritz T, Malik P, Lutzko C, Wood RE, & Trapnell BC (2014) Pulmonary macrophage transplantation therapy. *Nature* 514(7523):450-454.

193. Dranoff G, Crawford AD, Sadelain M, Ream B, Rashid A, Bronson RT, Dickersin GR, Bachurski CJ, Mark EL, Whitsett JA, & et al. (1994) Involvement of granulocyte-macrophage colony-stimulating factor in pulmonary homeostasis. *Science* 264(5159):713-716.

194. Schultze JL (2016) Reprogramming of macrophages--new opportunities for therapeutic targeting. *Curr Opin Pharmacol* 26:10-15.